Technologies for photonic integration

Gibbon, Mark

Award date:
1995

Awarding institution:
University of Bath

Technologies for Photonic Integration

submitted by Mark Gibbon
for the degree of PhD
of the University of Bath
1995

BNR Europe Limited
London Road, Harlow, Essex, CM17 9NA, England

ProQuest LLC
789 East Eisenhower Parkway
P.O. Box 1346
Ann Arbor, MI 48106-1346

To Jackie

for preserving my sanity through welcome diversion

Summary

Photonic integration is the fabrication of optical and optoelectronic semiconductor devices on the same substrate, so that light can be coupled between them. This dissertation describes the development of two technologies for photonic integration, and their demonstration through the fabrication of integrated devices.

The first technology was one to perform passive optical functions in a slab waveguide on an InP substrate. The optical operations were achieved by total internal reflection of the slab guided mode, from the vertical walls of appropriately shaped recesses. The recesses were defined by CH_4/H_2 reactive ion etching interposed with a novel oxygen plasma passivation scheme. The technology was demonstrated by the fabrication of a 2D demultiplexer on an InP substrate. The optical output from this device was almost diffraction limited and the dispersion was in good agreement with the calculated value. The loss on reflection from each vertical wall was between 2 and 2.5dB depending upon its function. It was the world's first InP based, slab waveguide demultiplexer.

The second technology was selective area MOCVD. The nature of this phenomenon was studied in a quantitative manner and a world-leading model of its behaviour was developed. The capability of the technology was then demonstrated by the integration of a laser and an electroabsorption modulator. This device was designed to be compatible with on-wafer testing technology. The loss in the selectively grown interface between the laser and the modulator was <0.2dB and more than 10mW of optical power was coupled from the laser into the modulator. An open eye was obtained at 5Gb/s and a pseudo random bit sequence was transmitted over 380km of standard fibre at 2.5Gb/s.

Acknowledgements

I am indebted to Ted Thrush and Cliff Cureton for the epitaxial growth of the material described in this thesis, and for their advice on all aspects of MOCVD. I would also like to thank Dave Moule, Sue Wheeler, Julie Morley, Darren Goodchild and Ron Turner for processing the demultiplexer and the integrated laser modulator. Dave and Sue provided excellent and cheerful advice in long sessions spent attempting to thrash out the optimum design for the above devices. Dave also worked with Steve Clements to develop the self-aligned lithography process required in the fabrication of the demultiplexer.

I am grateful to Colin Rogers and Bob Baulcomb for developing the electron beam grating fabrication process for the laser-modulator. Colin also made the photolithographic masks for the demultiplexer. I am indebted to John Stagg for his assistance with the assessment of selective area MOCVD. Thanks are also due to Chester Jones, Bob Mallard, Rhian Pritchard and Alison Chew, who applied their respective skills at cathodoluminescence, TEM, LTPL and SIMS to the same material. I would like to express my gratitude to Dave Boyle and Phil Davies, who developed the on wafer testing system, and to Bipin Patel, Mark Kimber, Pete Anslow and Thomas Lee for their help with systems testing. The devices were packaged and bonded for this testing by Paul Gurton and Kevin Warbrick. Julian Fells of Bath University provided invaluable chirp measurement data and advice.

I would particularly like to thank Robin Thompson and Professor Ian White for their advice and encouragement thoughout the progress of the research.

The development of the demultiplexer and of selective area MOCVD were partially supported by the UK Department of Trade and Industry under JOERS and LINK schemes respectively. The work on the integrated laser modulator was partially supported by the European Community RACE 1027 and 2006 programs.

Finally I would like to thank BNR Europe Limited, and in particular Alastair Hyndman and Paul Rosser, for funding this PhD and for giving me the liberty to do the work required.

Outline of this Dissertation

This dissertation describes the development of two integration technologies: one to perform passive optical functions on an InP substrate and the other to enable the integration of devices requiring different bandgaps. The technologies were demonstrated by the fabrication of a demultiplexer on an InP substrate and a laser integrated with an electroabsorption modulator.

The dissertation is constructed as follows. Chapter 1 describes the concept of photonic integration and the reasons why integrated devices may be desirable in the telecommunications industry. Chapters 2-5 deal with the technology development required for the demultiplexer. Chapters 6-10 describe that for the integrated laser modulator. Finally, chapter 11 outlines possible future developments in photonic integration. The blocks of chapters are broken down in the manner described below.

Chapter 2 reviews the performance that other workers had achieved with hybrid and integrated demultiplexing components at the time when we fabricated our device. (Subsequent developments are reviewed along with results from our device in chapter 5.)

Chapter 3 describes the demultiplexer fabricated at BNR Europe. This component was the concept and design of Robin Thompson. It was the first InP-based device to make use of two dimensional optics in a slab waveguide. It also contained a transmission echelon grating of unique design. My inputs to the design process were suggestions on how to make the device easier to manufacture and test.

Chapter 4 describes the development of the technology required for the demultiplexer. I developed the mirror etching process described in this chapter and used it to etch the mirrors and waveguides of the final demultiplexer. I also performed the analysis of the uniformity of the epitaxial growth.

Chapter 5 documents the fabrication of the demultiplexer, and my subsequent assessment of its performance. The chapter also discusses the design modifications and technology development required to make the performance

of the two dimensional demultiplexer competitive with that of its hybrid equivalents.

As mentioned above the second block of chapters deals with the technology development required for the integrated laser modulator. The first chapter of this block is chapter 6, which reviews methods of integrating devices which require different bandgaps.

Chapter 7 describes a detailed experimental and theoretical study of the technology required for one of the integration methods reviewed in chapter 6. The integration method studied was selective area MOCVD. There are a large number of publications on this topic but few authors have attempted a comprehensive quantitative study of the type described in chapter 7. The quantitative data produced in this study enabled the development of a model to predict the behaviour of selective area MOCVD. I am only aware of one other report of such a model. I designed the experiments and performed most of the measurements described in the chapter, though some of the investigations involved working with experts in other areas. The model of selective area MOCVD was also my invention.

Chapter 8 describes the behaviour of the component parts of an integrated laser modulator. I designed and assessed the selectively grown lasers described in this chapter. However, Robin Thompson initially performed the calculation of interface efficiency.

The design, fabrication and performance of the laser-modulator produced at BNR Europe are documented in chapter 9. We were not the first group to publish on the fabrication of an integrated laser modulator through the use of selective area epitaxy. However our work was already well advanced when M.Aoki of Hitachi and T.Kato of NEC reported their development of such devices. To the best of my knowledge, we were the first group to apply probe card testing to the fabrication of integrated laser modulators, though IBM in Zurich had already reported on the use of such technology in low cost laser fabrication. I designed the integrated laser modulator and the photolithographic masks required to make it. It was my idea to use probe card testing and I worked with Dave Boyle and Phil Davies to develop the required

apparatus. I also performed the continuous wave assessment of the first wafer of integrated laser modulators described in chapter 9. The systems part of this assessment was performed in collaboration with Mark Kimber, Bipin Patel and Pete Anslow.

The work described in chapters 7 to 9 spawned further development of the integrated laser modulator at BNR Europe. The output of this development activity is outlined in chapter 10, as it was in this period that some of the seeds sown in the design of the device started to bear fruit. In this phase of the project the size of the development team grew to a maximum of about 12 people. I co-ordinated this team, in conjunction with Chris Armistead. My technical input to the work described in this chapter was in the device design, the systems assessment and the analysis of test results. This chapter also compares the performance of laser modulators fabricated at BNR Europe with those fabricated at other laboratories.

List of Papers

In the course of the above research I have published the following papers as first author.

[1] M.Gibbon, G.H.B.Thompson, S.J.Clements, D.J.Moule, C.B.Rodgers and C.G.Cureton, **"Optical performance of integrated 1.5μm grating wavelength-demultiplexer on InP-based waveguide"**, *IEE Electronics Letters*, 1989, **25**, pp.1441-1442

[2] M.Gibbon, G.H.B.Thompson, S.J.Clements, D.J.Moule, C.B.Rodgers, and C.G.Cureton, **"Integrated 1.5μm grating wavelength-demultiplexer on InP-based slab waveguide"**, *Proceedings of 15th European Conference on Optical Communication (ECOC'89)*, (Novum Grafiska AB, Sweden, 1989), pp.316-319

[3] M.Gibbon, J.P.Stagg, C.G.Cureton, E.J.Thrush, C.J.Jones, R.E.Mallard, R.E.Pritchard, N.Collis and A.Chew, **"Selective-area low pressure MOCVD of GaInAsP and related materials on planar InP substrates"**, *Semiconductor Science and Technology*, 1993, 8, pp.998-1010

[4] M.Gibbon, G.H.B.Thompson, D.Boyle, J.P.Stagg, B.Patel, D.J.Moule, S.Wheeler, C.B.Rodgers, E.J.Thrush, K.Warbrick and P.Gurton, **"High speed electroabsorption modulator monolithically integrated with a 2xλ /8 DFB laser and back monitor by selective area MOVPE"**, *Proceedings of 19th European Conference on Optical Communication (ECOC'93)*, (Druckerei Richterswil AG, Richterswil, 1993), pp.325-328

[5] M.Gibbon, C.J.Armistead, D.Boyle, P.J.Rosser, B.Patel, D.J.Moule, S.Wheeler, J.Morely, C.B.Rodgers, E.J.Thrush, K.Warbrick and P.Gurton, **"Integrated laser modulators for low chirp high capacity transmission"**, *Rank Prize Funds meeting on all-optical networks, Grasmere, England, 11-14 April 1994*

I am also a subsidiary author on fourteen other papers.

Table of Contents

Chapter 10

Recent Developments in Laser-Modulator Integration

Chapter 11

The Future for Photonic Integration

Appendices

Chapter 1

Optoelectronic Devices for Future Telecommunications Systems

1.1. THE DEMAND FOR BANDWIDTH

Optical technology has made a significant impact on the communications industry, so that, to-day, much of the trunk route traffic is carried on optical fibre[1,2]. The demand for capacity over this trunk network is growing. One reason is the steady growth in the number of telephone lines per head of the population[3]. The demand for bandwidth is increased by the provision of new services over the existing telecommunications network. These include video conferencing, fax and data transmission[4]. Large capacities will soon also be required for subscriber links, as cable television and related interactive services start to make an impact in the United Kingdom[4].

At present the large capacity required in trunk links is provided by using several fibres, and by time division multiplexing[5] (TDM) a large number of channels onto the single wavelength carried by each fibre. In this situation an increase in the demand for capacity can be satisfied by simply laying more optical fibres. However, this is often an expensive solution as the costs of laying cable are high. The alternative is to increase the data carrying capacity of each fibre. This can be achieved by:

a) increasing the bit rate so that more channels can be time division multiplexed onto a single wavelength.
b) increasing the number of wavelengths carried by each fibre.

The merits of each of these approaches are discussed below.

1.2. HIGH BIT RATE SYSTEMS

The maximum transmission rate in wide commercial use to-day is 2.5Gb/s. When one attempts to increase this bit rate one encounters a number of problems. These include:

a) the difficulty of obtaining reasonably priced electronic components with sufficient performance[6,7].
b) the dispersion in conventional optical fibre.

The difficulties created by fibre dispersion are described below.

Standard single mode silica fibre has a dispersion zero at a wavelength of 1.3μm. However, most long haul transmission takes place at a wavelength of 1.55μm, where the loss is lower. The dispersion at the latter wavelength is typically around 17ps/nm/km. The effect of this dispersion is that the different optical frequencies in the transmitted bit pattern travel at different speeds, so that adjacent bits are smeared into each other. The distance that one can transmit before this occurs decreases with increasing data rate. The maximum transmission distance is also dependent on the range of optical frequencies contained within the signal. Fourier theory indicates that there is a fundamental lower limit for this frequency range, which is determined by the bandwidth of the transmitted signal[8]. Consequently there is a limit on the maximum transmission distance that can be achieved in standard fibre with an ideal source. This distance[9,10,11] is about 60km for modulation at 10Gb/s.

One solution to the dispersion problem is to use dispersion shifted fibre[12]. This has a much smaller dispersion coefficient than standard fibre at 1.55μm. However, if standard fibre is already installed, one must lay new cables which, as mentioned above, can be expensive. In this situation, one can compensate for the dispersion in existing fibre by introducing a dispersive element with dispersion of the same magnitude and opposite sign to that in the fibre[13,14,15]. Another solution is to control carefully the frequency excursions of the source, so that the transmission distance is maximised. In practice the frequency excursions of the source need to be well controlled even when dispersion compensation techniques are employed, as the correction is rarely perfect.

The source used in most of to-day's commercial links is a semiconductor laser[16]. The data pattern for transmission is superimposed on the optical output from the laser by modulating the drive current supplied to it. This is a simple solution as there is only one optical component in the transmitter. However, the optical frequency generated by such a source tends to fluctuate as the drive current is modulated[17]. These fluctuations in optical frequency are known as "chirp". The net result is that the range of optical frequencies contained in the signal are considerably in excess of the minimum imposed by Fourier theory[8]. Consequently transmission down dispersive fibre at high data rates is difficult to achieve with direct laser modulation.

The transmitter chirp can be reduced by driving the laser with a constant current and modulating its output with an external modulator[18]. In fact it is even possible to exceed the maximum transmission distance for an ideal zero chirp source with this arrangement[19]. This is achieved by driving the modulator to produce a higher than average optical frequency on the falling edge of a bit, and the converse on the rising edge. This frequency distribution causes pulse compression when combined with the dispersion in standard fibre. It is usually known as "negative chirp".

1.3. WAVELENGTH DIVISION MULTIPLEXED SYSTEMS

The data rate can also be increased by simultaneously transmitting on a number of wavelengths. This is known as wavelength division multiplexing (WDM)[20,21]. The advantage of this technique is that the electronics are easier to engineer than for an equivalent TDM system. Fibre dispersion is also less troublesome. In addition, wavelength division multiplexing opens up the possibility of novel network architectures where, for example, the transmitting node can be identified by the wavelength on which it transmits[22,23,24].

The disadvantage of a WDM system is that a number of transmitters and receivers are required. This tends to make WDM a more expensive option than TDM. An optical device to demultiplex the different wavelengths is also required[25].

1.4. PHOTONIC INTEGRATION FOR HIGH CAPACITY SYSTEMS

The above types of system can both be implemented using components that are already on the market. However, these implementations involve making hybrid sources or detectors which contain a number of optical and optoelectronic components. Hybrid devices of this type are expensive as the components inside them must be individually aligned. The hybrid assembly must also be designed to withstand temperature and vibration over a long time period. The expense is probably not a serious issue for the highest capacity systems, as many of the components in such systems are expensive, and they are produced in relatively low volumes. However it does become a serious problem when such systems start being deployed in larger numbers. It is in this situation that photonic integration[26] becomes attractive. Such integration

involves coupling light between optical and optoelectronic components monolithically integrated on the same chip.

The advantage of photonic integration is that the integrated components are rigidly aligned to each other by a common substrate. This alignment automatically takes place during the fabrication process. Integration also offers potential performance advantages when joining waveguide based devices. For example, there is often an improvement in the efficiency with which light is coupled from one device to the next. The optical polarisation is also automatically maintained as light passes between devices. However, integration is only a practical proposition if:

a) the performance of the integrated device is comparable to or better than that of its hybrid equivalent.
b) the devices are easy to make, so that the cost benefits in packaging are not negated by a more complicated and lower yield fabrication process.

1.5. FABRICATION TECHNOLOGIES FOR PHOTONIC INTEGRATION

If one considers the components that are required for WDM and TDM then it is apparent that two useful integration technologies are:

a) the ability to perform passive optical functions, such as diffraction, on an optical substrate which is compatible with active optoelectronic devices.
b) the ability to make an interface between devices with different bandgaps.

The work on which this dissertation is based involved developing technologies to perform both of the above functions. The objectives of this dissertation can be summarised as follows.

a) To illustrate how operations normally carried out by free space optics may be performed in two dimensions in a slab waveguide on an InP substrate. The viability of such technology is demonstrated by the fabrication of a grating spectrometer for use as a demultiplexer.

b) To demonstrate how devices requiring different epitaxial layer structures may be integrated together with minimum additional fabrication complexity. The technology required for this is demonstrated by the integration of an electroabsorption modulator with a DFB laser.

1.6. REFERENCES

1 R.Herz, Communications International (Siemens sponsored supplement), Oct 1987, pp.23-28

2 P.Cochrane, M.Brain, IEEE Communications Magazine, Nov 1988, pp.45-60

3 The number of telephone lines per 100 people in the United Kingdom grew from 34 to 46 in the period from 1982 to 1992. [Source D.Sherlock, *"European Communications: Technologies and Regualtions of the Single Market"*, (Blenheim, London, 1989), pp.1-13]

4 D.Sherlock, *"European Communications: Technologies and Regualtions of the Single Market"*, (Blenheim, London, 1989), pp.41-48

5 F.G.Stremler, *"Introduction to communication systems"*, (Addison-Wesley, New York, 1990), pp.377-384

6 J.M.Senior and S.D.Cusworth, IEE Proc.J, 1989, **136**, pp.183-202

7 R.Tucker, G.Eisenstein, S.Korotky, J. Lightwave Technology, 1988, **6**, pp.1737-1749

8 F.G.Stremler, *"Introduction to communication systems"*, (Addison-Wesley, New York, 1990), pp.82-218

9 Private communication with E.M.Kimber, BNR Europe.

10 G.P.Agrawal, *"Non-linear fibre optics"*, (Academic Press, London, 1989), pp.54-73

11 A.F.Elrefaie, R.E.Wagner, D.A.Atlas and D.G.Daut, *Journal of Lightwave Technology*, 1988, 6, pp.704-709

12 J.Senior, *"Optical fibre communications: princples and practice"*, (Prentice-Hall, Englewood Cliffs, NJ, 1985), pp.94-98

13 M.Onishi, H.Ishikawa, M.Shigematsu, H.Kanamori and M.Nishimura, *Proceedings of conference on optical fibre communication*, 1994, (IEEE Catalog No. 94CH3422-3), pp.224-225

14 A.M.Vengsarkar, A.E.Miller, M.Haner, A.H.Gnauck, W.A.Reed and K.L.Walker, *Proceedings of conference on optical fibre communication*, 1994, (IEEE Catalog No. 94CH3422-3), pp.225-227

15 B.Eggleton, P.A.Krug, L.Poladian, *Proceedings of conference on optical fibre communication*, 1994, (IEEE Catalog No. 94CH3422-3), p.227

16 G.P.Agrawal and N.K.Dutta, *"Long wavelength semiconductor lasers"*, (Van Nostrand Reinhold, New York, 1986)

17 J.E.A.Whiteaway, B.Garrett, G.H.B.Thompson, A.J.Collar, C.J.Armistead and M.J.Fice, *IEEE Journal of Quantum Electronics*, 1992, **28**, pp.1277-1293

18 A. Djupsjobacka, *IEEE Photonics Technology Letters*, 1992, **4**, pp.41-43

19 F.Koyama and K.Iga, *Journal of Lightwave Technology*, 1988, **6**, pp.87-93

20 S.S.Wagner and H.Kobrinski, IEEE Communications Magazine, Mar 1989, pp.22-30

21 A.Lord, L.C.Blank, J.M.Boggis and W.A.Stallard, Br Telecom Technol J, 1988, **6**, pp.18-23

22 P.A.Kirkby, Electron. Lett., 1990, **26**, pp.19-21

23 P.A.Kirkby, J Lightwave Technology, 1990, **8**, pp.202-211

24 D.B.Payne and J.R.Stern, Journal of Lightwave Technology, 1986, **LT-4**, pp.864-869

25 Y.Kanabar and N.Baker, Electron. Lett., 1989, **25**, pp.817-819

26 U.Koren, T.L.Koch, B.I.Miller and A.Shahar, *Topical meeting on integrated and guided wave optics (IGWO), Houston, Texas, 1989*, pp.68-71

Chapter 2

Component Technology for Wavelength Division Multiplex Systems

2.1. INTRODUCTION

As mentioned in chapter 1, a key component for WDM systems is a device which will either demultiplex the different wavelengths emerging from a fibre or perform the reverse operation. This chapter reviews the performance that other workers have achieved with hybrid and integrated demultiplexing components.

2.2. BULK OPTIC AND FIBRE BASED WDM COMPONENTS

It is quite possible to construct a demultiplexer using discrete optical components and technologies that are available today. For example Tekippe et al[1] have demonstrated a fused fibre coupler in which the coupling length was adjusted so that it discriminated between wavelengths of 1320 and 1550 nm. Insertion losses and crosstalk levels were of the order of 0.1 and 17 dB respectively. Fibre couplers are easy to make, and are stable to environmental fluctuations but it is impossible to separate more than two channels in each component, and difficult to separate channels which are closely spaced in wavelength[2].

An alternative approach is to select the different wavelengths by means of dielectric thin film filters[3]. Hendricks and coworkers[4] have demonstrated such a dielectric filter device. In this device four channels at 10 nm wavelength spacings were demultiplexed with interchannel crosstalk levels of less than -28 dB. However when a large number of channels must be separated dielectric filter devices become somewhat complicated. The reason is that each filter must be illuminated in turn so that alignments become critical and the insertion losses increase. In these circumstances, a device based on a single dispersive element, such as a diffraction grating, becomes attractive. A number of such grating based devices have already been demonstrated. For example, Kanabar et al[5] have recently tested a demultiplexer in which the output from a fibre was collimated onto a grating and then focused down onto an array of

photodiodes. Using this arrangement it was possible to separate sixteen channels of 2 nm bandwidth, with a channel spacing of 4 nm. Insertion losses were less than 3 dB and crosstalk, which was dominated by interacting electrical rather than optical signals, was in the range of -23 to -27 dB.

2.3. HYBRID AND MONOLITHICALLY INTEGRATED WDM COMPONENTS

The results summarised in the preceding section indicate that it is already possible to construct demultiplexers which have adequate performance for use in a commercial digital communication system. However, all of these devices must be individually assembled and, with the exception of fused fibre couplers, carefully aligned. This not only increases their cost, thus restricting them to specialist application, but also opens questions about their stability when subject to vibration or temperature fluctuations. Monolithic integration is one way of overcoming these difficulties, as a large number of devices can be produced on one wafer, and all the alignments are simultaneously defined by means of photolithography. However such an approach will only be successful if the performance of integrated devices is at least comparable to that of the hybrid alternatives.

Integrated multiplexers and demultiplexers can be classified into groups which, perhaps not surprisingly, are closely related to the hybrid devices discussed above. For example, the integrated equivalent of the fused fibre coupler is the wavelength dependent coupler[6,7,8,9,10], in which two waveguides are brought close together so that their evanescent fields interact with each other. In the same way, dielectric thin film filters can be compared with Bragg reflecting filters[11,12,13,14,15], where the thin films are replaced by a periodic perturbation in the effective index of a waveguide. Integrated devices based on these two concepts may well be desirable if one only needs to separate a few channels but, as the number of channels increases the individual components must be cascaded[16], so that the losses accumulate and a larger area of semiconductor is required. Once again, as in the bulk optic case, it seems desirable to use a single dispersive element, such as a two dimensional diffraction grating, to overcome these difficulties. A slab waveguide device, incorporating such a diffraction grating, has been demonstrated by Valette and coworkers[17] in the silica on silicon system. In this device four channels at 20 nm wavelength spacings were demultiplexed with a fibre to fibre loss of about 12 dB. However it is not easy to monolithically integrate detectors which operate at a wavelength of 1.5 μm with the silica on silicon system, and hence it

is of interest to develop an equivalent device in the InGaAsP/InP material system, where it is possible to integrate with active components[18,19,20,21,22,23,24,25]. Chapter 3, 4 and 5 describe the design, fabrication and assessment of such a device.

2.4. REFERENCES

1 V.J.Tekippe, C.M.Lawson, P.M.Kopera and T.Y.Hsu, Proc. SPIE, 1985, **574**, pp.92-99

2 H.Yanagawa, T.Ochiai, H.Hayakawa and H.Miyazawa, IEE Electronics Letters, 1988, **24**, pp.312-313

3 D.J.McCartney, D.B.Payne and S.S.Duncan, Optics Letters, 1985, **10**, pp.303-305

4 H.D.Hendricks, Proc. SPIE, 1983, **417**, pp.5-12

5 Y.Kanabar and N.Baker, Electron. Lett., 1989, **25**, pp.817-819

6 R.Marz and H.P.Nolting, Optical and Quantum Electronics, 1987, **19**, pp.273-287

7 C.De Bernardi, S.Morasca, C.Rigo, B.Surdo, A.Stano, I.R.Crosten and T.P.Young, Electron. Lett., 1989, **25**, pp.1488-1489

8 G.H.B.Thompson, J.Lightwave Techology, 1986, **LT-4**, pp.1678-1693

9 F.Rottmann and E.Voges, IRR Electronics Letters, 1987, **23**, pp.1007-1008

10 B.Broberg, B.S.Lindgren, M.G.Oberg and H.Jiang, Journal of Lightwave Technology, 1986, **LT-4**, pp.196-203

11 G.Winzer, J. Lightwave Technol., 1984, **LT-2**, pp.369-378

12 T.Suhara and H.Nishihara, IEEE J Quantum Electronics, 1986, **QE-22**, pp.845-867

13 R.C.Alferness, C.H.Joyner, M.D.Divino, M.J.R.Martyak and L.L.Buhi, Applied Physics Letters, 1986, **49**, pp.125-127

[14] C.Cremer, G.Heise, R.Marz, H.Riechert and M.Schienle, IEE Electronics Letters, 1987, **23**, pp.321-322

[15] D.C.Park and S.K.Kim, IEE Electronics Letters, 1988, **24**, pp.232-233

[16] K.Imoto, H.Sano and M.Miyazaki, IEE Electronics Letters, 1987, 23,pp.735-736

[17] S.Valette, P.Gidon, J.P.Jadot, Proc European Conf on Integrated Optics ECIO 87, Glasgow, 1987, pp.145-147

[18] M.Erman, P.Riglet, P.Jarry, B.G.Martin, M.Renaud, J.F.Vinchant and J.A.Cavailles, IEEE Proceedings-J, 1991, **138**, pp.101-108

[19] M.Renaud, J.F.Vinchant, P.Jarry, J.Le Bris, J.G.Provost, J.A.Cavailles and M. Erman, IEEE Photonics Technology Letters, 1992, **4**, pp.1372-1374

[20] M.Erman, M.Renaud, J.A.Cavailles, J.Vinchant, P.Jarry and C.Graver, Journal of Lightwave Technology, 1992, **10**, pp.1409-1414

[21] K.Kato, S.Hata, A.Kozen, S.Oku, S.Matsumoto and J.Yoshida, Electronics Letters, 1992, **28**, pp.1140-1142

[22] M.Gibbon, G.H.B.Thompson, S.J.Clements, D.J.Moule, C.B.Rodgers and C.G.Cureton, Electronics Letters, 1989, **25**, pp.1441-1442

[23] J.B.D.Soole, A.Scherer, J.P.LeBlanc, N.C.Andreadakis, R.Bhat, M.A.Koza, Electronics Letters, 1991, **27**, pp.132-134

[24] J.B.Soole, A.Scherer, Y.Silberberg, H.P.LeBlanc, N.C.Andreadakis, C.Caneau and K.R.Poguntke, Electronics Letters, 1993, **29**, pp.558-560

[25] C.Cremer, G.Ebbinghaus, G.Heise, R.Muller-Nawrath, M.Schienie and L.Stoll, Applied Physics Letters, 1991, **59**, pp.627-629

Chapter 3

Design of a 2D Grating Wavelength Demultiplexer

3.1. INTRODUCTION

The fabrication procedure for an integrated device can be simplified by using the same process to create components with different functions. This chapter describes how the above philosophy was applied to the design of the 2D demultiplexer. It also explains how the optical arrangement of the device was chosen to optimise its performance in its intended application.

3.2. DEVICE DESIGN

The design of the 2D grating wavelength demultiplexer is illustrated in Figure 3.1. The device was based on a single mode slab waveguide[1] formed by the epitaxial growth of a layer of GaInAsP on an InP substrate. All optical operations were performed by the total internal reflection of the slab-guided mode from semiconductor-air interfaces, which were produced by etching vertically sided recesses through the epitaxial layer into the substrate. This arrangement allowed use of conventional Fourier Transform optics[2], but with the light confined in the vertical direction. Light was input to the device by means of a single-mode ridge waveguide[1]. The diverging output from this guide was collimated by a parabolic mirror (created by etching a recess with an appropriately shaped wall), diffracted from a grating, and then focused down onto an output waveguide by a second curved mirror.

The diffraction efficiency of the grating was of paramount importance as, if an integrated demultiplexer is to be an economic proposition, the losses on diffraction must be controlled to values close to those of the bulk optical devices discussed in the preceding chapter. A large dispersion coefficient was also advantageous as it allowed one to reduce the size of a device, which in turn reduced the effects of any material non-uniformities (see section 4.2). A broad bandwidth, on the other hand, was less important as the device was intended for use with silica fibre. The low loss window in silica fibre spans only a relatively small range of wavelengths[3]. A high degree of resolution was

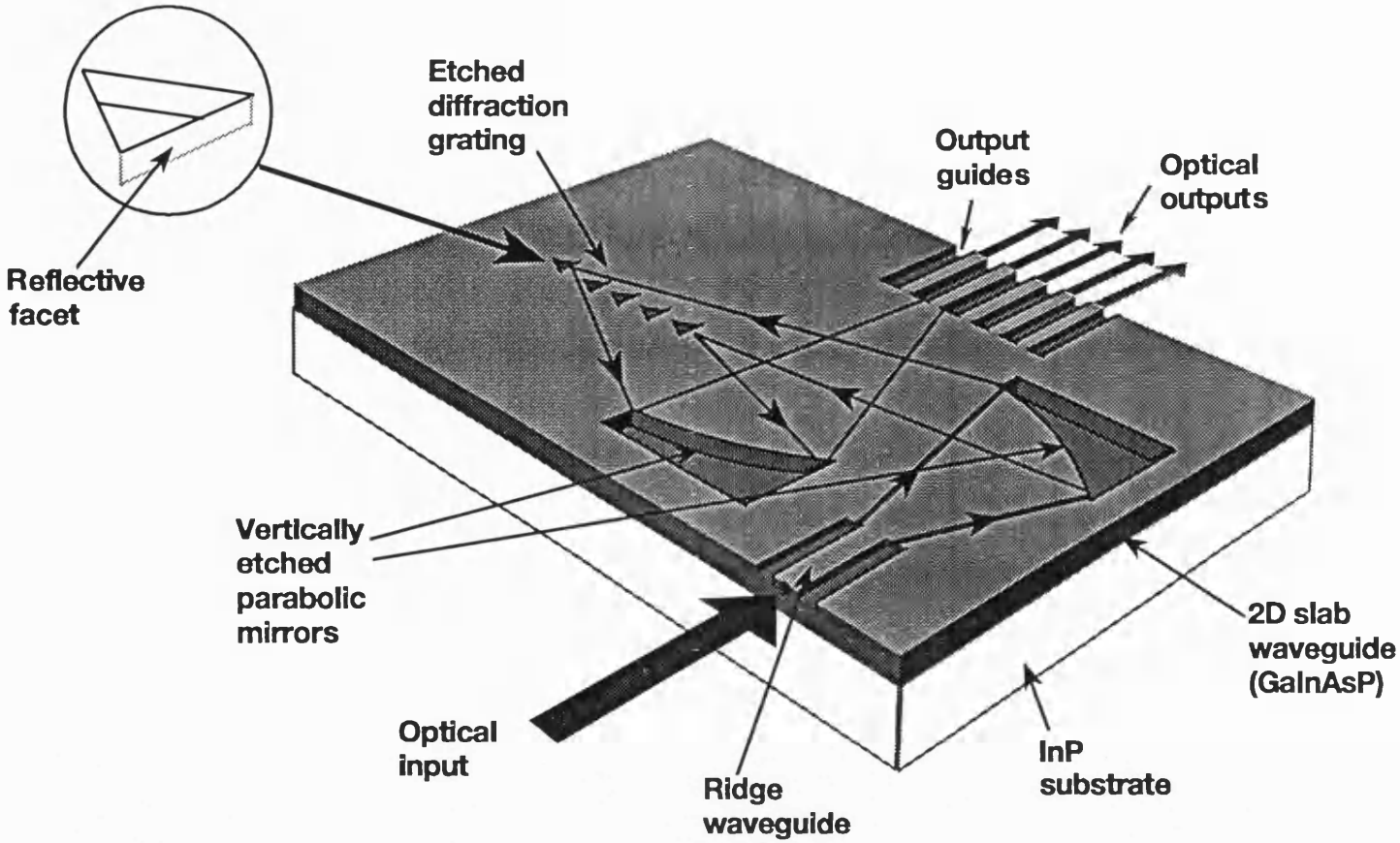

Fig 3.1 Integrated 1.5μm grating wavelength demultiplexer

also unnecessary, as one only needs to collect light within the range of wavelengths defined as the tolerance for a given channel.

The above performance objectives were added to the practical constraint that the grating elements had to be sufficiently large to enable accurate definition with conventional ultraviolet lithography.

The requirement for a high diffraction efficiency meant that the grating had to operate by reflection from each element, rather than by the periodic removal of light from the input beam. One possible choice, by analogy with free space optics, was an echelon grating[4] such as that shown in Figure 3.2. However this type of grating would not have been efficient when directly incorporated into an InP based waveguide as, for total internal reflection, the light must be incident at an angle of greater than ~18^0. This difficulty could not be resolved by simply angling the incident beam. The reason was that angling the beam would have reduced the diffraction efficiency, because each element would have shaded the output from the adjacent one, in the manner shown in Figure 3.3. The problem was overcome by fabricating a novel design of echelon grating (shown in Figure 3.4) that operated in transmission. This grating satisfied the efficiency requirement by transmitting all of the optical power in the incident beam.

The angular dispersion $d\Delta\theta/d\lambda$ of the grating shown in Figure 3.4 was calculated from

$$\frac{d\Delta\theta}{d\lambda} \approx \frac{2}{\lambda}\left(1-\frac{\lambda}{n}\frac{dn}{d\lambda}\right).\tan\alpha$$

where λ was the free space wavelength and n was the effective index of the slab waveguide. The other parameters are defined in Figure 3.4 and the derivation of the above equation is given in Appendix A. The dispersion at the output facet of the device shown in Figure 3.1 was given by the product of the angular dispersion and the focal length of the final mirror. Consequently significant adjustments to the dispersion of the device could only be made by altering the angle of incidence at the grating or the focal length of the mirrors. It was desirable to keep the focal length of the mirrors within reasonable bounds, so that the device did not become large enough to suffer from material uniformity problems. The adjustment range of the angle of incidence at the grating was also limited by the resolution limits of photolithography. The angle of incidence chosen for the final device was 45^o. With this angle, and the

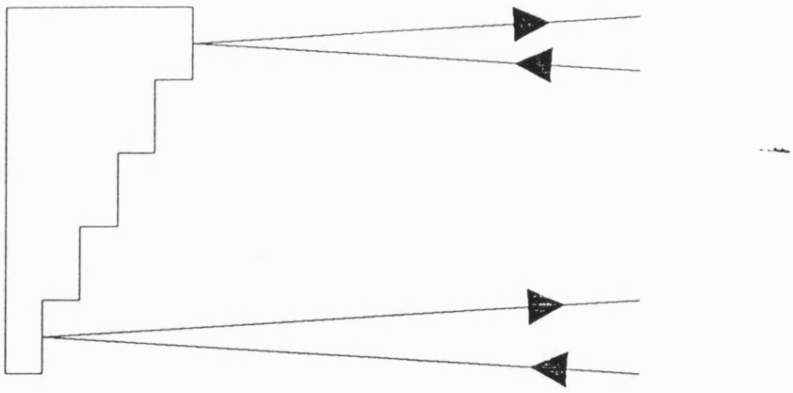

Fig 3.2 Echelon grating under conventional illumination

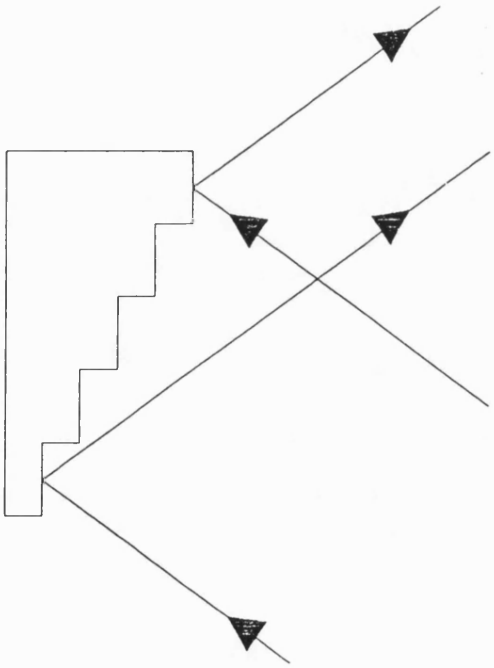

Fig 3.3 Echelon grating under angled illumination

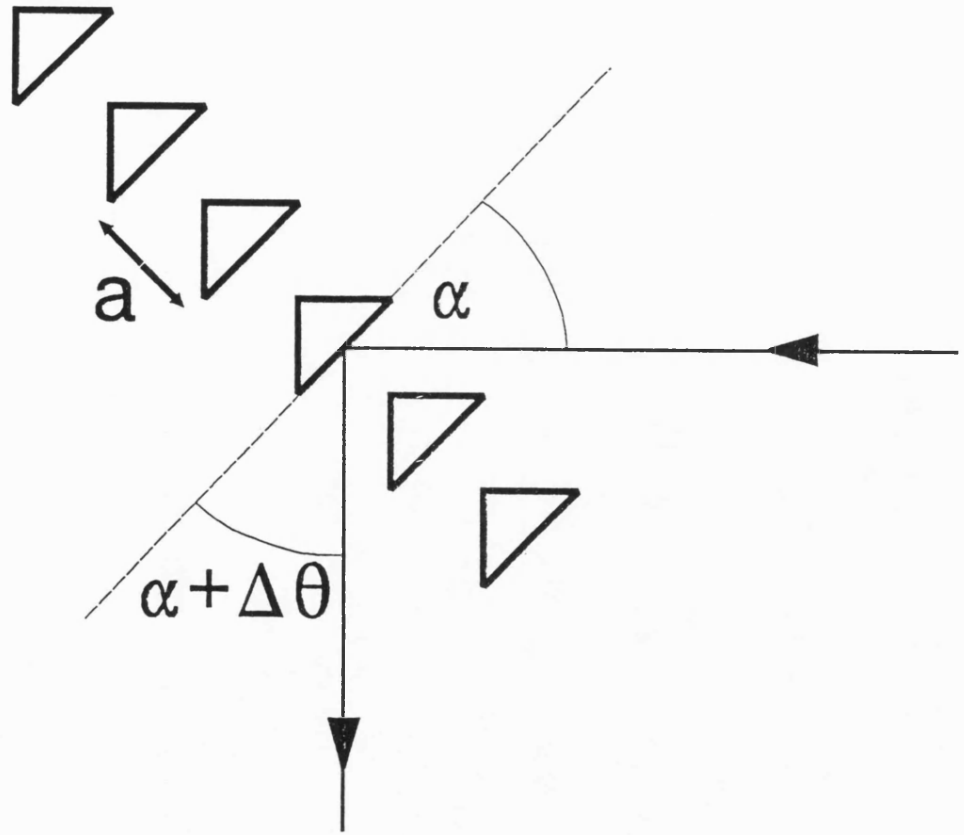

Fig 3.4 Echelon grating operating in transmission

specifications given in Appendix B, a theoretical dispersion of 0.94μm along the output facet per nm change in input wavelength was calculated.

The fact that there was a resolution limit for photolithography also meant that it was advantageous to make each grating element as large as possible, so that the shapes of the grating elements on the device were almost identical to those on the photolithographic mask. However the derivation in Appendix A showed that the wavelength separation $\Delta\lambda$ required to make adjacent diffraction orders superimpose was

$$\Delta\lambda = \frac{\lambda^2}{2an.\left(1-\frac{\lambda}{n}\frac{dn}{d\lambda}\right).\sin\alpha}$$

where a was the grating pitch. Consequently, increasing the element size decreased the optical bandwidth that the device could tolerate before adjacent diffraction orders superimposed. The 14μm element separation adopted in the final device was a compromise between these conflicting requirements. This element spacing meant that the demultiplexer was operated around the 44^{th} diffraction order and had an optical bandwidth of ~31nm. The specifications of the slab waveguide required for this calculation are given in Appendix B.

The element separation also determined the element width presented to the incident optical beam. This in turn determined the extent of the diffraction pattern at the device output. Each element was essentially an aperture with sharp edges as shown in Figure 3.4. Consequently the electric field envelope function for the diffraction pattern was a sinc function of the type described in Appendix A. The separation between adjacent minima of this sinc function was identical to the separation between diffraction orders. This meant that only the central diffraction order was transmitted when the grating was illuminated with light which diffracted at the blaze angle. The effect is illustrated in Figure 3.5. The result of this phenomenon was that almost all of the incident optical power was transmitted into one diffraction order for wavelengths diffracted close to the blaze angle. This was a useful feature in a device where efficiency was of great importance. The effect arose from the fact that the width of each grating element was closely related to the grating period.

The resolution of the grating was determined by its total width and the profile of the incident illumination. An approximate theoretical analysis of the grating resolution was made by assuming that it was illuminated with a Gaussian beam. Under this illumination arrangement each diffraction order was convoluted with the Fourier transform, F, of the Gaussian input truncated by

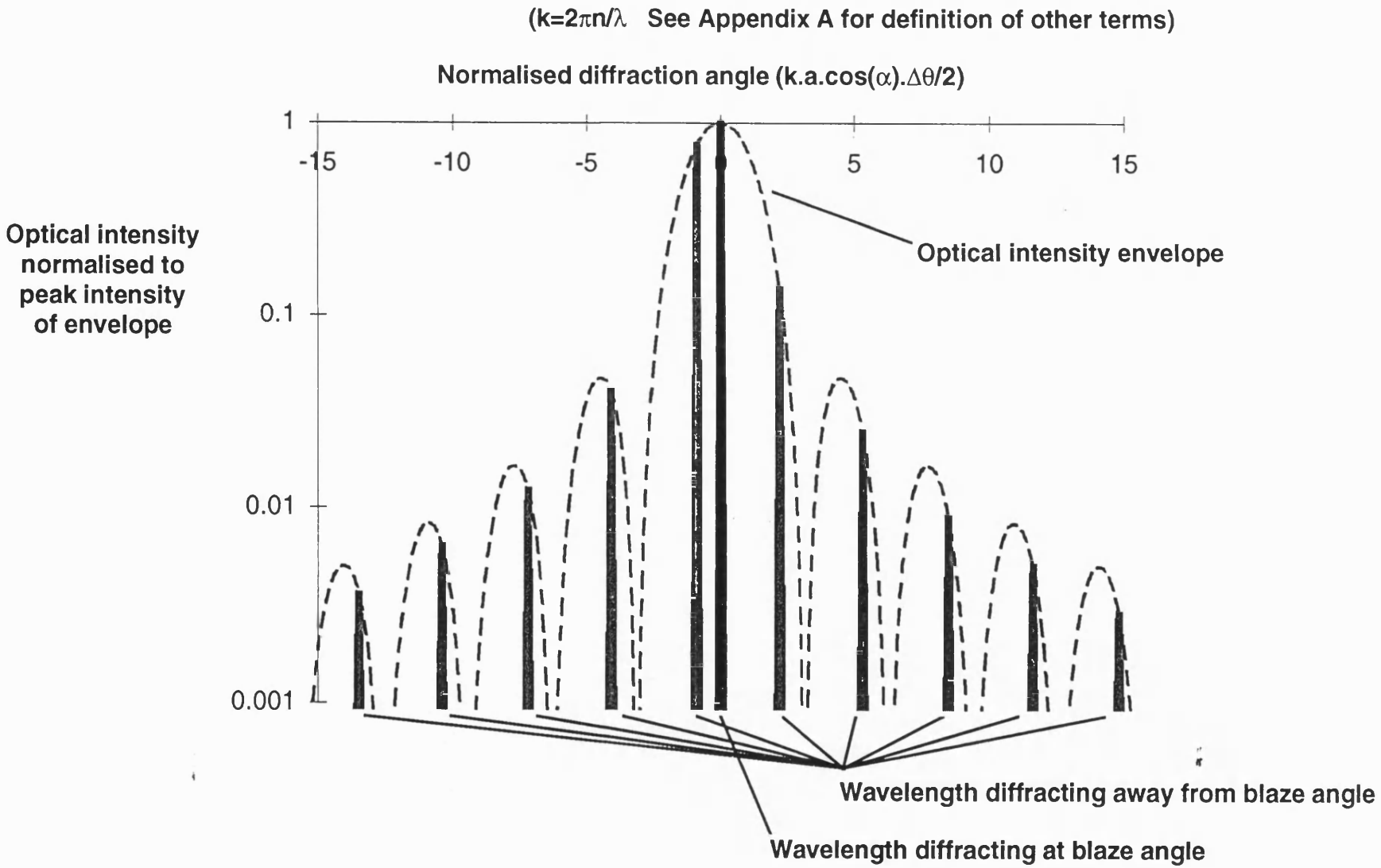

Fig 3.5 Diffraction pattern from echelon grating

the grating width. In other words the electric field resolution function F was given by

$$F = B.\int_{-\frac{w_g}{2}}^{\frac{w_g}{2}} e^{-\frac{4y^2}{w_0^2}}.e^{i\frac{2\pi n.\sin(\Delta\theta)}{\lambda}.y}dy$$

where w_0 was the width of the Gaussian beam measured to its $-1/e^2$ intensity points and w_g was the width of the grating projected onto the incident wave front. B was a constant. The optical power resolution function F^2 is plotted for several effective grating widths w_g in Figure 3.6. The technique used to calculate the curves shown in this figure is given in Appendix A. The grating resolution was derived from plots of this type and is shown in Figure 3.7. The results shown in the latter figure indicated that the wavelength resolution of the output (measured to the -20dB points) steadily improved as the effective width of the grating w_g was increased, until a point was reached when the effective grating width was about 1.5 times the width of the Gaussian beam w_0. Further increases in w_g had little effect on the wavelength resolution of the grating, but continued to reduce the intensity of subsidiary peaks in the diffraction pattern. In the final device the ratio of the effective width of the grating to the width of beam (w_g/w_0) was chosen to be about 1.5. The above analysis indicates that the subsidiary peaks in the diffraction pattern from a grating of this width should be suppressed by at least 30dB. This should be more than adequate for a digital communication link.

3.3. REFERENCES

1 G.H.B.Thompson, *"Physics of semiconductor laser devices"* (John Wiley and sons, Chichester, 1980) pp.165-239

2 E.Hecht and A.Zajac, *"Optics"*, (Addison-Wesley, Reading, Massachusetts, 1974) pp.397-423

3 J.M.Senior, *"Optical Fibre Communications"* (Prentice-Hall, London, 1985) pp.63-76

4 D.H.McMahon, W.A.Dyes, R.F.Cooper, W.C.Robinson and A.Mahapatra, *Applied Optics*, 1987, **26**, pp.2188-2196[1]

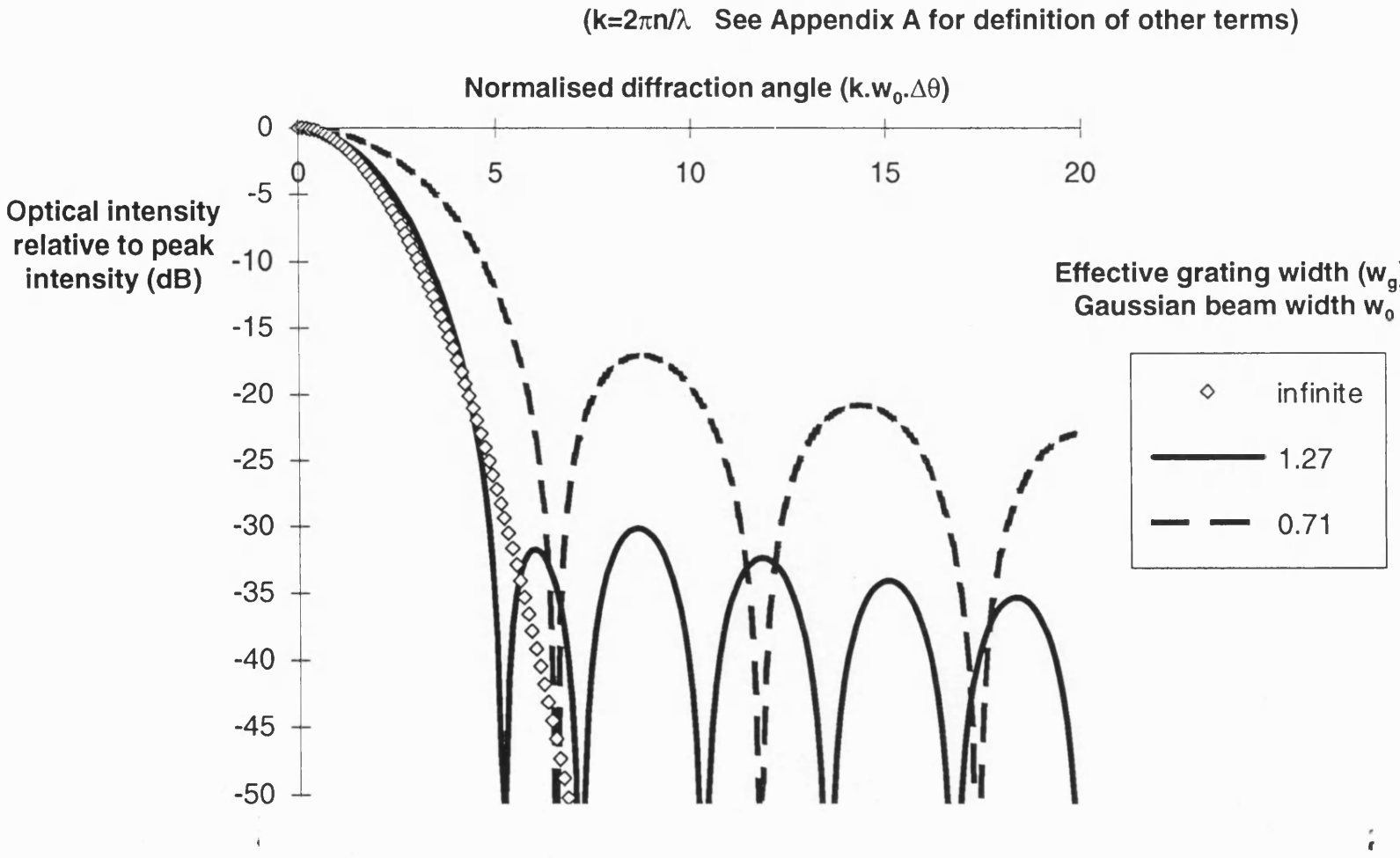

Fig 3.6 Effect of finite grating on diffraction of Gaussian beam

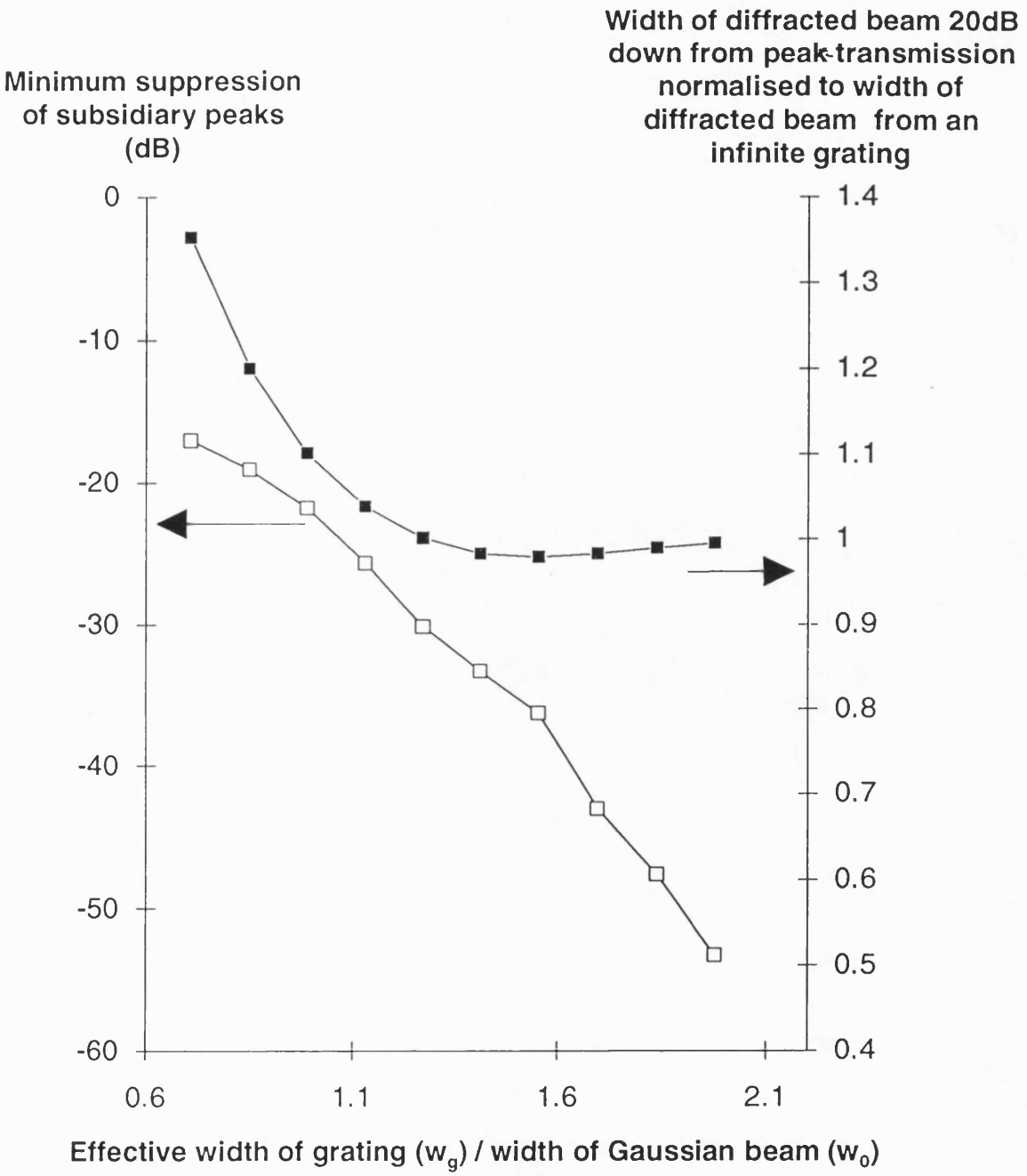

Fig 3.7 Effect of grating width on resolution

Chapter 4

Enabling Technologies for Demultiplexer Fabrication

4.1. INTRODUCTION

Much of the technology required to fabricate the demultiplexer described in chapter 3 was already available at the time when work on the project started. However, the unusual nature of the device meant that two new technologies had to be developed. These were a self aligned lithography procedure, and an etching process to create the vertical walls required in the demultiplexer. The suitability of one old technology, that of MOCVD, also had to be assessed using new criteria. These development and assessment activities are described in the following text.

4.2. ASSESSMENT OF EPITAXIAL GROWTH

The GaInAsP waveguide layer for the device shown in Figure 3.1 was grown by Metal Organic Chemical Vapour Deposition (MOCVD). This process can be very briefly described as one in which gaseous precursors are passed over a heated wafer at low pressure, as illustrated in Figure 4.1. For example, if one wishes to grow GaInAsP, common precursors are trimethyl indium, trimethyl gallium, arsine and phosphine. These precursors diffuse towards the wafer surface where they undergo pyrolysis reactions which ultimately yield semiconductor material of the appropriate composition. The chemistry of this process is complex and will not be discussed here. Detailed treatments can be found in the references[1,2,3,4]. The details of the MOCVD reactor used to grow the layer structure for the above device have also been published[5].

One aspect of the growth which is worth considering further at this point, is the uniformity of the epitaxial layers. Such uniformity is of paramount importance in a device where the optical field is not laterally confined, as variations in the composition or thickness of the slab waveguide change its effective index. Such index changes cause the two dimensional beam to deviate from its intended course. An approximate estimate of the degree to which the composition and thickness need to be controlled, can be made by determining the gradient of the

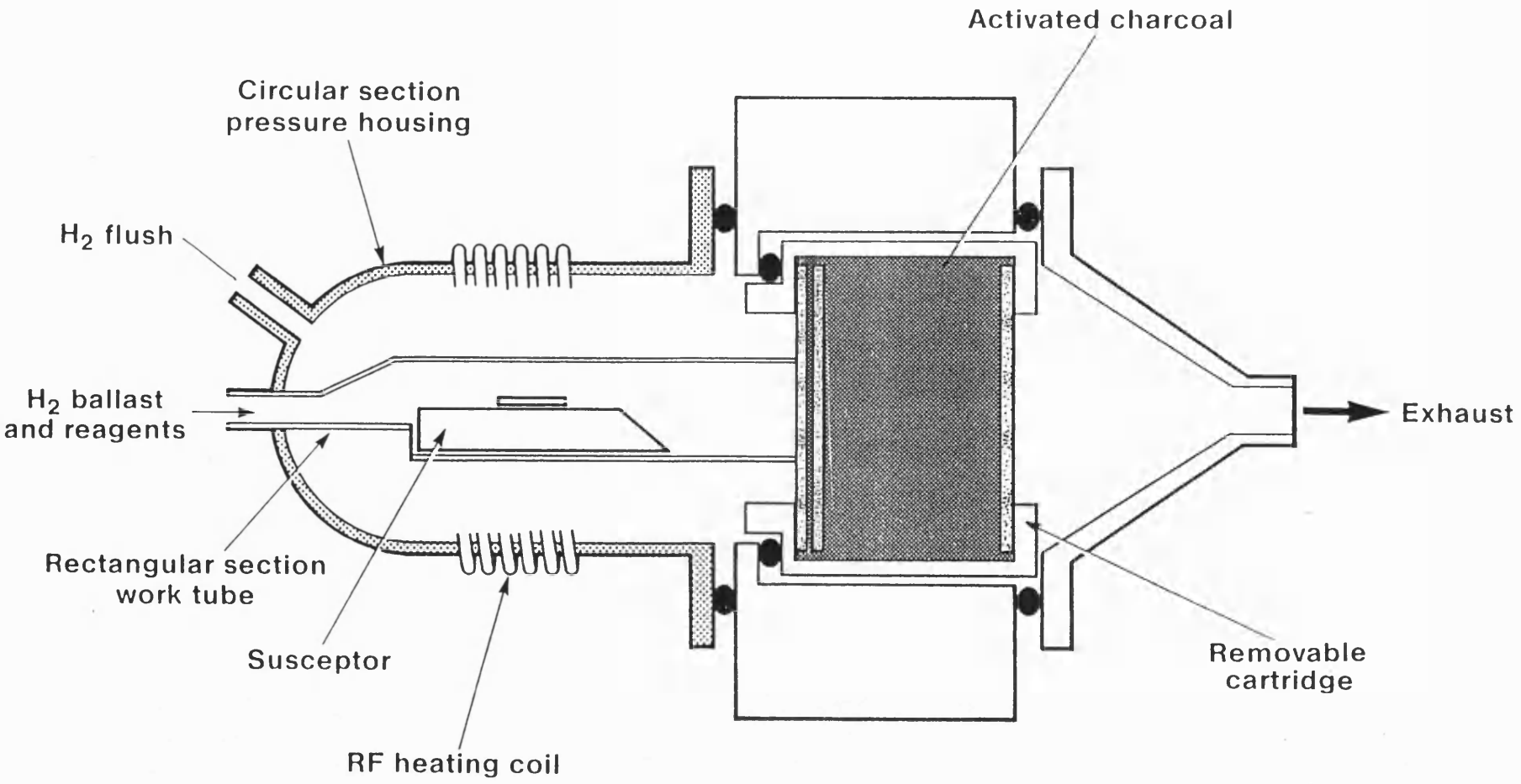

Fig 4.1 MOCVD reactor cell

AW 8777-2

parameter in question required to give a set path difference between the most widely separated rays passing through the device. In the investigations below the path difference has been set to one fifth of a wavelength. The calculation in Appendix C indicates that such a path difference should correspond to a lateral shift of about 0.3μm in the position of the device output. A shift of this magnitude only corresponds to a coupling loss of about 0.08 dB[6] between the slab mode and the ridge waveguide. It has even less effect if the waveguides are replaced by a monolithically integrated array of photodiodes.

An effective index gradient in the direction in Figure 4.2 has the largest effect on the position of the device output; the beam propagates in such a way that the effects of a gradient in the perpendicular direction almost cancel. Taking this dominant gradient, one can then allow for the divergence and convergence of the beam at the ends of its optical path, and the angles at which it propagates, by representing the two most widely separated beams as shown in Figure 4.3. Applying the λ/5 criterion to this indicates that the maximum tolerable gradient in the effective index is given by

$$\frac{\partial n}{\partial x} = \frac{\lambda}{5pd} = 1.54.10^{-6}\,\mu m^{-1} \qquad (4.1)$$

where λ is the free space wavelength (assumed to be 1.51μm), d is the width of the beam (175μm), and p is the effective path length as shown in Figure 4.3.

Having established the maximum permissible gradient in the effective index, the next problem is to relate this to parameters that can be measured. As stated above the two parameters that will determine the uniformity of the effective index are the compositional, and layer thickness, uniformity of the GaInAsP quaternary. Dealing with the compositional uniformity first, let's assume to start with that the quaternary layer is perfectly lattice matched to the InP substrate. (The effects of strain are considered below.) In this situation the effective index of the slab waveguide will be determined by:

a) the refractive index of the waveguide layer.
b) the degree to which light is confined to the waveguide layer.

The refractive index of the waveguide can be related to its bandgap via the Afromowitz Modified Single Oscillator Model[7,8,9]. The degree of confinement can be accurately calculated using the waveguide equations[10]. Consequently the effective index of the waveguide can be determined as a function of the

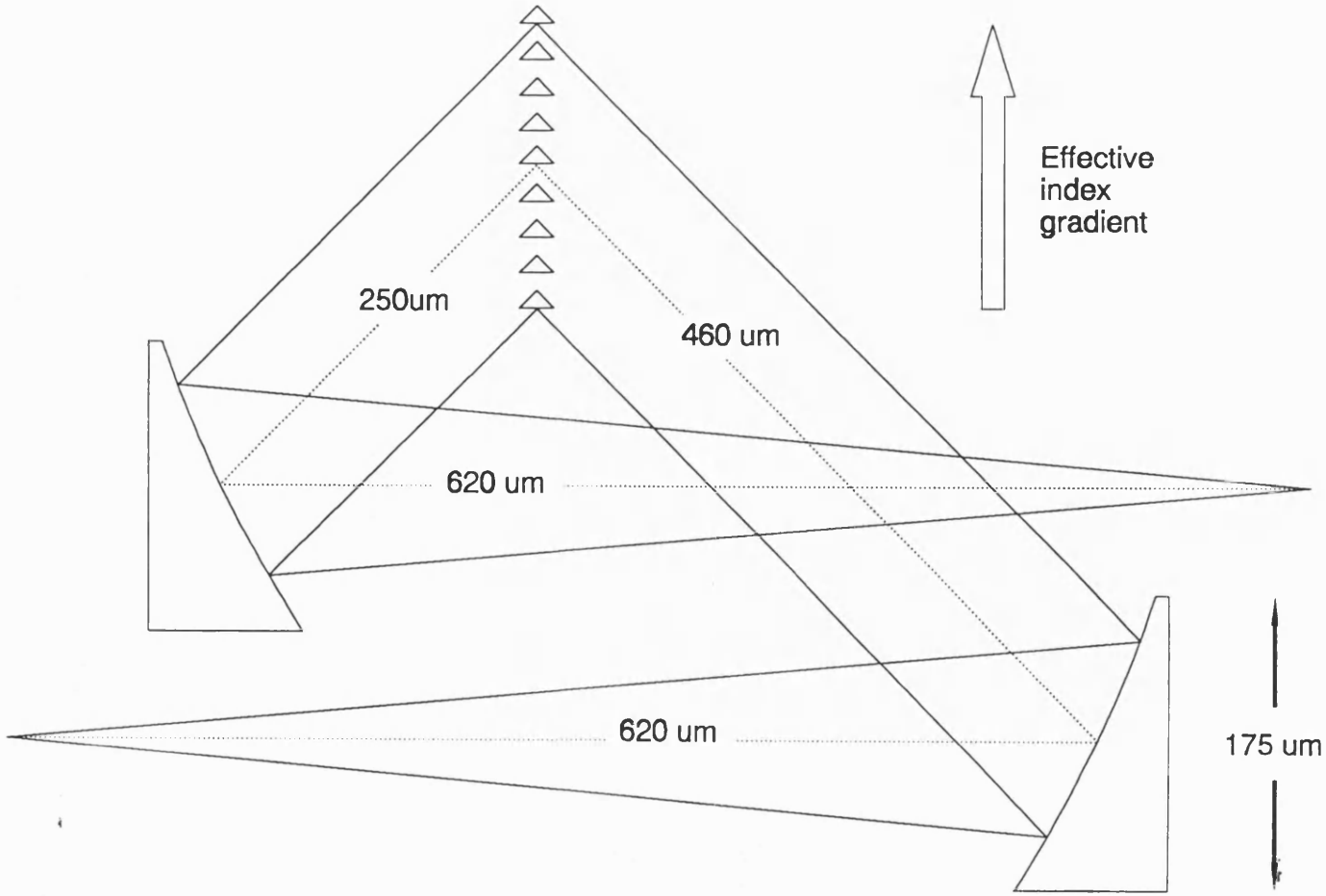

Fig 4.2 Direction of effective index gradient which will have greatest effect on position of output

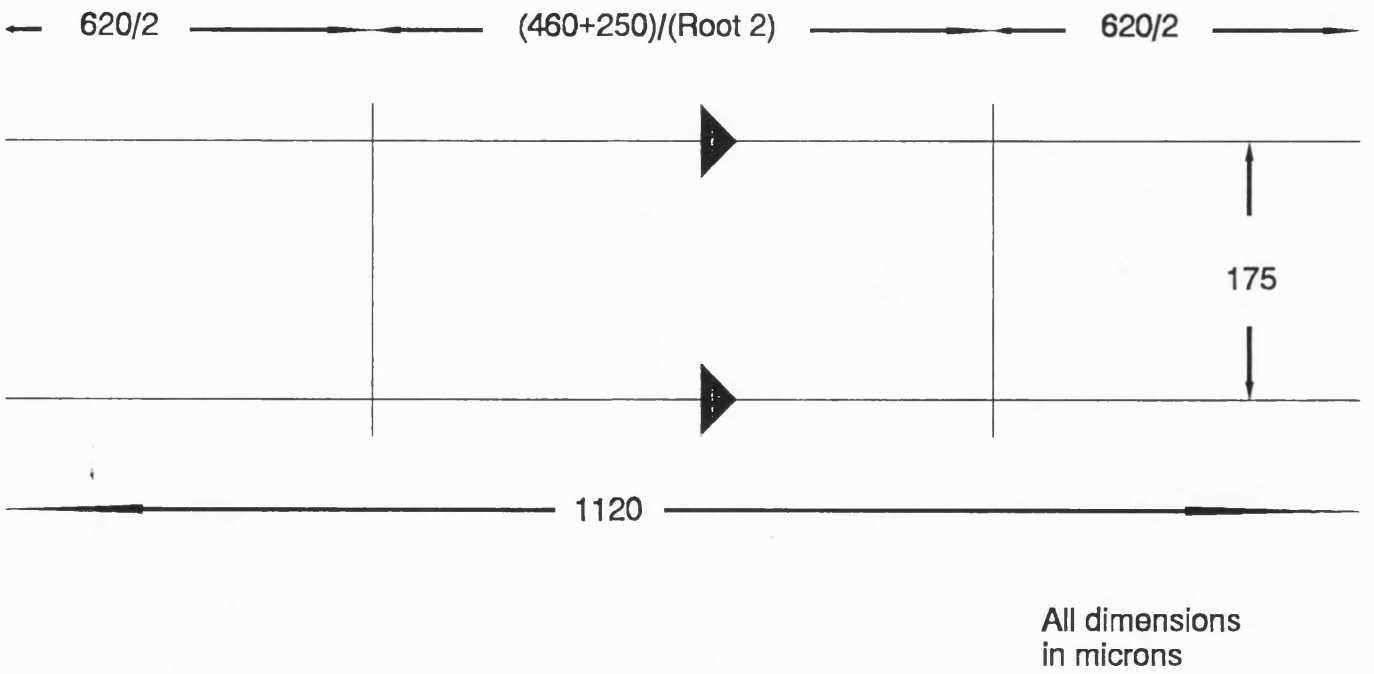

Fig 4.3 Simplified structure for path difference calculations

photoluminescence wavelength of the quaternary layer[11]. The results of such calculations, based on the layer specifications given in Appendix B, are shown in the following table (Computer program to do this by courtesy of Dr J.E.A. Whiteaway).

Table 4.1 **Compositional uniformity required to meet λ/5 benchmark**
All unquoted parameters as in Appendix B

	TE	TM
Change in effective index per μm change in guide layer photoluminescence wavelength	0.46	0.42
Maximum allowable gradient in λ_{PL} which still meets criterion in equation (4.1) (μm change in λ_{PL} / μm displacement)	$3.3.10^{-6}$	$3.7.10^{-6}$
Maximum allowable change in λ_{PL} over 5mm (nm)	16	18

Combining these results with the λ/5 criterion indicates that the maximum permissible gradient in the photoluminescence wavelength is $3.3.10^{-6}$, as shown in the above table. This gradient corresponds to a 17 nm change in the photoluminescence wavelength as one scans a distance of 5 mm across the epitaxial layer, if one assumes that the variations in the bandgap are smooth and long range. The above number can be directly compared with the photoluminescence map of the wafer used to make the final device, which is shown in Figure 4.4 (Data points are on a 5 mm grid). From this figure it can be seen that, over the bulk of the wafer, the variations in photoluminescence wavelength are less than half the 17 nm tolerance required to meet the λ/5 benchmark.

As mentioned above, we also need to consider the effects of strain before deciding whether the compositional uniformity is satisfactory. This strain arises when the lattice constant of the GaInAsP waveguide layer is not matched to that of the InP substrate. The net result is that the waveguide layer is left under biaxial tension or compression. This deformation can be represented as the sum of a hydrostatic compression and an axial strain[12,13], as shown in Appendix D. The effect of the former distortion on the bandgap structure is to increase the energy of the conduction band Γ minimum by about 100 meV/% lattice mismatch. The latter distortion splits the heavy and light hole valence band maxima equally about their original position, with the magnitude of the

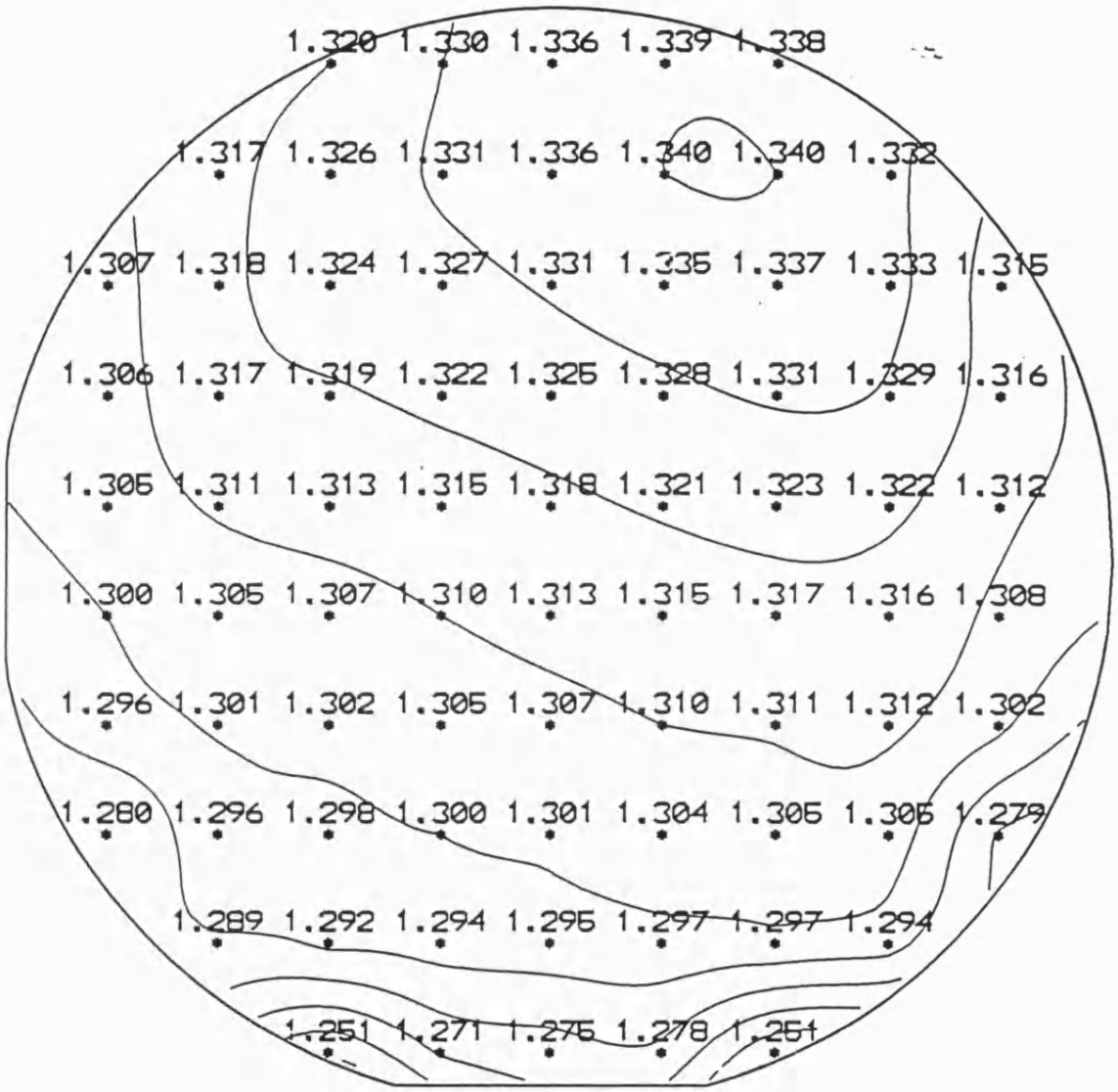

Fig 4.4 Photoluminescence wavelength of wafer C324 in μm

split being about 60 meV/% lattice mismatch. We can place an upper limit on the change in the refractive index of the strained layer using these figures and the Afromowitz model. The reason is that the Kramers-Kronig relationships[14,15] indicate that changes in the energy levels of bands far away from the bandgap will have little effect on the refractive index. If we use this approach, where the changes in refractive index are determined solely by changes in the bandgap, we find that the effect of strain on the index seen by the TE mode has already been accounted for in the map of photoluminescence wavelength. However there is a complication, which relates to the fact that the TM mode of the slab waveguide only interacts with the light hole band (at the valence band maximum), while the TE mode interacts predominantly with the heavy hole band. Our photoluminescence apparatus operates at room temperature and is configured so that it measures the bandgap associated with the TE mode provided that the lattice mismatch is not less than -5000ppm. Consequently we need to confirm that strain does not cause excessive additional variations in the effective index of the TM mode. This can be done by analysing the X-ray map of lattice mismatch for the wafer used to make the final device. The map of mismatch, with data points on a 5mm grid, is shown in Figure 4.5. The map indicates that, if wafer edge effects are ignored, the lattice mismatch varies by less than 200 ppm between adjacent data points. This corresponds to a 1.2 meV change in the separation of the light and heavy hole valence band maxima, which in turn corresponds to a 1.6 nm shift in the photoluminescence wavelength. Adding this correction to the photoluminescence wavelength map does not shift the variations in wavelength outside the 17 nm required to meet the $\lambda/5$ criterion. This means that we can conclude that the compositional uniformity of the GaInAsP layer is satisfactory for both the TE and the TM modes.

The final uniformity problem to consider is that associated with variations in the thickness of the waveguide layer. The effect of these variations on the effective index can be accurately described by the waveguide equations. The results of calculations based on these equations, and the waveguide parameters of the final device, are shown in Table 4.2.

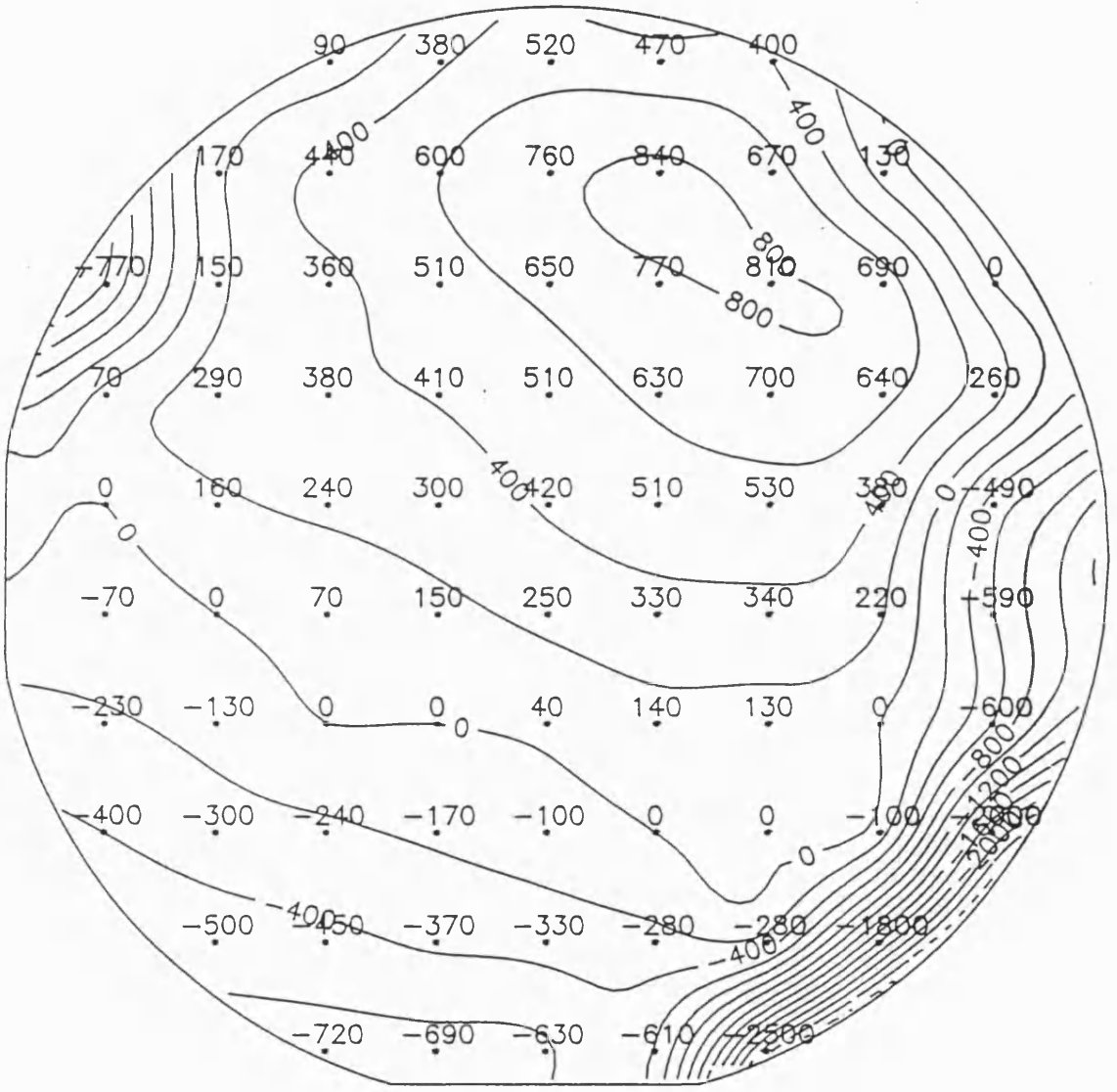

Fig 4.5 Mismatch of wafer C324 in ppm

Table 4.2 **Thickness Uniformity Required to Meet λ/5 Benchmark**
All unquoted parameters as in Appendix B

	TE	TM
Change in effective index per μm change in guide layer thickness	0.23	0.30
Maximum allowable gradient in thickness which still meets criterion in equation (4.1) (μm change in thickness / μm displacement)	$6.7.10^{-6}$	$5.1.10^{-6}$
Maximum allowable change in guide layer thickness over 5mm (μm)	0.033	0.026

The calculations indicate that, if the λ/5 benchmark is to be satisfied, the layer thickness should vary by less than 26 nm over a distance of 5 mm. This corresponds to a 4% change in the thickness of the epitaxial layer. Unfortunately it is difficult to determine the degree to which this criterion is met as layer thickness is measured by ball cratering[16]. This technique is only accurate to within about ±5%. It is also destructive so data has to be gathered from a similar wafer, such as that shown in Figure 4.6. Looking at this plot it seems likely that the λ/5 criterion will be met, but the measurement errors are so large that it is difficult to say so with complete certainty. However there is no doubt that the benchmark will be satisfied if it is relaxed by a factor of 2 to λ/2.5.

In conclusion it appears that the only parameter that may not quite reach the required tolerance is the thickness uniformity and, even with this parameter, the problem is more likely to be one of measurement than one of growth control.

4.3. SELF-ALIGNED LITHOGRAPHY

The demultiplexer shown in Figure 3.1 will only perform as anticipated if the mirrors and waveguides are accurately located with respect to each other. This indicated that they should both be defined in a single lithographic step, so that the positional accuracy on the wafer approached that on the original mask. Such "self-aligned" procedures are common in the electronics industry[17]. However, in this case there was an additional complication, in that the mirrors had to be etched right through the guide layer while, if the ridge waveguides were to remain single mode, the channels defining them could only be etched

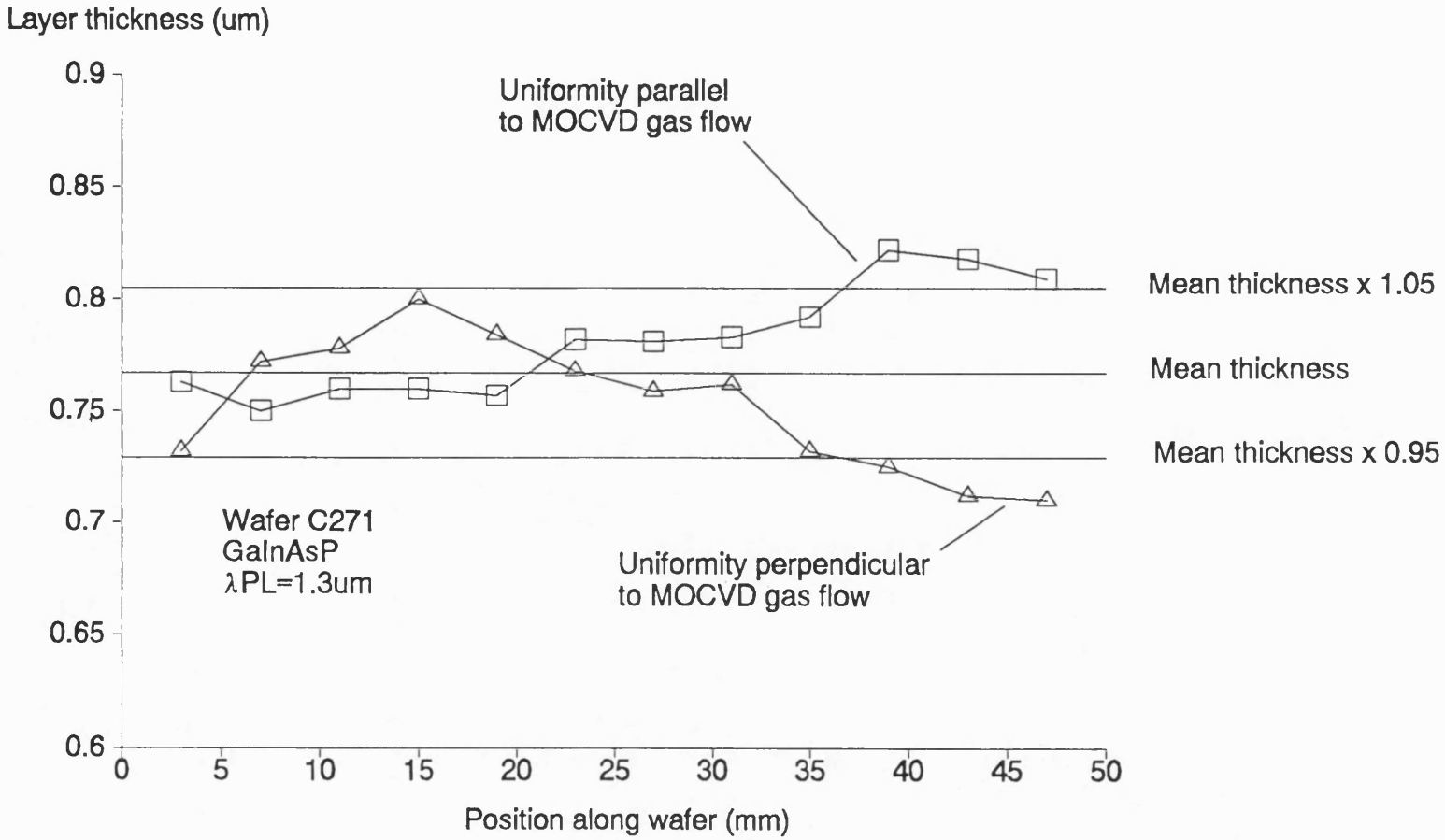

Fig 4.6 Thickness uniformity of MOCVD grown epitaxial layer

through a fraction of this layer (see Figure 4.7). This was achieved by protecting the channels that defined the waveguides with a second level mask for the bulk of the mirror etch. Ideally, this second level mask should have been both resistant to the etching system used to make the mirrors, and soluble in an etchant that did not attack either the first level mask or the semiconductor underneath. Unfortunately, it was difficult to satisfy both of these requirements simultaneously. For example, one natural choice would have been a silicon dioxide and photoresist combination, as it was possible to remove resist without damaging the underlying layers. However, it was soon discovered that resists could not survive prolonged exposure to the methane/hydrogen plasma that was used to etch the mirror recesses. The final solution adopted was to use the double silicon dioxide masking system shown in Figure 4.7. The bottom layer was deposited by plasma enhanced chemical vapour deposition (PECVD), and the top one by a thermal deposition process. Both of these layers were resistant to attack by the methane/hydrogen plasma, but there was no truly selective etchant that would remove the upper oxide layer without attacking the lower one. Fortunately, it was possible to achieve some selectivity, as the thermally deposited mask etched about twice as fast in buffered hydrofluoric acid (BHF). By making use of this difference in etch rate, and by arranging for the upper SiO_2 layer to be relatively thin, it was possible to achieve a situation where the upper layer could be removed in BHF without significantly affecting the edge definition of the lower one.

The double layer system can be seen in the optical micrograph of a partially processed device shown in Figure 4.8. The darkest areas were regions in which both SiO_2 layers were present; the grey areas were only protected by one layer; and the light areas were regions of exposed semiconductor. The lower SiO_2 layer defined the mirrors and the waveguide channels as shown in the figure. The upper layer was completely opaque, save for the rectangular windows which were opened up around each mirror and grating patch.

One final point which is worth considering is the accuracy with which the features were placed on the original chrome mask. The masks for the device illustrated in Figure 3.1 were written by electron beam lithography at BNR Europe. In this system the position of the electron beam is ultimately calibrated against a laser interferometer, which is mounted on the stage that carries the wafer. This arrangement allows one to accurately correct for problems such as lens aberrations, and distortion introduced by beam deflection. The details of this correction procedure can be found in the references[18]. On the finished

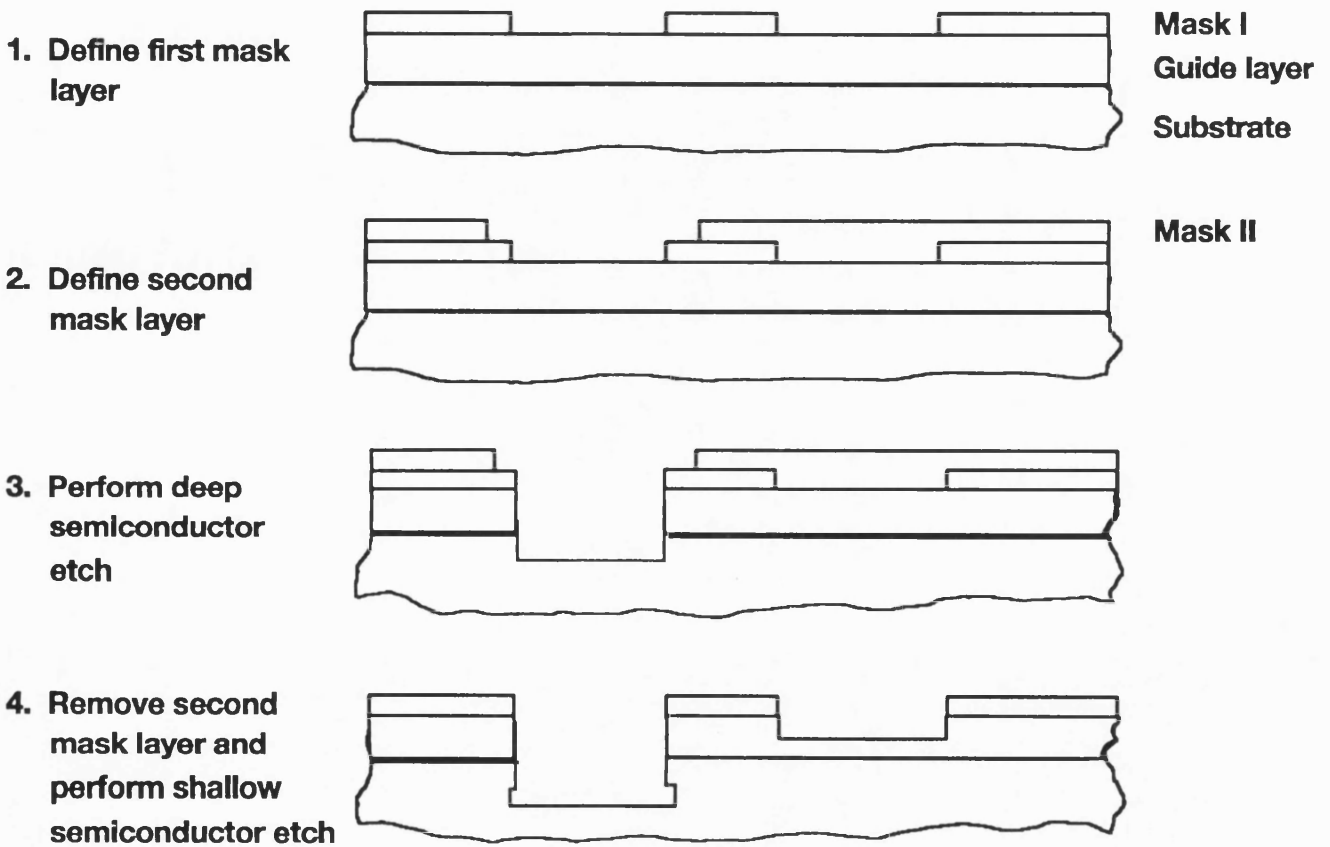

Fig 4.7 Two stage self aligned process

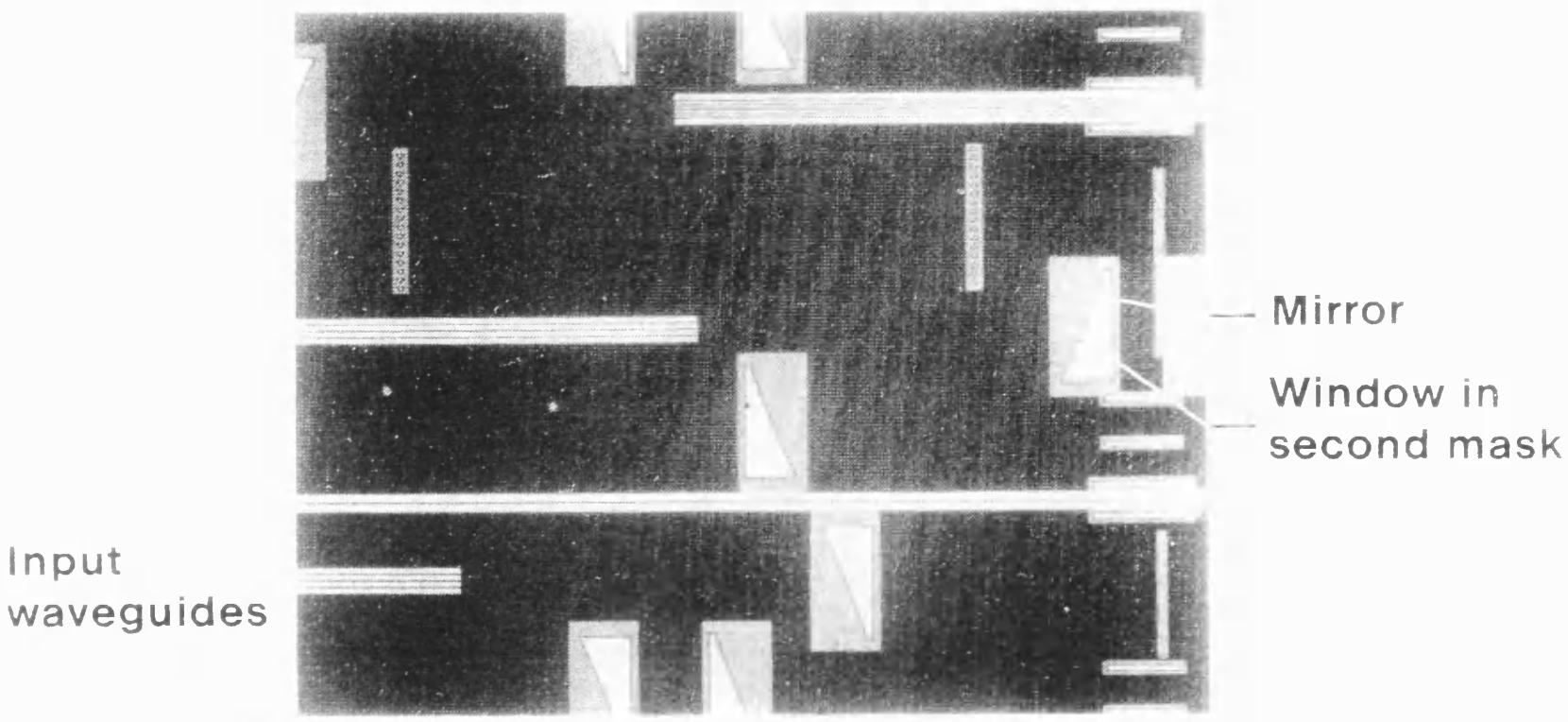

Fig 4.8 Part processed demultiplexer with mask levels intact

mask the largest positional errors usually occur at the corners of the units or "fields" in which the pattern is written as, even after correction, the distortions are greatest in the regions where the beam deflection is at its maximum value. Typically these errors are about 50 nm. This should not significantly affect the performance of the demultiplexer discussed above.

4.4. MIRROR DESIGN AND FABRICATION

4.4.1. Tolerance on Mirror Design

The insertion losses in bulk optic grating based devices are typically around 3dB (see section 2.2). Consequently, if integrated devices are to be competitive, their insertion losses must be reduced to about this level. If the input coupling loss is ignored (it is considered in section 5.5), the insertion loss in a demultiplexer can be attributed to a combination of the loss of the ridge and slab waveguides, and the loss on reflection from each mirror. There is a considerable amount of evidence in the literature that it is possible to produce low loss waveguides on material grown by MOCVD[19]. This was confirmed by the fact that ridge waveguides fabricated on the same wafer as the demultiplexer exhibited average losses of 0.9 dB/cm[20]. The optical path length in the demultiplexer was much shorter than 1 cm, and hence waveguide losses should have been almost insignificant. However it is considerably more difficult to fabricate low loss etched mirrors. In principle the losses on reflection from the semiconductor-air interfaces of such mirrors can be attributed to:

a) lack of wall verticality
b) insufficient mirror depth
c) etched wall roughness

In the following text the losses associated with each of these problems are considered in turn.

An estimate of the loss on reflection from an off vertical interface can be made by approximating the slab guided mode to a Gaussian beam of the same optical width, and performing an overlap integral[6]. This integration indicates that one would anticipate a loss of α dB given by

$$\alpha = \theta^2\left(\frac{2\pi\omega n}{\lambda}\right)^2 . \; 10\log_{10}e \qquad (4.2)$$

when a Gaussian beam of radius ω is reflected from a mirror inclined at θ radians, in a waveguide of effective index n. For example, one would expect a loss of about 0.5 dB on reflection from a mirror inclined at 4° in a slab waveguide of the specifications given in Appendix B. This loss increases as the square of the wall angle, and hence it is imperative that the wall angle should be within a few degrees of vertical.

The depth of the mirror should be sufficient to reflect the bulk of the evanescent wave below the quaternary guiding layer. An estimate of the depth required for a given reflection coefficient can be made by overlap integration, with the near field immediately after reflection assumed to be that of the slab waveguide, but truncated by the depth of the mirror. A plot of the theoretical power reflection coefficient as a function of the mirror depth in the final device is shown in Figure 4.9. The analysis indicated that the mirrors needed to be etched to a depth of at least 1.1 μm if one wished to obtain a reflection coefficient of greater than 99%.

The effects of mirror roughness are not easy to determine, as they are both difficult to measure and to calculate. An approximate analysis has been made by Iga et al[21,22] but in this model the phase of the reflected wave was adjusted according to the deviation of the mirror wall from its average position. The resulting wave was then overlapped with the incoming one. Unfortunately it was difficult to extend this analysis to cover our application. The reason was that much of the roughness observed on our mirrors was of such short periodicity, that it could only have coupled the incoming field to evanescent modes. These modes could not have carried power away from the mirror surface and hence would not have affected the magnitude of the reflection coefficient.

4.4.2. Reactive Ion Etching

It is difficult to use wet chemical etching to define a mirror which is both curved in plan view, as shown in Figure 3.1, and near vertical, as the [0 1 1] and [0-1 1] directions in InP based semiconductors are not crystallographically identical. Consequently, wet etchants which can produce recesses with near vertical walls only do so when this wall is aligned to a particular crystal orientation. This means that one is unlikely to make much progress by relying on the different etching properties of different crystal planes when the crystal is exposed to an essentially isotropic etch. Fortunately alternative etching

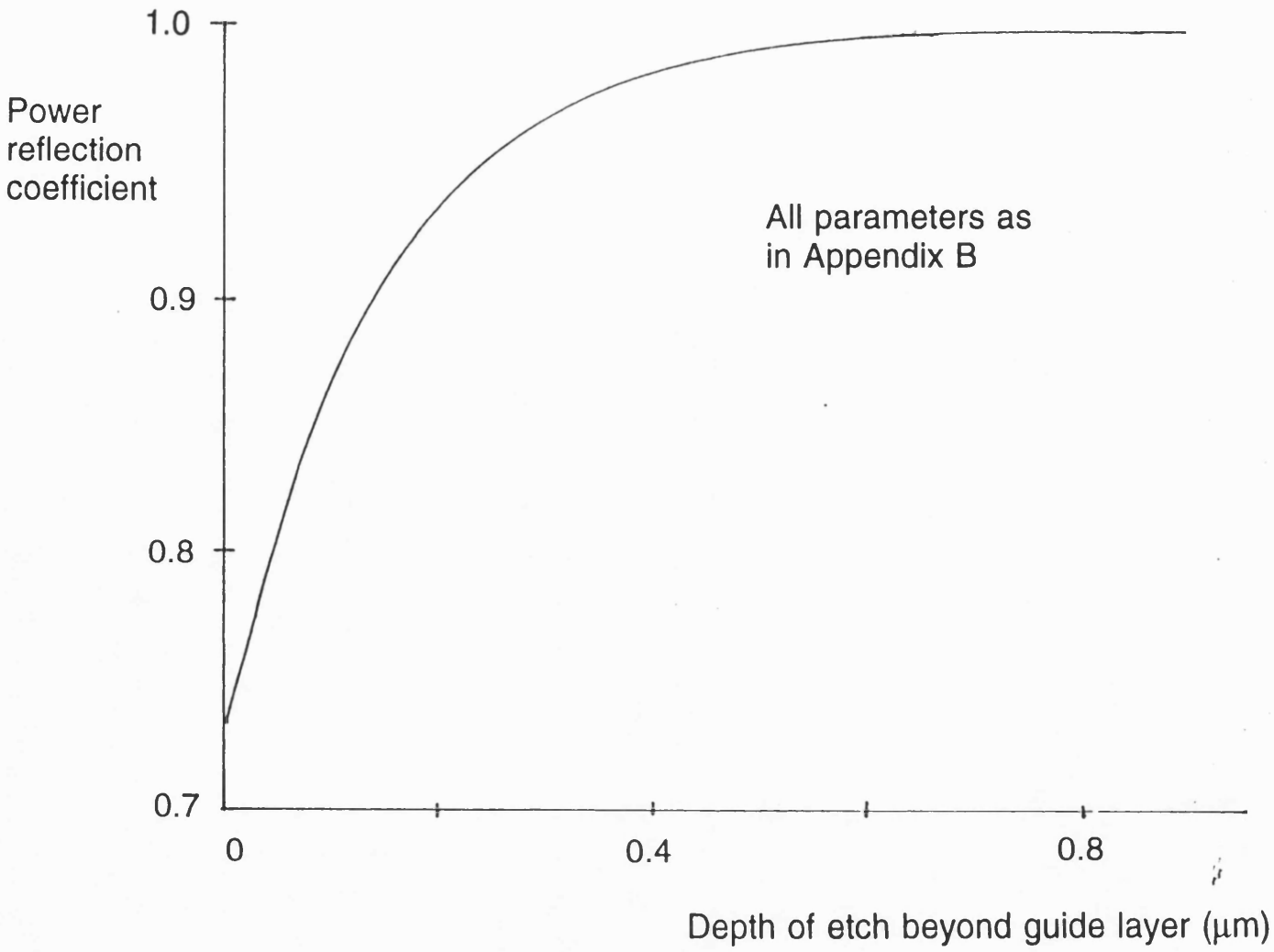

Fig 4.9 The effect of mirror depth on reflectivity

systems exist in which the etching process is directional, and the crystal behaves in an almost isotropic manner. These systems are gaseous and rely on the acceleration of charged particles to produce the required directional flux at the wafer surface[23,24]. One such system is that for Reactive Ion Etching (RIE) which can be schematically represented as shown in Figure 4.10. The semiconductor is removed as a gaseous product after reaction with appropriate free radicals, which diffuse to the wafer surface from the plasma above it. The activation energy for the rate limiting step of the adsorption, reaction, desorption process illustrated in Figure 4.10, is provided by positive ions which bombard the wafer surface. This ion flux is predominantly vertical and hence the etching process is directional.

The apparatus in which appropriate conditions for RIE are obtained is schematically represented in Figure 4.11. The free radicals which react with the semiconductor are generated by collision processes in the plasma. Electrons and ions are also generated by collisions in this plasma, and hence the plasma is an equipotential, as the electrons have a very small mass and can rapidly respond to any fluctuations in potential. However, when a probe or an electrode is placed in contact with the plasma, a current-voltage characteristic similar to that shown in Figure 4.12 is obtained. The reason for the non-linear shape of this characteristic is that, on average, the electrons in the plasma have much higher kinetic energies than the ions. This means that:

a) The saturated electron current to the electrode is greater than the saturated ion current, as the electron mean speed is greater.
b) The electrons can overcome a greater potential barrier than the ions, and hence the electrode must be negatively biased with respect to the plasma if one is to obtain zero net current flow. The amount of negative bias required is known as the floating potential, V_f.

The current-voltage characteristic for an r.f. excitation is not identical to that shown in Figure 4.12. The reason is that the ions cannot respond to fields with frequencies greater than about 1MHz. Consequently they see an average potential. However, the electrons, which are lighter, can still follow the changing field and, as their contribution to the current-voltage characteristic is much greater than that of the ions, its shape is little changed.

In practice the applied r.f. potential is considerably greater than the floating potential V_f. This means that the floating potential can be ignored and the system can be represented by the equivalent circuit shown in Figure 4.13. If an

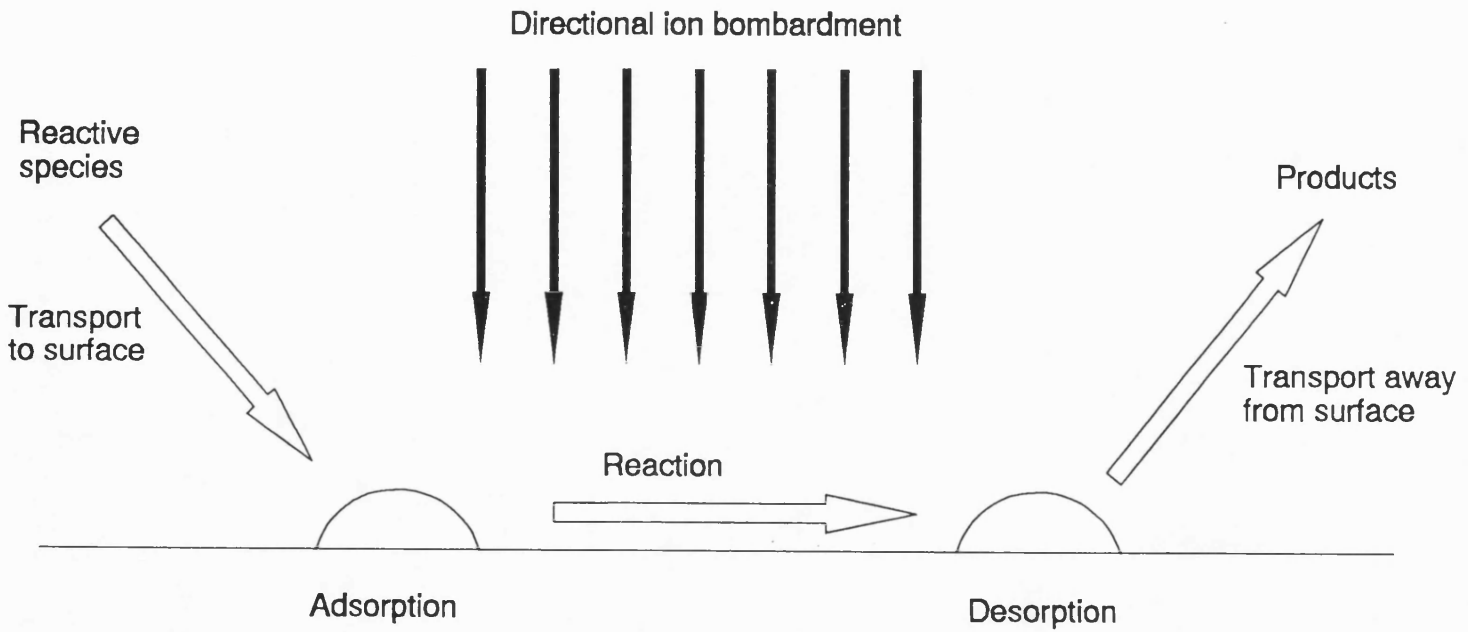

Fig 4.10 Schematic representation of reactive ion etching process

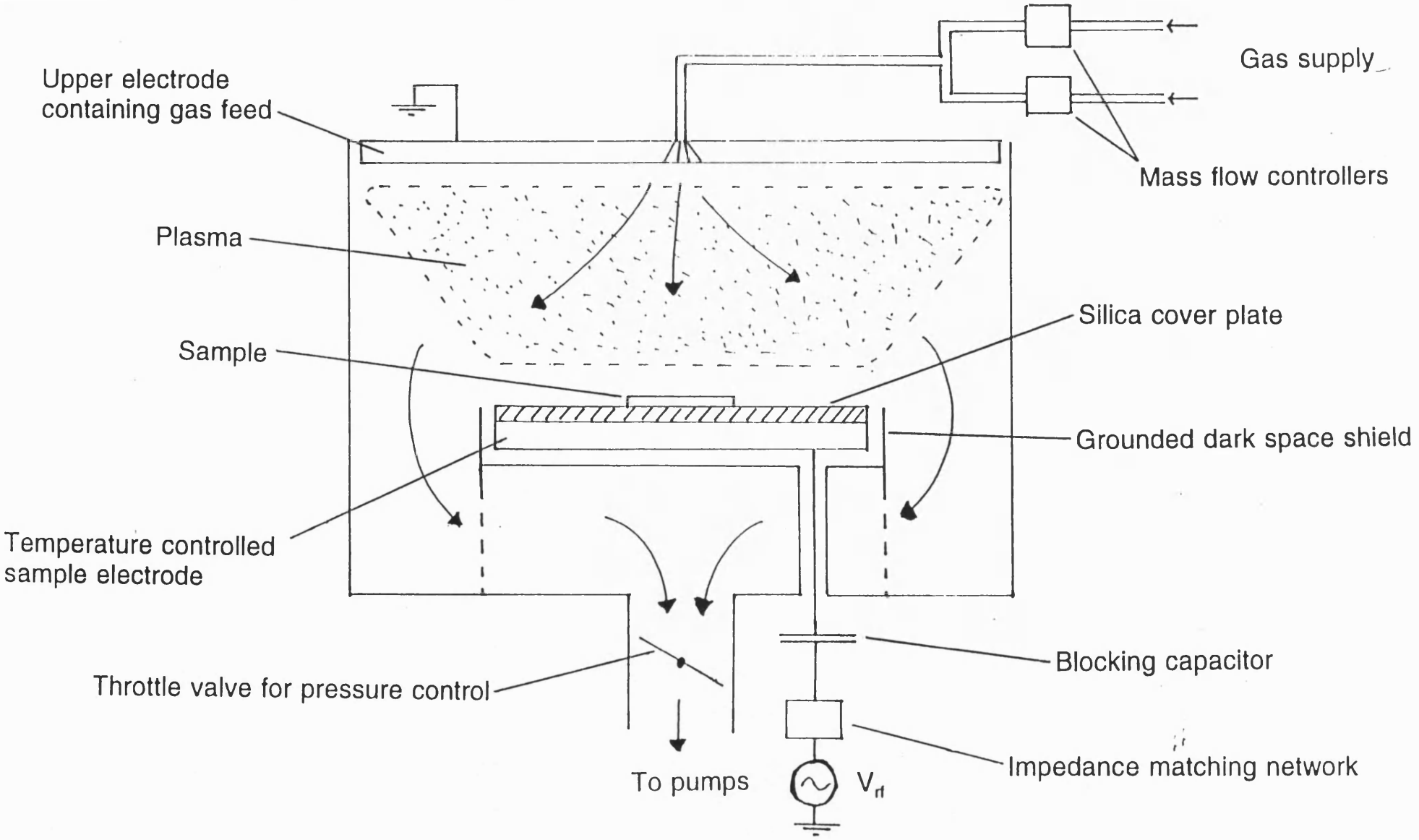

Fig 4.11 Schematic of Plasmalab μP RIE etching system

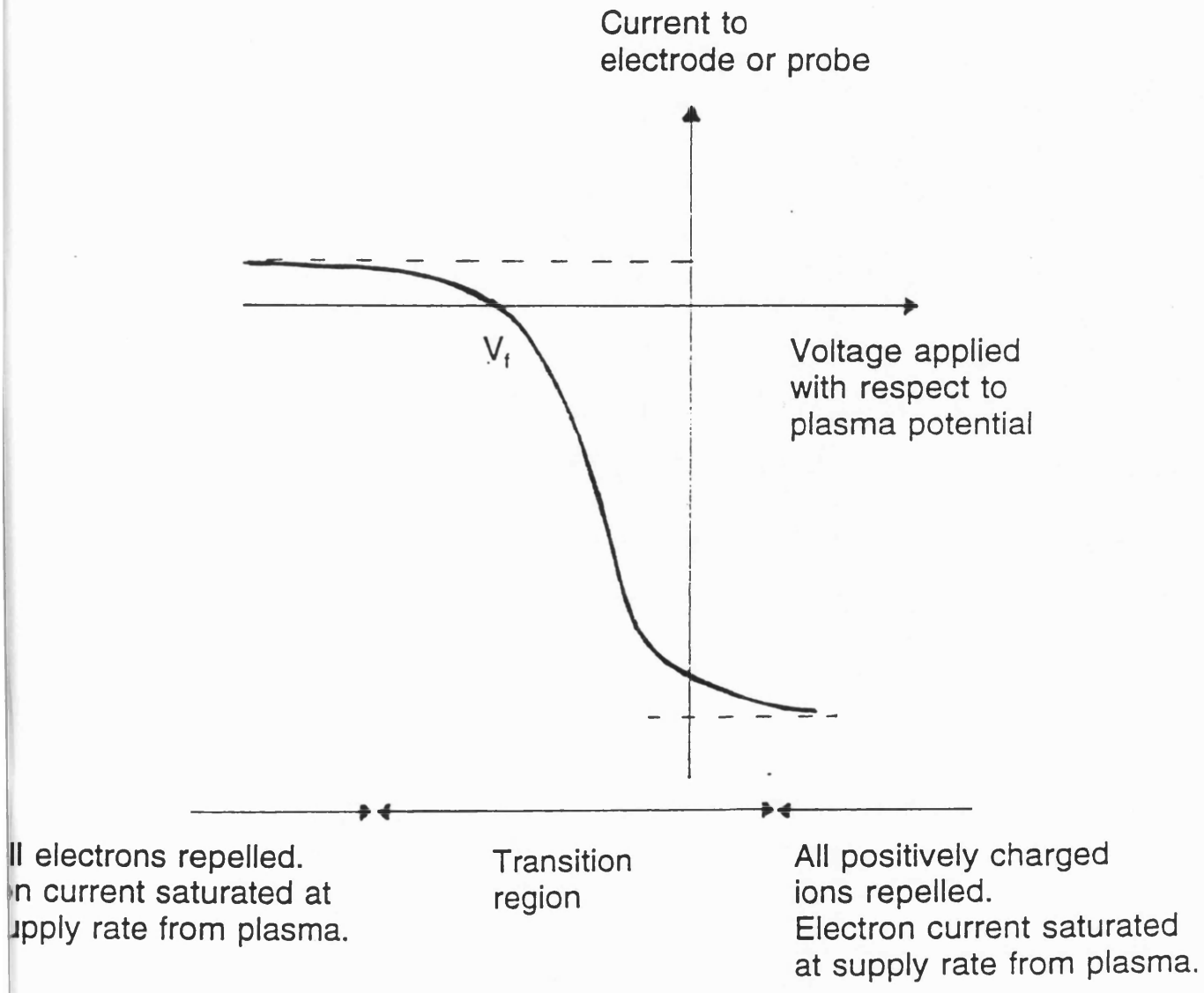

Fig 4.12 d.c. current voltage characteristic for probe in contact with a plasma

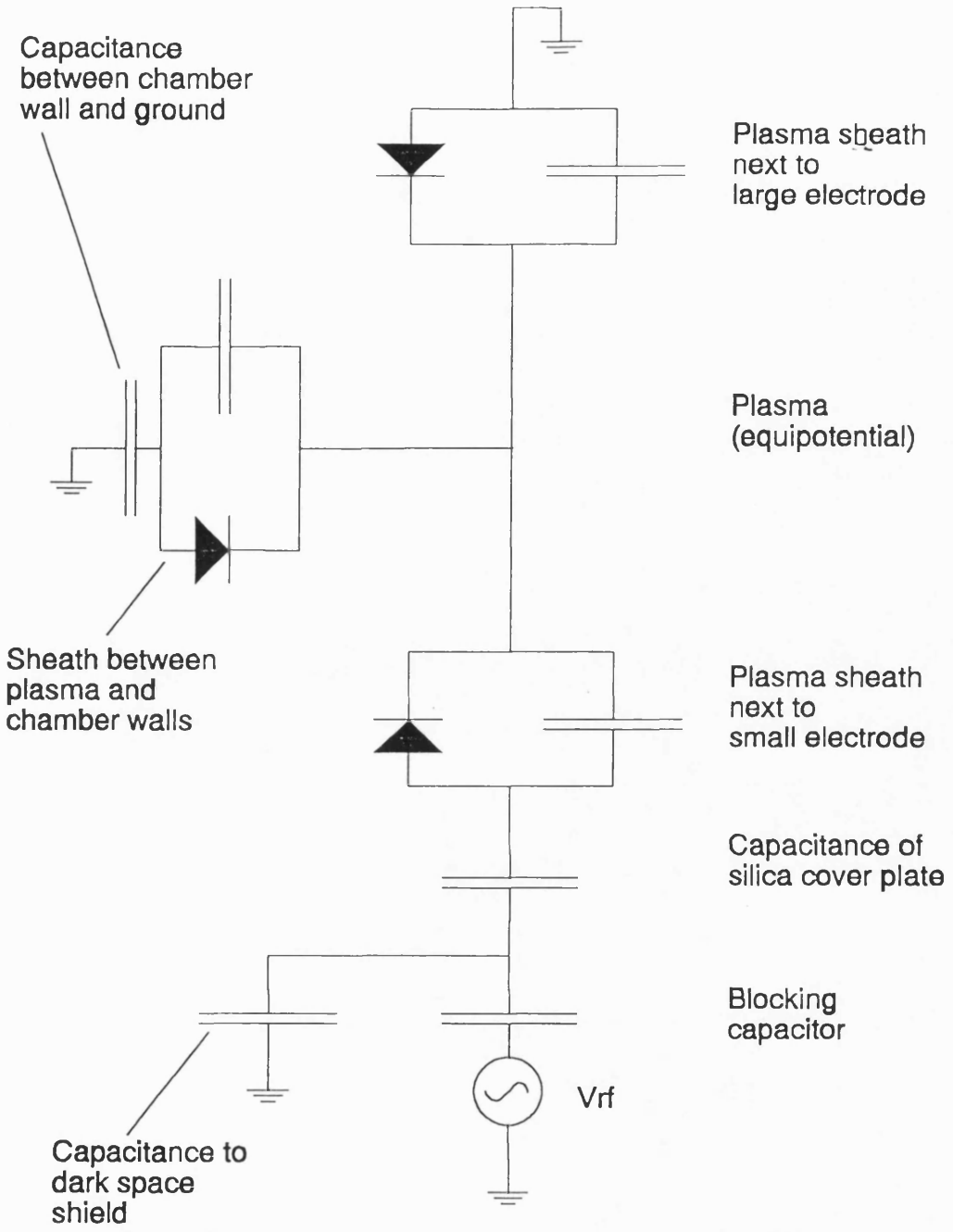

Fig 4.13 Simplified equivalent circuit for the r.f. discharge in an RIE system

oscillating potential is applied to the terminals of this circuit one can see that the net current flow must average to zero, as charge cannot pass through the blocking capacitor. This condition must also be satisfied at each of the sheaths between the plasma and the electrodes. However these regions also behave like diodes, and hence the plasma becomes positively biased with respect to the electrodes. It is this bias which provides the accelerating potential for the positive ions which bombard the wafer surface. The bias also reduces the electron density next to the electrode surface so that the sheath glows less than the bulk of the plasma.

The r.f. driving voltage is divided across the blocking capacitor and the plasma sheaths at the upper and lower electrodes in the inverse ratios of their capacitances. As might be expected, the capacitance of a plasma sheath is proportional to the area of the associated electrode. However it also depends on the sheath thickness, which decreases as the voltage between the plasma and the electrode is reduced. The net result is that the ratio of the voltages across the two sheaths is superlinearly dependant on the ratio of the electrode areas. The exact form of this relationship is a matter of some debate but it can be approximately represented as

$$\left(\frac{V_1}{V_2}\right) = \left(\frac{A_2}{A_1}\right)^{\alpha} \qquad (4.3)$$

where A and V are respectively the area of, and sheath voltage at, a given electrode. α is a parameter whose value lies between 1 and 4. One consequence of the larger potential across the sheath next to the smaller electrode, is that the ions bombarding this electrode are more energetic than those which bombard the larger one. It is for this reason that the sample is placed on the smaller electrode in RIE systems, while in plasma etching, which is essentially a chemical process, it is placed on the larger one.

In practice RIE is a difficult process to analyse exactly, as a change in any one of the parameters that can be easily controlled, such as gas pressure or composition, will cause a number of changes to the physics and chemistry of the plasma in the chamber. There is a considerable amount of effort throughout the world to comprehend these changes but, at present, they are not fully understood. Consequently the approach of most research workers has been fairly empirical, and this was the procedure adopted in studying the optimum conditions for mirror definition.

The mirrors for the demultiplexer were etched using the CH_4/H_2 RIE system that was first described by Niggebrugge et al[25,26,27,28,29]. When this system is used to etch InP one finds that phosphorous is still removed even when the plasma is solely based on hydrogen, but that precursors based on methane are required to remove indium in a volatile form. This type of chemistry is reminiscent of MOCVD in reverse, though the analogy should not be stretched too far as the two processes operate under very different conditions.

Other workers have demonstrated, and we have confirmed that, at a constant r.f. power input, the InP etch rate initially increases with the partial pressure of methane in the reaction chamber. The rate eventually reaches a peak at a partial pressure of about 25 mτ. The etch rate decreases again with further increases in the partial pressure of methane, owing to the deposition of a hydrocarbon polymer on the etching surface. The polymer is deposited on the mask at all methane partial pressures, thus preventing mask erosion. This means that the process is highly selective, so that only a thin mask is required even when etching to considerable depths. The polymer is conventionally removed in an oxygen plasma at the end of the etching process, so that it does not interfere with subsequent processing.

The RIE experiments described below were conducted in a Plasma Technology "Plasmalab μP" (see Figure 4.11) which was evacuated by a roots-rotary pumping combination. The upper and lower electrodes were of 452 and 227 cm^2 in area respectively and were temperature controlled by a recirculating heater-chiller unit. The sample was placed on a silica plate which covered the entire lower electrode, thus preventing backsputtering of the electrode material. The methane and hydrogen process gases were fed into the chamber through a shower head in the upper electrode, after passing through mass flow controllers. A hydrogen plasma was used to recondition the chamber after the polymer described above had been removed in an oxygen plasma.

The samples were patterned with an SiO_2 mask of ~1000Å in thickness which was deposited by PECVD. Initial trials indicated that the process suffered from loading effects[30] (i.e. the etch rate was dependant on the area of semiconductor exposed). Consequently, subsequent experiments were conducted with a dark field mask, so that relatively little semiconductor was exposed, and with samples of approximately constant area (50 mm^2). Fortunately, in most real applications where RIE could be used to etch mirrors, the masks are also dark

field, and hence loading should not significantly upset the process so long as the wafers are not too large.

It was also discovered that the etch rate was dependant on the position of the sample on the electrode, though there was a central region in which the etch rate was fairly constant as shown in Figure 4.14. All subsequent experiments were conducted with the sample in this region.

The typical profile produced in InP by the standard etching conditions of the time (100mτ chamber pressure, 100 sccm total flow rate, 20% methane ,157 W rf power, base electrode at 11^{0}C) is shown in Figures 4.15 and 4.16. The majority of the etched wall was 13^0 off vertical, and heavy polymer deposition was observed on top of the mask. The bulk of this polymer could be removed in an oxygen plasma, but it was difficult to dislodge when it was sheltered from ion bombardment by the eaves of the undercut mask. The etched walls were also undesirably rough, possibly as a consequence of uneven polymer deposition. The profile was reproducible over a period of at least several months, provided that the etcher was maintained in a clean condition.

The effect of progressively reducing the methane content was to give a corresponding reduction in the etch rate, off vertical angle, undercut, edge roughness and polymer deposition rate. For example, a change in the methane content from 20 to 10% (see Figure 4.17) reduced the etch rate by 20% and the off-vertical angle from 13 to 8^0.

Lowering the chamber pressure had similar consequences with, for example, a pressure reduction from 100 to 25 mτ giving a 44% reduction in the etch rate and a decrease in the off-vertical angle from 13 to 5^0 as shown in Figure 4.18.

Etching at a lower temperature did not cause dramatic changes in either the etch rate or the wall angle, though a drop in the base electrode temperature from 25 to 0^{0}C did marginally reduce the off-vertical angle. However, it should be noted that the temperature of the wafer was probably considerably higher than that of the base electrode, owing to the poor thermal conductivity of the silica coverplate.

Unfortunately it was not possible to transfer these results directly from InP to its lattice matched GaInAsP derivatives. For example, the etching conditions that produced the smallest off-vertical angle of 5^0 in InP, produced a profile

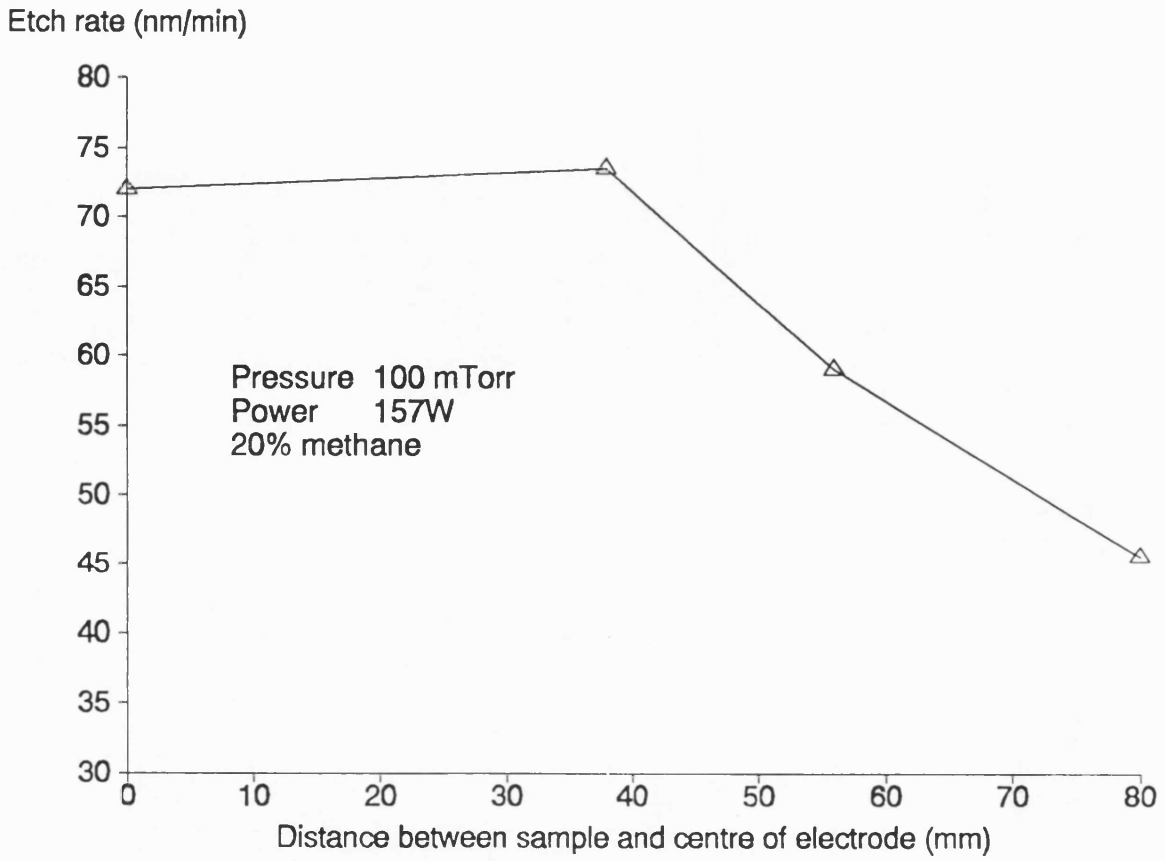

Fig 4.14 RIE etch rate as a function of sample position

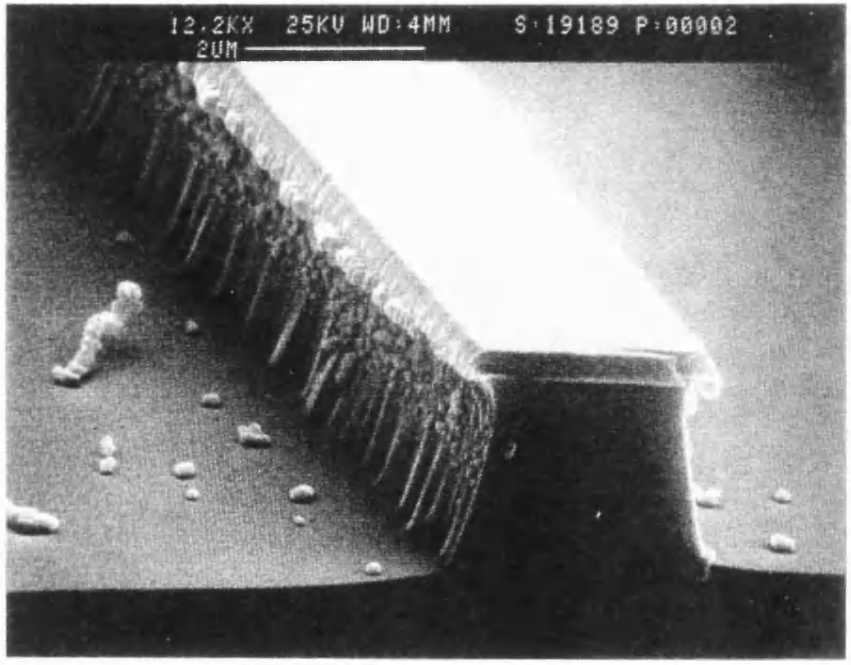

As etched

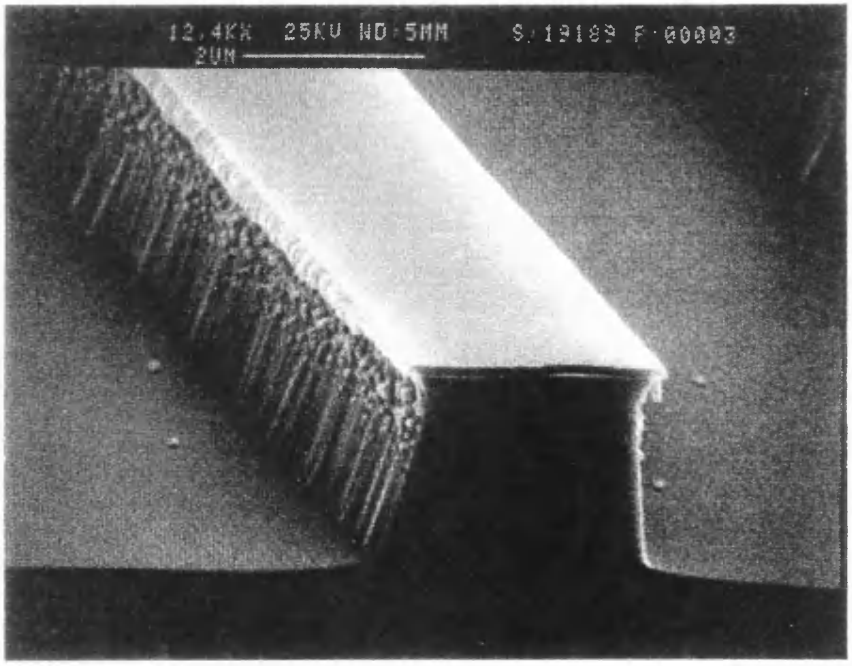

Polymer deposits removed in oxygen plasma

Fig 4.15 Etched profile in InP with oxide mask
(30 min, 157W, 100 mTorr, 20% methane)

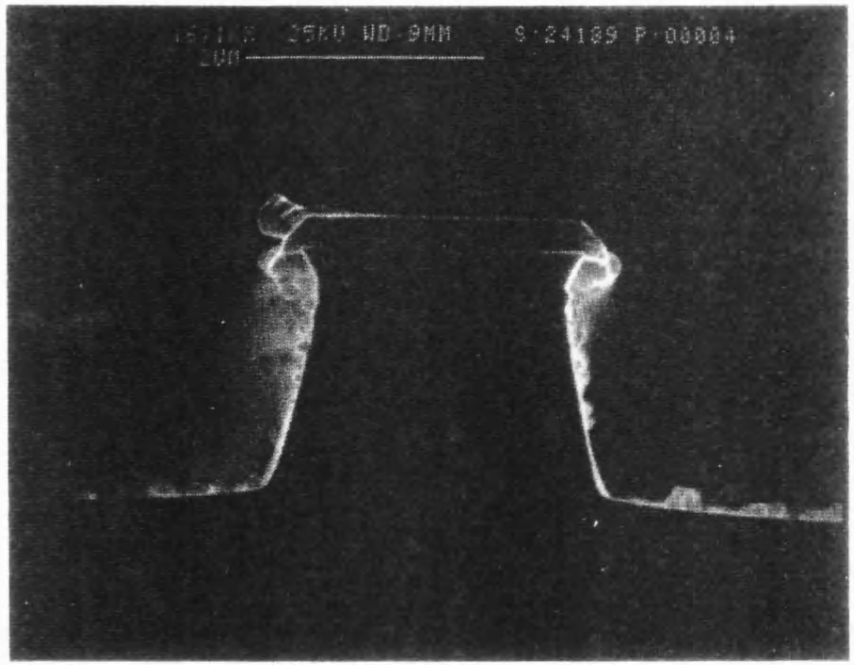

As etched

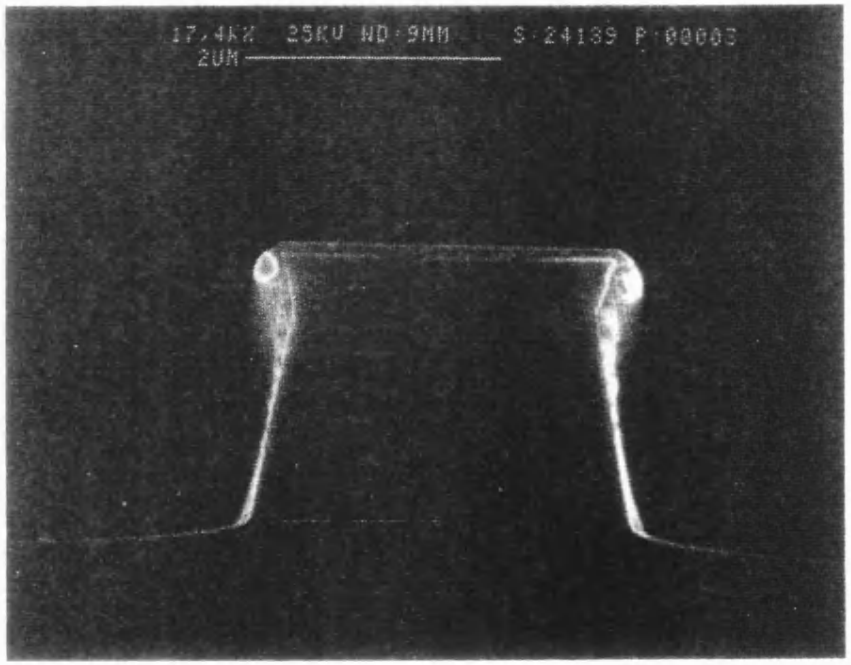

Polymer deposits removed in oxygen plasma

Fig 4.16 Etched profile in InP with oxide mask
(30 min, 157W, 100 mTorr, 20% methane)

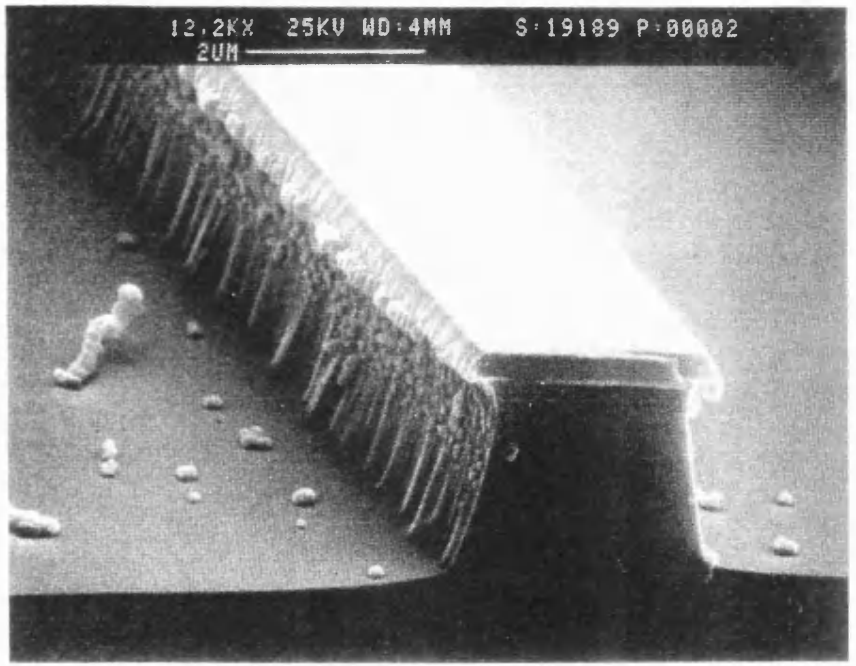

20% methane

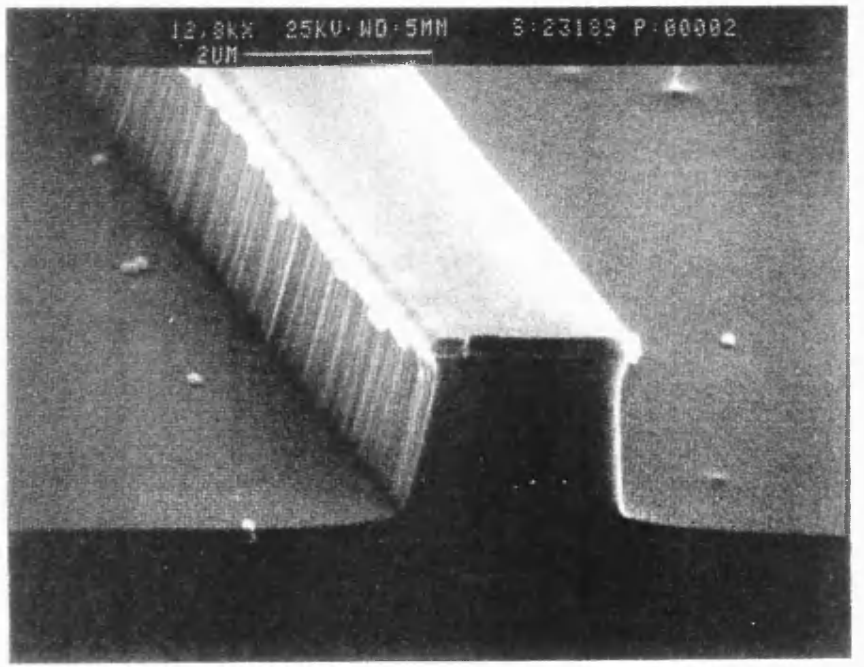

10% methane

Fig 4.17 Effect of methane content on etched profile in InP (30 min, 157W, 100 mTorr)

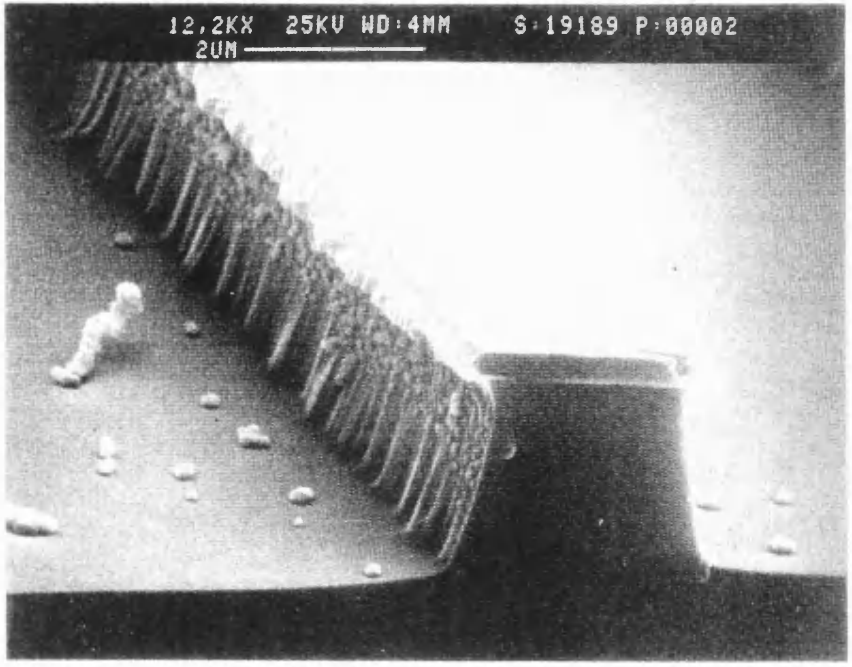

100 mTorr

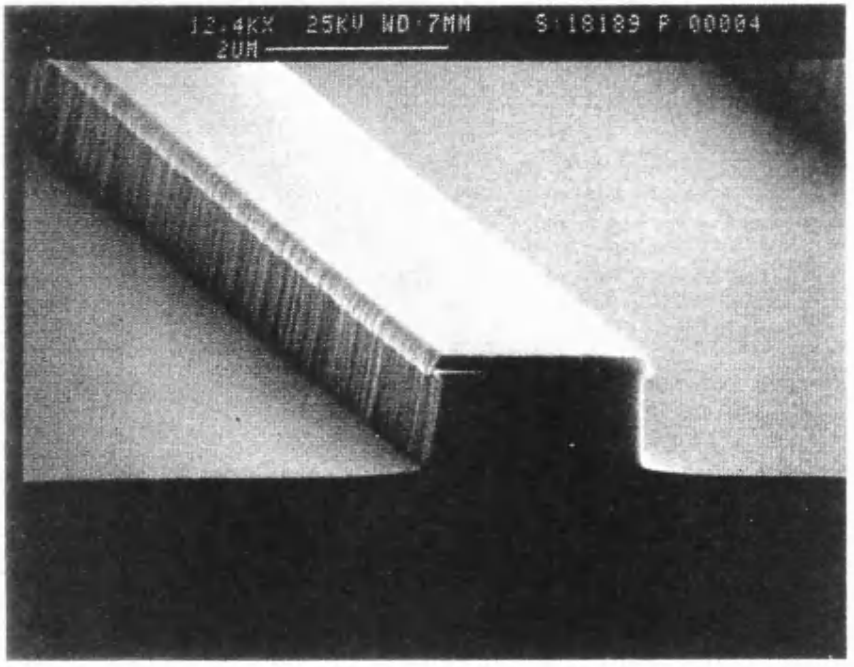

25 mTorr

Fig 4.18 Effect of pressure on etched profile in InP
(30 min, 157W, 20% methane)

with an off-vertical angle of 14^0 in GaInAsP quaternary material with a photoluminescence wavelength of 1.3 μm (see Figure 4.19). The etch rate of the latter material was only 45% of that for InP.

The profiles shown in the above figures are of similar general shape to those reported by other workers, though accurate data on wall angles is only reported in a few cases. The origin of the characteristic undercut profile with a gently rising channel floor next to the mask is not fully understood at present. The two most likely explanations for its shape appear to be:

a) That there is a slow essentially chemical sideways etching process at the same time as the more rapid ion assisted downwards one. Evidence for this mechanism has been found by Thomas et al[30], in that the wall angle and the self bias potential differ in their dependence on the partial pressure of methane in the chamber.
b) That the bombarding ions are scattered by collision processes in the plasma sheath, so that they have a distribution of angular velocities. Shaqfeh et al have devised a model[31,32] which shows that the interaction of this distribution with the topology of the etching surface can be used to explain the type of profile that we observe. In this model the rising channel floor next to the mask is attributed to the obstruction of incoming ions from certain angles by the adjacent mesa. Similarly the overhanging eave of material under the mask is caused by the small number of ions which approach at an extreme angle of incidence.

Unfortunately, at the time of device fabrication, the scope for further reductions in the wall angle through adjustment of the process parameters appeared to be limited, as the use of lower pressures or methane contents would not only have placed demanding stability requirements on the mass flow controllers, but would also have lead to impracticably long etch times. However, it was discovered that it was possible to achieve the desired reduction in the angle of the wall, by interleaving the methane-hydrogen plasma with an oxygen one. The oxygen plasma appeared to passivate the wall against further attack, possibly through the formation of an oxide on the exposed surface. The completed wall consisted of a series of profiles corresponding to each etching stage, stacked on top of each other. A profile of this type is shown in Figure 4.20(a). This development meant that I was able to trade a profile with a finite wall angle for a series of mini-profiles, each with the same wall angle. Such an exchange seemed desirable, as the optical loss on reflection from a

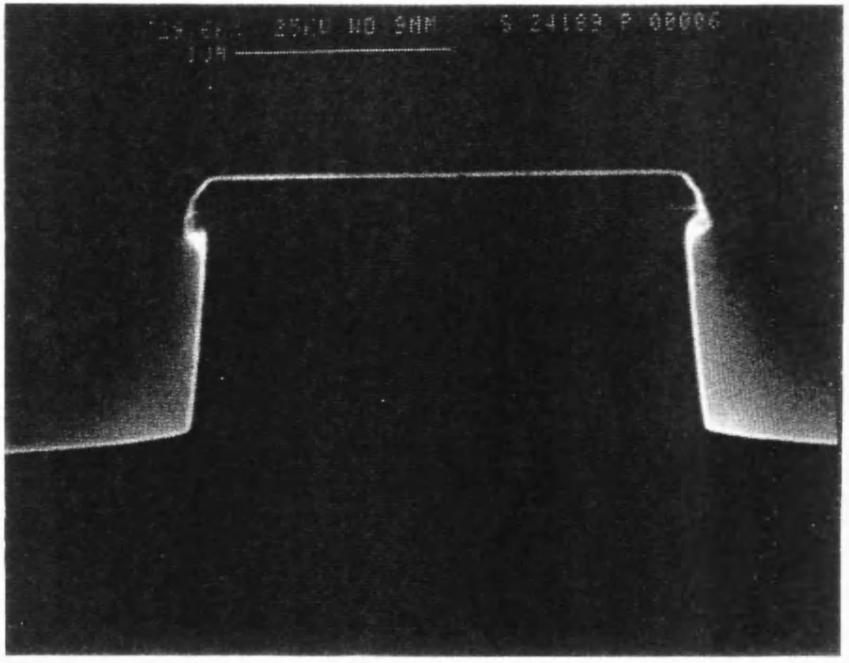

30 min InP

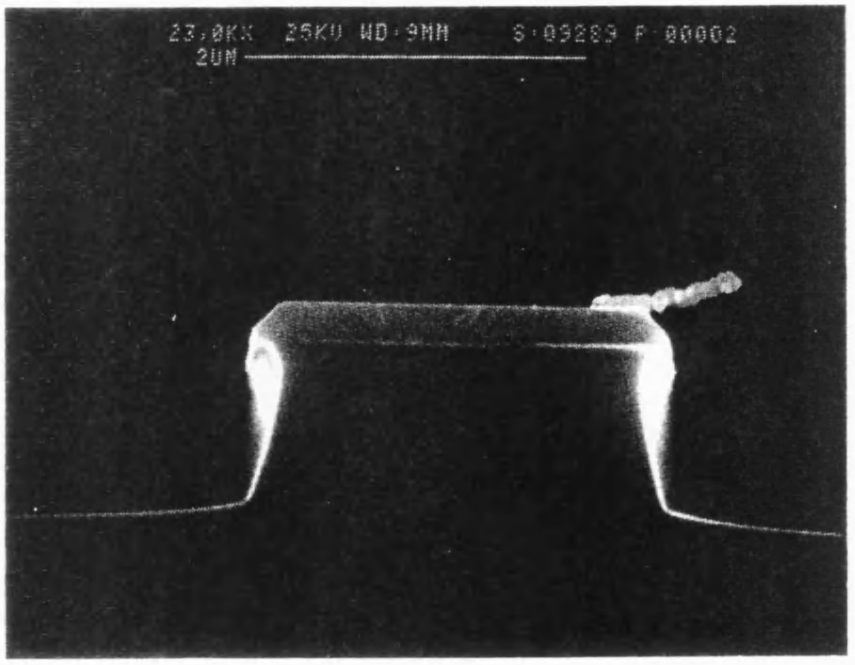

49 min 1.3 μm quaternary

Fig 4.19 Effect of material on etched profile in InP
(157W, 25 mTorr, 20% methane)

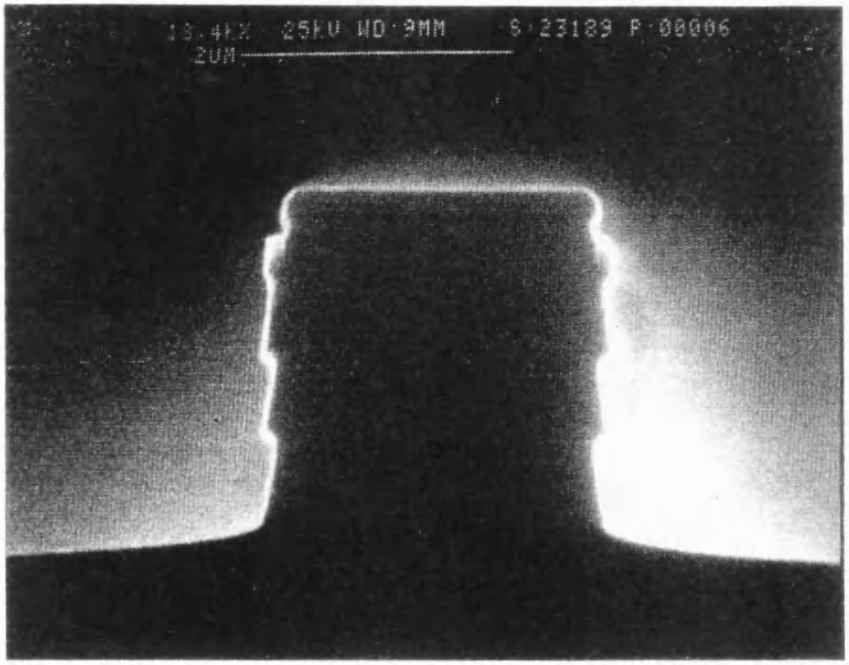

(a)

10 min, 157 W, 100 mTorr, 10% methane
5 min, 157 W, 100 mTorr, oxygen
Cycle repeated four times

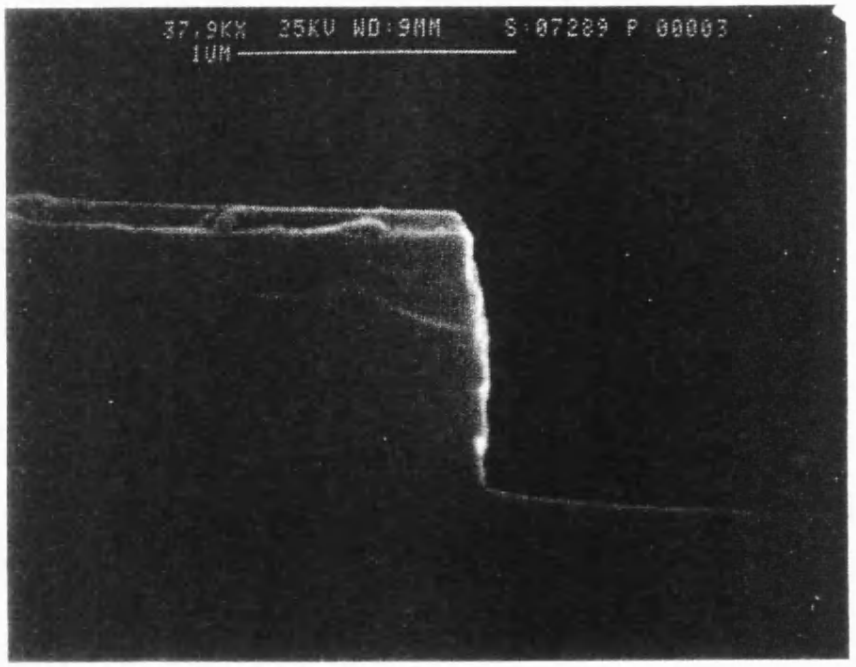

(b)

6 min, 157 W, 25 mTorr, 20% methane
3 min, 157 W, 100 mTorr, oxygen
Cycle repeated five times

Fig 4.20 Multistep etched profiles in InP

mirror is related to the total variation in phase across the reflected wavefront, rather than the absolute mirror angle.

It was possible to reduce the magnitude of the ripple on the multi-step etched wall by:

a) reducing the chamber pressure so that the off-vertical wall angle on each of the mini-profiles was reduced.
b) increasing the number of etching steps.

Unfortunately, the total number of etching steps was limited by a problem with mask erosion which caused an overcut profile as shown in Figure 4.20(b). This erosion problem was probably associated with the fact that the edge of the SiO_2 mask was tapered rather than vertical. It might be possible to eliminate it in the future by adjustment of the photolithographic and oxide etching processes. However, the mirrors for the device on which results are reported below, were etched using a compromise solution, in which only three etching steps were employed so that mask erosion was not excessive. The plasma conditions employed (25mτ, 50sccm flow, 20%CH_4, 157W, 25^{0}C) were those that gave the best wall angle in a single stage etch. A scanning electron micrograph of the resulting wall, which was ~4^0 off vertical, is shown in Figure 4.21.

4.5. REFERENCES

1 G.B.Stringfellow, "Organometallic Vapour Phase Epitaxy"(Academic Press Inc., London, 1989)

2 M.J.Ludowise, J. Appl. Phys., 1985, 58, pp.R31-R55

3 M.R.Leys, *Chemtronics*, 1987, **2**, pp.155-164

4 A.W.Nelson, R.H.Moss, P.C.Spurdens, S.Cole and S.Wang, *Br. Telcom Technol. J.*, 1986, **4**, pp.85-103

5 E.J.Thrush, C.G.Cureton, J.M.Trigg, J.P.Stagg and B.R.Butler, *Chemtronics*, 1987, **2**, pp.62-68

6 M.Saruwatari and K.Nawata, *Appl. Optics*, 1987, **18**, pp.1847-1856

7 M.A.Afromowitz, *Solid State Commun.*, 1974, **15**, pp.59

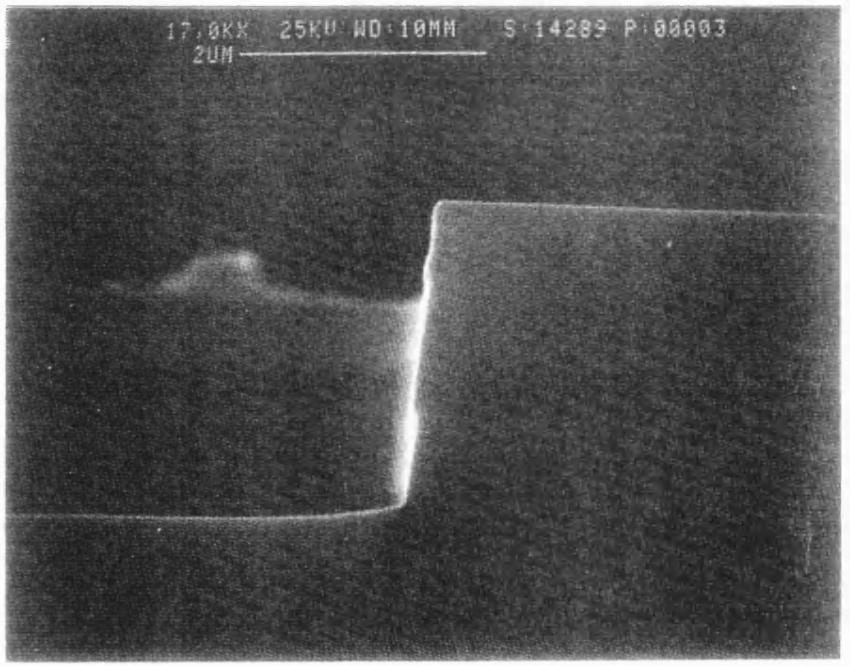

Fig 4.21 Cleave through demultiplexer mirror wall

[8] K. Utaka, Y.Suematsu, K.Kobayashi and H.Kawanishi, *Jpn. J. Appl. Phys.*, 1980, **19**, pp.L137-L140

[9] B.Broberg et al, *J.Appl.Phys.*, 1984, **55**, pp.3376

[10] G.H.B.Thompson, *"Physics of Semiconductor Laser Devices"*(Wiley, Chichester, 1980)

[11] T.P.Pearsall, *"GaInAsP Alloy Semiconductors"* (Wiley, New York, 1982)

[12] E.P. O'Reilly, *Semicond. Sci. Technol.*, 1986, **1**, pp.128-132

[13] E.P. O'Reilly, *Semicond. Sci. Technol.*, 1989, **4**, pp.121-137

[14] F. Stern, *Solid State Physics*, 1963, **15**, pp.299-408

[15] A. Abragam, *"Principles of Nuclear Magnetism"* (Clarendon, 1961)

[16] B. M^{c}Donald and A. Goetzberger, *J. Electrochem. Soc.*, 1962, **109**, pp.141-144

[17] U. Niggebrugge, P. Albrecht, W. Doldissen, H.P. Nolting and H. Schmid, *Proc. Fourth European Conf on Integrated Optics ECIO 87*, Glasgow, 1987, pp.90-93

[18] M.E.Jones and C.Dix, *Br. Telecom Technol. J.*, 1989, **7**, pp.25-43

[19] A.Carenco, *Proc. Fourth European Conf on Integrated Optics ECIO 87*, Glasgow, 1987, pp.1-7

[20] R.G.Walker, *Electronics Letters*, 1985, **21**, pp.581-583

[21] K. Iga, K. Wakao and T. Kunikane, *Applied Optics*, 1981, **20**, pp.2367-2371

[22] H. Saito and Y. Noguchi, *Japn. J. Appl. Phys.*, 1989, **28**, pp.1836-1842

[23] B. Chapman, *"Glow Discharge Processes"* (Wiley, New York, 1980)

[24] D.E. Ibbotson and D.L. Flamm, *Solid State Technology*, 1988, pp.105-108

[25] U. Niggebrugge, M. Klug and G. Garus, *Proc. 12th Symposium on GaAs and Related Compounds*, Karuizawa, Japan, 1985, pp.367-372

[26] L. Henry, C. Vaudry and P. Granjoux, *IEE Elect. Lett.*, 1987, **23**, pp.1253-1254

27 T.R. Hayes, *Plasma Technology Seminar*, Tegal, 1989

28 T.R. Hayes, M.A. Dreisbach, P.M. Thomas, W.C. Dautremont-Smith and L.A. Heimbrook, *J. Vac. Sci. Technol. B*, 1989, **7**, pp.1130-1140

29 D.J. Thomas and S.J. Clements, *Proc. 20th European Solid State Device Research Conference ESSDERC 90*, Nottingham, 1990, pp.121-124

30 V.J. Law, G.A.C. Jones, N.K. Patel and M. Tewordt, *"Microcircuit Engineering 89"* (Elsevier Science Publishers, Amsterdam, 1990), pp.611-614

31 E.S.G. Shaqfeh and C.W. Jurgensen, *J. Appl. Phys.*, 1989, **66**, pp.4664-4675

32 C.W. Jurgensen and E.S.G. Shaqfeh, *J. Vac. Sci. Technol. B*, 1989, **7**, pp.1488-1492

Chapter 5

Demultiplexer Fabrication and Measurement

5.1. INTRODUCTION

The details of individual fabrication processes used in the construction of the demultiplexer have already been described in the chapter 4. This chapter explains how they were fitted together to form the final processing scheme. It also documents the assessment of the device, and the findings of this assessment.

5.2. DEMULTIPLEXER PROCESS OUTLINE

The processing scheme used for the demultiplexer can be summarised as follows.

a) Grow GaInAsP (λ_{PL} =1.3μm) on an InP substrate by MOCVD.
b) Deposit a layer of SiO_2 on the wafer by PECVD.
c) Transfer the mirror and waveguide pattern into the SiO_2 layer by photolithography.
d) Deposit of a second layer of SiO_2 by thermal deposition.
e) Pattern the second layer to open windows over the grating and mirror regions.
f) Etch the mirrors by CH_4/H_2 RIE.
g) Remove the second SiO_2 layer in BHF.
h) Etch the waveguides by CH_4/H_2 RIE.
i) Remove the first SiO_2 layer in BHF.
j) Cleave the wafer to separate the devices.

A summary of the specifications of the final wafer of devices is given in Appendix B. An optical micrograph of a complete demultiplexer, and scanning electron micrographs of its component parts are shown in Figure 5.1.

5.3. MASK DESIGN

A series of devices of progressively increasing complexity was fabricated alongside each complete demultiplexer, so that the performance of the

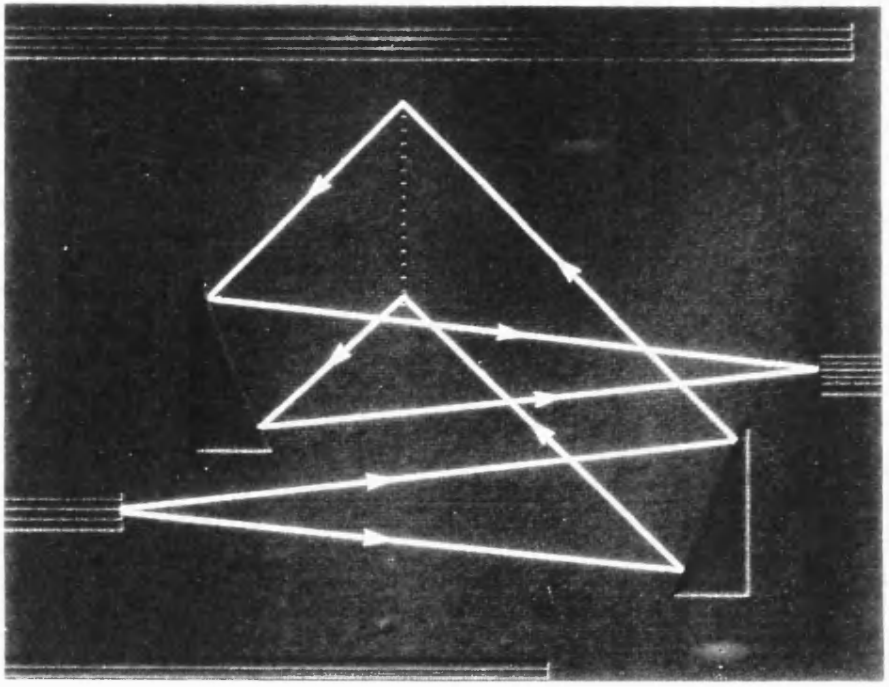

500 µm

Light path through device

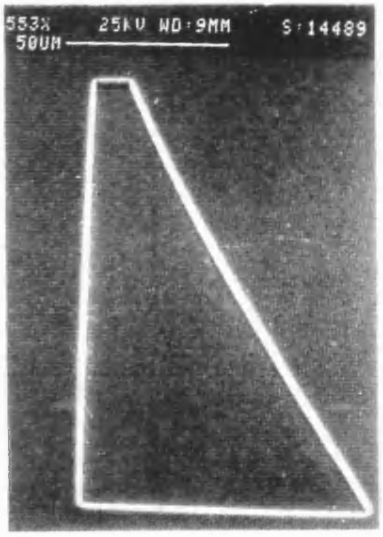

Detail of mirror

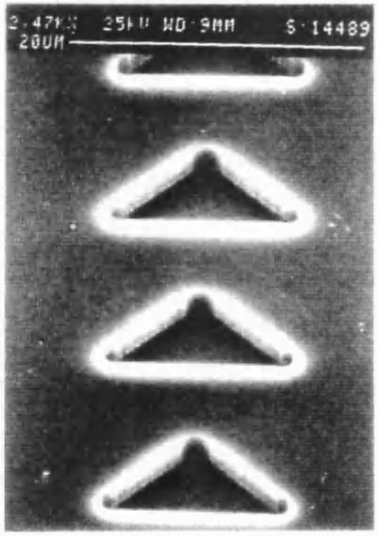

Detail of grating

Fig 5.1 Micrographs of the demultiplexer

component parts of the latter could be deduced. The range of devices within each unit cell can be seen in Figure 5.2. This range consisted of:

a) A pair of ridge waveguides.
b) Two parabolic mirrors in a periscope formation. These were arranged to collect light from an input waveguide and focus it onto a cleaved edge. The mirrors were separated by 250μm.
c) A periscope like b) except focusing light onto an output waveguide.
d) A periscope like c) except with the mirrors separated by 710μm. This corresponded to the optical path between the mirrors in the demultiplexer.
e) A complete demultiplexer as shown in Figure 3.1 except with the output focused onto a cleaved edge instead of an array of waveguides.
f) A complete demultiplexer as shown in Figure 3.1.

Each device was provided with three input and, where applicable, five output waveguides, arranged as shown in Figure 5.3. This combination allowed one to measure the performance of the grating at 1/8 of an order intervals and ensured that, for any wavelength, there was a response close to the direction for which the grating was blazed. Crosstalk between these closely spaced groups of waveguides was minimised by making them of different widths, alternately large and small, to offset their respective phase velocities. Calculations[1] showed that the intensity coupling between any two of these waveguides was less than 4%. The waveguides were created by etching two channels on either side of the ridge. This meant that the top of the ridge was flush with the slab waveguide at the point where the lateral guiding was removed. There should be virtually no coupling loss at this type of termination.

The groups of waveguides were placed centrally between deep trenches which were etched at the same time as the mirror recesses. These trenches extended across the intended cleave position as shown in Figure 5.2. They were used as reference marks to determine the exact location of device outputs. The cleaves, which defined the image plane for devices without output waveguides, all propagated within 5μm of the desired location. This degree of offset should not significantly affect the observed width of near fields.

5.4. DEVICE ASSESSMENT

An initial assessment of the near fields produced by the above devices was made by illuminating the input waveguides with 1.51μm radiation from a DFB

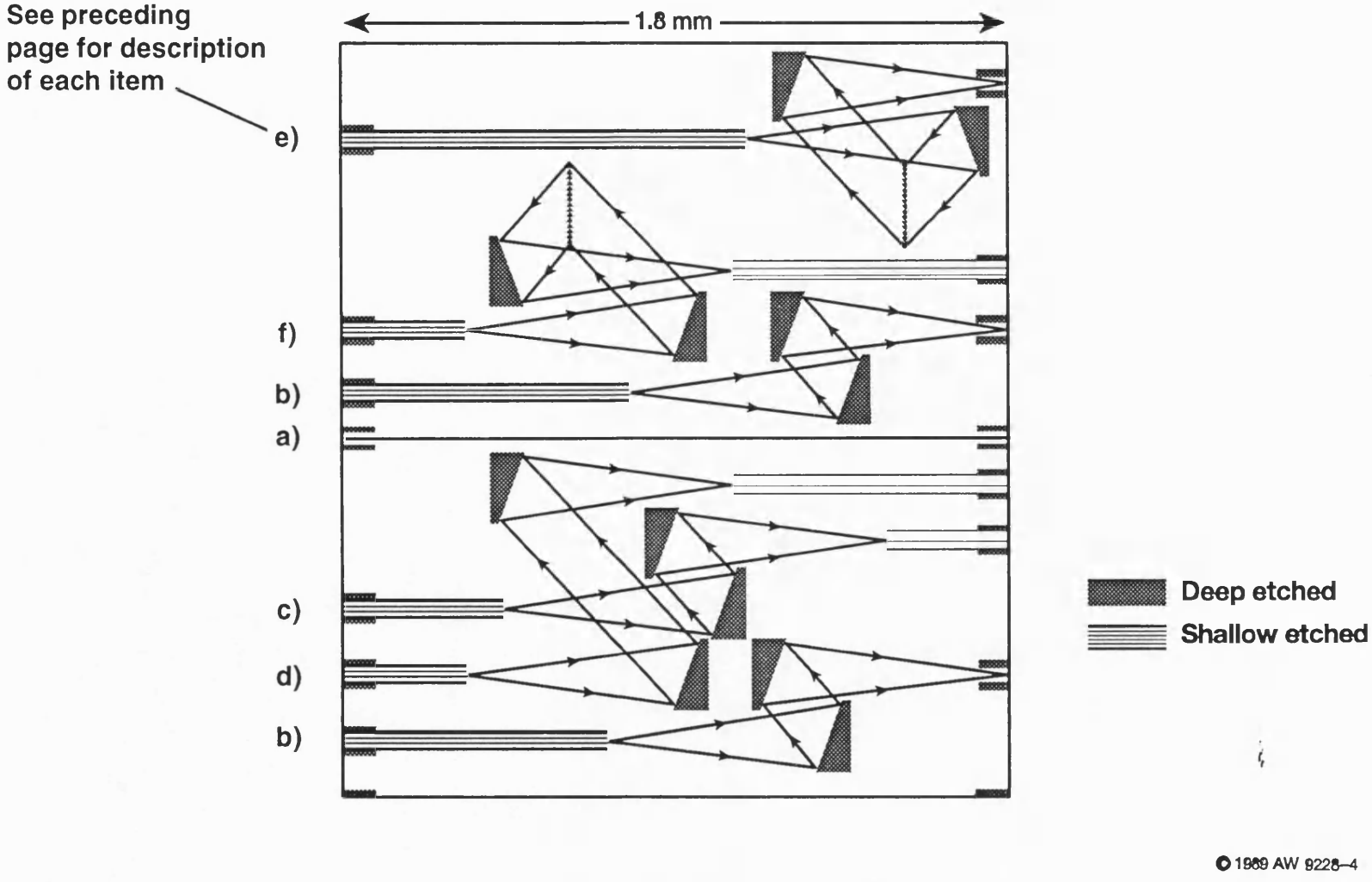

Fig 5.2 Device layout

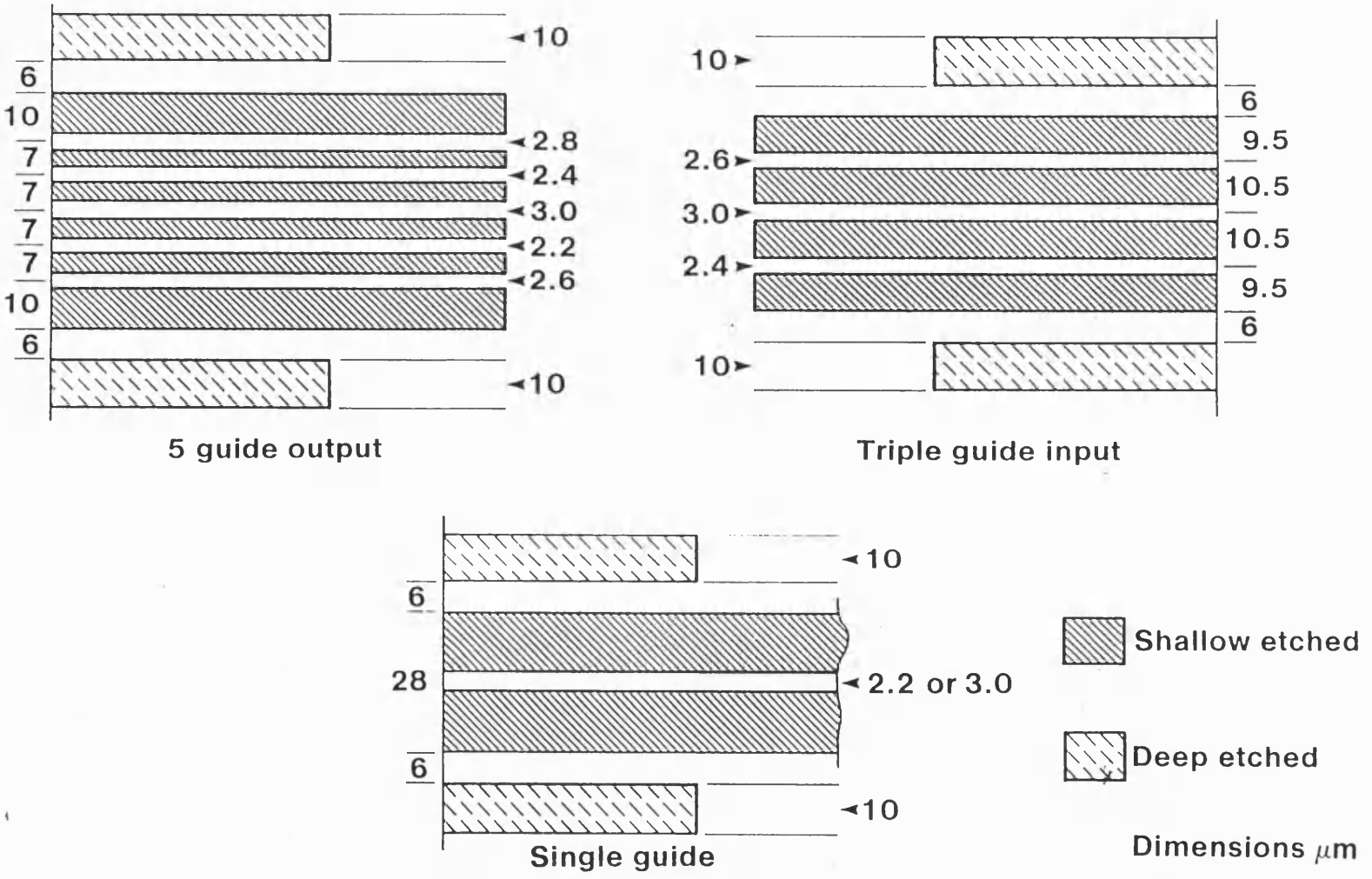

Fig 5.3 Disposition of sets of output and input guides and test guide markers

laser[2]. The apparatus is shown in Figure 5.4. The device outputs were imaged onto an infra-red camera and are shown in Figure 5.5.

The image from the periscope focused onto the cleaved edge was similar to that from the input waveguide, and was never more than 1μm from the desired position. The demultiplexer focused onto the cleaved edge also produced a similar output, though the near field contained one or two diffraction orders depending on which one of the input guides was illuminated.

Near field relative power measurements were then made by dumping a video line, which was aligned to the slab waveguide, onto a chart recorder. The non-linear response of the camera was calibrated by reference to a photodiode. The results confirmed that the outputs from the periscope and the spectrometer were close to the diffraction limit. (Equivalent Gaussian spot radii for the waveguide, periscope, and spectrometer were 2.3, 2.5 and 3.0μm respectively.) However the measured signal to noise ratios for both the periscope and the spectrometer were only 15-20 dB (see for example Figure 5.6). Earlier theoretical calculations, such as those discussed in section 3.2, had indicated that the main signal should be at least 30 dB above subsidiary peaks. It is suspected that the background level arose from coupling losses when light was launched into the input waveguide, as its intensity rose rapidly when the input was slightly decoupled. In future it should be possible to eliminate some of this noise by incorporating a two dimensional iris into the structure.

The optical losses of the demultiplexer components were measured by direct comparison of the power transmitted through the uninterrupted waveguides, with that through each device. The loss in each 1.8mm long uninterrupted waveguide is unlikely to have been large, as identical waveguides on the same wafer exhibited losses[3] of 0.9 dB/cm. All the transmitted powers were measured with both a DFB laser, and a FP laser of similar wavelength, in order to determine the influence of Fabry-Perot fringes between the cleaved facets. The data from these two sets of measurements was virtually identical, thus confirming that such fringes were suppressed by broadening of the DFB linewidth associated with optical feedback from the demultiplexer facet. This finding agreed with previous experience, when it was necessary to insert about 20 dB of additional attenuation between the laser and the waveguide to measure waveguide losses by the Fabry-Perot technique. A summary of the measured losses is given in the following table.

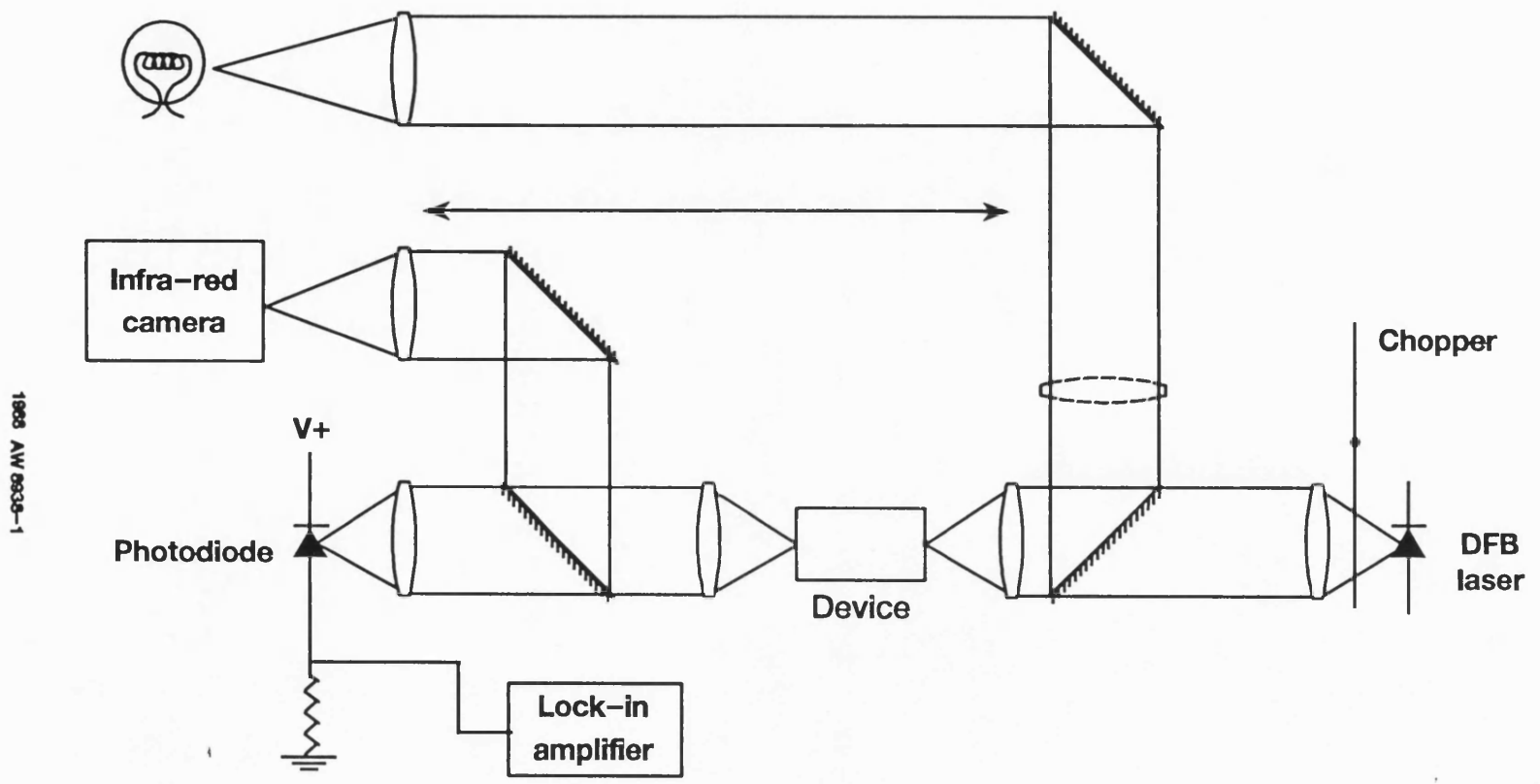

Fig 5.4 Assessment apparatus

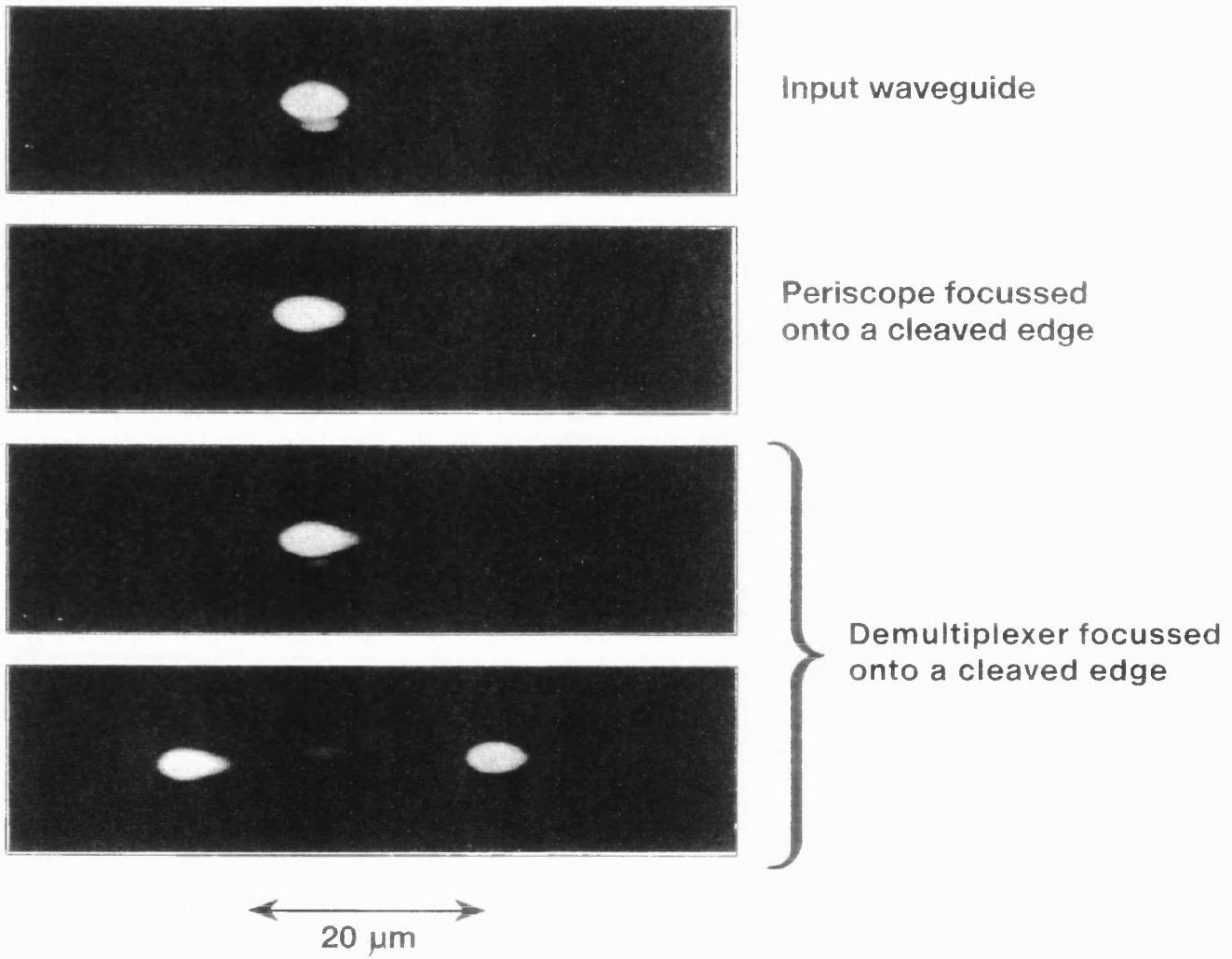

Fig 5.5 Device near fields

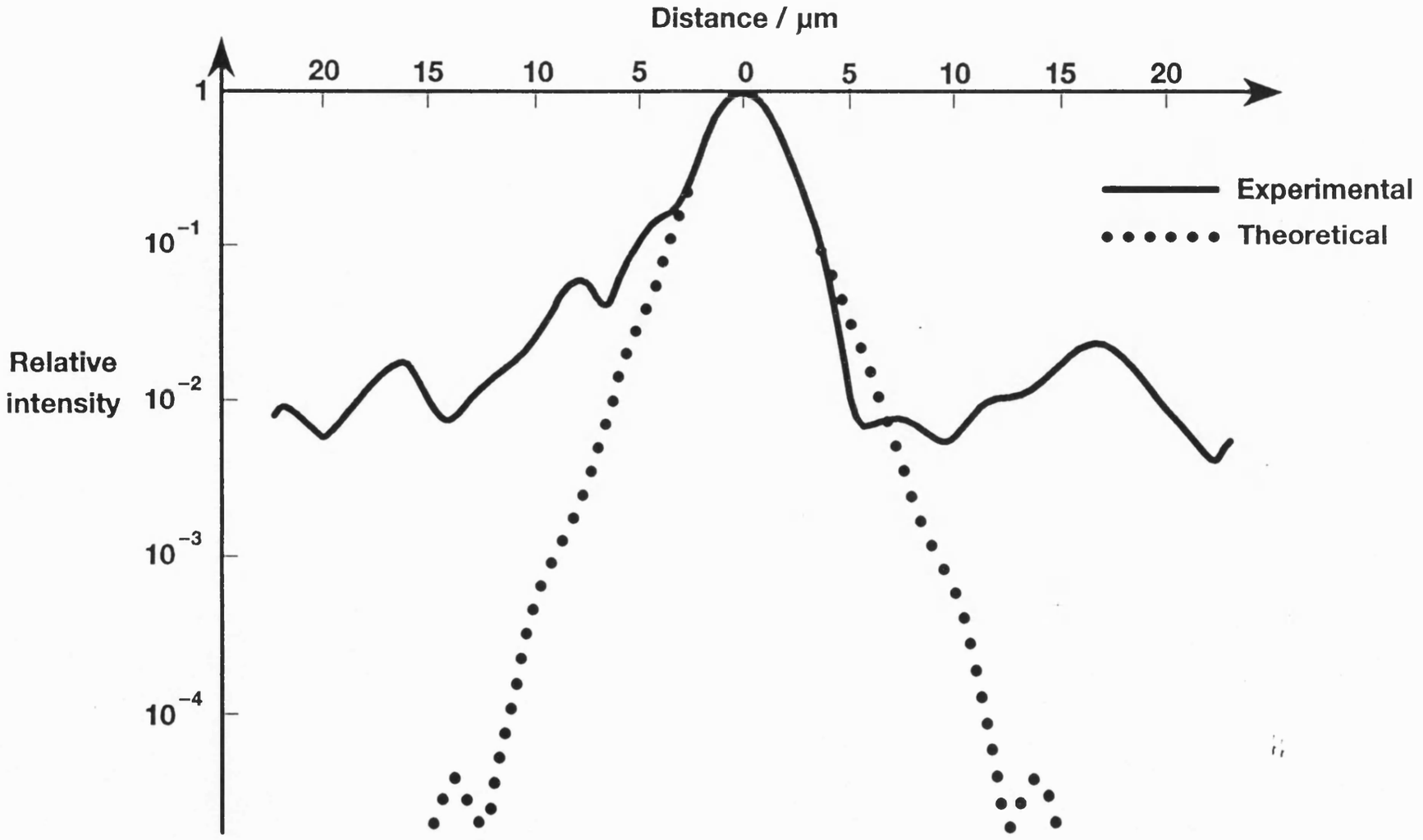

Fig 5.6 Demultiplexer near field

Table 5.1 Losses of Demultiplexer Components

Device	Output collected via	Excess loss over straight guide /dB
Two parabolic mirrors separated by 250 μm	Cleaved edge	4.2±0.5
Two parabolic mirrors separated by 250 μm	Waveguide	4.1±0.3
Two parabolic mirrors separated by 710 μm	Waveguide	4.7±0.3
Integrated spectrometer (two mirrors 710 μm apart and a grating)	Cleaved edge	7.2±0.3
Integrated spectrometer as above	Waveguide	7.6±0.3

Periscopes with long and short path lengths exhibited losses of 4.7±0.3 and 4.1±0.3 dB respectively. This indicated that most of the loss was occurring at the reflecting surfaces, with about 2 dB being lost per reflection. Lack of perfect mirror verticality only accounts for about 0.5 dB of this, so the remainder must have originated from other causes such as roughness.

The demultiplexer focused onto the cleaved edge showed a loss of 7.2±0.3 dB. This meant that the additional loss caused by the insertion of the grating was about 2.5 dB. This figure is only 0.5 dB greater than the loss caused by the insertion of a mirror, and indicates that the diffraction efficiency was high.

The additional loss on coupling light from the periscope with the 250μm path length back into a waveguide was insignificant. This confirmed the accurate positioning and quality of the near fields described above.

The dispersive properties of the grating were measured by using a colour centre laser to excite the central input waveguide of the demultiplexer focused onto the cleaved edge. The device output was then imaged onto the infra-red camera, so that its position could be monitored while the laser wavelength was tuned from 1.51 to 1.55μm, in 5nm steps. A plot of the location of this output as a function of the input wavelength is shown in Figure 5.7. The series of lines corresponds to the progression of diffraction orders that became visible as the wavelength was altered. The separation between adjacent diffraction orders at a given wavelength was (29.6±0.8)μm. Calculations based on the Afromowitz

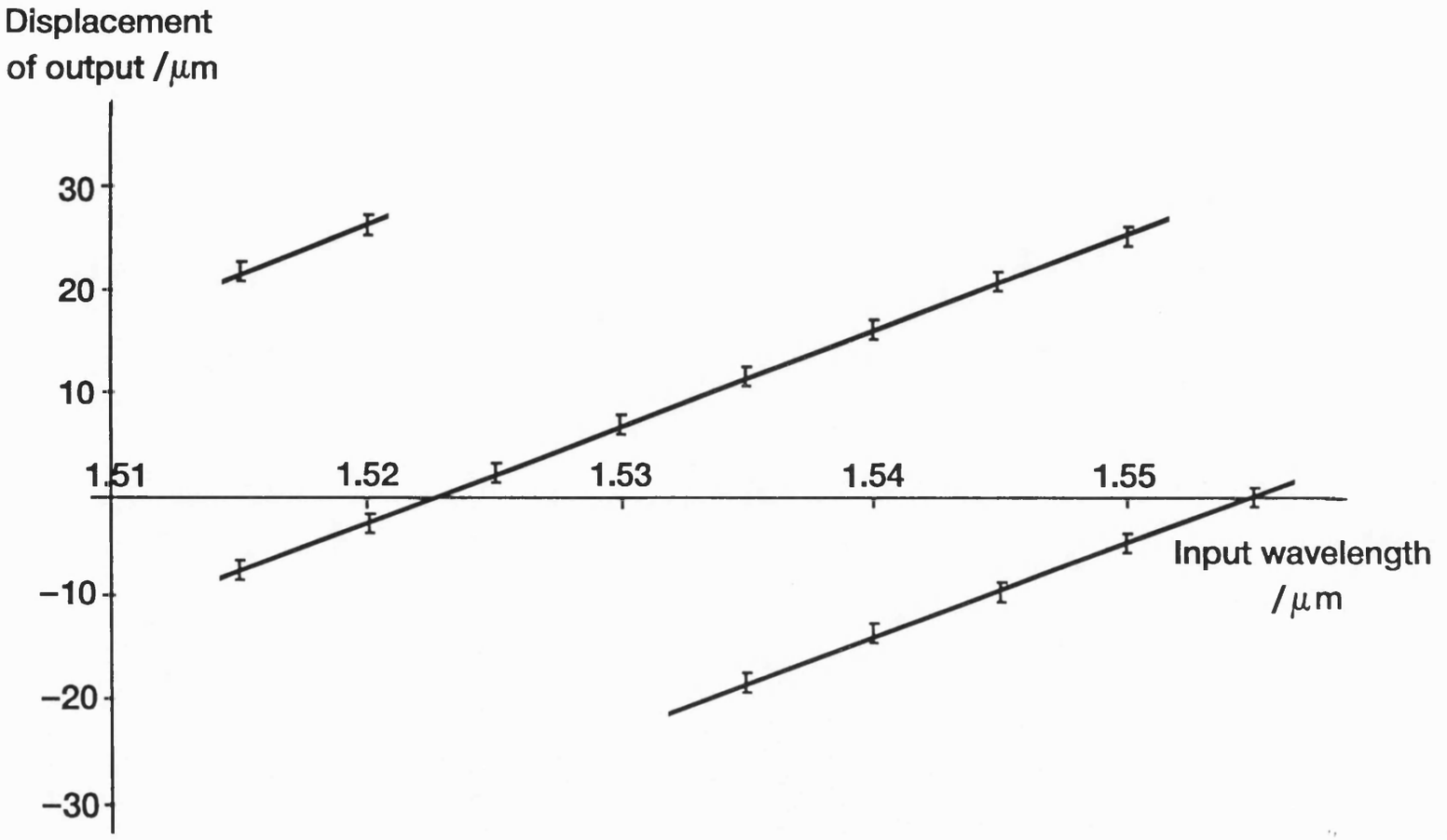

Fig 5.7 Dispersion of the demultiplexer

1989 AW 9295–04

modified single oscillator model for refractive index[4,5,6], and the waveguide equations[7], indicated that the anticipated theoretical spacing was 29.0 μm. The measured dispersion of (0.94±0.4)μm along the cleaved edge, per nm change in input wavelength, was also in good agreement with the theoretical prediction of 0.94μm/nm. Details of the theoretical calculations are given in Appendix A.

The polarisation sensitivity of the demultiplexer was tested by illuminating its input with radiation from a DFB laser which was angled at 45° to the slab waveguide. The output of the device was then imaged onto the infra-red camera. It is shown in Figure 5.8. The separation between the images formed by the TE and TM modes was (10±1)μm. This was obviously unsatisfactory in a device where adjacent diffraction orders were separated by 29μm. The separation of the polarisations was a consequence of the different effective indices for the TE and TM modes. Theoretically the magnitude of this separation d is given by

$$d = l.\frac{\Delta\varepsilon}{\varepsilon} \qquad (5.1)$$

where $\Delta\varepsilon$ is the difference in the effective relative permittivities for the TE and TM modes and ε is the mean effective relative permittivity. l is the mirror focal length. Calculations based on the above equation, the Afromowitz single oscillator model, the waveguide equations, and the device specifications given in Appendix B, indicated that the theoretical separation was (8.6±1.8)μm. This figure was in reasonable agreement with the experimental result. These calculations also indicated that the polarisation discrimination could be reduced by:

a) increasing the thickness of the guide layer.
b) moving from a single to a double heterostructure.
c) reducing the photoluminescence wavelength of the guide layer.

as all of these changes decreased the value of $\Delta\varepsilon$. The magnitudes of the improvements that could be obtained with each of these modifications are shown in Tables 5.2 and 5.3. The numbers in the tables indicated that the polarisation discrimination could be reduced to a manageable value by, for example, moving to a guide layer with a photoluminescence wavelength of 1.05 μm and a double heterostructure waveguide.

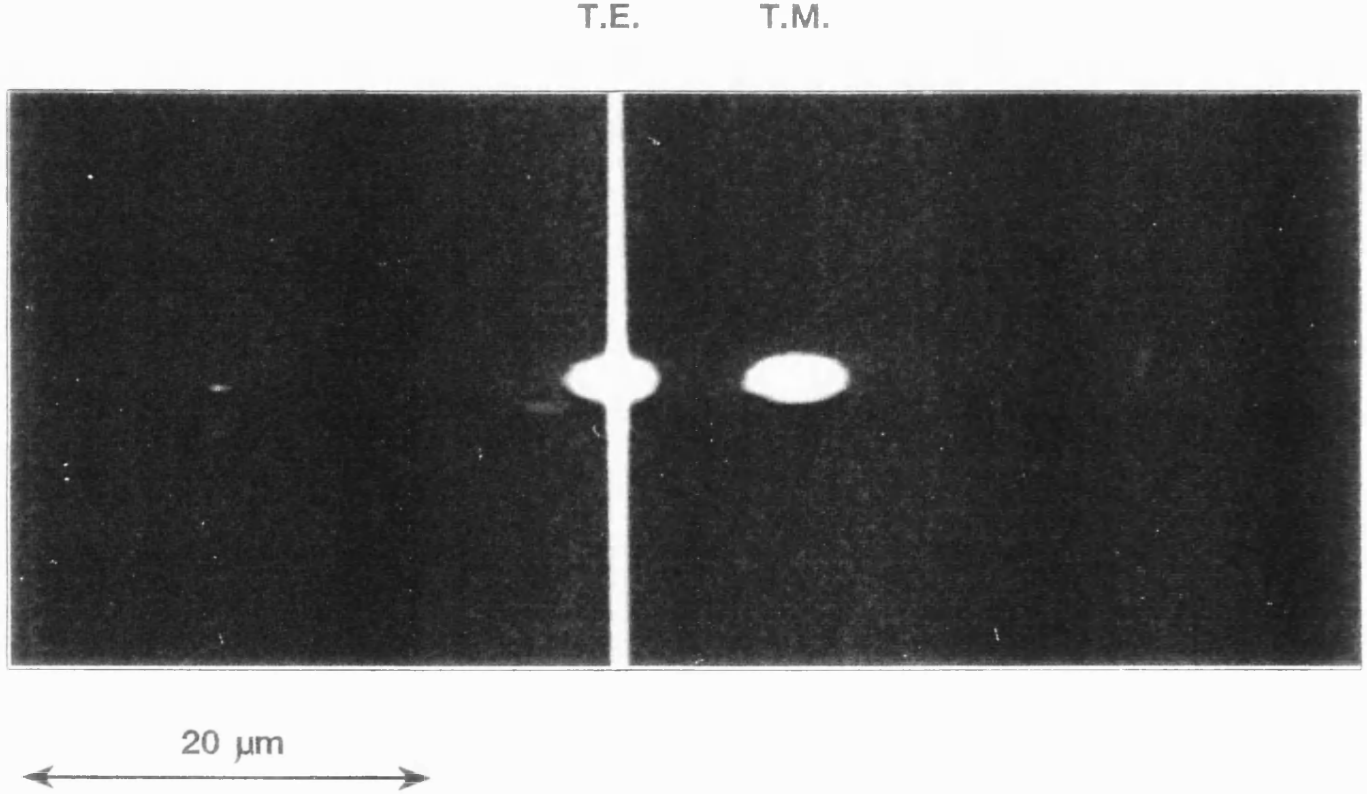

Fig 5.8 Polarisation discrimination in the demultiplexer

Table 5.2 Effect of guide layer thickness on polarisation discrimination

Single heterostructure slab waveguide

Guide layer

Material GaInAsP

λ_{PL} 1.31 μm

Probe wavelength 1.51 μm

All other parameters, except those quoted below, as in Appendix B

Guide layer thickness (μm)	Separation between the two polarisations at the output facet (μm)	Equivalent wavelength difference to achieve same separation (nm)
0.5	11.2	11.9
0.6	8.6	9.2
0.7	6.5	6.9
0.8	5.0	5.3

Table 5.3 Effect of guide layer composition on polarisation discrimination

Guide layer material GaInAsP

Probe wavelength 1.51 μm

All other parameters, except those quoted below, as in Appendix B

Guide	layer composition λ_{PL} (μm)	1.27	1.18	1.10	1.05
Single hetero-structure	Layer thickness (μm) (max for single mode operation)	0.89	1.03	1.24	1.45
	Separation between the two polarisations at the output facet (μm)	3.8	2.7	1.8	0.89
	Equivalent wavelength difference to achieve same separation (nm)	4.0	3.0	2.0	1.0
Double hetero-structure	Layer thickness (μm) (max for single mode operation)	0.64	0.74	0.88	1.02
	Separation between the two polarisations at the output facet (μm)	1.8	1.2	0.59	0.36
	Equivalent wavelength difference to achieve same separation (nm)	1.9	1.3	0.67	0.41

The modifications which reduce the polarisation sensitivity of the demultiplexer also increase the optical width of the slab guided mode. This places more stringent demands on the mirror angle. The reason is that the phase difference between the top and bottom of the mirror determines the loss on reflection, rather than the absolute angle of the wall. Consequently, as even the 2 dB loss per reflection measured above was excessive, the mirror fabrication technology had to be improved if 2D optics was to become a practical proposition.

5.5. COUPLING EFFICIENCY

One aspect of the demultiplexer which has not yet been considered is the input coupling efficiency. This was not measured in the apparatus described above, as, in a real application, light would probably be coupled to the device via a lensed fibre. However, it was possible to estimate the lensed fibre coupling efficiency, as, to a first approximation, such a fibre can be considered to emit a Gaussian beam with a waist diameter of ~5μm. The far field of the waveguide can also be approximated to a Gaussian beam, so that a simple overlap integral can be performed[8]. The results of such calculations indicated that, for a device of the specifications given in Appendix B with anti-reflection coated facets, one would expect an input coupling loss of about 5 dB. This is greater than the entire insertion loss in some of the bulk optical devices discussed in the section 2.2.

Fortunately, the measures to reduce polarisation discrimination discussed in section 5.4 would also improve the input coupling efficiency. For example one would expect an input coupling loss of 2-3 dB if one used a "1.05" GaInAsP double heterostructure waveguide. In the future it may be possible to reduce this loss even further by making use of waveguide tapers to adiabatically couple the optical mode from the fibre to the dispersive element. Waveguide tapers of this type have already been shown to improve the coupling efficiency between a laser and an optical fibre.[9,10,11]

5.6. DISCUSSION

In the period since the completion of the above work there have been a number of reports of demultiplexers on InP substrates. The most active groups working on grating based demultiplexers have been led by J.B.Soole of

Bellcore[12,13,14,15,16] and C.Cremer of Siemens[17,18]. These groups have used vertical etching processes to create reflection echelon gratings of the type shown in Figure 5.9. As mentioned in section 3.2, this type of grating suffers from ~5dB of excess optical loss, as a result of incomplete reflection of the slab guided mode. Both groups have observed this loss in practice. They are now developing methods of placing reflective metal coats on the etched walls to reduce its magnitude.

Soole and Cremer have both used curved gratings which simultaneously diffract and focus the output beam. This has made the design of the grating more complicated, but has reduced the number of etched mirrors in the optical path. Such an approach is advantageous when there is a significant optical loss at each etched wall.

The development of the BNR grating demultiplexer has also continued[19,20], though I have only been involved in an advisory capacity. In this work the difficulties with polarisation were overcome by the use of a double heterostructure as described in section 5.3. The losses on reflection from an etched mirror have been reduced to ~1dB by using a methane, hydrogen and carbon dioxide mixture in the reactive ion etcher. It is believed that the oxygen radicals generated from the breakdown of carbon dioxide may passivate the etched wall in the same manner as the oxygen plasma described in section 4.4.2. The mask design has also been modified to reduce the grating period, increase the angle of incidence at the grating and increase the focal length of the final mirror. As a result the device can now carry 8 channels at a 4nm spacing rather than 4 channels at an 8nm spacing.

In period since the completion of the above work there have also been reports of a new design of InP based demultiplexer. This type of device is constructed from an array of waveguides and two star couplers. An illustration is shown in Figure 5.10. The wavelength selectivity is obtained from the fact that there is a constant length difference, and hence a wavelength dependent phase shift, between each pair of adjacent arms of the waveguide array. Three active workers in the development of such devices are H.Bissessur of Alcatel[21], M.Zirngibl of AT&T[22] and M.R.Amersfoot[23] of Delft University.

The best results achieved by each of the above groups are summarised in the following table.

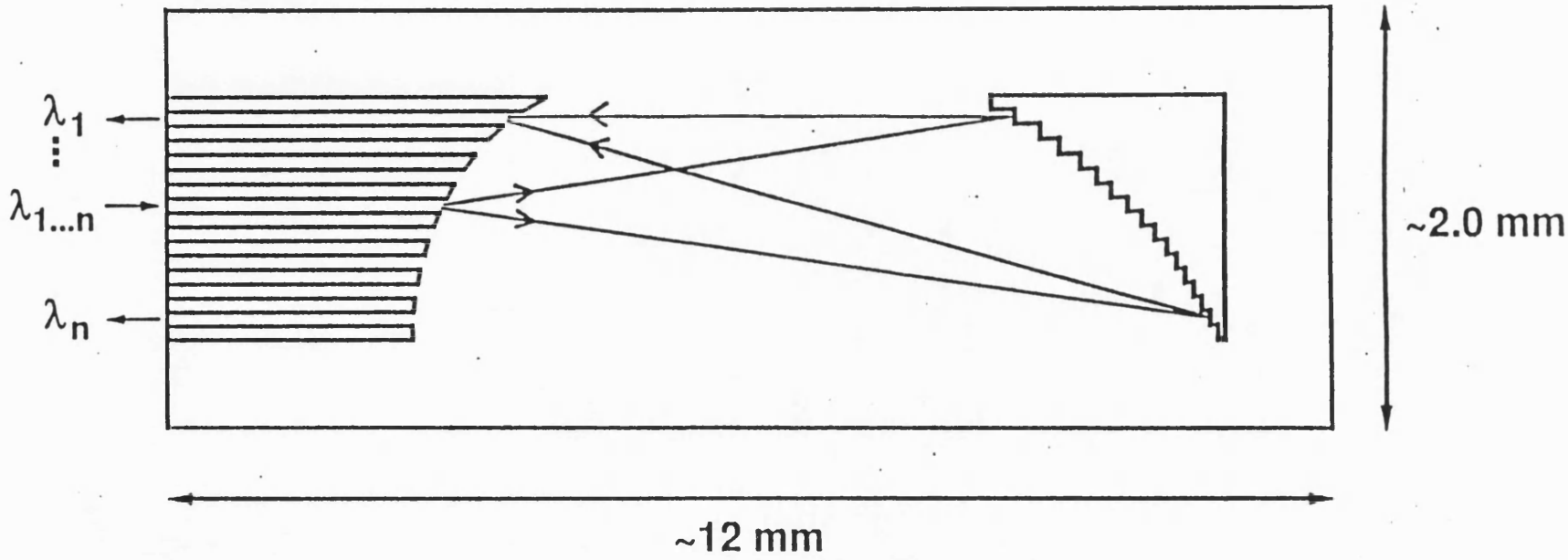

Fig 5.9 Reflection echelon grating in an InP based slab waveguide
(After Soole et al, *IEE Electronics Letters*, 1991, 27, pp.132-134)

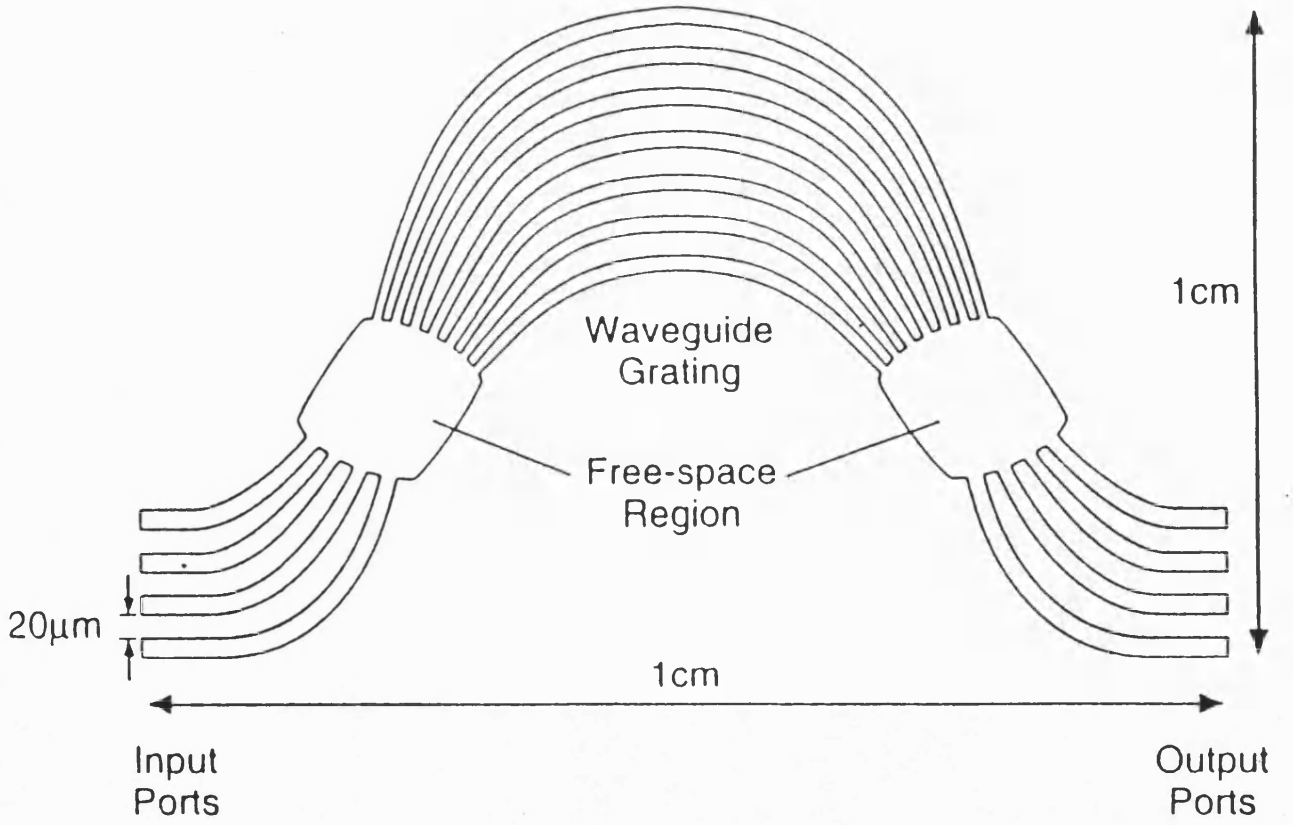

Fig 5.10 Phased waveguide array demultiplexer
(After Zirngibl, *Photonics Technology Letters*, 1992, 4, pp.1250-1253)

Table 5.4 **Performance of InP based demultiplexers**

Author	Thompson	Soole	Cremer	Bissessur	Amers-foort
Location	BNR	Bellcore	Siemens	Alcatel	Delft
Device type	Grating			Phased array	
No. of channels	8	32, 65[14]	30	16	4
Channel spacing (nm)	4	1	3.7	1.8	2
TE/TM discrimination (nm)	<1	0.23	0.5	0.48	4
Nearest neighbour crosstalk (dB)	-30	-19	-27	<-9	<-18
Losses on the chip (dB)	6.5 (TE) 8 (TM)	16*	14+,10[18]	7-12	4-5
Mirror angle off vertical	<1°	3°	5°	n/a	n/a
Device size (mm)	2x2	11x1.6	3x2	28x2.9	3.3x3.9
Reference unless otherwise stated	20	12	17	21	23

*Before use of reflective coating which should reduce loss by 5 dB.

+Assumes that grating is reflection coated. Estimate only.

Looking at the above table one can see that a larger number of channels and a smaller channel spacing have been obtained with grating based devices. However, one should note that a very long device is required to support closely spaced channels. Long devices introduce concerns about material uniformity and hence optical loss. The nearest neighbour crosstalk also tends to be superior for grating based devices, but the lowest loss has been obtained with a phased array device. The fabrication complexity of the two components is similar. In practice the type of device deployed will probably depend on the application.

As mentioned in section 2.3, the object of working on an InP substrate is to enable monolithic integration of the demultiplexer with photodetectors. Indeed, if one does not intend to do this, then it is preferable to work with a material system such as silica on silicon, where the waveguide dimensions can be closely matched to those of a single mode fibre. The first hurdle to be

overcome when integrating a passive waveguide based device with an array of detectors, is that of efficiently coupling light from material of one bandgap to that of another. This is the subject is discussed in the remainder of the dissertation.

5.7. REFERENCES

1 G.H.B.Thompson, *J.Lightwave Techology*, 1986, **LT-4**, pp.1678-1693

2 J.E.A.Whiteaway, G.H.B.Thompson, A.J.Collar and C.J.Armistead, *IEEE Journal of Quantum Electronics*, 1989, **6**, pp.1261-1279

3 R.G.Walker, *Electronics Letters*, 1985, **21**, pp.581-583

4 M.A.Afromowitz, *Solid State Commun.*, 1974, **15**, pp.59

5 K. Utaka, Y.Suematsu, K.Kobayashi and H.Kawanishi, *Jpn. J. Appl. Phys.*, 1980, **19**, pp.L137-L140

6 B.Broberg et al, *J.Appl.Phys.*, 1984, **55**, pp.3376

7 G.H.B.Thompson, *"Physics of Semiconductor Laser Devices"*(Wiley, Chichester, 1980)

8 M.Saruwatari and K.Nawata, *Appl. Optics*, 1987, **18**, pp.1847-1856

9 I.F.Lealman, M.J.Robertson, L.J.Rivers, M.J.Harlow, S.D.Perrin and C.P.Seltzer, *Conference Digest of 14th IEEE International Semiconductor Laser Conference* 1994, (IEEE Catalog Number 94CH3379-5), pp.189-190

10 R.Ben-Michael, U.Koren, B.I.Miller, M.G.Young, M.Chien and G.Raybon, *Conference Digest of 14th IEEE International Semiconductor Laser Conference* 1994, (IEEE Catalog Number 94CH3379-5), pp.187-188

11 H.Kobayashi, H.Soda, M.Ekawa, N.Okazaki, S.Ogita and S.Yamazaki, *Conference Digest of 14th IEEE International Semiconductor Laser Conference* 1994, (IEEE Catalog Number 94CH3379-5), pp.191-192

12 J.B.D.Soole, A.Scherer, J.P.LeBlanc, N.C.Andreadakis, R.Bhat, M.A.Koza, *Electronics Letters*, 1991, **27**, pp.132-134

[13] J.B.D.Soole, A.Scherer, H.P.LeBlanc, N.C.Andreadakis, R.Bhat and M.A.Koza, *Applied Physics Letters*, 1991, **58**, pp.1949-1951

[14] J.B.Soole, A.Scherer, Y.Silberberg, H.P.LeBlanc, N.C.Andreadakis, C.Caneau and K.R.Poguntke, *Electronics Letters*, 1993, **29**, pp.558-560

[15] K.R.Poguntke, J.B.D.Soole, H.P.LeBlanc, N.C.Andreadakis, P.Grabbe, R.Bhat, C.Caneau and M.A.Koza, *IEE Electronics Letters*, 1994, **6**, pp.512-513

[16] J.B.D.Soole, R.Bhat, H.P.LeBlanc, N.C.Andreadakis, P.Grabbe, C.Caneau and M.A.Koza, *IEE Electronics Letters*, 1994, **30**, pp.664-666

[17] C.Cremer, G.Ebbinghaus, G.Heise, R.Muller-Nawrath, M.Schienie and L.Stoll, *Applied Physics Letters*, 1991, **59**, pp.627-629

[18] C.Cremer, N.Emeis, M.Schier, G.Heise and G.Ebbinghaus, *IEE Proc. J*, 1993, **140**, pp.71-74

[19] S.M.Ojha, G.H.B.Thompson, C.G.Cureton, C.B.Roders, S.J.Clements, M.Asghari and I.H.White, *IEE Electronics Letters*, 1993, **29**, pp.805-807

[20] G.H.B.Thompson, S.M.Ojha, S.Clements, I.H.White and M.Asghari, *Proceedings of the European Conference on Integrated Optics*, (Switzerland, 1993)

[21] H.Bissessur, F.Gaborit, B.Martin, P.Pagnod-Rossiaux, J.L.Peyre and M.Renaud, *IEE Electronics Letters*, 1994, **30**, pp.336-338

[22] M.Zirngibl, C.Dragone and C.H.Joyner, *IEEE Photonics Technology Letters*, 1992, **4**, pp.1250-1253

[23] M.R.Amersfoort, C.R.de Boer, F.P.G.M.van Ham, M.K.Smit, P.Demeester, J.J.G.M.van der Tol and A.Kuntze, *IEE Electronics Letters*, 1994, **30**, pp.300-301

Chapter 6

The Integration of Devices with Different Epitaxial Layer Structures

6.1. Introduction

As mentioned at the end of chapter 5, the InP based 2D demultiplexer must be integrated with photodiodes, or other optoelectronic devices, if it is to become a practical component for optical communications systems. One major problem to be overcome when integrating such a passive waveguide with optoelectronic devices, is that of efficiently coupling light from material of one bandgap to that of another. There are several ways to produce such an "active-passive" interface. These interfaces have a number of applications in addition to the integration of 2D optical components with photodetectors. Examples include the fabrication of tuneable lasers and the monolithic integration of lasers and modulators. The remainder of this dissertation describes a study of one type of active-passive interface, and its demonstration through the fabrication of an integrated laser-modulator.

6.2. Types of Active-Passive Interface

A summary of some of the more popular ways to couple light from material of one bandgap to that of another is given below.

6.2.1. Butt Joint

The butt coupling technique is illustrated in Figure 6.1. The details of the fabrication schemes used to make butt interfaces vary from laboratory to laboratory but a general outline is given below.

a) Grow material of bandgap 1.
b) Protect the material of bandgap 1 in the required areas with an appropriate mask.
c) Etch away the material of bandgap 1 in the areas not protected by the mask.
d) Grow material of bandgap 2 in the regions where the material of bandgap 1 has been removed.
e) Remove the mask and overgrow with material of appropriate bandgap and doping.

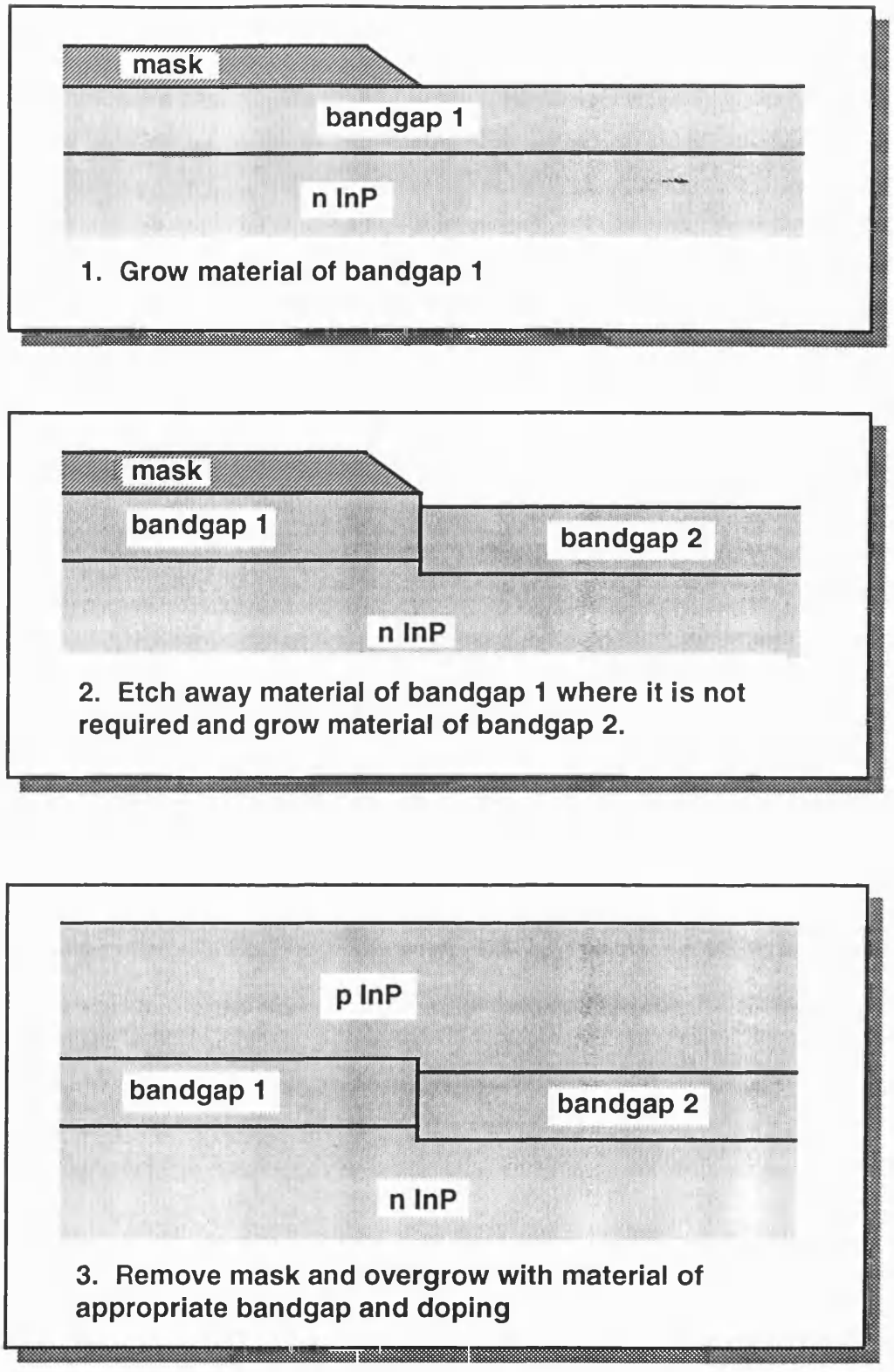

Fig 6.1 Fabrication of a butt coupled interface

Several early butt interfaces were fabricated using liquid phase epitaxy (LPE)[1]. For example, Tohmori, then at the Tokyo Institute of Technology, fabricated DBR lasers with two active-passive interfaces using three LPE growths[2]. In the manufacture of these devices, the mask was removed before the second epitaxial growth. Consequently, the material of bandgap 2 was grown on top of the material of bandgap 1, as well as elsewhere. The success of this procedure was assisted by the fact that surface of the material being grown by LPE tended to become more planar as the growth progressed[3]. The lasers that Tohmori fabricated had a threshold current of 28mA and a differential quantum efficiency of 10.8%/facet. The length of the active region was 100μm.

The planarising properties of LPE were exploited further by Lesterlin[4], who fabricated DBR lasers with one active-passive interface. Once again the mask was removed before the growth of the material of bandgap 2 by LPE. However, on this occasion the material of bandgap 2 was grown until it was considerably thicker than required, so that the growing surface became completely planar. The excess material was then etched away to create a interface with an almost ideal cross section. The DBR devices fabricated in this manner were 400μm long and had a 200μm long active section. The differential quantum efficiencies from the cleaved and the DBR facets of these devices were 24 and 11% respectively. The mean pulsed threshold current was 10mA. Similar threshold currents were obtained for 150μm long devices containing the active region only. The above figures indicated that the losses at the active-passive interface and in the passive waveguide were <3dB. It is likely that waveguide loss accounted for a significant proportion of this figure and hence the interface must have been fairly efficient.

LPE based butt coupling has also been used in the manufacture of integrated laser-modulators by Soda of Fujitsu[5,6,7]. In these devices the butt joint was formed on top of a quaternary guiding layer which was continuous throughout the device. The mask was not removed before the second epitaxial growth. Consequently the material of bandgap 2 was not deposited on top of that of bandgap 1, as the mask inhibited deposition in this region. The authors reported that the optimisation of the growth at the laser-modulator interface was difficult. It was achieved by adjusting the shape of the selectively etched facet exposed at the butt joint and the thicknesses of the regrown layers. The reported efficiency of the interface was 80% and the ex-facet power output was 17mW at a laser drive current of 150mA.

Butt coupling with an all MOCVD process has also been demonstrated by a number of workers. For example, when Tohmori moved to NTT he continued to fabricate DBR devices with two active passive interfaces, but using the MOCVD growth process[8]. These devices were 1mm long with a 200μm long active section. They exhibited thresholds of 20mA and a single mode output power of 7mW.

MOCVD based butt coupling has also been used in the fabrication of laser-modulators by Oshiba of Oki[9], Ojala of Ericsson[10], Suzuki and Tanaka of KDD[11,12,13] and Kuindersma of Philips[14]. All of these groups, save Suzuki's, left the mask on the material of bandgap 1 during the second epitaxial growth. The mask inhibited the deposition of the material of bandgap 2 on top of the material of bandgap 1 and thus removed a selective etching step from the integrated laser modulator fabrication process. Ojala reported the largest ex-facet power output of 15mW at a drive current of 150mA. The only researcher to comment on the interface efficiency was Oshiba, who stated that the laser modulator interface coupling loss was <3dB.

The advantage of the butt coupling approach is that, in principle, it allows one to couple together two devices with arbitrary layer structures. In addition, overlap integration[15] calculations indicate that the theoretical coupling efficiency of this type of interface is typically in the region of 80 to 90%[16]. It seems possible that interface coupling efficiencies close to the above value have been achieved when the interface is grown by LPE[4]. However, LPE has now been superseded by MOCVD in most laboratories and, unfortunately, it seems that the high theoretical coupling efficiency is difficult to achieve when the butt joint is fabricated by this growth technique[17]. It seems likely that this difficulty is related to the fact that the material of bandgap 2 must be grown over a step at the butt joint. In real devices this material usually consists of a multilayer stack of GaInAsP layers with different compositions. The growth of each of these quaternary layers is complicated as a number of crystal facets develop in the region next to the step[18,19,20,21]. The type and area of each facet exposed depends on the crystallographic orientation of the step, the growth conditions, the composition of the GaInAsP layer and the time elapsed since the start of deposition[19,21]. This means that the multilayer stack is in general not planar in the region adjacent to the butt joint. The difficulty is compounded by the fact that the composition of GaInAsP alloy deposited from a given source mixture, depends on the crystallographic orientation of the facet on which it is deposited[19]. Consequently the material deposited in the region of the butt joint

may not be lattice matched to the substrate. The effects of such compositional variations are discussed in Appendix E.

In principle all the above of the above difficulties can be overcome by developing an adequate understanding of the behaviour of epitaxial deposition over contoured surfaces. However the complexity of the problem means that a substantial amount of effort would have to be invested in such an activity.

The second disadvantage of butt coupling is the fact that an additional epitaxial growth run is required to grow the material of bandgap 2. It is difficult to maintain wafer cleanliness to the standards required for the growth of this material. An indication of the reason for this difficulty can be obtained by observing that high quality quaternary multilayer structures are normally grown on top of a thick InP buffer layer. Indeed, at BNR Europe we have experimental evidence that the surface morphology of quaternary and ternary layers deteriorates as the thickness of the InP buffer layer decreases. In addition, substrates are usually prepared for the growth of quaternary multilayer structures by removing several microns of material. This procedure ensures that deposition takes place on a surface with minimal contamination. The use of such aggressive etching techniques, and the growth of a thick InP buffer layer, are difficult when one is growing a second set of epitaxial layers on a partially processed wafer. This does not mean that the use of multiple growth fabrication processes is uncommon in the III-V optoelectronics industry; in fact the reverse is true[22,23,24,25]. However almost all of the secondary epitaxial growth runs in to-day's industrial processes, involve growing a thick layer of InP before growing any ternary or quaternary material.

6.2.2. Growth of Multilayer Structures over a Step

This approach involves growing the material of bandgap 1, a spacer layer of InP and then the material of bandgap 2. The layer structure is grown over a substrate in which steps have been etched prior to epitaxial growth. The waveguides containing the material of different bandgaps align in the vicinity of the steps, as shown in Figure 6.2.

The technique was pioneered in the GaAs/AlGaAs material system by Azoulay of CNET[26]. Azoulay demonstrated the feasibility of the approach by fabricating FP devices containing active-passive interfaces. The coupling efficiency between the active and passive sections was deduced to be 70% by

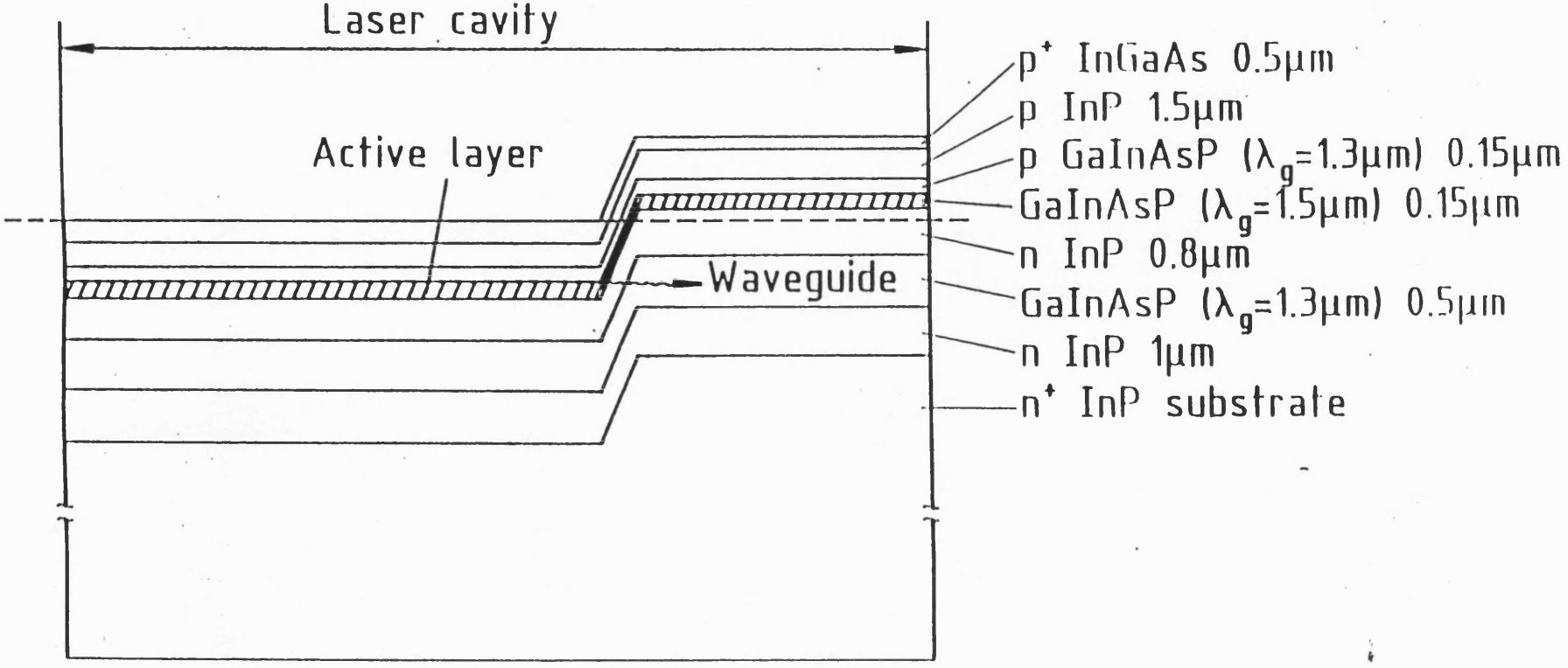

Fig 6.2 Interface formed by the growth of a multilayer structure over a step
(After Rose et al., *Journal of Crystal Growth*, 1991, 107, pp.850-854)

comparison of the differential quantum efficiencies of devices with different numbers of interfaces.

The technique was applied to the InP/InGaAsP material system by Rose, also at CNET[27]. Rose used atmospheric pressure MOCVD to fabricate buried ridge structure FP devices containing active-passive interfaces. The threshold current of 1.5mm long devices with a 250μm long active region was 25mA. The average coupling coefficient between the active and passive regions was 50%. Coupled cavity effects[28] were observed in these devices as a result of the weak reflection from the active-passive interface[29].

The advantage of this approach over the butt joint process is the fact that no additional epitaxial growth runs are required. A thin InP buffer layer can also be used to help obtain quaternary material with sufficient epitaxial quality. However the problems with epitaxial composition and uniformity in the vicinity of a step are still present (see section 6.2.1). In addition, the material of both bandgaps is present in the layer structures of each device. This imposes restrictions on the device doping profiles, which in turn imposes constraints on the types of devices that can be coupled together. To give an example, one could use this technique to couple a laser to a passive waveguide, but not a laser to a modulator.

6.2.3. Evanescent Coupling

This technique involves growing the material with the smaller bandgap directly on top of that of the larger bandgap. The material of the smaller bandgap can then be removed where it is not required by means of selective etching. The procedure is sometimes known as "evanescent coupling". A schematic of a longitudinal section through such an interface is shown in Figure 6.3.

Murata of NEC[30] and Koch of AT&T[31,32] have both used the evanescent coupling technique to fabricate tuneable lasers with passive tuning regions. In these devices the active layers were removed from the grating regions so that the gain, and the nature of the feedback, could be independently controlled. The active layers of Koch's devices were only 0.08μm thick as they consisted of four GaInAs quantum wells separated by 10nm GaInAsP barriers. As a result the coupling efficiency across the interface where the active layer was terminated was high.

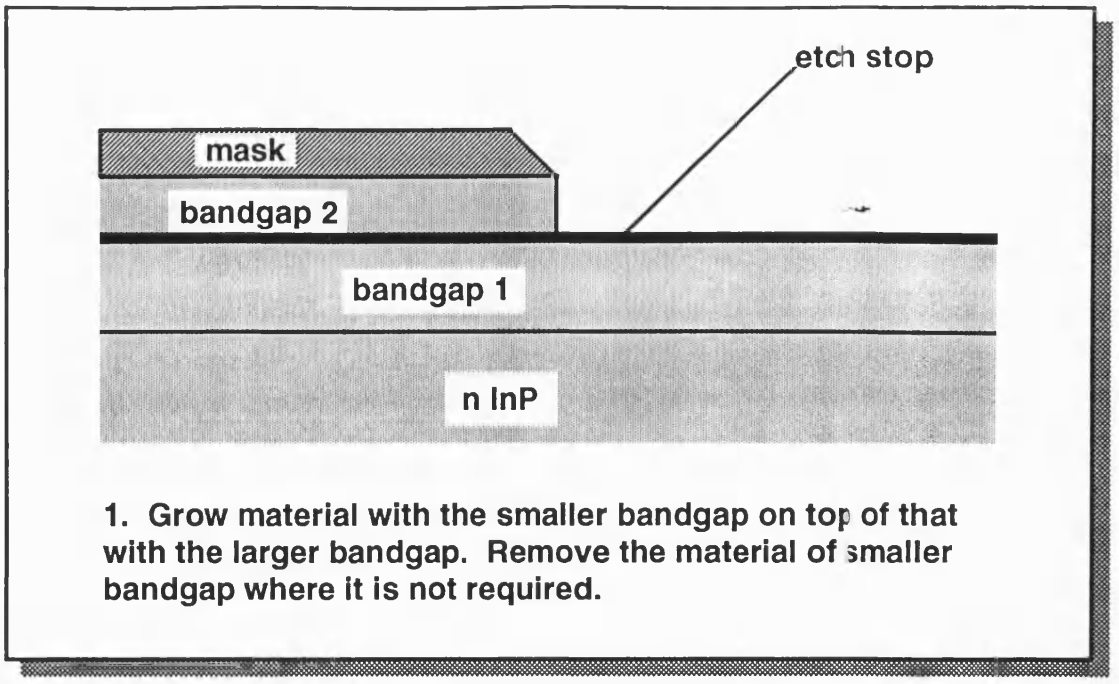

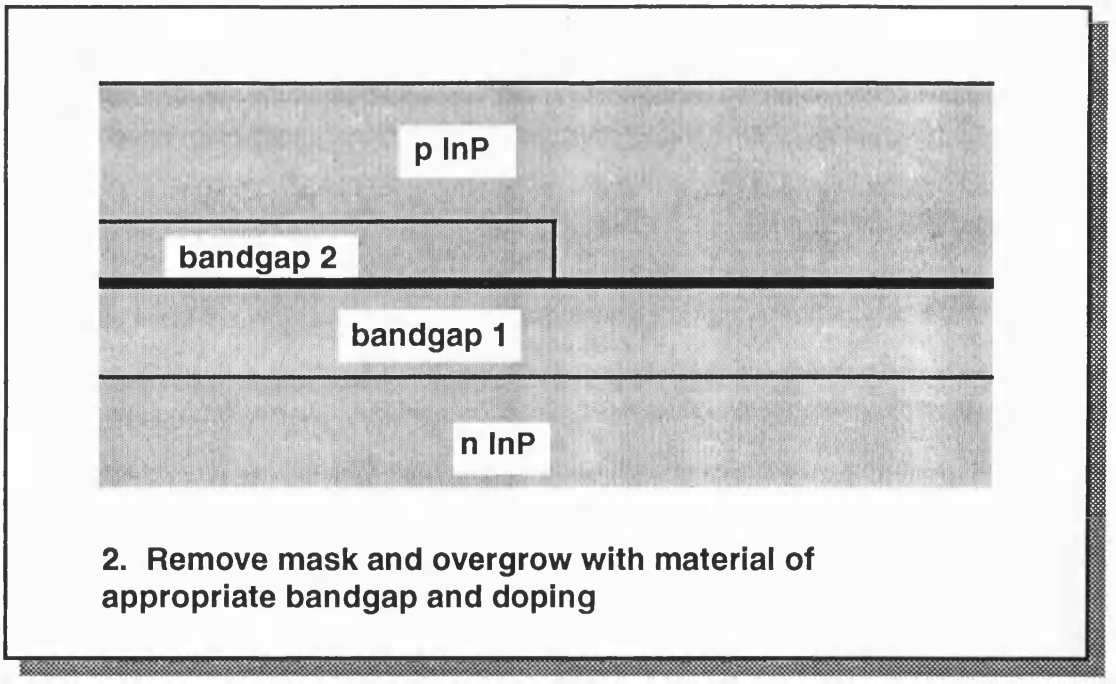

Fig 6.3 Interface constructed by removal of material with smaller bandgap

Koren, also at AT&T, has applied the evanescent coupling technique to the integration of lasers and amplifiers[33]. Koren's devices contained two active-passive interfaces, one between the laser active and grating regions, and the other between the laser and the amplifier. If the amplifier was held at zero bias while current was injected into the laser a photocurrent was detected in the former component. The differential current transfer efficiency between the two components was 33%. This is a high value when one considers that it includes the laser and amplifier quantum efficiencies, as well as the interface coupling losses.

Brosson of AAR has calculated the coupling efficiency of an evanescent interface in which a 0.09μm thick GaInAsP active layer (λ_{PL}=1.53μm) is removed from the top of a 0.14μm thick GaInAsP waveguide layer (λ_{PL}=1.3μm)[34]. The calculation was performed by overlap integration[15] and gave an interface coupling efficiency of 90%.

The evanescent coupling scheme has been applied to laser-modulator integration by Sato of NTT[35]. In Sato's devices four laser quantum wells were grown on top of eight modulator ones by MOCVD. The two sets of quantum wells were separated by an InP layer so that the laser wells could be selectively removed in a wet etchant, thus creating the laser modulator interface. The coupling coefficient across the interface was calculated to be 90% by overlap integration[15]. This result agreed well with the experimental value of 92%. The latter number was derived from a measurement of the amount of stray light radiating into the substrate.

The merits of the evanescent coupling technique are that no additional epitaxial growth runs are required, and the preparation of the wafer for epitaxial growth can be as rigorous as that for conventional discrete devices. In addition the interface coupling efficiency can be very high. The disadvantage is that the device which operates using the material of smaller bandgap must also contain the material of larger bandgap. This can compromise its performance. For example, if one attempts to integrate a laser and a modulator using the evanescent technique then the laser region must also contain the modulator active region. The presence of the modulator active region has several effects on the performance of the laser:

a) The coupling coefficient of the optical mode to the laser active region is less than can be achieved if the modulator active region is not present. This means that more gain is required to reach threshold, and hence the threshold current is higher.

b) Electrons bound for the laser active region must be injected through the undoped modulator active region which may contain quantum wells.

c) The efficiency of the laser is reduced if the residual optical losses of the modulator region are significant.

Raybon of AT&T has demonstrated a method of laser modulator integration which employs evanescent coupling but overcomes some of the above objections[36]. Raybon's devices contained two evanescent interfaces in which the laser and the modulator were separately coupled to a passive waveguide which ran from one end of the device to the other. The disadvantage of Raybon's approach is that an extra epitaxial growth is required, as in the butt coupling scheme. However, the device does not contain an interface which was created by growing quaternary material over a step. Consequently this approach is an intermediate option between the butt and evanescent coupling schemes.

6.2.4. Local Adjustment of QW Layer Thickness

In this approach the bandgap is adjusted by making local adjustments to the growth rate, and hence the thickness of quantum wells. A schematic of a longitudinal section through such an interface is shown in Figure 6.4. There are several ways in which the growth rate can be modified to create such an interface. These are summarised below.

In low pressure MBE type systems the growth rate can be locally enhanced by relying on surface migration off etched facets of a particular crystallographic orientation. Arent of IBM has shown that there is surface migration from (311)A facets to surrounding (100) surfaces during the growth of strained InGaAs on structured GaAs substrates[37]. The migration length of In was ~25μm, while that of Ga was <1μm. This phenomenon reduced the bandgap of 7nm wide GaInAs quantum wells, grown on 10μm wide mesas next to (311)A crystal facets, by 60meV.

In higher pressure MOCVD type systems it is more difficult to make use of surface migration techniques, as the migration lengths tend to be much

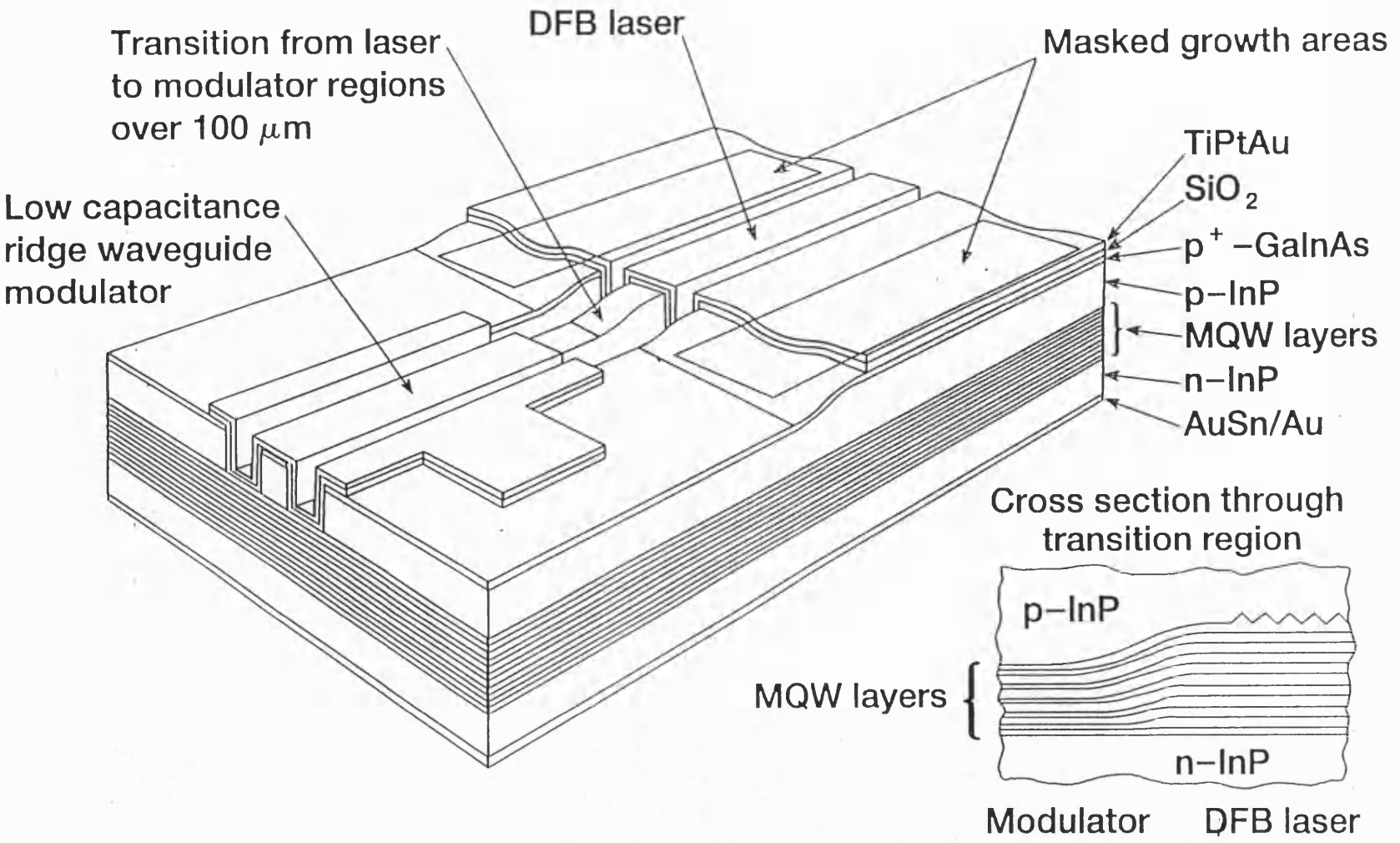

Fig 6.4 Example of bandgap adjustment through changes in QW thickness

shorter[38]. However Koyama of AT&T has observed bandgap changes in strained GaInAs quantum wells grown on a structured InP substrate by atmospheric pressure MOCVD[39]. The magnitude of the bandgap reduction, when the quantum wells were grown on 10μm wide mesas, was 31meV. The threshold current density of the quantum well material was not adversely affected by this bandgap change, and the technique was used to fabricate an integrated amplifier and electroabsorption modulator.

It is also possible to make local adjustments to the growth rate of MOCVD by increasing or decreasing the gas phase concentration of reactive species. Local increases in the growth rate are normally obtained by means of selective area epitaxy. In this process the gas phase concentration of reactive species is enhanced in the vicinity of dielectric masks, which inhibit the deposition of epitaxial material. Johnson of AT&T[40], Aoki of Hitachi[41] and Kato of NEC[42] have now all used this approach for laser-modulator integration. Johnson and Aoki fabricated conventional buried heterostructure devices from the material grown between widely separated selective growth masks. The length of the transition region between the laser and the modulator in these components was ~70μm. Aoki reported that the loss of this transition region was less than 0.5dB and that the bandgap reduction employed for the laser region was 40meV. Kato used a different approach in which the material for the active region was grown between a pair of masks separated by only 2μm. The advantage of this approach was that the lateral optical confinement required for the laser modulator was automatically obtained from the nature of the selective growth in the narrow aperture. However the active regions of devices fabricated in this manner are bounded by epitaxial growth on unusual crystal planes. This raises concerns about lattice mismatch and reliability.

Local decreases in the growth rate can also be obtained by growing the QW material in a recess. Demeester of Gent University has demonstrated the feasibility of this technique by growing GaAs/AlGaAs quantum wells in recesses with undercut side walls by atmospheric pressure MOCVD[43,44]. The growth velocity was reduced in these recesses because there was an increased local area on which deposition could take place. Surface migration may also have played a role. A 60meV increase in the emission wavelength of LEDs grown in 8μm wide recesses was observed. Unfortunately, it may be difficult to transfer this approach to the material system based on InP, as etchants with a very high selectively are required to remove the unwanted material at the top of the recess after growth.

The advantages of the layer thickness adjustment techniques described above are that, no additional growth runs are required, and the layer thicknesses change smoothly and slowly so the coupling efficiency is close to 100%. The quality of the unperturbed material is almost as good as that grown for discrete devices as some etching of the substrate before growth is possible, and a thin InP buffer layer can be grown. However it is only possible to adjust the bandgap of the quantum well material by a limited amount, before the quality of the perturbed material suffers. In addition, the devices to be integrated must have almost identical layer structures.

6.2.5. Quantum Well Intermixing

The bandgap of a quantum well stack can also be adjusted by processing the wafer so that local intermixing of the wells and barriers takes place. There are several ways to induce such intermixing. One method is to implant impurities into the quantum well region and then anneal the wafer to remove much of the damage caused by the implantation process[45]. It is believed that the implantation step creates defects, such as vacancies or interstitials, which increase the inter-diffusion rate of the matrix elements during the annealing part of the process. The direction and rate of the bandgap change can depend on the implanted impurity, the composition of the quantum wells, the annealing conditions, the implantation conditions and the nature of the substrate on which the quantum wells are grown[45]. Much of the work on impurity induced disordering (IID) has involved implanting GaAs/AlGaAs quantum wells with Si or Zn. These dopants are electrically active after the process has been completed, thus causing problems with electrical isolation and waveguide loss in integrated devices. However O'Neill et al[46] have demonstrated that boron and fluorine, which are electrically neutral, can be used to induce blue shifts in GaAs/AlGaAs quantum wells. Waveguides fabricated from intermixed material in which a blue shift of 60meV was observed[47] exhibited losses as low as 4.7dB/cm. Marsh et al[48] have shown that the same impurities can be used to disorder GaInAs/GaInAsP quantum wells. Fluorine enhanced the blue shift normally seen when such material is annealed, while boron reduced it and even produced a red shift under some circumstances.

Andrew et al[49] have used fluorine based impurity induced disordering to integrate a 600μm passive waveguide with a 600μm long active section. The material on which the devices were fabricated contained two GaAs quantum

wells surrounded by GaAlAs barriers. The active-passive Fabry Perot lasers had threshold currents down to 60mA. This compared favourably with the threshold current of 55mA obtained from all-active 600μm long devices fabricated on the same wafer. These measurements suggested that the loss of the passive section was less than $2cm^{-1}$ and that the interface coupling efficiency was close to 100%.

The disadvantages of impurity induced disordering are that, even neutral impurities introduce substantial changes in material resistivity, and the implantation damage raises concerns about device reliability. One alternative for active devices is to use impurity free vacancy disordering (IFVD). In this process QW disordering during an anneal is promoted or impeded by the presence or absence of appropriate dielectric caps. The mechanism is that the nature of the cap modifies the way in which defects, such as vacancies, are generated at the semiconductor surface. The procedure produces less damage than impurity induced disordering, though unfortunately the reproducibility is poor[45]. Beauvais et al[50] have used this technique to fabricate extended cavity lasers in the GaAs/AlGaAs quantum well system. In the fabrication of these devices blue shift of the laser region was inhibited by the deposition of a SrF_2 cap. The blue shift of the passive waveguides was enhanced to 88meV by the use of a SiO_2 mask. The loss in the passive waveguide was only 17dB/cm.

Emery et al[51] have used impurity free vacancy disordering to fabricate extended cavity lasers in the GaInAsP material system. In this case the blue shift normally observed when such quantum well material is annealed was selectively inhibited by the presence of a SiO_2 mask. The interface coupling efficiency and the passive waveguide loss were estimated to be ~100% and $30cm^{-1}$ respectively. A 30dB extinction ratio was obtained from a 400μm long modulator fabricated on material which had been blue shifted by 80nm.

Quantum wells in the GaInAsP material system can also be intermixed by photoabsorption-induced disordering[45]. The technique takes advantage of the limited thermal stability of the material system and induces intermixing using the absorption of laser light to heat the QW region. McLean et al[52] have demonstrated that the intermixing can be localised with a spatial resolution of ~100μm by patterning the surface of the material with a gold reflecting layer. McKee et al[53] have demonstrated a 160nm shift in the emission wavelength of broad area lasers fabricated on such disordered material. This shift was only associated with a 20% increase in the threshold current, thus indicating that the

intermixed material was still of reasonable quality. Finally Lullo et al[54] have shown that extinction ratios of 27dB can still be obtained from modulators fabricated on material blue shifted by 80nm. These reports indicate that the photoabsorption-induced disordering process is certainly compatible with the integration of active devices.

The advantages of quantum well intermixing are that the coupling efficiency between regions of different bandgap is close to 100% and no additional growth runs are required, though some additional processing is necessary. In addition, the quality of material disordered by the photoabsorption and capping processes is almost as good as that of unperturbed material. However, it is only possible to shift the bandgap by a limited amount, and the devices to be integrated must have identical layer structures. It is also worth noting that intermixing processes are only just reaching the maturity required for the reproducible integration of several active components.

6.3. Choice of Integration Approach

In the first chapter I stated that photonic integration is only a practicable proposition if:

a) the performance of the integrated device is comparable to or better than that of its discrete equivalent.
b) the integrated device is relatively easy to make so that the cost benefits in packaging are not offset by a more complicated and lower yield fabrication process.

This philosophy can be summarised by stating that we should select the simplest process which can deliver the required device performance. However, when one reads the literature, one can see that the judgement of which process is most simple depends on the laboratory. I believe that these differences in judgement are related to the fact that one's chances of success are not only dependent on the interface design, but also on the skills and past experience of the fabrication team. Looking from the perspective of BNR Europe, I believe that the selective epitaxy integration process is the least complicated of the procedures described in section 6.2.

The rest of this dissertation describes the application of selective area MOCVD to the integration of a laser and a modulator. The selective growth approach was chosen for this integration task because the laser and modulator had very similar layer structures, and only required slightly different bandgaps.

Consequently, the coupling technique which was likely to offer the best and most repeatable performance, was the one in which there was least interference with the optical waveguide between the laser and the modulator. A contributing factor in this decision was the fact that we had a solid understanding of selective area MOCVD. The way in which we gained this understanding is described in Chapter 7, and its application to the fabrication of an integrated laser modulator is described in Chapters 8 and 9.

6.4. References

1 G.P.Agrawal and N.K.Dutta, *"Long wavelength semiconductor lasers"*, (Van Nostrand Reinhold, New York, 1986), pp.143-151

2 Y.Tohmori, H.Oohashi, T.Kato, S.Arai, K.Komori and Y.Suematsu, *IEE Electronics Letters*, 1986, **22**, pp.138-140

3 S.E.H.Turley, G.D.Henshall, P.D.Greene, V.P.Knight, D.M.Moule and S.A.Wheeler, *IEE Electronics Letters*, 1981, **17**, pp.868-870

4 D.Lesterlin, M.Gilleron, G.Chaminant, D.Robein and J.C.Bouley, *Japanese Journal of Applied Physics*, 1990, **2**, pp.L312-L314

5 H.Soda, M.Furutsu, K.Sato, N.Okazaki, S.Yamazaki, H.Nishimoto, H.Ishikawa, *IEE Electronics Letters*, 1990, **26**, pp.9-10

6 H.Soda, M.Furutsu, K.Sato M.Matsuda and H.Ishikawa, *IEE Electronics Letters*, 1989, **25**, pp.334-335

7 H.Ishikawa, *Fujitsu Jounal of Science and Technology*, 1991, **27**, pp.329-337

8 Y.Tohmori and M.Oishi, *Japanese Journal of Applied Physics*, 1988, **27**, pp.L693-L695

9 S.Oshiba, K.Yamada, S.Arahira and Y.Ogawa, *IEE Electronics Letters*, 1993, pp.1528-1530

10 P. Ojala, C.Pettersson, B.Stoltz, A.C.Morner, M.Janson and O.Sahlen, *IEE Electronics Letters*, 1993, **29**, pp.859-860

11 M.Suzuki, K.Tanake, S.Akiba and Y.Kushiro, *Journal of Lightwave Technology*, 1988, **6**, pp.779-785

[12] H.Tanaka, M.Suzuki, M.Usami, H.Taga, S.Yamamoto and Y.Matsushima, *Journal of Lightwave Technology*, 1990, 8, pp.1357-1362

[13] H.Tanaka, M.Suzuki, H.Taga, S.Yamamoto and Y.Matsushima, *IEE Electronics Letters*, 1991, **27**, pp.390-391

[14] P.I.Kuindersma, P.P.G.Mols, G.L.A.v.d.Hofstad, G.Cuypers, M.Tomesen, T.v.Dongen and J.J.M.Binsma, *IEE Electronics Letters*, 1993, **29**, pp.1876-1878

[15] K.F.Riley, *"Mathematical Methods for the Physical Sciences"*, (Cambridge University Press, Cambridge, 1983), pp.173-182

[16] P.J.Williams, P.M.Charles, K.Griffith, L.Considine and A.C.Carter, *IEE Electronics Letters*, 1990, **26**, pp.142-143

[17] Personal experience and private communication between Dr.G.H.B.Thompson and Y.Tohmori.

[18] H.Sugiura, A.Rudra, J.F.Carlin, H.J.Buhlmann, D.Araujo and M.Ilegems, *Semiconductor Science and Technology*, 1993, 8, pp.1063-1068

[19] E.J.Thrush, J.P.Stagg, M.A.Gibbon, R.E.Mallard, B.Hamilton, J.M.Jowett and E.M.Allen, *Materials Science and Engineering* , 1993, **B21**, pp.130-146

[20] E.J.Thrush, M.A.Gibbon, J.P.Stagg, C.G.Cureton, C.J.Jones, R.E.Mallard, A.G.Norman and G.R.Booker, *Journal of Crystal Growth*, 1992, **124**, pp.249-254

[21] B.Garrett and E.J.Thrush, *J.Crystal Growth*, 1989, **97**, pp.273-284

[22] G.P.Agrawal and N.K.Dutta, *"Long wavelength semiconductor lasers"*, (Van Nostrand Reinhold, New York, 1986), pp.172-219 and 287-292

[23] C.J.Armistead, S.A.Wheeler, R.G.Plumb and R.W.Musk, *IEE Electronics Letters*, 1986, **22**, pp.1145-1147

[24] C.J.Armistead, B.R.Butler, S.J.Clements, A.J.Collar, D.J.Moule and S.A.Wheeler, *IEE Electronics Letters*, 1987, **23**, pp.592-593

[25] J.E.A.Whiteaway, G.H.B.Thompson, A.J.Collar and C.J.Armistead, *IEEE Journal of Quantum Electronics*, 1989, **6**, pp.1261-1279

[26] R.Azoulay, D.Remiens, L.Menigaux and L.Dugrand, *Appl. Phys. Lett.*, 1989, **54**, pp.1857-1858

[27] B.Rose, D.Riemens, V.Hornung, D.Robein, *J.Crys. Growth*, 1991, **107**, pp.850-854

[28] G.P.Agrawal and N.K.Dutta, *"Long wavelength semiconductor lasers"*, (Van Nostrand Reinhold, New York, 1986), pp.333-363

[29] L.Menigaux, D.Remiens, L.Dugrand, P.Sansonetti and A.Carenco, *Proc 11th IEEE Semiconductor Laser Conference, Boston* (IEEE Service Centre, New York, 1988) pp.172-173

[30] S.Murata, I.Mito and K.Kobayashi, *IEE Electronics Letters*, 1987, **23**, pp.403-405

[31] T.L.Koch, U.Koren, R.P.Gnall, C.A.Burrus and B.I.Miller, *IEE Electronics Letters*, 1988, **24**, pp.1431-1433

[32] T.L.Koch, U.Koren and B.I.Miller, *Applied Physics Letters*, 1988, **53**, pp.1036-1038

[33] U.Koren, B.I.Miller, G.Raybon, M.Oron, M.G.Young, T.L.Koch, J.L.DeMiguel, M.Chien, B.Tell, K.Brown-Goebeler and C.A.Burrus, *Applied Physics Letters*, 1990, **57**, pp.1375-1377

[34] P.Brosson, CLabourie, L.le.Gouezigou, J.L.Lievin, J.Jacquet, F.Leblond, A.Olivier and D.Leclerc, *IEE Electronics Letters*, 1989, **25**, pp.1623-1624

[35] K.Sato, I.Kotaka, K.Wakita, Y.Kondo and M.Yamamoto, *IEE Electonics Letters*, 1993, **29**, pp.1087-1088

[36] G.Raybon, N.M.Froberg, U.Koren, B.I.Miller, M.G.Young, M.Chien, A.M.Johnson, P.B.Hansen, C.A.Burrus, J.J.Veselka and A.H.Gnauck, *Conference Digest of 14th IEEE International Semiconductor Laser Conference* 1994, (IEEE Catalog Number 94CH3379-5), pp.43-44

[37] D.J.Arent, S.Nilsson, J.D.Galeuchet, H.P.Meier and W.Walter, *Applied Physics Letters*, 1989, **55**, pp.2611-2613

[38] O.Kayser, *J. Crystal Growth*, 1991, **107**, 989-998

[39] F.Koyama, K.Y.Liou, A.G.Dentai, G.Raybon and C.A.Burrus, *IEE Electronics Letters*, 1993, **29**, pp.2104-2106

[40] J.E.Johnson, T.Tanbun-Ek, Y.K.Chen, D.A.Fishman, R.A.Logan, P.A.Morton, S.M.G.Chu, A.Tate, A.M.Sergent, P.F.Sciortino,Jr. and K.W.Wecht, *Conference Digest of 14th IEEE International Semiconductor Laser Conference* 1994, (IEEE Catalog Number 94CH3379-5), pp.41-42

[41] M.Aoki, M.Suzuki, M.Takahashi, H.Sano, T.Ido, T.Kawano and A.Takai, *IEE Electronics Letters*, 1992, **28**, pp.1157-1158

[42] T.Kato, T.Sasaki, K.Komatsu and I.Mito, *IEE Electonics Letters*, 1992, **28**, pp.153-154

[43] P.Demeester, L.Buydens, I.Moerman, D.Lootens and P.Van Daele, *Journal of Crystal Growth*, 1991, **107**, pp.161-165

[44] P.Demeester, L.Buydens and P.Van Daele, *Applied Physics Letters*, 1990, **57**, pp.168-170

[45] J.H.Marsh, *Semiconductor Science and Technology*, 1993, **8**, pp.1136-1155

[46] M.O'Neill, A.C.Bryce, J.H.Marsh, R.M.De La Rue, J.S.Roberts and C.Jeynes, *Applied Physics Letters*, 1989, **55**, p.1373

[47] M.O'Neill, A.C.Bryce, J.H.Marsh, R.M.De La Rue, J.S.Roberts, C.Button and R.Gwilliam, *IEE Electronics Letters*, 1990, **26**, pp.1613-1615

[48] J.H.Marsh, S.A.Bradshaw, A.C.Bryce, R.Gwilliam and R.Glew, *Journal of Electronic Materials*, 1991, **20**, pp.973-978

[49] S.R.Andrew, J.H.Marsh, M.C.Holland and A.H.Kean, *IEEE Photonics Technology Letters*, 1992, **4**, pp.426-428

[50] J.Beauvais, S.G.Ayling and J.H.Marsh, *IEEE Photonics Technology Letters*, 1993, **4**, pp.372-373

[51] J.Y.Emery, C.Stark, E.Gaumont-Goarin, M.Boulou, C.Fortin, O.Legouezigou, L.Goldstein, D.Lesterlin, F.H.Julien and C.Francis, *Conference Proceedings of 1994 IEEE 6th International Conference on InP and Related Materials*, 1994, pp.355-358

[52] C.J.McLean, A.McKee, J.H.Marsh and R.M.De La Rue, *IEE Electronics Letters*, 1993, **29**, pp.1657-1659

[53] A.McKee, C.J.McLean, A.C.Bryce, R.M.De La Rue and J.H.Marsh, *Applied Physics Letters*, 1994, **65**, pp.2263-2265

[54] G.Lullo, A.McKee, C.J.McLean, A.C.Bryce, C.Button and J.H.Marsh, *IEE Electonics Letters*, 1994, **30**, pp.1623-1625

Chapter 7

Selective Area MOCVD

7.1. INTRODUCTION

The ability to grow epitaxial material on predetermined areas of a semiconductor substrate has a number of applications in the fabrication of advanced optoelectronic devices. It is possible to achieve such selective growth using CBE[1,2,3], MOMBE[4] and MOCVD[4]. The selectivity is obtained by patterning the wafer with a dielectric mask, which inhibits the deposition of epitaxial material.

The thickness and composition of epitaxial layers grown by CBE and MOMBE are, in general, not perturbed by the presence of a dielectric mask[1]. However, the composition and thickness of material grown by MOCVD does change close to a mask, as some of the material which would have grown on the mask is deposited in its vicinity[4,5,6,7,8]. Thickness and compositional changes of this type are a hindrance in many applications of selective growth, but there are situations where the changes can be used to one's advantage. One example is in the fabrication of mode converters, where one can use selective area epitaxy to create waveguides which gradually taper in thickness[9]. The thickness change caused by selective growth can also be converted into a change in the position of a bandedge, by growing quantum well material[10,11,12]. Consequently one can simultaneously grow materials of different bandgap which are connected by smooth transition regions. The application of such quantum well selective growth to the integration of lasers and modulators has already been demonstrated[10].

The success of device fabrication procedures of the type described above depends upon a detailed knowledge of selective area epitaxy. In an attempt to gain such knowledge, the behaviour of selective growth at BNR Europe was initially investigated by examining the nature of selective

epitaxy over a complicated mask pattern[13]. The variety of features on this pattern allowed us to develop a qualitative understanding of selective area epitaxy as a function of mask density, feature shape and orientation. However, it was difficult to interpret our observations of selective growth over this mask in a quantitative manner, because the perturbations generated by adjacent features interacted with each other. This difficulty was of particular concern when light field areas (more exposed wafer than mask) were next to dark field ones (more mask than exposed wafer) as the extent of the perturbations generated by masked regions increased with their area.

In an attempt to overcome the above difficulty I designed a second mask which was entirely light field and in which the individual features were so far apart that they were essentially isolated under our standard growth conditions. This chapter describes quantitative observations and analysis of selective growth over the light field pattern.

7.2. EXPERIMENTAL

Experiments on the growth of GaInAsP and related materials were performed on (1 0 0) InP substrates in a low pressure MOCVD apparatus at 650 °C and 150 torr. A detailed description of the apparatus can be found in the references[14]. Trimethylindium (TMI), trimethylgallium (TMG), arsine and phosphine were used as the source materials and the gas velocity in the reactor tube was ~1.6 ms^{-1}. Growth rates varied between 2 and 5 μm/hr according to the composition of the epitaxial material.

A 3000Å thick silicon dioxide film was used as the selective growth mask. The oxide film was deposited on InP substrates by plasma enhanced chemical vapour deposition and was patterned using conventional photolithographic techniques. The patterned substrates were not exposed to InP etchants before growth.

The features on the mask pattern were so far apart that they were essentially isolated under our standard growth conditions. Each isolated feature consisted of an adjacent pair of rectangular masked regions as shown in Figure 7.1. The rectangles, which were either 600 or 800μm in length, were much longer than the distance over which the growth was perturbed. Consequently, the masks could be treated as if they were infinitely long, providing measurements were made near the central region. This arrangement eased assessment and subsequent theoretical analysis, as one could simply scan along a line perpendicular to the masks rather than mapping an area. The reduction in the number of dimensions that needed to be considered also proved useful when employing techniques which automatically map areas, such as spatially resolved secondary ion mass spectroscopy, as one could average the signal along a line parallel to the masks to reduce noise.

The pairs of rectangles were aligned to the [0 1 1] and [0-1 1] crystal directions in different regions of the pattern. The rectangle widths were varied in a series of steps (3, 7, 11, 15, 20, 25 and 30 μm) across each cell of the pattern so that we could determine the influence of the masking density on the epitaxial growth. The gap between these masks was also varied in three discrete steps (6, 16 and 30μm) in different regions of the pattern. A relatively large unperturbed area was left between each cell of the pattern to facilitate zero calibration of measurement systems.

Under some selective growth conditions polycrystalline deposition occurs on the masked regions[4]. It was not observed in any of the following experiments.

7.3. RESULTS

7.3.1. Selective Growth of InP

The quantitative behaviour of selective growth over the light field pattern was first investigated by growing undoped InP in growth run C804. The epitaxial layer thickness at unperturbed regions far away from any masks was 0.45μm and the unperturbed growth rate was 2.2μm/hr.

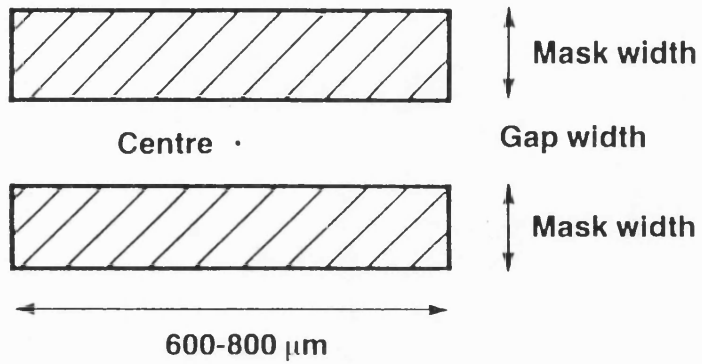

Mask widths 3-30 μm
Gap widths 6,16 and 30μm

Fig 7.1 Features on selective growth mask

After growth the epitaxial material was first examined by means of scanning electron microscopy. This examination revealed that the edges of the mesas of material which grew between the masks were defined by (1 1 1)B and (1 1 1)A type planes for features aligned to [0 1 1] and [0-1 1] respectively. A considerable amount of growth took place on (1 1 1)A type planes (1.8 μm in the most extreme circumstances) and consequently the edges of growing mesas defined by these planes progressively extended over the mask. Both the edges and the top surfaces of such mesas were uneven in this region of lateral growth. There was virtually no growth on (1 1 1)B type planes and the material grown between masks aligned to [0 1 1] was well behaved in all but the two most extreme circumstances (6 μm gap widths, 25 and 30 μm mask widths). In these two cases fast growing regions developed next to either one or both mesa edges.

After this initial investigation the epitaxial material was further assessed by means of surface profiling with a Sloan Dektak II. A typical example of the output from this instrument is shown in Figure 7.2. The oxide mask was removed before measurement so that we could determine the unperturbed growth thickness α in the manner shown in the figure. The excess growth thickness β was then deduced by comparison of the measured height at a given location, with that at a point far away from the previously masked regions. In the following analysis we have worked with the normalised excess thickness β/α as this allows us to readily compare layers of different thickness and composition. In addition, all subsequent thickness profiles are folded around the central point illustrated in Figure 7.2, so that points at the same distance on either side of the central point are plotted at the same position on the x axis. This procedure should alert one to the presence of gas flow effects, as such effects will upset the symmetry of a purely diffusion based process.

The first regions of study were the areas in which the masks were aligned to [0 1 1] and the gas flow. All profiles from these regions were symmetrical around the central point to within the error in the measurement and scans over identical mask patterns at different locations gave identical results. The normalised excess thickness at a given distance

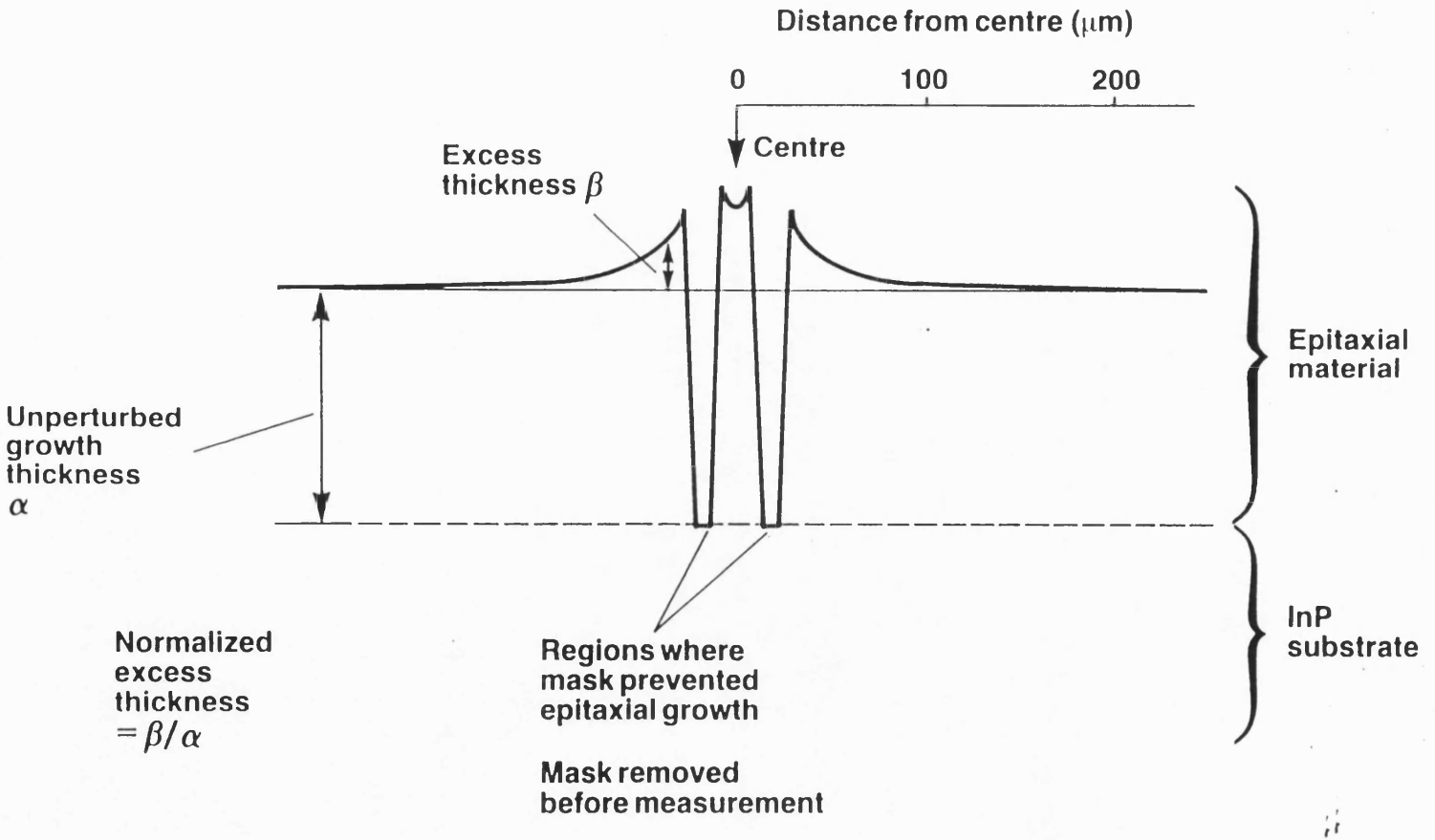

Fig 7.2 Typical thickness measurement

from the centre of a pattern containing two masks of a given width was almost independent of the gap between them, as shown in Figure 7.3. However, the normalised excess thickness at a given distance from the centre of a pattern containing two masks separated by a given gap rose rapidly with the width of the masks on either side of the gap, as shown in Figure 7.4. Consequently, one can conclude that the extent of the perturbation generated by a masked region is determined predominantly by its area and rises rapidly with this area.

The normalised excess growth rate at the central point between the two rectangular masks increased linearly with the mask width in the manner shown in Figure 7.5.

Scans over features in regions where the masks were aligned to [0-1 1] and hence lay across the gas flow, were also symmetrical. This result indicated that gas flow effects were insignificant in the growth regime that we were investigating.

Profiles over identical patterns aligned to [0 1 1] and [0-1 1] were identical to within the error of the measurement. Hence, we were able to conclude that, on the scale measured by the Dektak, perturbations in growth were independent of both the orientation of the pattern with respect to the substrate and the direction of the gas flow.

7.3.2. Selective Growth of InGaAs

The growth of InP on a substrate patterned with the light field mask was followed by the growth of InGaAs on an identical wafer (run C809). The ternary material was grown at the same temperature, pressure and TMI flow as the binary. The unperturbed thickness of the epitaxial layer was 0.49 μm and the growth rate was 4.5 μm/hr.

An initial assessment of the quality of the (1 0 0) surface of the InGaAs layer was made by Nomarski interference contrast microscopy. This technique indicated that the surface morphology, which was of high quality in regions of low masking density, deteriorated as the masking

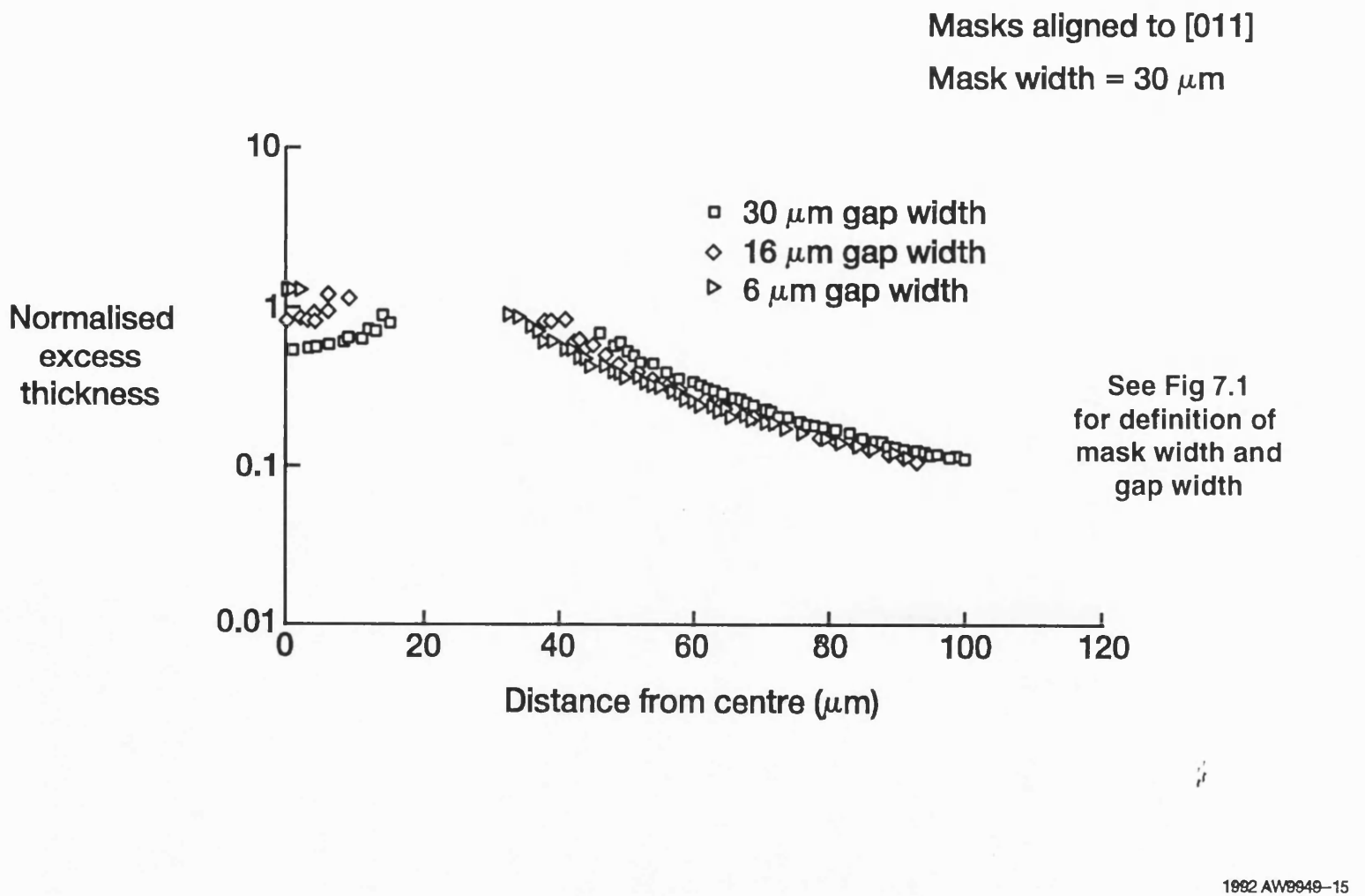

Fig 7.3 Effect of gap width on selective growth of InP

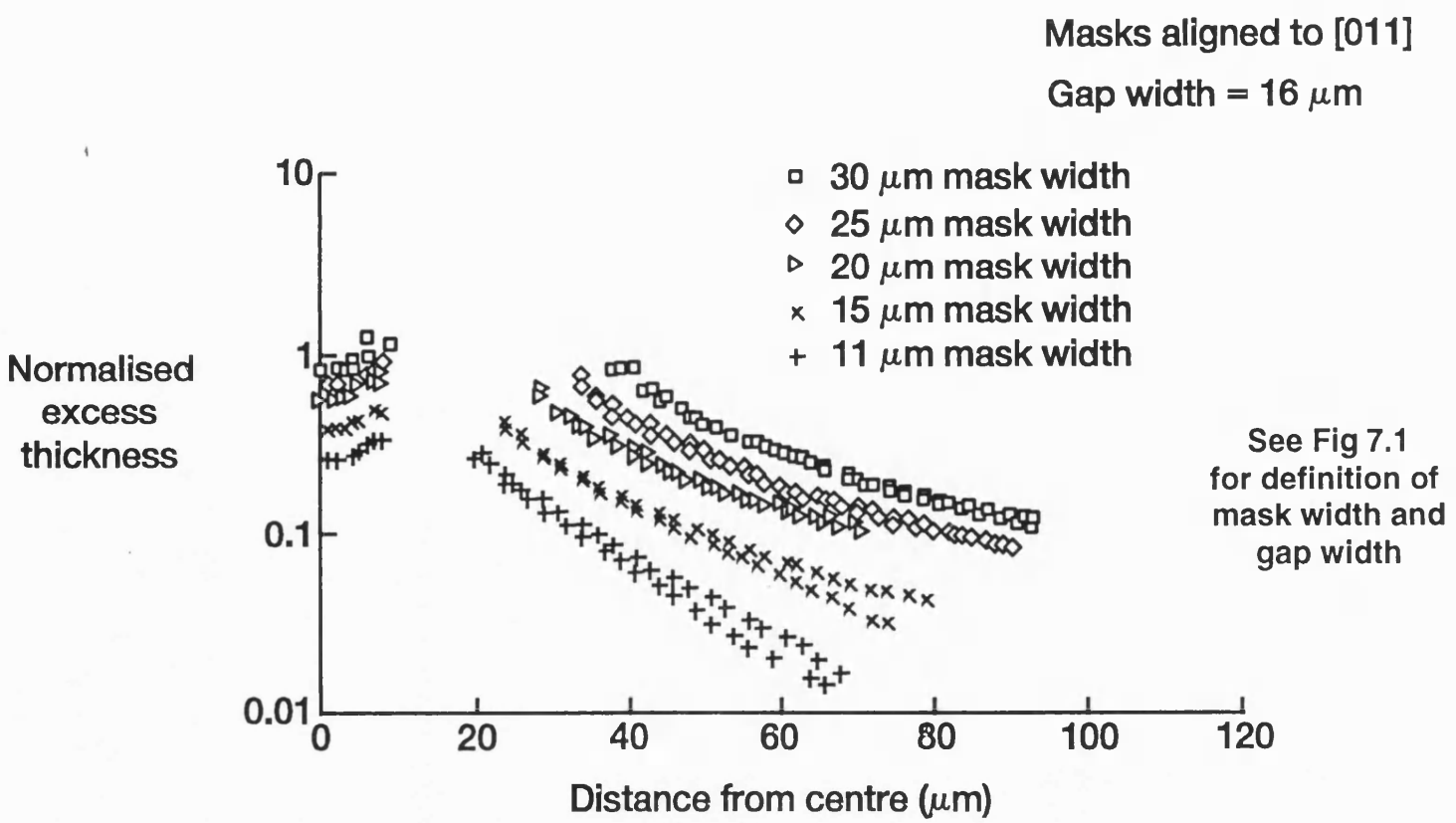

Fig 7.4 Effect of mask width on selective growth of InP

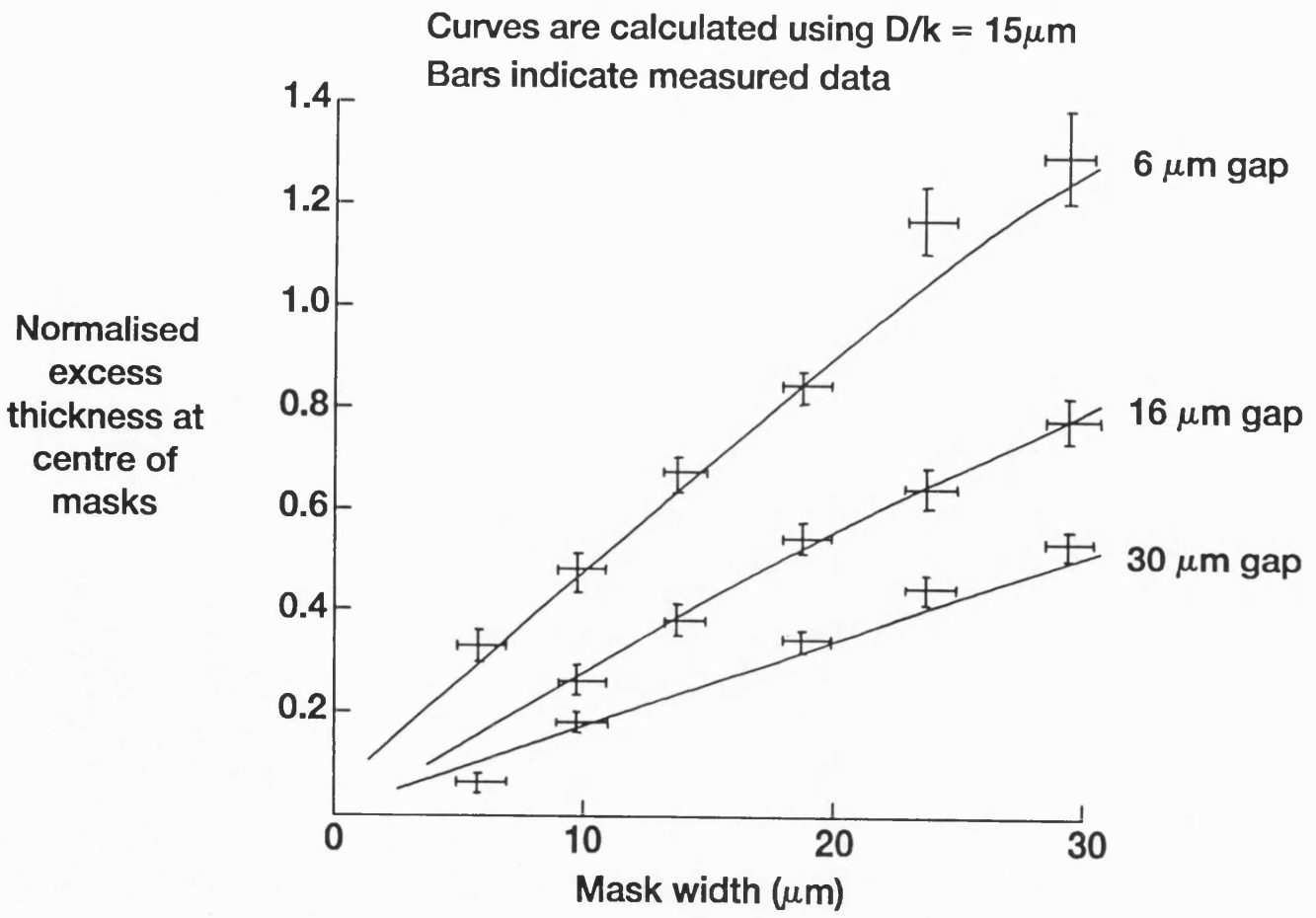

1992 AW9949–05

Fig 7.5 Increase in InP growth rate at centre of mask pattern

density increased. The morphology around identical patterns was strongly dependent on their orientation, being much worse when the masks were aligned to [0-1 1].

After optical examination the selectively grown ternary material was further assessed by scanning electron microscopy of cleaved (0 1 1) and (0-1 1) surfaces. It was confirmed, by staining one specimen, that there were no significant mass transport effects occurring in the reactor heat up cycle before growth. As before, the material growing on the exposed regions between the masks was bounded by planes of (1 1 1)A and (1 1 1)B type, as appropriate for the feature direction. There was some growth on (1 1 1)A type planes but the growth rate of InGaAs on these planes was much less than that of InP. This finding is in agreement with those of Kayser[4]. The lateral growth on (1 1 1)A type planes was associated with the development of a ragged edge on the side of the growing mesa.

There was virtually no growth on (1 1 1)B type planes and the material grown between masks aligned to [0 1 1] was well behaved in all but the two most extreme circumstances.

The thickness of the selectively grown InGaAs layer was measured by surface profiling with the Sloan Dektak II, in the manner described previously. The effects of varying mask width, gap and orientation were qualitatively similar to those described for InP. Once again no gas flow effects were observed.

Quantitative analysis revealed that the increase in the growth rate near the mask was slightly less for InGaAs than for InP. This difference can be seen when one compares Figure 7.6, which shows the relationship between the masking density and the excess thickness of InGaAs at the central point, with the corresponding figure for InP (Figure 7.5). The reduction in the magnitude of the perturbation in growth thickness was accompanied by an increase in the area over which it extended.

The profiles of normalised excess thickness for ternary material must be a combination of the profiles for excess In and Ga, as it is the group III

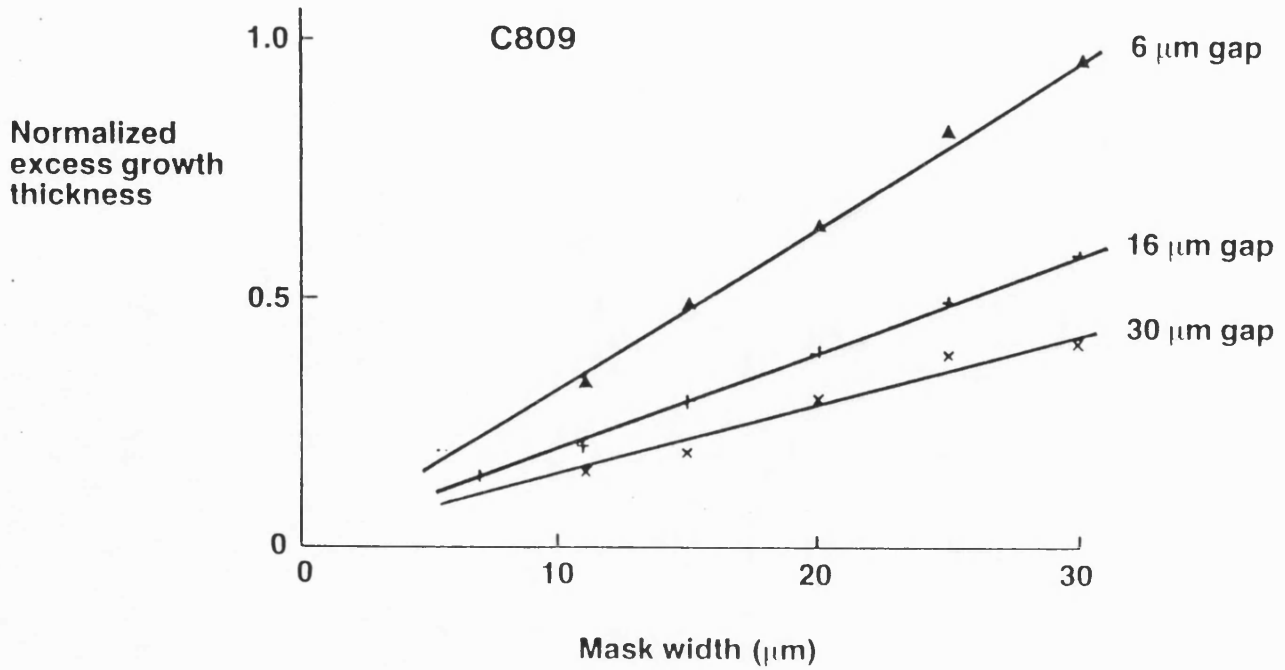

Fig 7.6 Measured increase in InGaAs growth rate at the centre of the mask pattern

elements that determine the growth rate[15,16]. It is possible to derive a profile for the excess Ga in ternary material by comparing thickness measurements from ternary and binary material. However, such an analysis assumes that the movement of the In containing species is identical in the growth of InP and InGaAs. At the time of the above measurements it was not immediately obvious that this should be the case, so we set out to determine the profiles of excess In and Ga by measuring the composition of the selectively grown ternary material.

The material composition was first investigated by energy dispersive X-ray analysis in a scanning electron microscope (SEM-EDX). The electron beam energy was limited to 10 keV to prevent emission from the InP substrate. We confirmed that such emission was absent by monitoring the X-ray spectrum for a phosphorus signal. The spectrum was analysed using a standardless ZAF correction routine which was finely calibrated by adjusting the correction factors to make x (in $In_{1-x}Ga_xAs$) equal to 0.47 in unperturbed regions far away from any masks. Different unperturbed areas were monitored on several occasions throughout the course of the experiment to check for drift. This set of calibration checks indicated that the standard deviation in the measurement of x was 0.2%. The arsenic signal was also monitored throughout the entire set of 32 measurements. The measured concentration of this element was (50.0±0.2) atomic percent. The area sampled for each measurement was 1½ μm x 2 μm.

The mismatch at the central point between the mask pairs increased with the masking density as shown in Figure 7.7. The deviation of x from its unperturbed value was independent of the orientation of the masks. Material grown between the masks was always indium rich and hence positively mismatched but, as the distance from the masks increased, the ternary composition moved through that for lattice match, to become slightly Ga rich, before slowly decaying back to the lattice matched value far away from any masks. An example of this behaviour can be seen in Figure 7.8.

The bandgap of the ternary material was also measured by spatially resolved photoluminescence at 77K[17]. This technique gave similar results

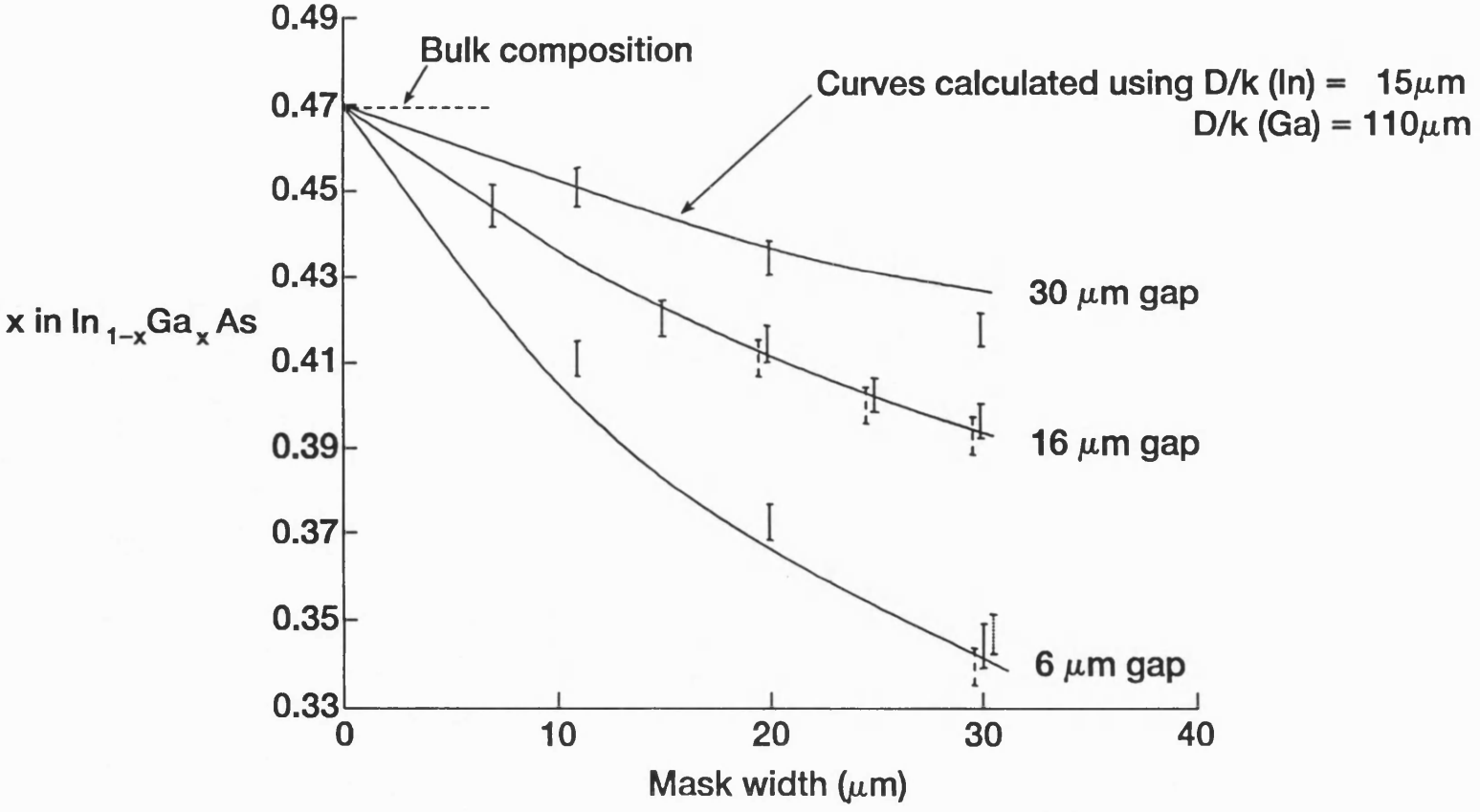

Fig 7.7 Composition of $In_{1-x}Ga_xAs$ at centre of mask pattern

(Solid error bars represent measurements between masks aligned to [011])
(Dotted error bars represent measurements between masks aligned to [0-11])

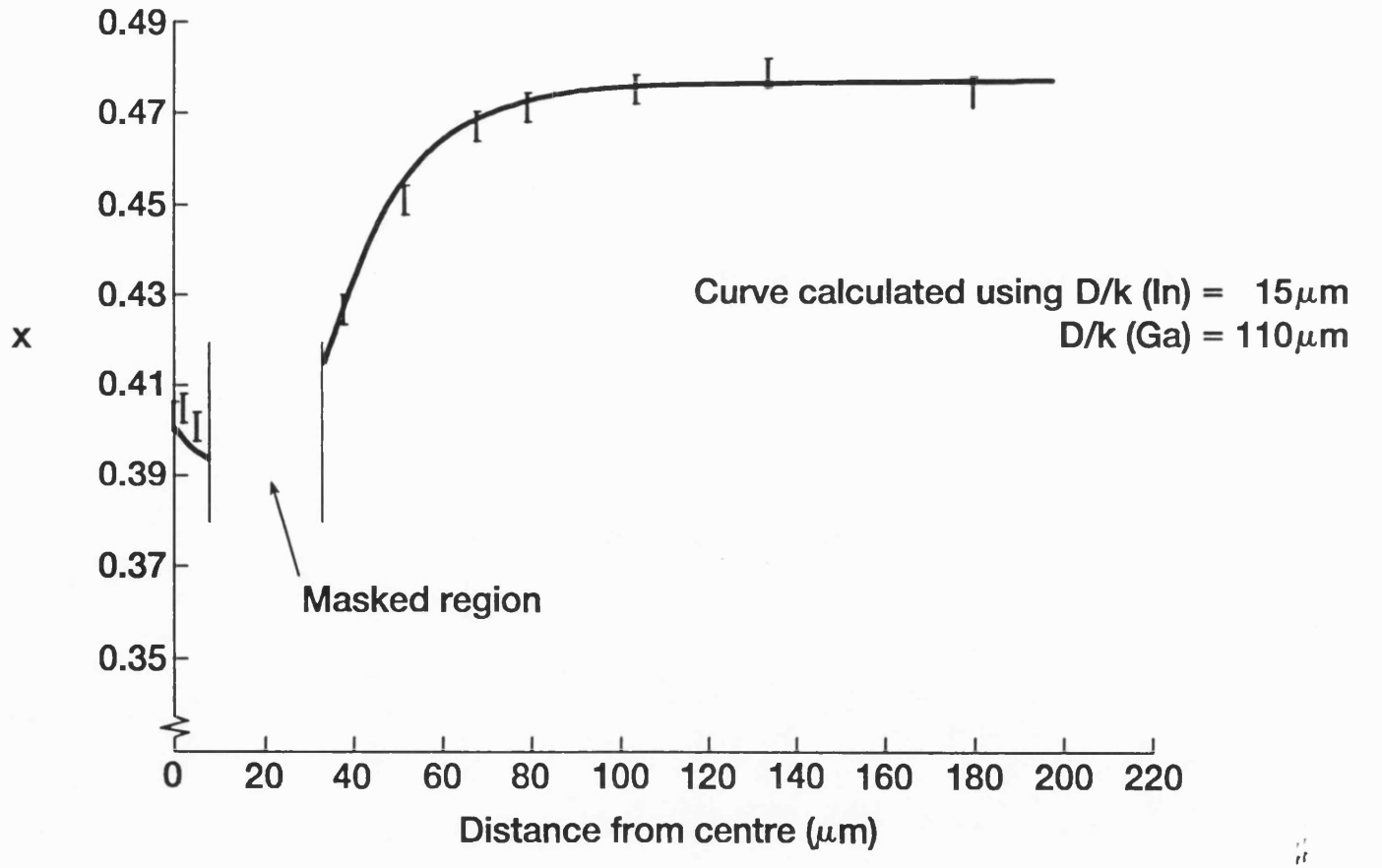

Fig 7.8 $In_{1-x}Ga_xAs$ composition as a function of distance from centre of mask pattern

1992 AW9949-03

to those from the EDX measurements. An example of such a measurement is shown in Figure 7.9. In the case of this figure the scanning spot has been moved across the gap at the end of a mask pair. It can be seen that the bandgap changes from its perturbed to its unperturbed value over a distance of about 100μm.

After making the above measurements, the decay lengths for excess In and Ga were separated by combining the thickness and compositional data. This analysis indicated that the decay length for excess Ga was about three times that for In. The hypothesis that the movement of In was the same in the growth of InGaAs and InP was then tested by plotting the graph shown in Figure 7.10. In this graph the normalised excess In deposition at a given location in the growth of InGaAs, is plotted against that at the same location in the growth of InP. The former data was deduced from compositional and thickness measurements on C809 (InGaAs) and the latter from thickness measurements on C804 (InP). The measurements came from points in a wide variety of locations with respect to the masking pattern and the range of excess deposition values arose from the fact that these locations lay in regions of different masking density. The plot confirmed that the In species did indeed move in an identical manner during the growth of the two materials, in all but the two most extreme circumstances. The latter deviation is not surprising as these extreme circumstances correspond to the two most perturbed structures, where growth was rather irregular. The conclusion that the movement of In is similar in the growth of InP and InGaAs is similar to that reached by Caneau et al[18].

The above X-ray and photoluminescence analyses implicitly assume that the composition of InGaAs growing at a particular location did not change during the course of the epitaxial growth. This surmise has been tested by spatially resolved secondary ion mass spectroscopy (SIMS). The measurements were made in a Cameca ims 3f machine equipped with a Charles Evans and Associates resistive anode encoder imaging system. Cs^+ bombardment and positive ion detection were used to monitor the matrix element signals $^{115}In^+$ and $^{69}Ga^+$ from 150 μm wide areas of the (1 0 0) surface. After the measurement, depth profiles of the concentrations

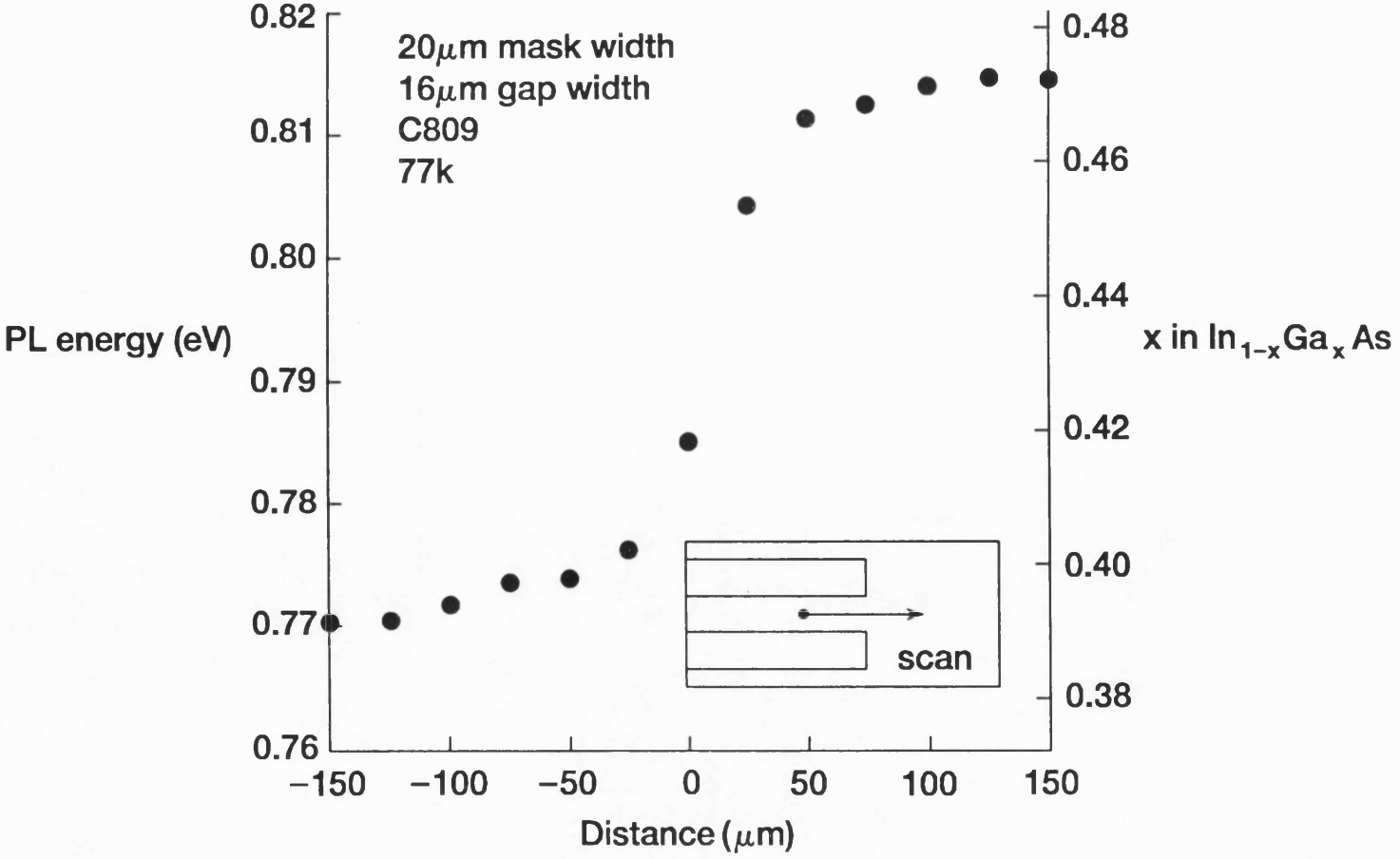

Fig 7.9 Bandgap energy versus distance from end of mask pair

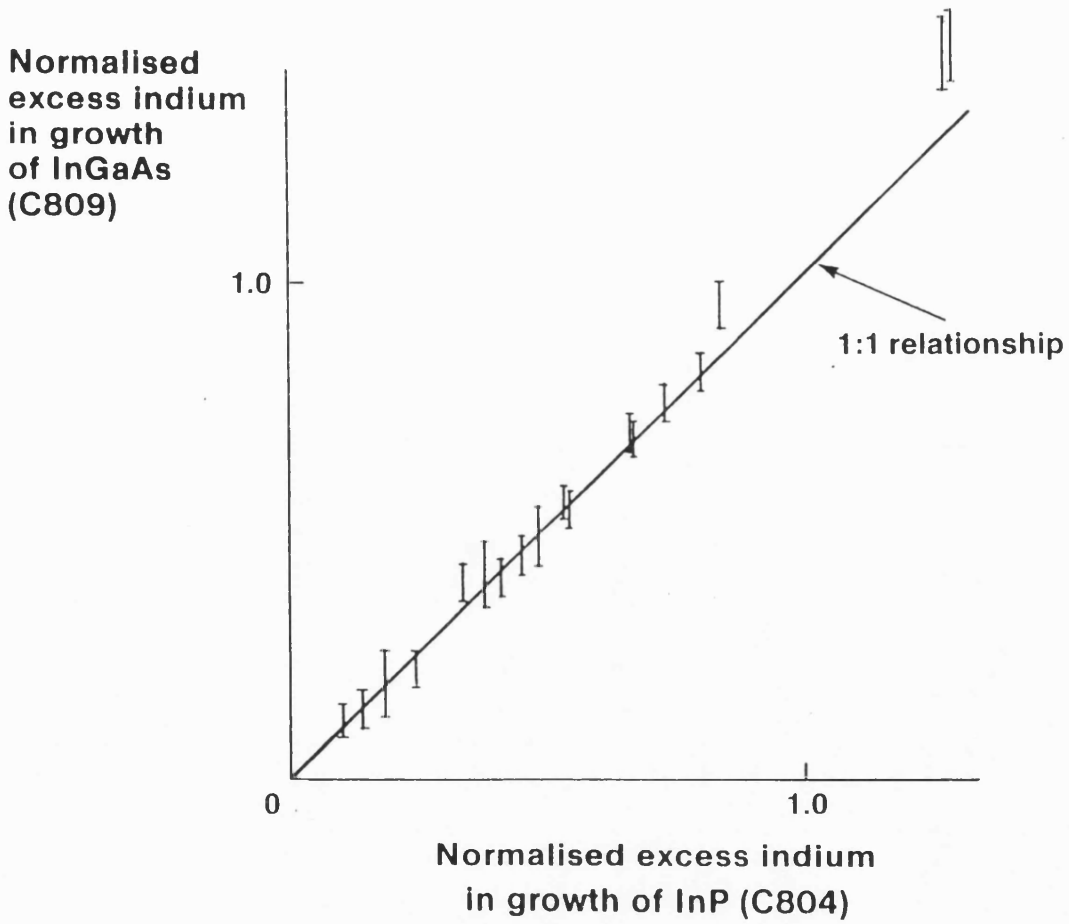

Fig 7.10 Comparison of In movement in the growth of InP and InGaAs

of Ga and In at different locations were obtained by analysing the raw data to find the signal for each ion in specified areas of the eroded region. The SIMS apparatus was not calibrated to measure the absolute concentrations of the matrix elements and hence all measurements were relative. However, the apparatus was certainly capable of observing the compositional perturbations seen in the SEM-EDX measurements and we were able to confirm that the Ga to In ratio was independent of the depth at which it was measured. The relative error in this measurement was 2% or less.

The optical emission properties of the selectively grown ternary layer were investigated by means of spatially resolved cathodoluminescence. The luminescent emission was not spectrally resolved, though optical emission from the InP substrate was blocked out with a filter. The silicon dioxide mask was removed before the measurements.

In regions of low masking density the emission from the ternary material was of uniform intensity, both between and around the regions which had been masked during growth. However, as the masking density increased dark line defects appeared between and, in some areas, outside the masks. These defects were clearly aligned to the [0 1 1] direction when the masks lay along [0-1 1]. The situation was not so clear when the masks were aligned to [0 1 1] as dark lines never appeared outside the region containing the masked pair of rectangles.

The defect density next to any given mask pattern was considerably greater when the masks were aligned to [0-1 1] and consequently features aligned to [0 1 1] could tolerate a much higher masking density before defects were observed. The data is summarised in the Table 7.1.

Table 7.1

Mask Orientation	Maximum mask width consistent with defect free structure (μm)		
	6 μm gap	16 μm gap	30 μm gap
[0 1 1]	11	25	30 (i.e. defect free in all cases)
[0-1 1]	Defects in all structures	7	N/A

These observations are consistent with those from the Nomarski interference microscopy described earlier. However, as mentioned above, the EDX measurements indicated that the compositional variations over a given pattern did not depend on its orientation. Consequently one can conclude that material mismatched to a given degree contains a greater density of defects when bounded by (1 1 1)A planes than when bounded by (1 1 1)B ones.

7.3.3. Selective Growth of GaInAsP

After analysing the selectively grown InGaAs, the series of experiments was extended by growing GaInAsP over the light field pattern (run C968). In unperturbed regions far away from any masks the thickness of the epitaxial layer was 0.54μm and its photoluminescence emission wavelength was 1.18μm. The unperturbed growth rate was 3.6μm/hr.

The characteristics of C968 were measured in the same manner as those of C809. The qualitative behaviour of the selectively grown quaternary material was very similar to that of the ternary: Dektak traces from the two wafers were of similar shape, the movement of excess In was similar to that in the growth of InP, the compositional variations over a given pattern did not depend on its orientation and material mismatched to a given degree contained a greater density of dislocations when bounded by

(1 1 1)A planes than when bounded by (1 1 1)B planes. However, one observation of particular interest was that the As to P ratio was not perturbed by the presence of the dielectric mask. This behaviour is consistent with a model where the diffusion-limited supply of group III precursors controls the growth rate. The effect of the mask density on the composition of the quaternary material at the central point is illustrated in Figure 7.11.

7.3.4. Selective Growth of QW Material

The suitability of selective area epitaxy for the fabrication of integrated devices was assessed by growing a quantum well structure over the light field mask (run number C885). The layer structure (see Fig. 7.12a) was similar to that of a MQW semiconductor laser and contained 6 InGaAs quantum wells which were embedded in the centre of a GaInAsP waveguide. In unperturbed regions far away from any masks the total thickness of the waveguide layer was 0.38μm and its room temperature photoluminescence wavelength was 1.18μm.

The bandgap of the MQW structure was investigated by means of spectrally and spatially resolved cathodoluminescence. The electron beam energy was 25 keV and the focused beam was continually rastered over an area of about 1½ μm x 2 μm during each spectral measurement. The mean peak emission wavelength of unperturbed regions far away from any masks was (1480±5)nm.

The emission wavelength at the central point between any two masks increased monotonically with the local masking density, as shown in Figure 7.12. Identical patterns aligned to [0 1 1] and [0-1 1] gave identical results to within the error in the measurement. At the ends of the mask pairs the emission wavelength relaxed back to its unperturbed value over a distance of about 100 μm in the manner shown in Figure 7.13. This distance was almost independent of the mask width and separation.

The optical quality of the selectively grown substructure was assessed by removing the spectrometer so that the cathodoluminescence was spatially,

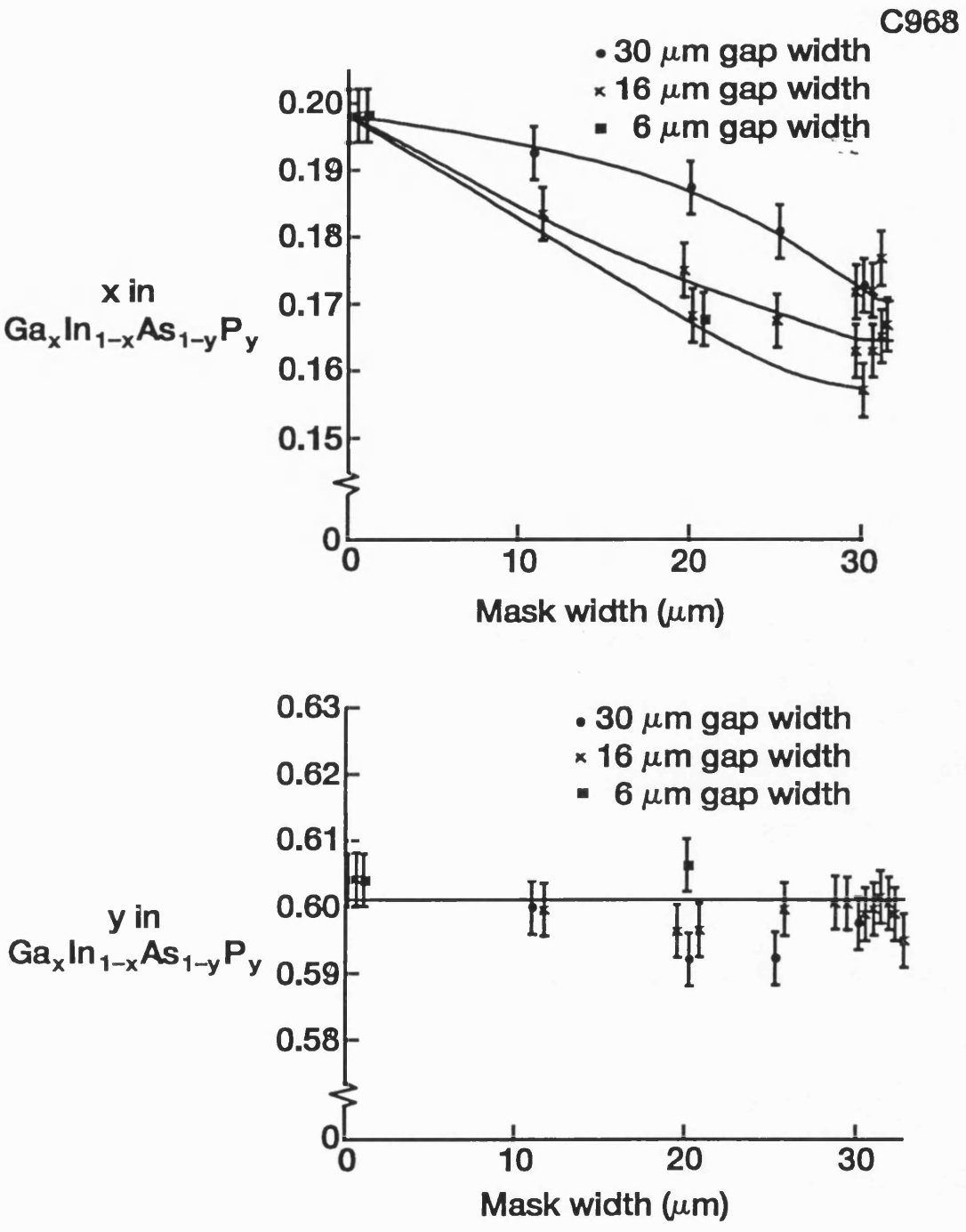

Fig 7.11 Effect of masking density on composition of GaInAsP at centre of gap between masks

Layer Structure GROWTH\C885 22.1.91

Nominal Specification				
Layer thickness (μm)	Material		Doping	
			Type	Value (cm^{-3})
300	InP substrate		S	
0.2	InP buffer layer		Si	5.10^{17}
0.142	GaInAsP (λ_{PL}=1.18μm) lower waveguide		None	
0.008	GaInAsP (λ_{PL}=1.18μm) barrier	MQWs Cycle x6	None	
0.006	GaInAs well		None	
0.15	GaInAsP (λ_{PL}=1.18μm) upper waveguide		None	
0.1	InP cap		None	

Fig 7.12a Unperturbed layer structure of wafer C885

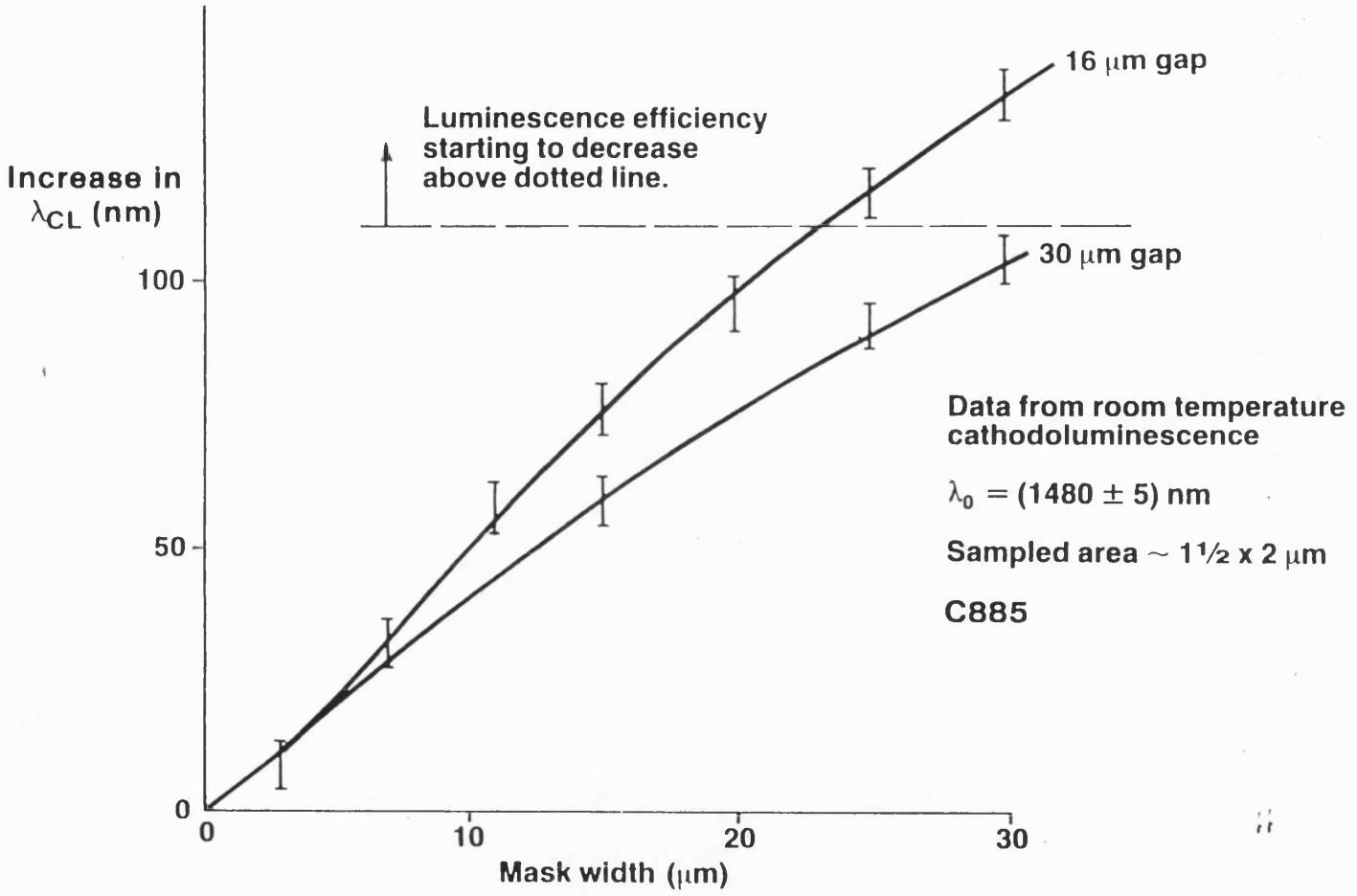

Fig 7.12 Effect of the mask dimensions on the emission wavelength of the MQW structure

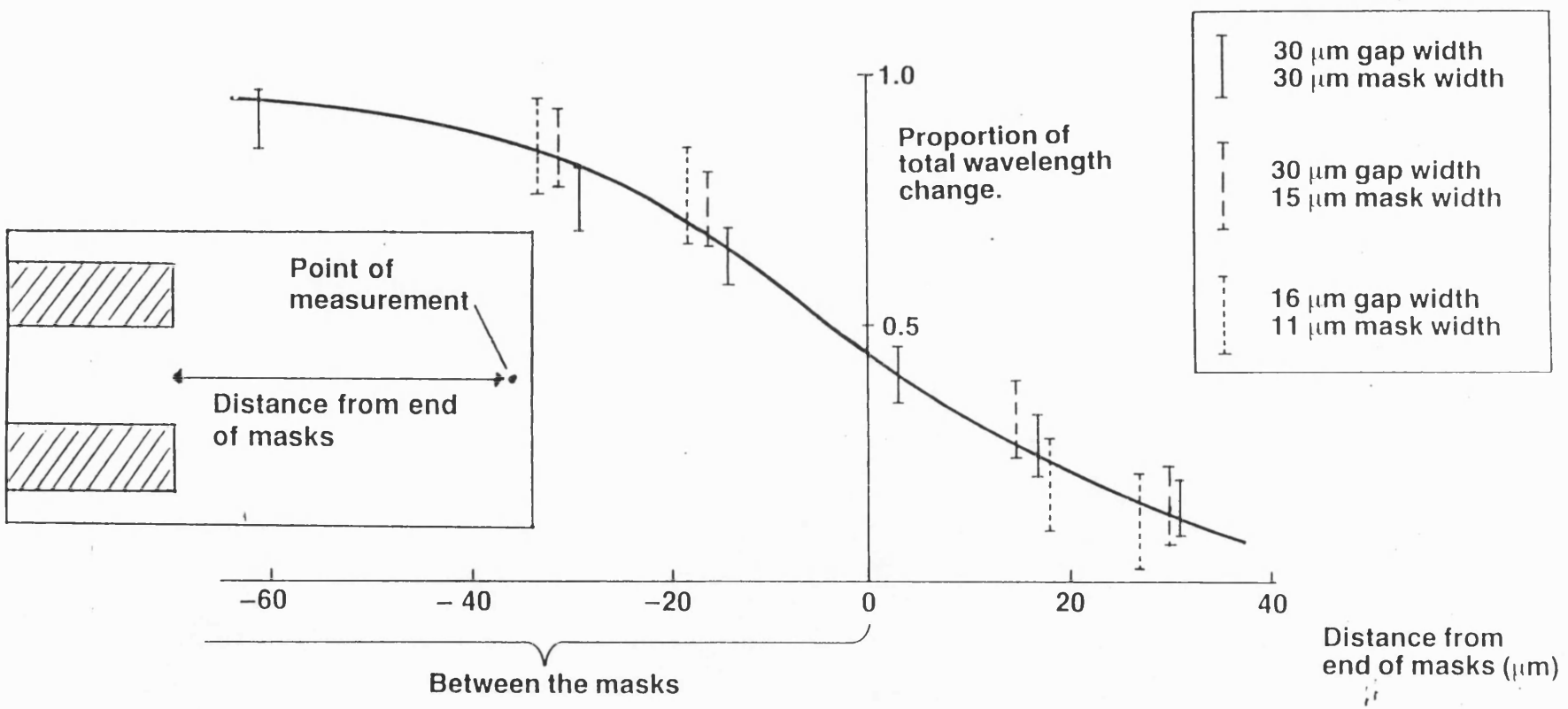

Fig 7.13 Relaxation of MQW emission wavelength

but not spectrally, resolved. The emission properties of the perturbed regions were then deduced by comparison of the signal from the region between the masks, with that from the regions outside the masks. It was discovered that the emission wavelength of the MQW material could be increased by ~100 nm before such intensity reductions occurred.

The crystallographic quality of the selectively grown MQW material was further investigated by plan view transmission electron microscopy. The material examined was that grown in 30μm wide gaps between two 30μm wide masks, with the pairs of masks aligned to either [0-1 1] or [0 1 1].

In general, the selectively grown MQW material was of high crystallographic quality. Any dislocations arising in the epilayers as a result of the perturbations caused by the masks were confined to the immediate vicinity of the masks. However, there was a difference in the density of dislocations found next to masks aligned to the two orientations. This difference can be seen in Figure 7.14, which contains g=<022> plan view micrographs of regions next to the mask edges. When the masks were aligned to [0 1 1] only a few dislocation tangles were observed. These tangles were confined to within 100nm of the mask edge. However, when the masks were aligned to the orthogonal orientation, a much greater density of dislocation tangles was observed. The latter tangles extended to a distance of approximately 0.4μm from the mask edge. Occasional threading dislocations extending up to 1μm from the [0-1 1] mask edges were also observed. These longer dislocations appeared to eventually bend upwards, through the quantum wells, to terminate at the surface of the epitaxial material.

The higher density of defects in material grown between masks aligned to [0-1 1] is consistent with the lower intensity of cathodoluminescence emission from such material.

7.3.5. Mechanism of Selective Growth

In the past, there has been some debate about whether the long range thickness perturbations observed in selective area epitaxy are caused by

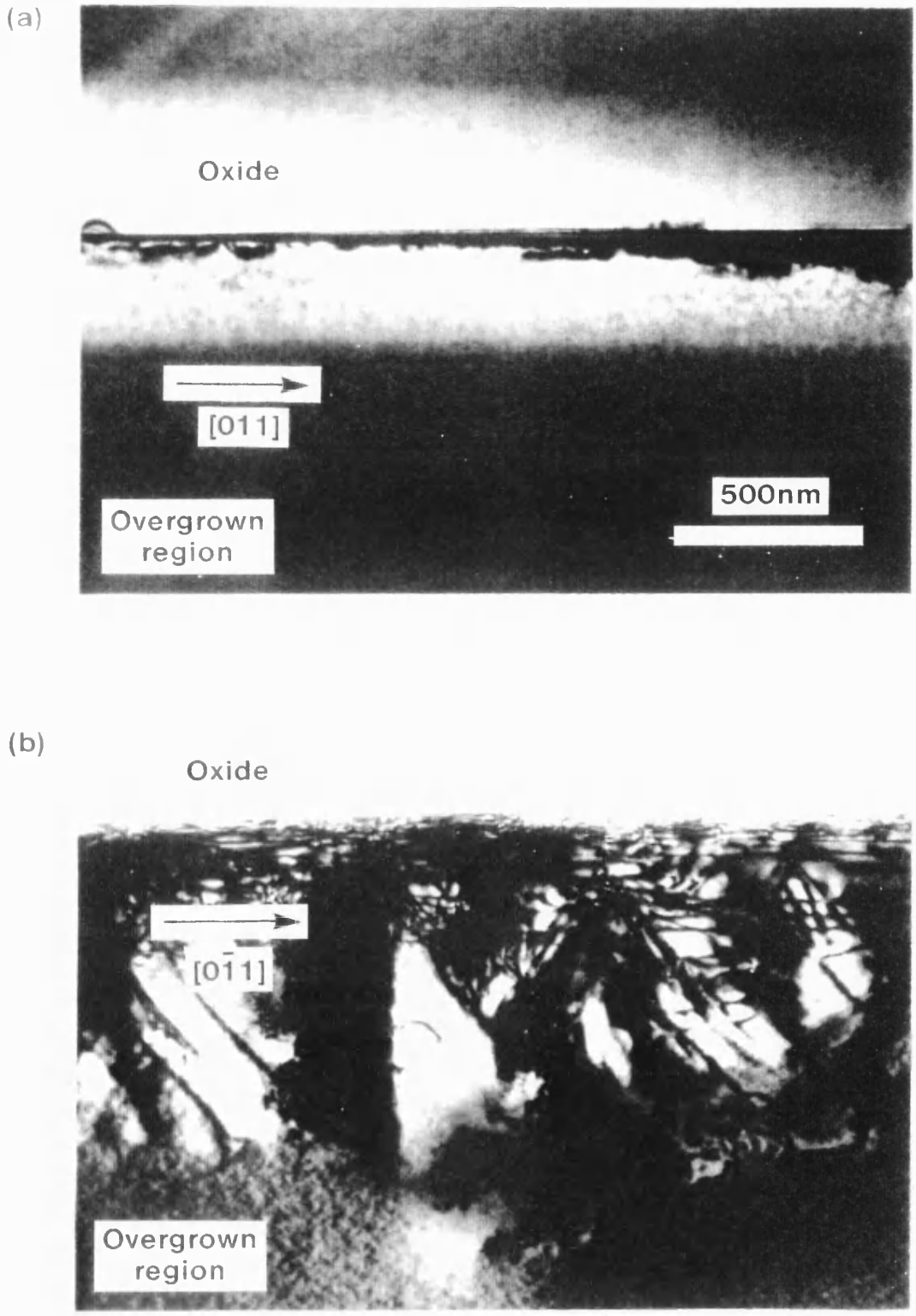

Fig 7.14 <022> BF TEM plan view micrographs of GaInAsP/GaInAs QW structure adjacent to (a) [011] aligned and (b) [01̄1] aligned oxide masks

lateral diffusion of growth precursors in the gas, or on the wafer surface[4,19,20,21]. We have attempted to verify which of these mechanisms is responsible for the lateral transfer of material, by growing on wafers in which deep trenches have been etched in the vicinity of the light field mask pairs. A schematic cross section of such a wafer is illustrated in Figure 7.15. The trenches were etched to a depth of 55μm by a combination of methane-hydrogen reactive ion etching and wet etching in a $HCl:H_3PO_4$ mixture. The function of the InGaAs layer shown in the figure was to mark the bottom of the selectively grown material, so that we could monitor any surface height changes caused by mass transport before growth. The neck of the trench was only 4μm wide. This narrow aperture should have only a small effect on the concentrations of growth precursors in the gas phase. Consequently, in a situation where lateral diffusion takes place predominantly in the gas above the wafer, the trench should only have a small effect on the profile of normalised excess thickness. However, it should have a major effect if lateral migration of reactant takes place predominantly on the surface, as the excess growth precursors diffusing off the oxide mask would have to migrate over an extra 120μm of semiconductor material to reach the far side of the trench. It seems unlikely that the precursors could cover such a distance without being depleted by deposition on the semiconductor surface and hence, when surface migration dominates, one would expect the profile over the structure shown in Figure 7.15 to be asymmetric.

The growth mechanism responsible for the lateral transfer of excess material was first tested by growing a layer of InP over the structure shown in Figure 7.15 (run C1179). The unperturbed thickness of the epitaxial layer was 0.56μm.

The profile of the epitaxial deposition over the different mask structures was measured with the Dektak. An example of such a measurement is shown in Figure 7.16. The measured profiles were all symmetrical, thus indicating that lateral diffusion was taking place in the gas phase.

The experiment was repeated by growing 0.5μm of InGaAs over an identical structure (run C1267). The growth profiles were once again

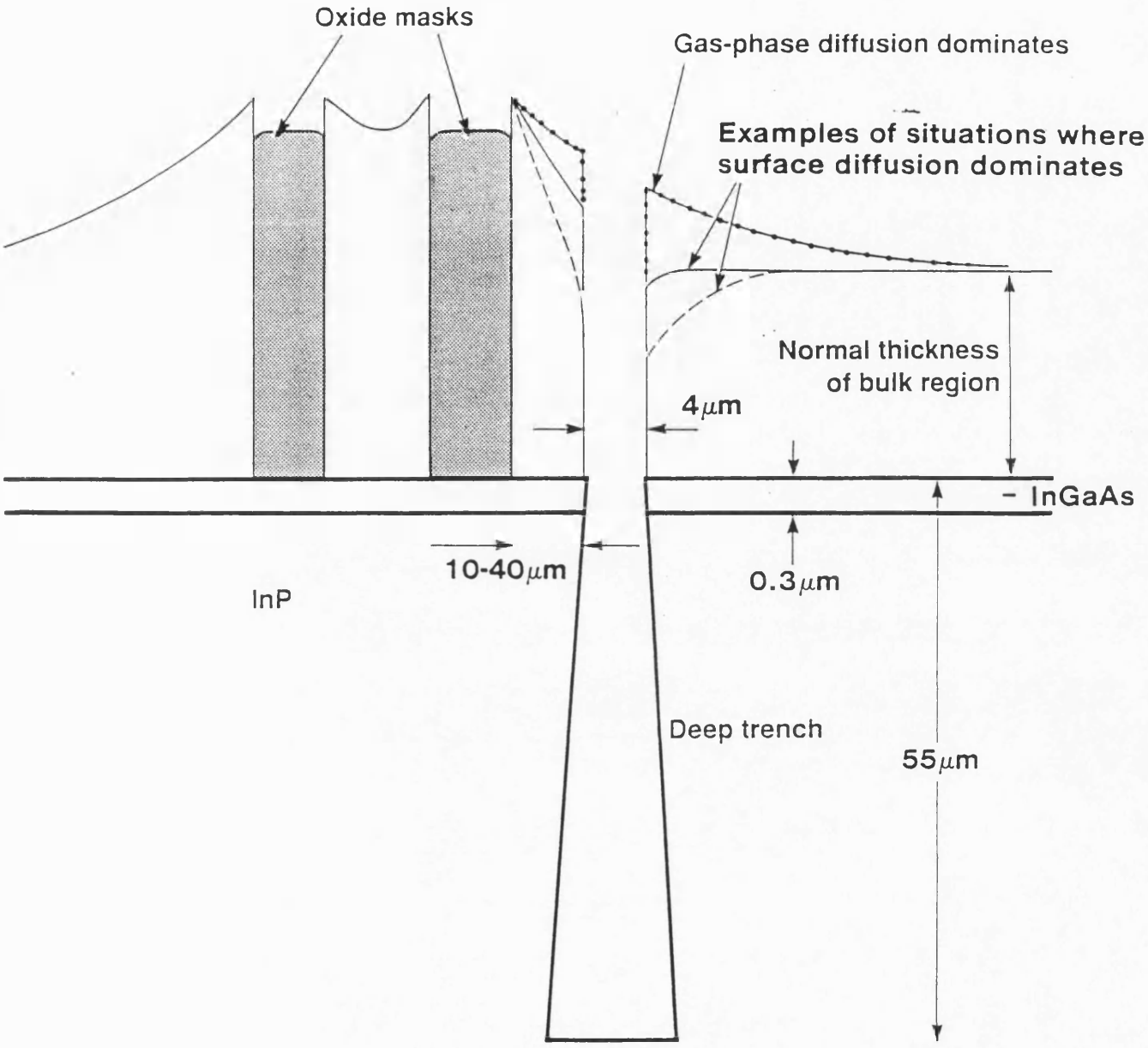

Fig 7.15 Schematic diagram of the profiles of the excess thickness of InP grown over the trenched wafer

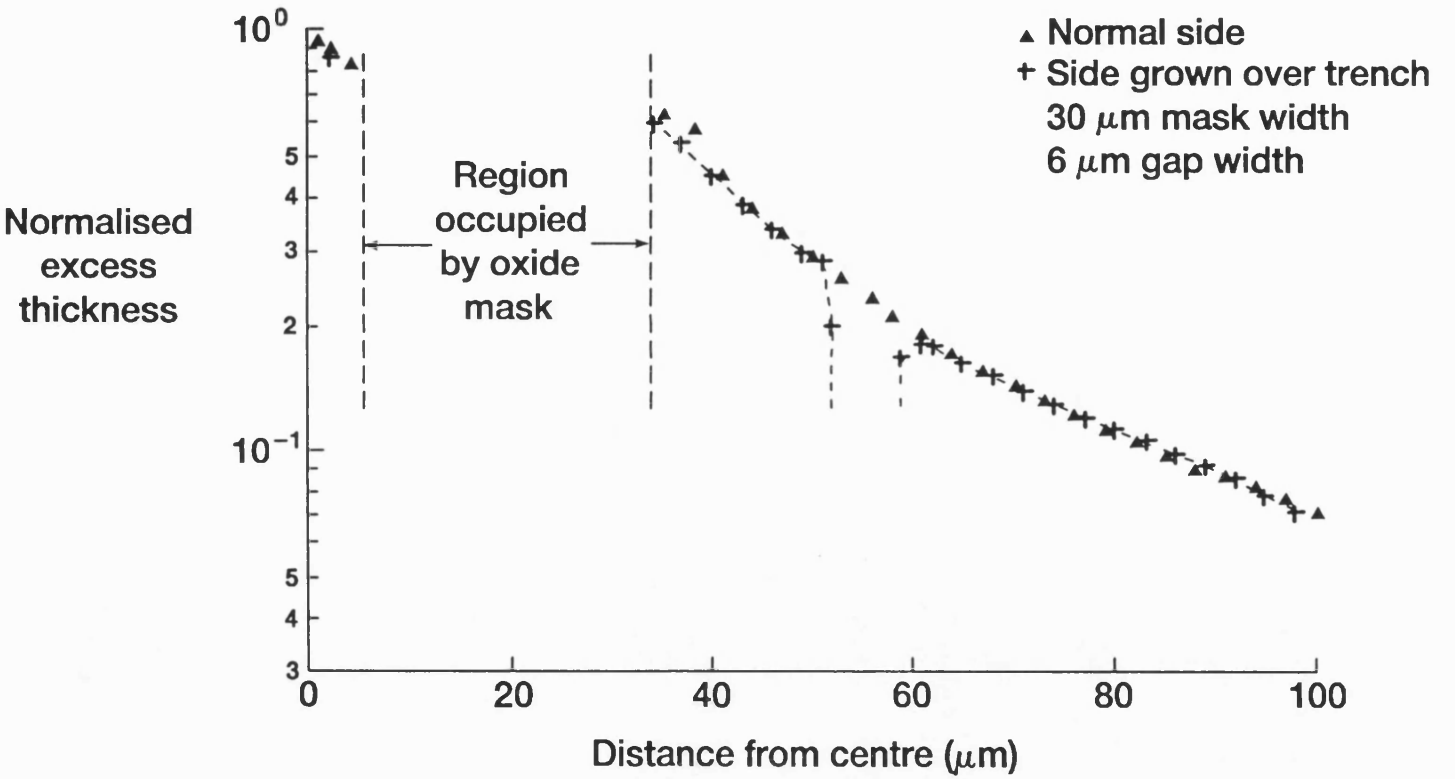

1992 AW9949-12

Fig 7.16 Normalised excess thickness of InP grown over trenched wafer

assessed by measurement with the Dektak. The results were similar to those for the InP growth above, save for the fact that there were small perturbations in the excess thickness extending about 5μm from each side of the trench. We believe that the small perturbations were caused by surface migration of precursors off the (1 1 1)B facets that terminated the epitaxial layer at the edges of the trench. However, as the profiles were symmetrical in all regions except in the immediate vicinity of the trench, we concluded that the long range lateral perturbations that we observe in InGaAs growth are predominantly caused by diffusion in the gas phase.

The above experiments do not indicate that surface migration is absent from the MOCVD growth process. Indeed there is evidence in the literature indicating that surface migration does occur during such epitaxial growth[4,22,23]. We can only conclude that, under our growth conditions, the lateral movement of material on the 10-100μm scales that we have investigated is caused by lateral diffusion in the gas phase. This conclusion is similar to those reached by Kayser[4] and Colas[24].

7.4. ANALYSIS OF GROWTH OVER LIGHT FIELD MASKS

7.4.1. Model of Selective Area MOCVD

The reactions and gas flows in an MOCVD reactor are extremely complicated and hence it is difficult to develop a complete model of the process[25,26]. We attempted to simplify the problem by developing a model which depended on those features of the growth which we believed were of direct relevance to selective area epitaxy. If such a model agrees with experimental data, it is not only of use in helping one gain understanding of the selective epitaxy process, but is also of great assistance in device design.

The model operated by calculating the concentration profiles of In and Ga species in the gas above the wafer surface. The profiles were determined by independently solving Laplace's equation for the two types of precursor[27] in a window of width w and height d. This window is

illustrated in Figure 7.17. The boundary conditions at the edges of the window are also illustrated in Figure 7.17 and can be summarised as:

$$n = n_0 \quad \text{at the surface } z = d$$

$$\frac{\partial n}{\partial x} = 0 \quad \text{at the vertical boundaries, } x = 0 \text{ and } x = w$$

$$D\frac{\partial n}{\partial z} = kn \quad \text{at the semiconductor surface, } z = 0$$

$$\frac{\partial n}{\partial z} = 0 \quad \text{at the mask surface } z = 0$$

n was the concentration of the group III species and D was the diffusion coefficient of the group III species in hydrogen. k was the rate of adsorption of the species on the semiconductor surface per unit concentration in the gas above the surface. n_0 was a constant, z was the growth direction and x was perpendicular to both z and the long axes of the masks.

The boundary condition over the dielectric mask at the bottom of the calculation window was derived from Fick's law and the fact that there was no deposition in this region. The boundary condition over the semiconductor surface was derived from a combination of Fick's law and the Langmuir isotherm[15].

At the top of the window the boundary condition was described by a fixed concentration n_0. We always worked with normalised growth rates and hence, for the purposes of the calculation, we adjusted the value of n_0 to give a growth rate of unity in unperturbed regions far away from any masks. The height of the calculation window had to be sufficient to ensure that this fixed concentration did not disturb the perturbations in gas concentration over the masks. In practice, we confirmed that this condition was satisfied by checking that our solution was independent of d.

Having fixed n_0, the only adjustable parameter left was D/k, the ratio of the diffusion coefficient to the rate of adsorption on the semiconductor surface. A decrease in the value of this parameter, which had dimensions of length, increased both the normalised excess rate of deposition next to a mask and the rate at which the normalised excess thickness decayed with

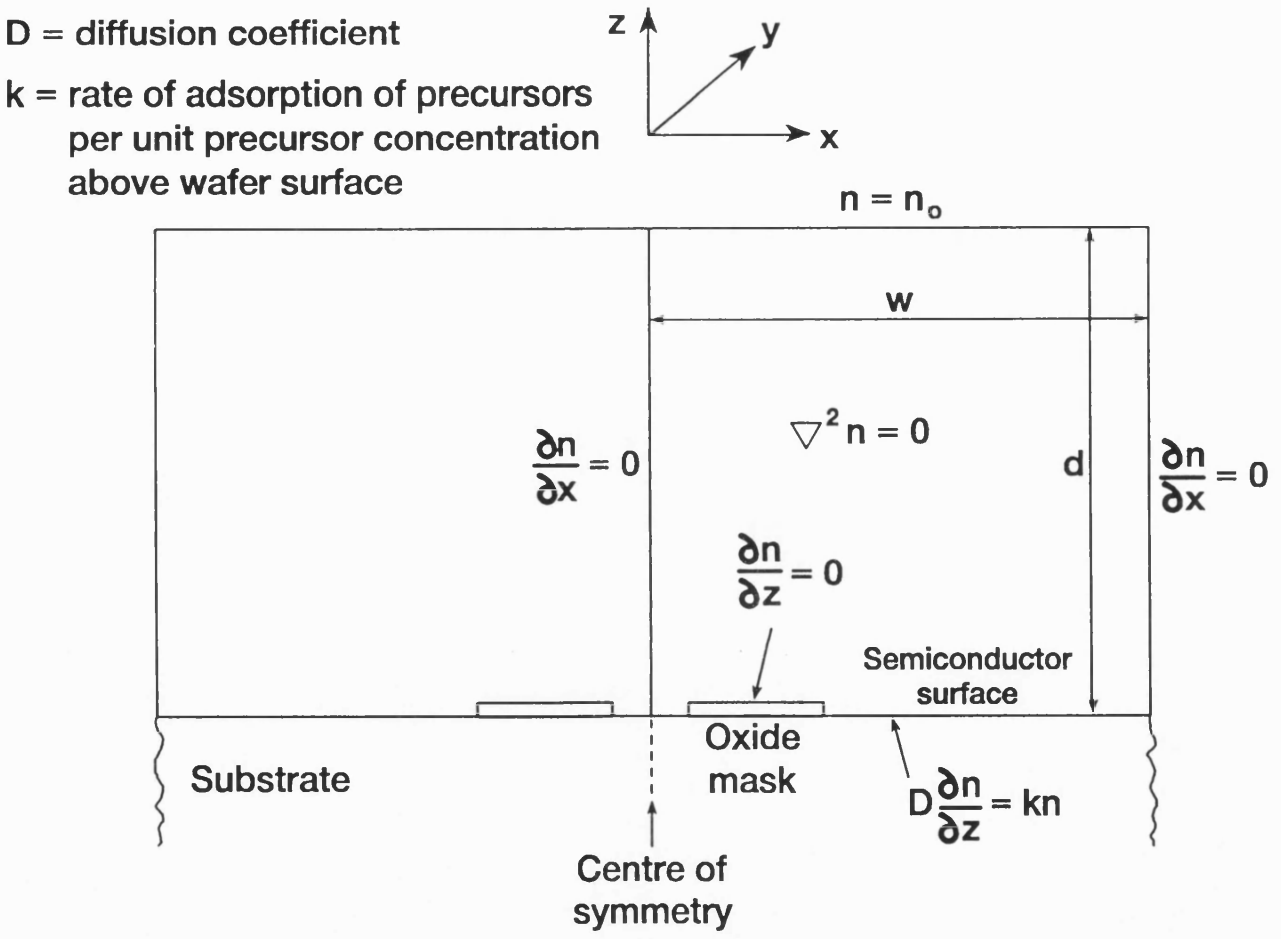

Fig 7.17 Geometry and boundary conditions used in MOCVD growth model

distance from the mask. The effects of such adjustments are illustrated in Figure 7.18. In practice we found D/k by adjusting its value until the modelled normalised excess thickness at the centre of a mask pattern fitted experimental data for that point. The validity of the model was then tested by noting the accuracy of theoretical predictions away from the centre of that particular pattern and on different patterns of the light field mask.

The equations were solved on a desk-top computer using an iterative Fourier method. This method is described in Appendix F.

The above analysis assumed that:

a) the lateral movement of material in selective area epitaxy took place in the gas phase. This assumption was based on the results of the deep trench experiments described previously.

b) the perturbations caused by selective area epitaxy were independent of the orientation of the mask with respect to the crystallographic axes of the wafer. We confirmed that this assumption was correct by surface profiling across identical features aligned to [0 1 1] and [0-1 1].

c) the effects of forced convection were insignificant. This assumption was based on the fact that we never observed gas flow effects in our experimental data. Our observation was not universally consistent with those of other authors, as Caneau et al[18] have observed flow effects in the selective growth of InP related materials. We believe that the discrepancy between our observations and those of Caneau was related to the fact that she was using masks which covered a much larger area.

d) the masks were infinitely long in the direction perpendicular to the plane of the paper in Figure 7.17. This assumption was useful in that it allowed one to model in two rather than three dimensions. We confirmed that it was valid by noting that the masked rectangles were much longer than the distance over which the growth was perturbed.

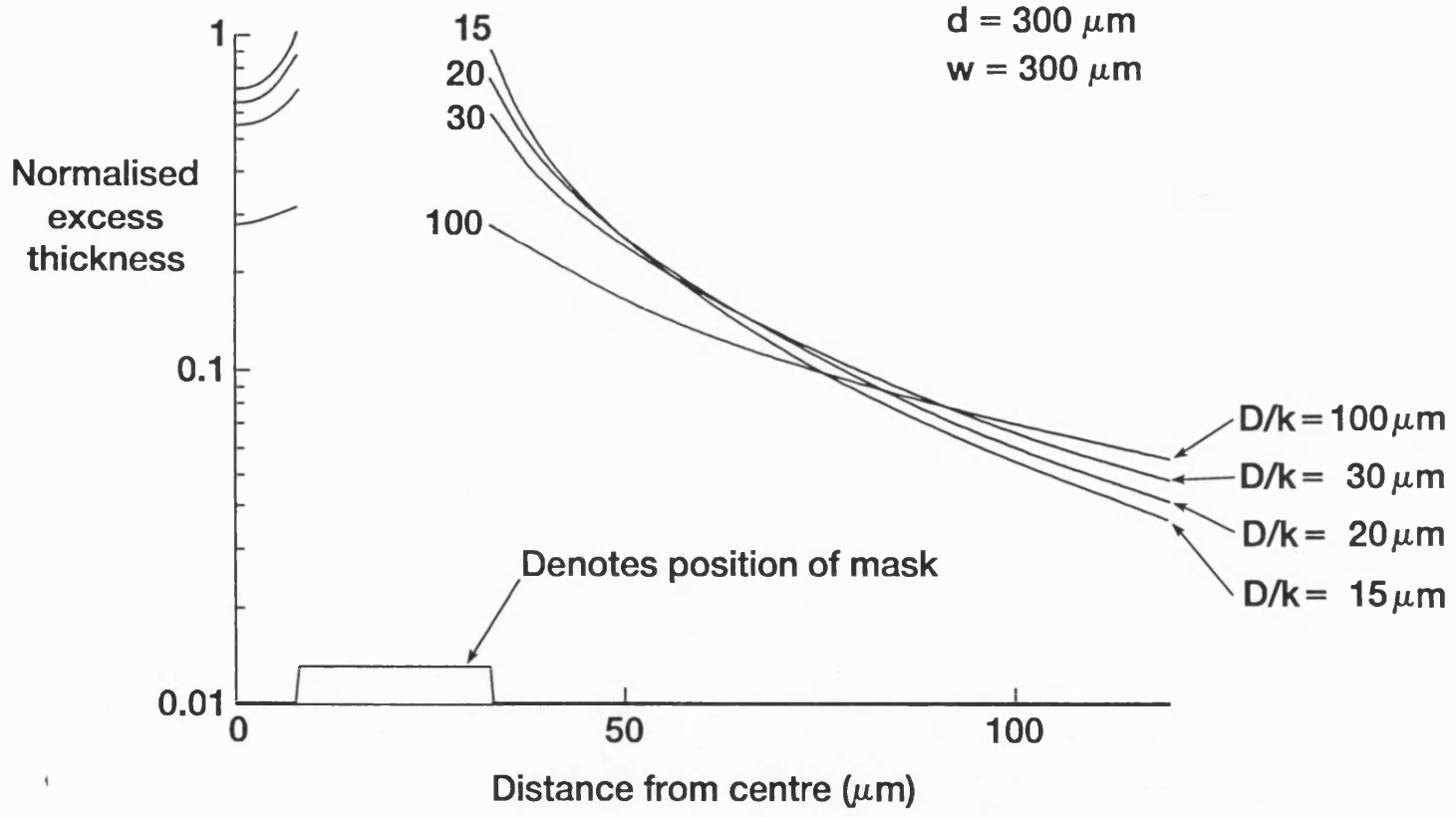

Fig 7.18 Computed profiles of normalised excess thickness for different values of D/k

e) the mask pattern was repeated periodically with a pitch of 2w, where w was the width of the calculation window. This pitch was derived from the fact that we assumed that the mask pattern was symmetrical around x=0 and x=w to eliminate diffusion across these boundaries. The edge of the window at x=0 was almost a true centre of symmetry for our rectangular patterns. The same was not always true for the edge at x=w but, as the features on the mask were essentially isolated, we could simply make w sufficiently large to make the normalised excess thickness at x=w very small.

f) the diffusion coefficient was constant over the calculation window. This assumption was similar to that made by Coronell and Jenson[27]. Strictly speaking it meant that we had also assumed that the temperature, T, was constant over the calculation window, as the diffusion coefficient[15] varies approximately as $T^{1.8}$. This assumption was invalid to some degree, as the gas entering the reaction chamber of an MOCVD reactor is not heated and hence, the temperature in the gas will decrease with altitude above the wafer surface. However, the dimensions of our masked features were small (<30μm) and hence, we believed that perturbations in the gas concentration occurred close to the wafer surface. It seemed plausible that the temperature in this small region was approximately constant. The only supporting evidence that we had for this assumption was the agreement between the theoretical and experimental data described below.

g) the rate at which species were adsorbed on the wafer surface was directly proportional to their concentration immediately above the surface. This assumption can be alternatively expressed by stating that we assumed, when using the Langmuir isotherm[15], that the fraction of the wafer surface covered by adsorbed species was much less than one. We tested this assumption by extending the model so that it is was capable of handling situations where the surface coverage was approaching unity. However, in practice we found that the best fit to experimental data was obtained when the surface coverage was much less than one, as described in the analysis above.

h) the group III precursors did not break down before they reached the semiconductor surface. Our level of understanding of MOCVD was not sufficient to enable us to decide whether such breakdown did or did not occur. However, our analysis may still have been valid in a situation where the precursors did break down above the wafer surface. The ability of the above equations to cope with this situation was related to the fact that they were linear. Consequently, the concentration of the group III precursor which was ultimately adsorbed onto the wafer surface, could be represented as the sum of its unperturbed concentration and the perturbation introduced by the presence of a dielectric mask. The boundary conditions for the unperturbed part of the above sum depended on the manner in which the precursors broke down. However, the boundary conditions for the perturbation were identical, regardless of whether the precursors broke down in the gas or not, so long as the presence of the dielectric masks did not affect the altitude at which breakdown occurred. The fact that D/k may have been different after the precursors had partially broken down did not matter as the value was obtained by fitting experimental data. Consequently, the above model may still have agreed with experimental data even if the group III precursors did break down before they reached the semiconductor surface.

7.4.2. Comparison of Model Predictions with Experiment

We first tested the model by comparing theoretical predictions with the experimental data from our first selective growth of InP (C804). The value of D/k used in this comparison was that required to fit the experimental normalised excess thickness at the centre of a 16μm wide gap, between two 25μm wide masks. The value of D/k obtained in this fit was (15±3)μm. The validity of the model was assessed by using this value of D/k to predict the normalised excess thicknesses around other features on the pattern. A comparison between the predicted and experimental normalised excess thickness values at the centres of the mask pairs is shown in Figure 7.5. The corresponding comparison between experiment and theory away from the centre of the mask pair chosen for the calibration is shown in Figure 7.19. In both plots, the experimental and

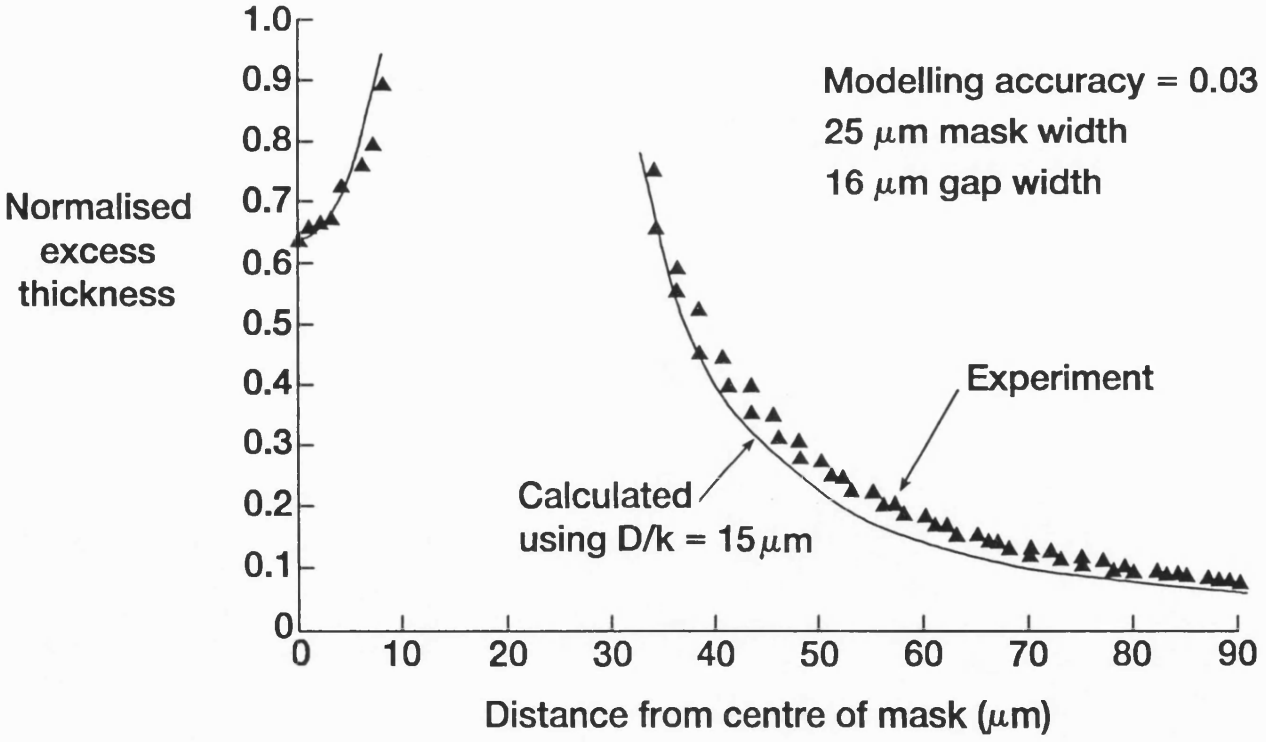

1992 AW9949-10

Fig 7.19 Normalised excess thickness of InP versus distance from centre

theoretical normalised excess thickness values agreed to within the error in the measurement.

We further tested the model by attempting to predict the thickness and compositional perturbations generated in the selective growth of InGaAs (run number C809). The values of D/k for In and Ga were determined by independent fits to the experimental normalised excess concentrations of each element. The point chosen for these fits was the centre of the pattern with 25μm wide masks and a 16μm wide gap. The optimum value of D/k for indium was (15±3)μm. The fact that this value is identical to that obtained for InP is not unexpected, when one recalls that we have already shown that the movement of In in the growth of InGaAs is identical to that in the growth of InP. The optimum value of D/k for Ga was (110±30)μm.

We tested this model of ternary selective growth by using the above values of D/k to predict the change in composition at the centre of all the other structures. We also predicted the change in composition as one moved away from the centre of the calibration structure. These predictions are compared with experimental data in Figures 7. 7 and 7.8 respectively. Once again we achieved agreement between experiment and theory to within the error of the measurement.

The different values of D/k for the In and Ga species were a quantitative representation of the different decay lengths for indium and gallium described in section 7.3.2. The value of D/k for the indium species was relatively small and hence, these species were rapidly adsorbed as they diffused from regions over a mask to those over a surrounding semiconductor surface. Consequently, ternary or quaternary material grown in the vicinity of a mask was indium rich. The value of D/k for gallium species was larger and hence, such species tended to move further from the mask before they were adsorbed. This meant that excess gallium was spread over a greater area than excess indium. Consequently ternary or quaternary material tended to be slightly gallium rich at intermediate distances from a mask, as the vast majority of the excess indium was deposited in the immediate vicinity of the mask. Far away from any masks the deposition rates of both species returned to their normal values.

7.4.3. SURFACE CHEMISTRY DURING MOCVD GROWTH

The values of D/k derived from the fits above provide some insight into the mechanism of MOCVD growth. For example, if one combines values of D/k with estimates of the diffusion coefficient D, derived from the kinetic theory of gases, then one is able to determine the ratio of k for In to that for Ga. It is difficult to derive k from measurements on unperturbed epitaxial material, as the growth rate of such material is predominantly controlled by the rate at which group III species diffuse through the gas and not by the rate at which they are adsorbed at the surface. Consequently, the effects of k are dominated by those of D. The advantage of using selective area epitaxy to probe the value of k, lies in the fact that the perturbations in gas concentration caused by selective growth occur close to the wafer surface.

If we proceed with the above analysis we find, from the kinetic theory of gases[28], that the diffusion coefficient for one gas diffusing through another is given by

$$D = \frac{3}{8}\left(\frac{\pi k_B T}{2}\frac{m_1 + m_2}{m_1 m_2}\right)^{\frac{1}{2}}\frac{k_B T}{\sigma P}$$

where k_B is Boltzmann's constant, T is the temperature, m_1 and m_2 are the masses of the two gas molecules, P is the total pressure and σ is the collision cross section. In the situation that we have considered above the temperature and pressure are constant throughout the region of interest. In addition, the masses of the metal-alkyl molecules used in MOCVD are much greater than those of hydrogen and hence the reduced mass in the above formula will be approximately equal to that of hydrogen. Consequently the differences in the diffusion coefficients of the metal-alkyl molecules will be predominantly related to the differences in their collision cross sections in collisions with hydrogen. The difference in the collision cross sections for TMI and TMG will be very small as the two molecules

are of very similar size, and hence the two molecules will have almost identical diffusion coefficients.

When we combine this information with the values of D/k derived from the growth of InGaAs in run C809, we can estimate the ratio of k for Ga to that for In.

$$\frac{k_{Ga}}{k_{In}} = 0.14$$

Of course one species may diffuse as the trimethyl-metal and one as the dimethyl-metal but its seems unlikely that such a change would make k_{Ga}/k_{In} greater than unity. The fact that this ratio is less than one is consistent with the fact that the methyl-gallium bond is stronger than the methyl-indium bond[15] and indicates that the energy required to break a metal-methyl bond may be the rate limiting step in the adsorption process.

The above diffusion equation is derived from an assumption that gas molecules behave as rigid elastic spheres when they collide. This is only an approximate description of what actually happens. More complicated equations can be obtained by making more realistic assumptions about the nature of intermolecular forces[28]. However using these advanced treatments does not change the nature of the argument given above.

7.5. SUMMARY

The conclusions drawn from the above work can be summarised as follows.

The deposition of epitaxial material by MOCVD can be inhibited by the presence of a silica mask. Epitaxial material deposited close to such a mask grows faster than normal, as some of the material which would have grown on the masked area is deposited in its vicinity. The factor by which the growth rate is enhanced increases with the fraction of the surrounding substrate which is covered by the mask.

At the edge of a mask, selectively grown material is bounded by an inclined facet. The growth rate on this facet depends on the orientation of the mask edge with respect to the crystallographic axes of the substrate. However, the behaviour of growth in the central region of an opening between two masks is independent of the crystallographic orientation of the pattern, provided that the fraction of the opening occupied by the facets is small. The behaviour of selective growth over our mask patterns is also independent of the orientation of the mask pattern with respect to the gas flow in the reaction chamber.

In general, ternary or quaternary material deposited next to a mask is indium rich with respect to that deposited far away from any masks. These compositional variations are caused by the fact that, under our growth conditions, the decay length of excess gallium is about three times that of excess indium. The lateral movement of excess In during selective growth is similar in the growth of InP, InGaAs and GaInAsP.

The arsenic to phosphorus ratio in quaternary materials is not affected by the proximity of dielectric masks. This observation is consistent with the fact that the group V precursors are in great excess in MOCVD.

The lateral movement of excess Group III precursors, over distances of the order of tens of microns, takes place in the gas phase. The way in which these precursors move can be predicted by a model based on Laplace's equation. When combined with experimental data, this simple model indicates that the activation energy for the adsorption of Ga species is greater than that for the adsorption of In species.

The cathodoluminescence emission wavelength of quantum well material can be shifted by at least 100nm, without degradation in emission efficiency, by selective growth techniques.

7.6. REFERENCES

1 Tsang W T, Yang L, Wu M C and Chan Y K 1991 *Electron. Lett* **27** 3

2 Wang Y L, Feygenson A, Hamm R A, Ritter D, Weiner J S, Temkin H and Panish M B 1991 *Appl. Phys. Lett.* **59** 443

3 Andrews D A, Rejman-Greene M A Z, Wakefield B and Davies G J 1988 *Appl. Phys. Lett.* **53** 97

4 Kayser O 1991 *J. Crystal Growth* **107** 989

5 Murata M, Katsuyama T and Hayashi H 1990 *Proc. 17th Int. Symposium on Gallium Arsenide and Related Compounds* ed Singer K E (Bristol: IOP Publishing) 181

6 Finders J, Geurts J, Kohl A, Weyers M, Opitz B, Kayser O, and Balk P 1991 *J. Crystal Growth* **107** 151

7 Bhat R 1992 *J. Crystal Growth* **120** 362

8 Chang J, Carey K, Turner J and Hodge L 1989 *J. Electronic Materials* **19** 345

9 Colas E, Shahar A, Soole B D, Tomlinson W J, Hayes J R, Caneau C and Bhat R 1991 *J. Crystal Growth* **107** 226

10 Joyner C H, Chandrasekhar S, Sulhoff J W and Dentai A G 1992 *IEEE Photon. Technol. Lett.* **4** 1006

11 Aoki M, Suzuki M, Takahashi M, Sano H, Ido T, Kawano T and Takai A 1992 *Electron. Lett.* **28** 1157

12 Kato T, Sasaki T, Komatsu K and Mito I 1992 *Electron. Lett.* **28** 153

13 Thrush E J, Gibbon M A, Stagg J P, Cureton C G, Jones C J, Mallard R E, Norman A G and Booker G R 1992 *Paper TuF5 at Sixth International*

Conference on Metalorganic Vapour Phase Epitaxy 1992 To be published in J. Crystal Growth

14 Thrush E J, Cureton C G, Trigg J M, Stagg J P and Butler B R 1987 *Chemtronics* **2** 62

15 Stringfellow G B 1989 *Organometallic Vapour Phase Epitaxy: Theory and Practice* (London: Academic Press)

16 Leys M R 1987 *Chemtronics* **2** 156

17 Pritchard R E, Collis N C, Hamilton B, Thompson J, Carr N and Wood A K 1992, *Semiconductor Science and Technology*, 1993, **8**, pp.1166-1172

18 Caneau C, Bhat R, Frei M R, Chang C C, Deri R J and Koza M A 1992 *Paper TuF4 at Sixth International Conference on Metalorganic Vapour Phase Epitaxy 1992 To be published in J. Crystal Growth*

19 Galeuchet Y D, Roentgen P and Graf V 1990 *J. Appl Phys.* **68** 560

20 Galeuchet Y D and Roentgen P 1991 *J. Crystal Growth* **107** 147

21 Colas E, Clausen E M, Kapon E, Hwang D M and Simhony S 1990 *Appl. Phys. Lett.* **57** 2472

22 Kayser O, Westphalen R, Opitz B and Balk P 1990 *J. Crystal Growth* **112** 111

23 Garret B and Thrush E J 1989 *J. Crystal Growth* **97** 273

24 Colas E, Clausen E M, Kapon E, Hwang D M and Simhony S 1990 *Appl. Phys. Lett.* **57** 2472

25 Jenson K F, Fotiadis D I and Mountziaris T J 1991 *J. Crystal Growth* **107** 1

26 Van de Ven J, Rutten G M J, Raaijmakers M J and Giling L J 1986 *J. Crystal Growth* **76** 352

[27] Coronell D G and Jenson K F 1991 *J. Crystal Growth* **114** 581

[28] Present R D 1958 *Kinetic Theory of Gases* (McGraw-Hill), p20,149

Chapter 8

The Component Parts of an Integrated Laser-Modulator

8.1. INTRODUCTION

It is difficult to develop a satisfactory integrated device if one is not already confident in one's ability to fabricate its component parts. Consequently a sound knowledge of lasers and modulators is an almost essential prerequisite to laser modulator integration. In addition, the structure[1] that one chooses for an integrated device is heavily influenced by the history of one's own laboratory. The reason is that one's chances of success depend on the skills and past experience of the fabrication team. It is for this reason that I designed a laser-modulator with a ridge waveguide structure and a phase shifted laser grating. In the interests of brevity, I have not attempted to review the development of such lasers by my colleagues at BNR Europe. However in this chapter I have briefly summarised the aspects of these devices which are relevant to the integration of lasers and modulators. The principles of modulator operation are summarised in more detail.

8.2. THE DFB LASER AT BNR EUROPE

A schematic of a typical distributed feedback (DFB) laser currently fabricated at BNR Europe[2,3,4] is shown in Figure 8.1. The laser is based on a ridge waveguide[1] which is aligned to the [0 1 1] crystal direction. The threshold currents of ridge lasers are usually higher than those of their buried heterostructure equivalents[1]. However ridge lasers are inherently more reliable[5,6] than buried heterostructure devices, as one does not have to etch through the active layer. In addition, there are fewer epitaxial stages in the ridge laser fabrication process, and epitaxy over severely structured surfaces is not required[1]. The simpler fabrication process of ridge devices is helpful when one is adding the complications of an integration procedure.

Both facets of the BNR Europe DFB laser are anti-reflection coated. The required feedback for laser operation is provided by means of a grating with two $\lambda/8$ phase shifts. The grating is written into the top of the laser waveguide by electron beam lithography[7]. The $2x\lambda/8$ structure was originally developed

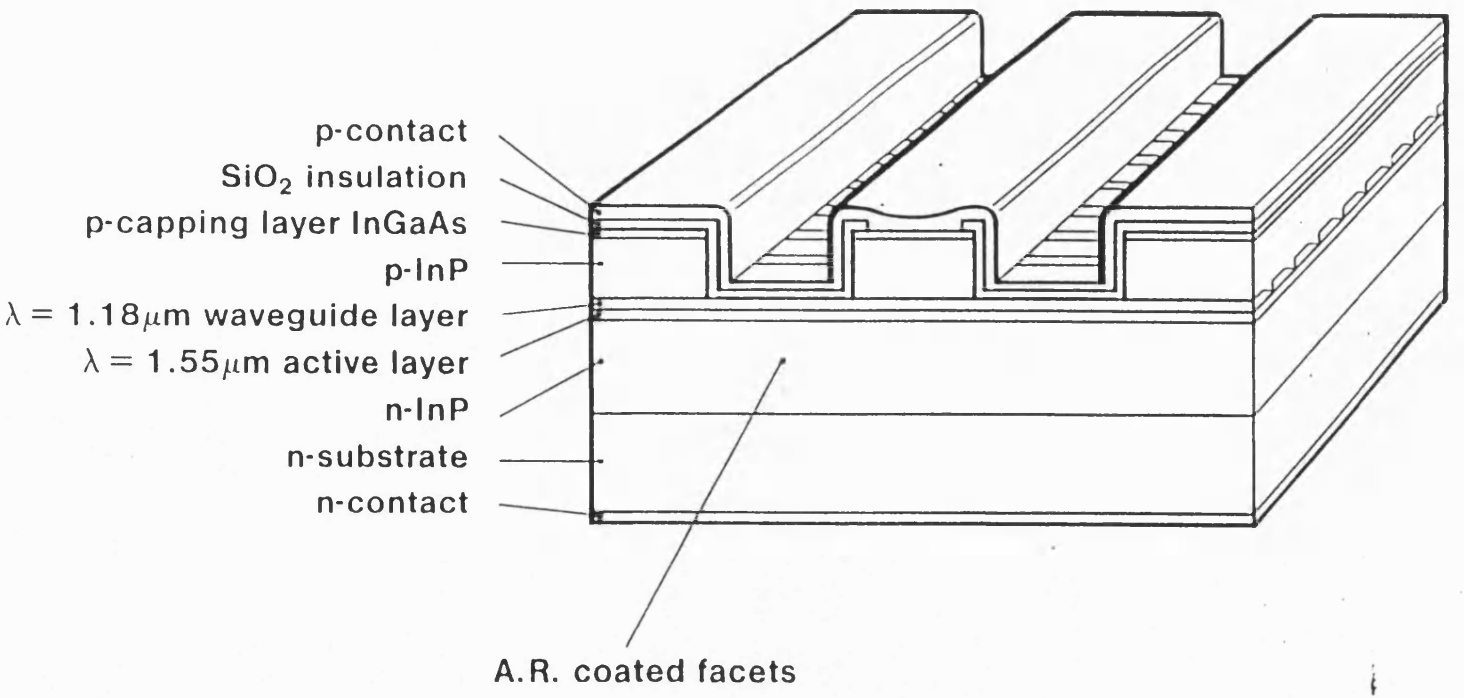

Fig 8.1 The DFB laser at BNR Europe

to combat the laser chirp seen in $\lambda/4$ phase shifted devices under high frequency modulation[8]. The chirp performance of the former lasers is superior because they have a more uniform distribution of optical power along the laser cavity. Consequently the amount of longitudinal spatial hole burning[9] is reduced[8]. The $2x\lambda/8$ device is also more suitable for use as a d.c. source as the reduced amount of hole burning means that it is less likely to mode hop as the operating current is increased. This fact makes it the more appropriate device for integration with a modulator.

The fabrication process for our DFB laser is illustrated in Figure 8.2. It is also described in the following text. The sections in italics indicate the objective of the process step in which they are placed.

8.2.1. DFB Laser Fabrication Procedure

a) Grow appropriate active and waveguiding layers on an n doped InP substrate[10,11].
b) Spin resist onto the substructure grown in a) and write gratings by means of electron beam lithography[7]. Transfer the gratings into the waveguide by wet etching. Remove the resist.
c) Overgrow the substructure with p-InP and p^+-GaInAs.
d) Deposit silicon dioxide[12,13] on the wafer. Pattern the oxide layer[14,15,16] so that only one edge of the wafer is exposed.
e) Remove the p type layers from the edge of wafer by selective wet etching[17,18,19] so that the gratings are left exposed in this region. Remove the oxide.
f) Deposit silicon dioxide again. Pattern the oxide with the ridge mask. The mask is aligned to the grating patches exposed in step e).
g) Remove the p type layers in the exposed regions of the wafer by selective wet etching. Remove the oxide. *This step creates the two channels on either side of each laser ridge shown in Figure 8.2.*
h) Deposit silicon dioxide and pattern it with the contact window mask so that only the top of the ridge is left exposed. *This step ensures that current will be injected into the ridge rather than the rest of the chip.*
i) Deposit Ti, Pt and Au on top of the wafer by electron beam evaporation[20,21].
j) Remove InP from the back surface of the wafer[22] until it is 100μm thick.
k) Deposit Au and Sn on the back surface of the wafer by thermal evaporation and alloy the metals by heating[23].
l) Cleave the wafer into bars

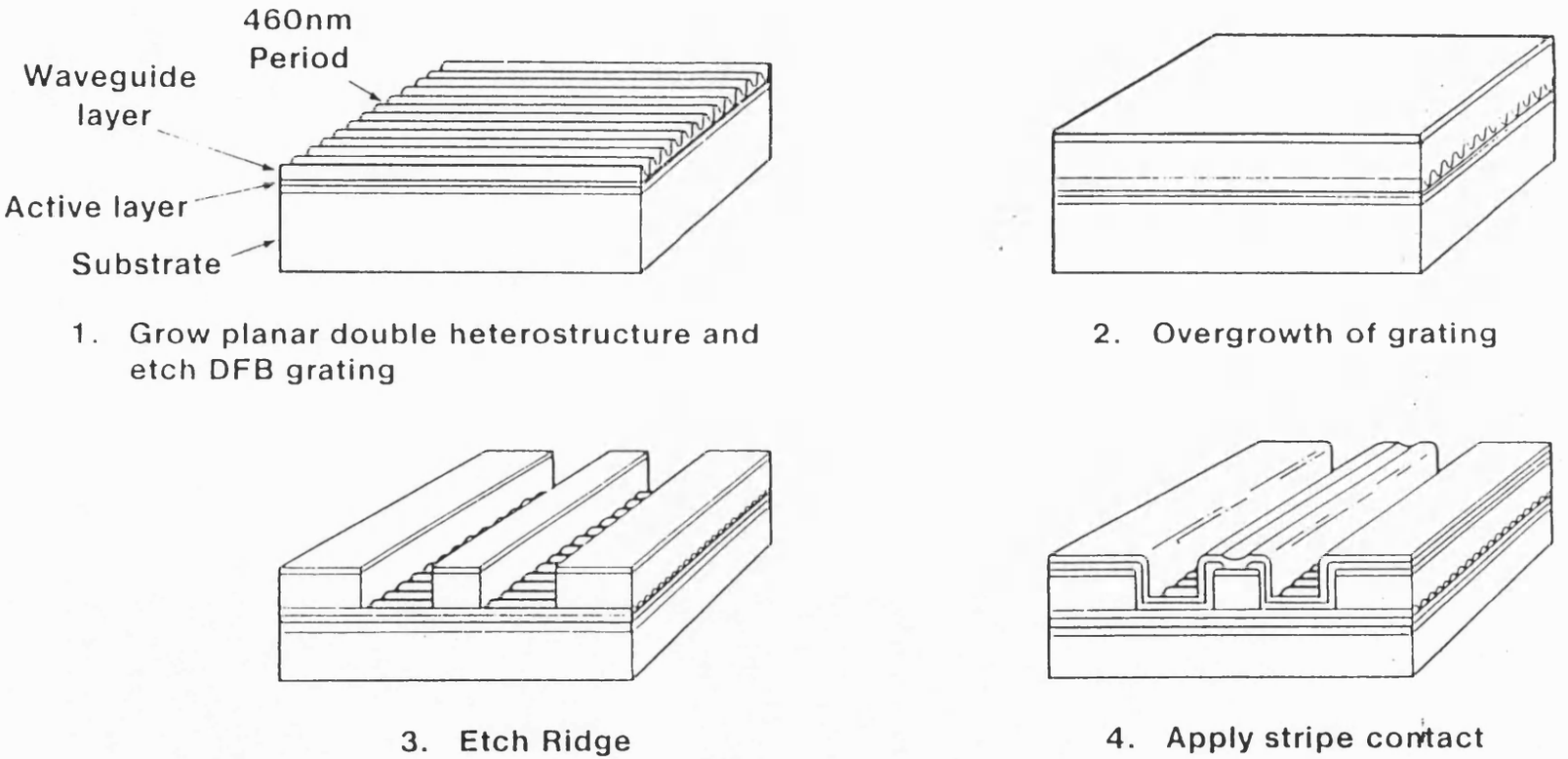

Fig 8.2 The fabrication process for a DFB laser at BNR Europe

m) Anti-reflection coat both facets of each bar by electron beam evaporation of a layer of TiO_2 followed by a layer of SiO_2[24].

n) Dice the bars into chips. Test the chips under low duty cycle pulsed conditions. *The low duty cycle prevents excessive heating of the devices.*

o) Bond the devices on gold coated copper heat sinks.

8.3. THE ELECTROABSORPTION MODULATOR

As mentioned in chapter 1 the reason for using an external modulator, rather than modulating the drive current to a laser, is to reduce chirp. An external modulator is effective in reducing chirp because in such a set-up the laser is driven under dc conditions. This means that there are no fluctuations in laser carrier concentration and hence the effective index of the laser waveguide does not change with time. Consequently the laser operating wavelength, which is determined by the product of the grating pitch and the effective index of the laser waveguide, remains constant.

One should note, however, that external modulators can also cause chirp if the refractive index of the active modulator material changes at the same time as the absorption coefficient. The Kramers-Kronig relationships[25,26] indicate that such index changes are almost inevitable, though the effects of such changes can be minimised by clever modulator design[27]. A small amount of negative chirp[28,29] is actually advantageous in high capacity links over dispersive fibre as it works with the fibre dispersion to cause pulse compression.

The desirable features of a modulator destined for use as a transmitter in a digital communication link can be summarised as follows. The extinction of the device should sufficiently large (~13dB) so that it causes a negligible penalty to the system sensitivity. This extinction should be achieved with a moderate drive voltage (~2V) so that impractical demands are not placed on the high frequency electronic drive circuit. The modulator chirp should be tailored to the fibre deployed in the system and the insertion loss of the modulator should be as low as possible.

In the interests of brevity, I have not reviewed merits and drawbacks of the different types of modulator which can be used for digital transmission. Details of the behaviour and fabrication of these different devices can be found in the references[27,30,31,32,33,34,35,36]. However it is worth briefly describing the operation and design of the modulator which was used in our integrated

device. This modulator operated using a phenomenon known as the quantum confined Stark effect (QCSE)[37,38]. The phenomenon is illustrated in Figure 8.3 and can be briefly described as follows.

The position of an electron or hole in a known energy state in a typical quantum well cannot be precisely determined, as this would defy the Heisenberg uncertainty principle[39]. The electrons and holes spend some of their time in the barriers with a probability distribution that can be determined from the Schrodinger equation[39]. The apparent bandgap of the QW is somewhere between that of the well and the barrier and can also be determined from the Schrodinger equation.

If an electric field is applied to the quantum well the electron and hole gain or loose potential energy as they travel in the direction of the field. This can be represented by tilting the bands as shown in Figure 8.3. Under these circumstances the Schrodinger equation indicates that the electron and the hole, when in their ground states, both move to minimise their potential energies. Such behaviour is consistent with the correspondence principle[39]. However, the electron and hole have opposite charges and consequently their probability distributions move to opposite sides of the well. The movement of the probability distributions has two major effects[34]:

a) the overlap between the electron and hole ground state wave functions decreases.
b) the bandgap decreases as the electron and hole states have both moved to lower their energy.

The latter change can be used to modulate light if the operating wavelength is positioned so that the quantum well material is transparent when no field is applied, and opaque when a field is applied. The change in absorption coefficient related to the movement of the bandgap occurs very rapidly, as it only depends on a rearrangement of the energy eigenstates of the QW. Consequently this is an appropriate operating mechanism for high data rate modulators.

In reality the electron and the hole are not isolated from each other but are bound together by Coulomb attraction to form an exciton[38]. The binding energy of this exciton decreases as the electric field is applied. However it is relatively small and has little impact on the argument above.

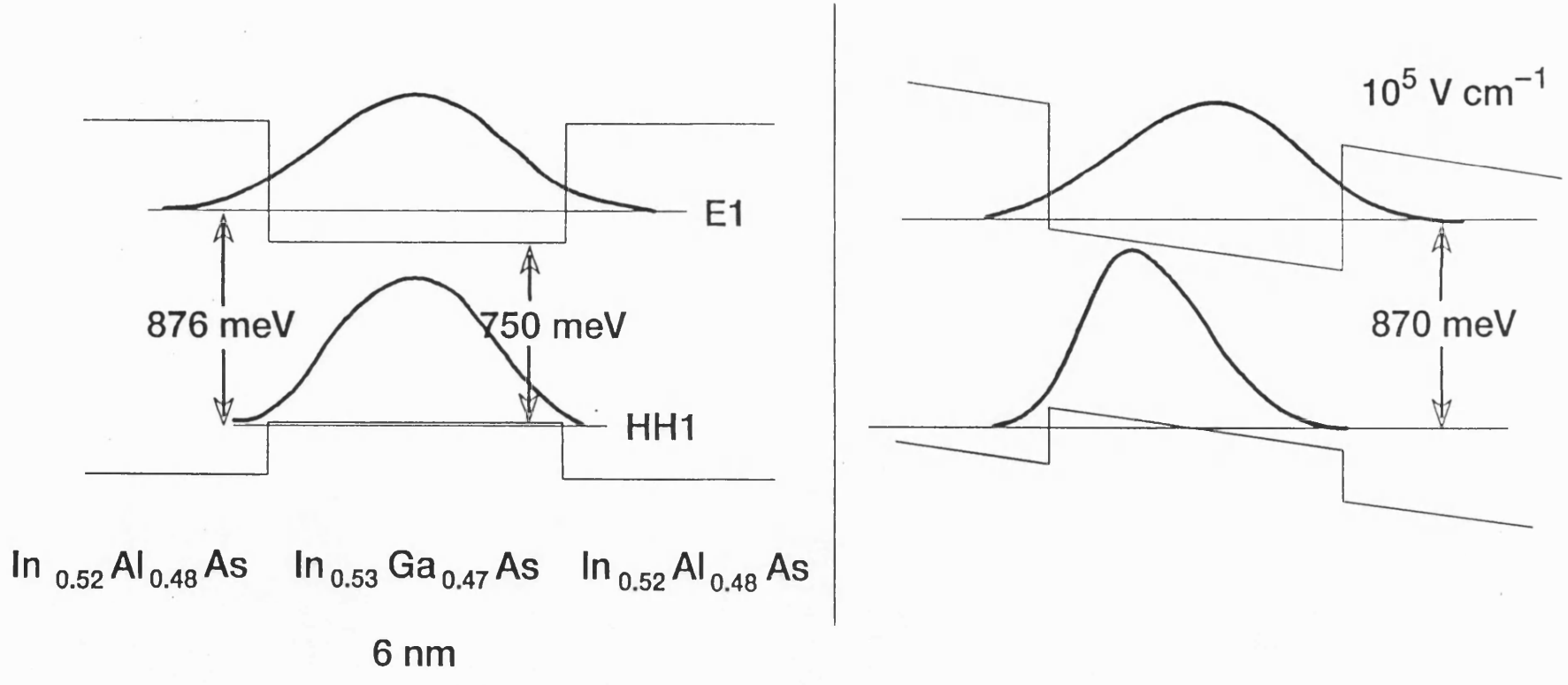

Fig 8.3 The Quantum Confined Stark Effect

The electric fields required for significant movement of the bandgap are large (~100kV/cm). Fortunately fields of this magnitude can be obtained with low drive voltages in a pn junction. An example of photocurrent spectra[40] taken from QWs fabricated in such a pn junction can be seen in Figure 8.4. The photocurrent generated in these measurements is proportional to the absorption coefficient in the quantum wells. The peak in the 0V trace of these measurements is the exciton. It can be seen from the figure that the exciton moves to a longer wavelength, and is reduced in intensity (owing to a smaller electron hole overlap) as a reverse bias is applied to the pn junction. This behaviour is consistent with the theory described above.

The quantum confined Stark effect can only be deployed if a practical device structure can be developed. Fortunately, the laser structure illustrated in Figure 8.1 is almost ideal vehicle for this task, as it can contain QWs in the centre of a pn junction. In addition, the vertical waveguide in the laser structure ensures that the overlap between the QWs and the optical mode is as large as possible. The fact that the laser and modulator structures can be so similar is very helpful when one is attempting to integrate the two devices together. Indeed, the major difference between the two devices is not the way in which they are fabricated, but the way in which they are driven: the laser is driven in forward bias with a current; the modulator is driven in reverse bias with a voltage.

The bandgap of the modulator quantum well active region depends on the polarisation of the input light, being smaller for the TE optical mode. This difference is caused by the fact that the TE mode interacts predominantly with the heavy hole band, while the TM mode interacts only with the light hole band[41,42]. In practice QCSE modulators are normally operated in the TE mode. This input polarisation must be maintained if the system is to operate in a satisfactory manner. Such control can be difficult to achieve in a system containing a discrete modulator, as the polarisation state obtained from a standard fibre varies with small changes in the environmental conditions[43]. Polarisation control is not a problem for an integrated device as, in this case, the input polarisation is determined by the fact that the laser and the modulator are on the same substrate.

In practice the maximum modulation rate of electroabsorption modulators is usually determined by their capacitance[34]. This speed limitation derives from the fact that the modulator is normally placed in a 50Ω circuit of the type

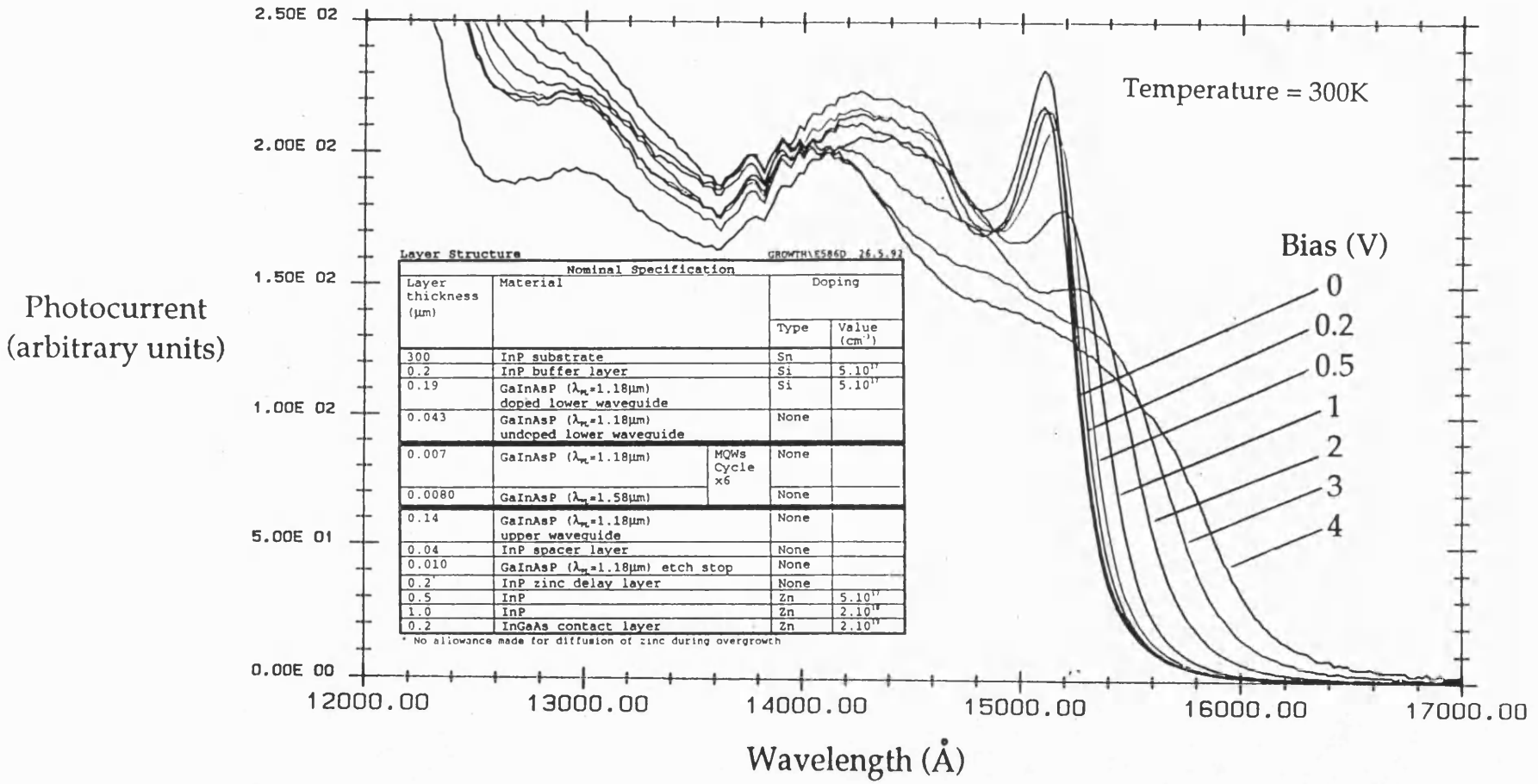

Fig 8.4 Photocurrent spectra from MQW material

shown in Figure 8.5. The 3dBe bandwidth of such a circuit occurs when the impedance of the modulator capacitance falls to 25Ω. To give an example; a 3dBe bandwidth of 10GHz will only be obtained when the modulators capacitance is reduced to a value of 0.64pF.

The modulator capacitance is normally composed of two parts: the capacitance of the pn junction; and the stray capacitance associated with the modulator contact. It is difficult to do much about the former capacitance without compromising the modulator performance. However size of the stray capacitance can be decreased by reducing the size of the modulator bond pad and by placing a thick dielectric layer underneath it.

The performance of QCSE modulators is very dependent on the difference between the input photon energy and the modulator bandgap. As the difference between these two energies decreases the following changes occur:

a) The absorption per unit length of the modulator increases at all values of applied bias (see Figure 8.4). In practice this usually means that a shorter modulator (which has a lower capacitance) is required to obtain a given extinction ratio.
b) The insertion loss of a modulator with a fixed extinction ratio increases (see Figure 8.4). This means that the device output power decreases.
c) The chirp parameter becomes less positive and eventually becomes slightly negative[44]. This enhances transmission over standard fibre.
d) The modulator eventually saturates when the absorption per unit length becomes so large that not all of the photo-generated carriers can be extracted.

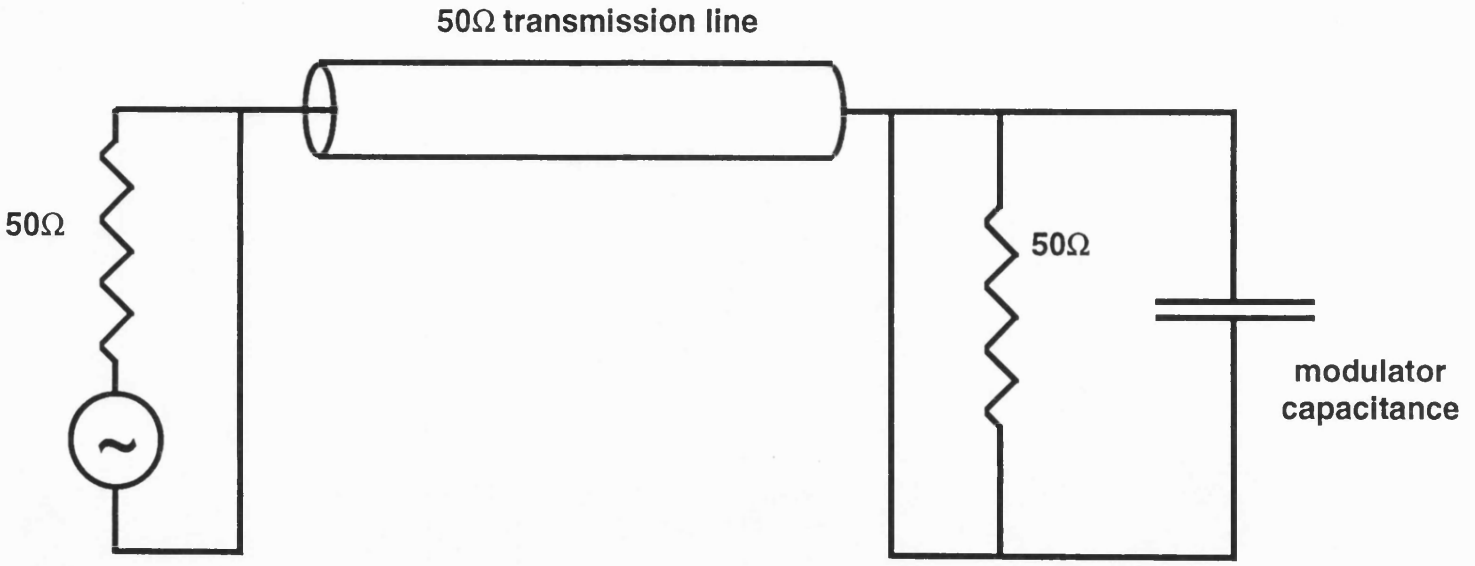

Fig 8.5 Typical modulator drive circuit

8.4. THE PERFORMANCE OF SELECTIVELY GROWN LASERS

The fact that modulators operate with an input photon energy which is smaller than their bandgap means that it is the laser part of an integrated laser-modulator which must be fabricated on selectively grown material. Such a device will only be successful if the lasing performance is not severely degraded by the selective epitaxy.

8.4.1. Fabry Perot Lasers

8.4.1.1. Device Performance

The effect of selective growth on laser performance was assessed by fabricating Fabry-Perot (FP) lasers on material grown in the 30μm gaps of the light field mask described in section 7.2. The layer structure (E256, Fig. 8.6a) contained 6 GaInAs quantum wells embedded in the centre of a GaInAsP waveguide. In unperturbed regions far away from any masks the total thickness of the waveguide layer was 0.38μm. The room temperature photoluminescence wavelength of the waveguide material was 1.18μm. The unperturbed photoluminescence emission wavelength of the QW stack was 1.502μm.

The selectively grown MQW substructure was processed into FP lasers by first removing the SiO_2 growth masks so that the wafer could be overgrown with p-InP and p^+GaInAs. The wafer was then fabricated into lasers using the process described in section 8.2. A schematic cross section of such a laser is shown in Figure 8.6.

The emission wavelengths and threshold currents of the selectively grown devices were measured under pulsed conditions. The results from these measurements were referenced to those from unperturbed control devices, which were interleaved with the selectively grown ones. The effect of the mask width on the laser threshold current and emission wavelength is shown in Figure 8.7 (data from wafer E256.C1091). In this case the emission wavelength was shifted from 1507 to 1626 nm without any measurable degradation in threshold performance. The lasing wavelength correlated reasonably well with earlier cathodoluminescence measurements though there was some deviation at wider mask widths.

The performance of selectively grown lasers was further assessed by making continuous wave (CW) measurements on FP devices from an identical wafer (C885.C942). Unfortunately it was not possible to derive a series of

Layer Structure GROWTH\C885.C942 22.1.91

Nominal Specification				
Layer thickness (μm)	Material		Doping	
			Type	Value (cm^{-3})
300	InP substrate		S	
0.2	InP buffer layer		Si	5.10^{17}
0.142	GaInAsP (λ_{PL}=1.18μm) lower waveguide		None	
0.008	GaInAsP (λ_{PL}=1.18μm) barrier	MQWs Cycle x6	None	
0.006	GaInAs well		None	
0.15	GaInAsP (λ_{PL}=1.18μm) upper waveguide		None	
0.5	InP		Zn	5.10^{17}
1.0	InP		Zn	2.10^{18}
0.2	InGaAs contact layer		Zn	2.10^{19}

Fig 8.6a Unperturbed layer structures of wafers C885.C942 and E256.C1091

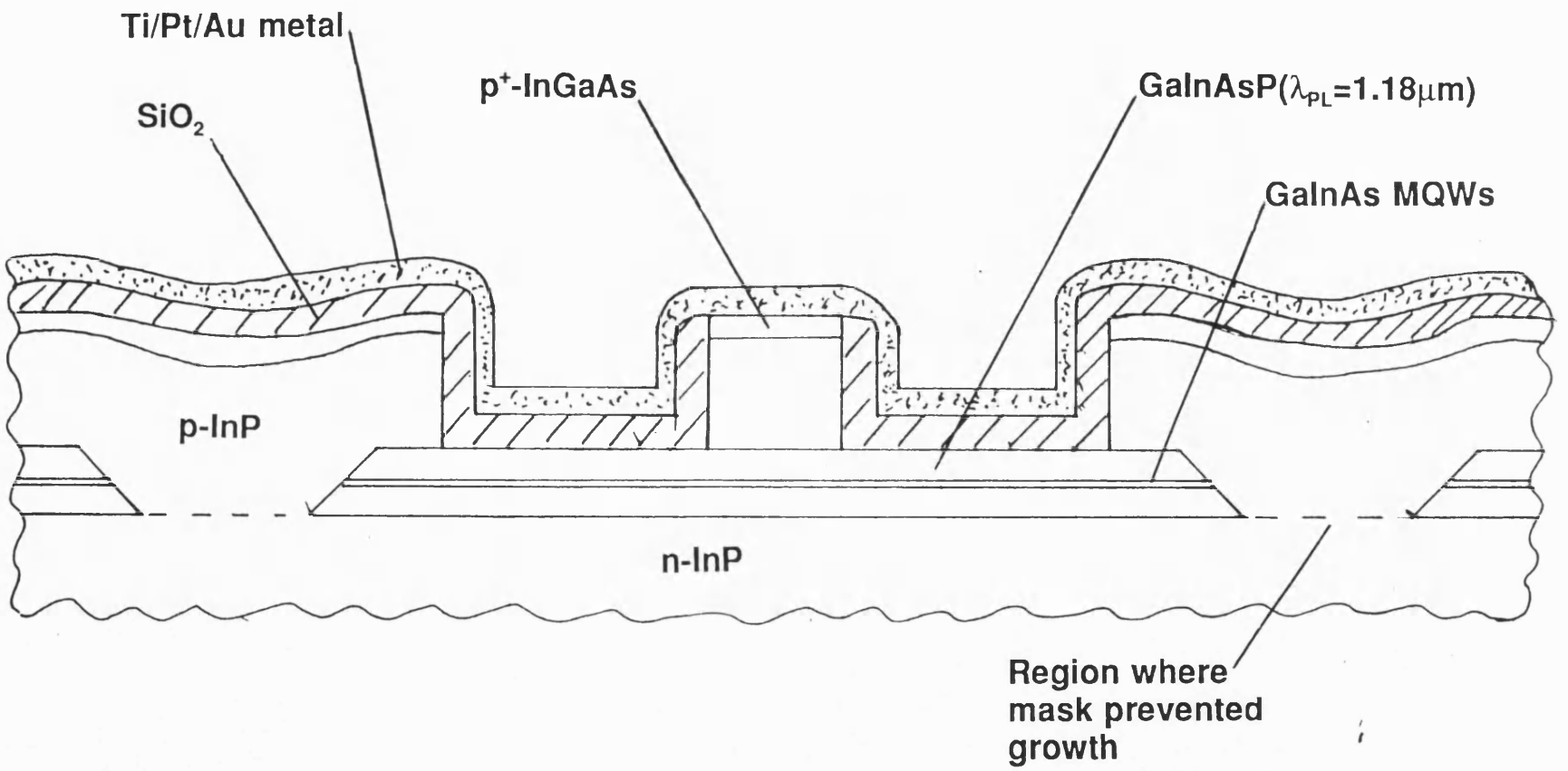

Fig 8.6 Cross section through selectively grown laser

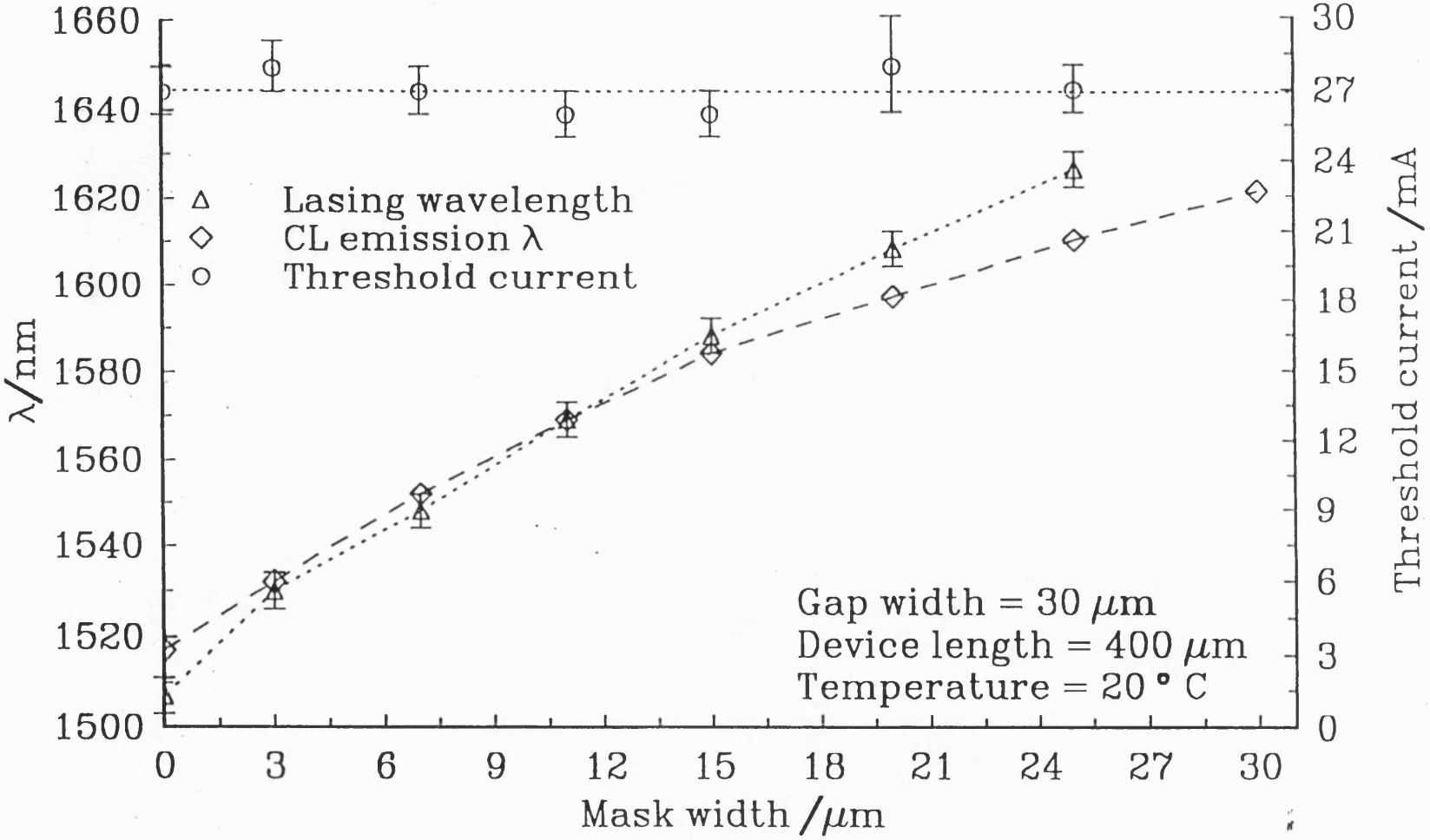

Fig 8.7 Effect of selective growth on laser threshold current

measurements of the type shown in Figure 8.7 from this material, owing to a contamination problem. However, in the unaffected areas, the threshold currents of perturbed and control devices were identical to within the error in the measurement. Light current characteristics from a control device, and one in which the active region was grown in a 30μm gap between two 20μm wide masks, are shown in Figures 8.8 and 8.9 respectively. These light current characteristics are similar in spite of the fact that the emission wavelength was shifted by about 70nm. The corresponding spectra are shown in Figures 8.10 and 8.11.

8.4.1.2. Interface Coupling Loss

The optical waveguide between a selectively grown laser and an electroabsorption modulator tapers in thickness, as the bandgap required for one component slowly changes to that required for the other. This tapered waveguide must be electrically pumped for at least some of its length, as laser active material is lossy when no drive current is supplied.

The losses of such tapered and pumped waveguides were investigated by cleaving the interface regions between perturbed and control devices out of one of the above wafers (E256.C1091). These devices were essentially 700μm long Fabry-Perot lasers. The laser ridges were fabricated on material grown between pairs of silica masks for 650μm of this device length, as shown in Figure 8.12. The tapered transition region extended about 40μm on either side of the end of this region. The separation between the above silica masks was held constant at 30μm. However the width of these masks was varied from 3 to 30μm, thus enabling investigation of tapers of progressively increasing severity.

The loss of the tapered waveguides was determined by measuring the threshold currents of the FP devices under pulsed conditions. The mean threshold current of all the devices was (26.7±0.8)mA. There was no correlation between the width of the selective growth mask and the device threshold current. This indicated that the loss of the tapered regions did not depend on the severity of the taper, for the range of tapers investigated. However, it did not prove that the loss of any tapered region was insignificant. The reason was that the above threshold measurements could not be compared with those of 700μm long control devices, as it was impossible to cleave such devices out of the wafer.

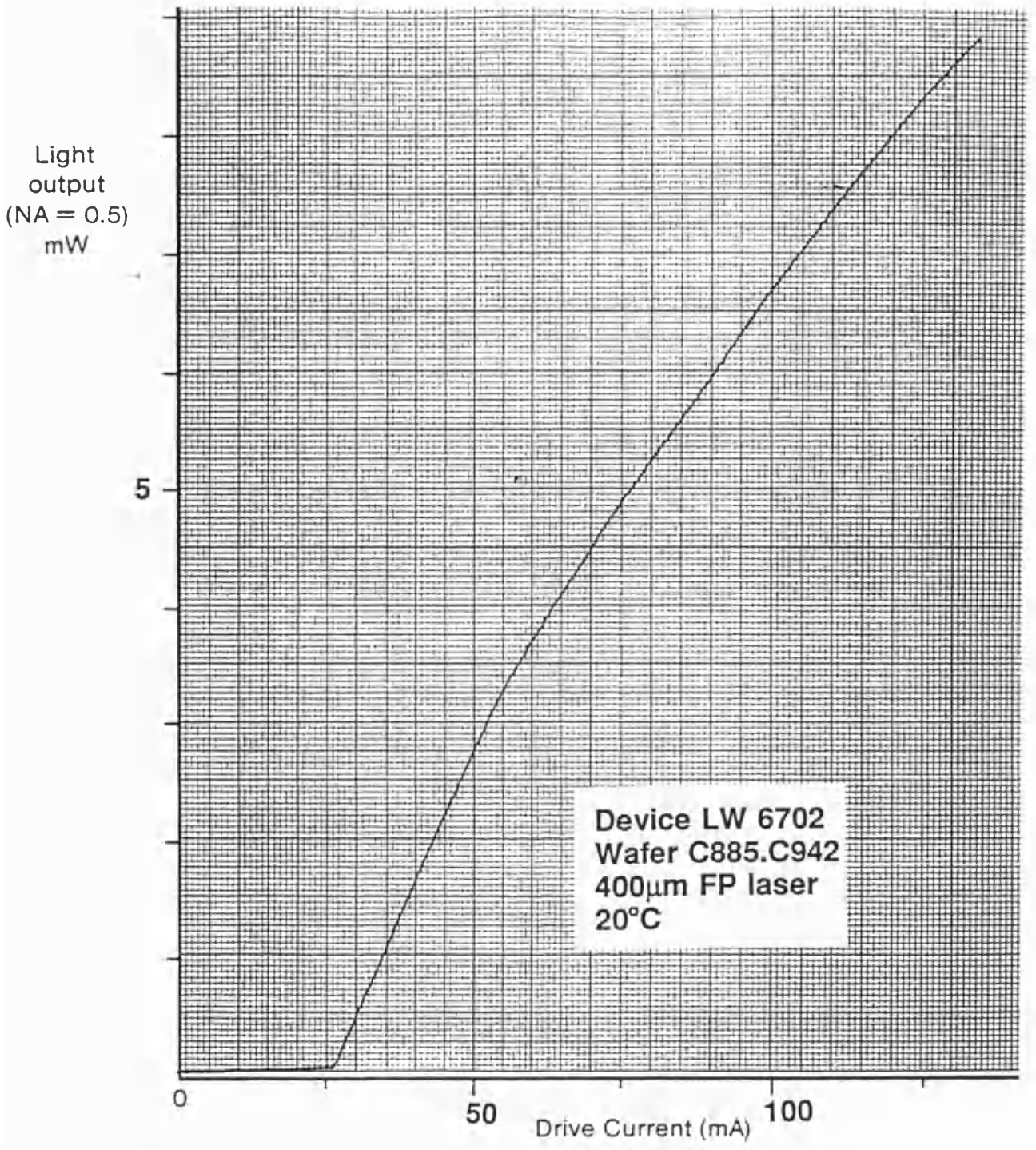

Fig 8.8 **Light current characteristic from control device**

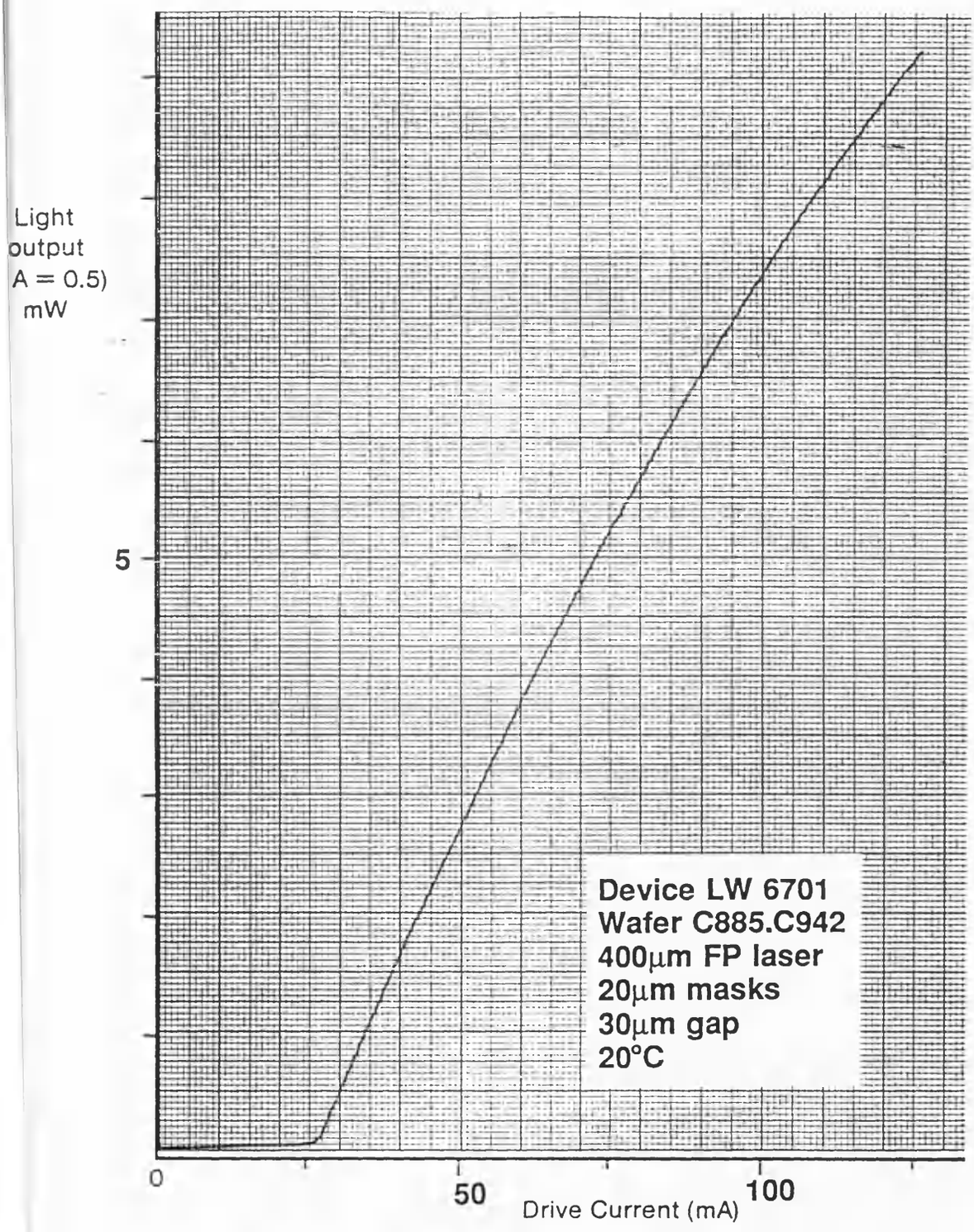

Fig 8.9 **Light current characteristic from selectively grown device**

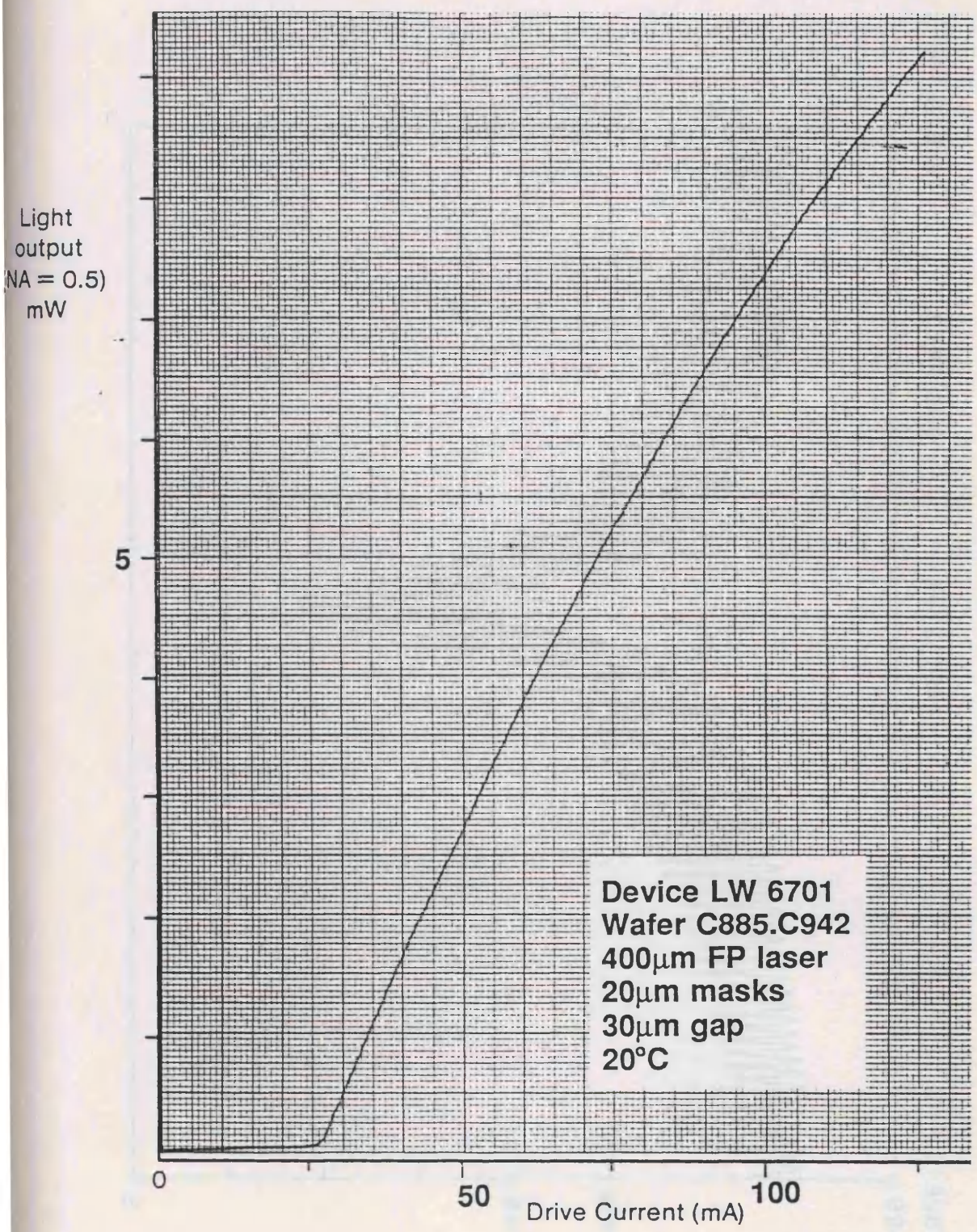

Fig 8.9 Light current characteristic from selectively grown device

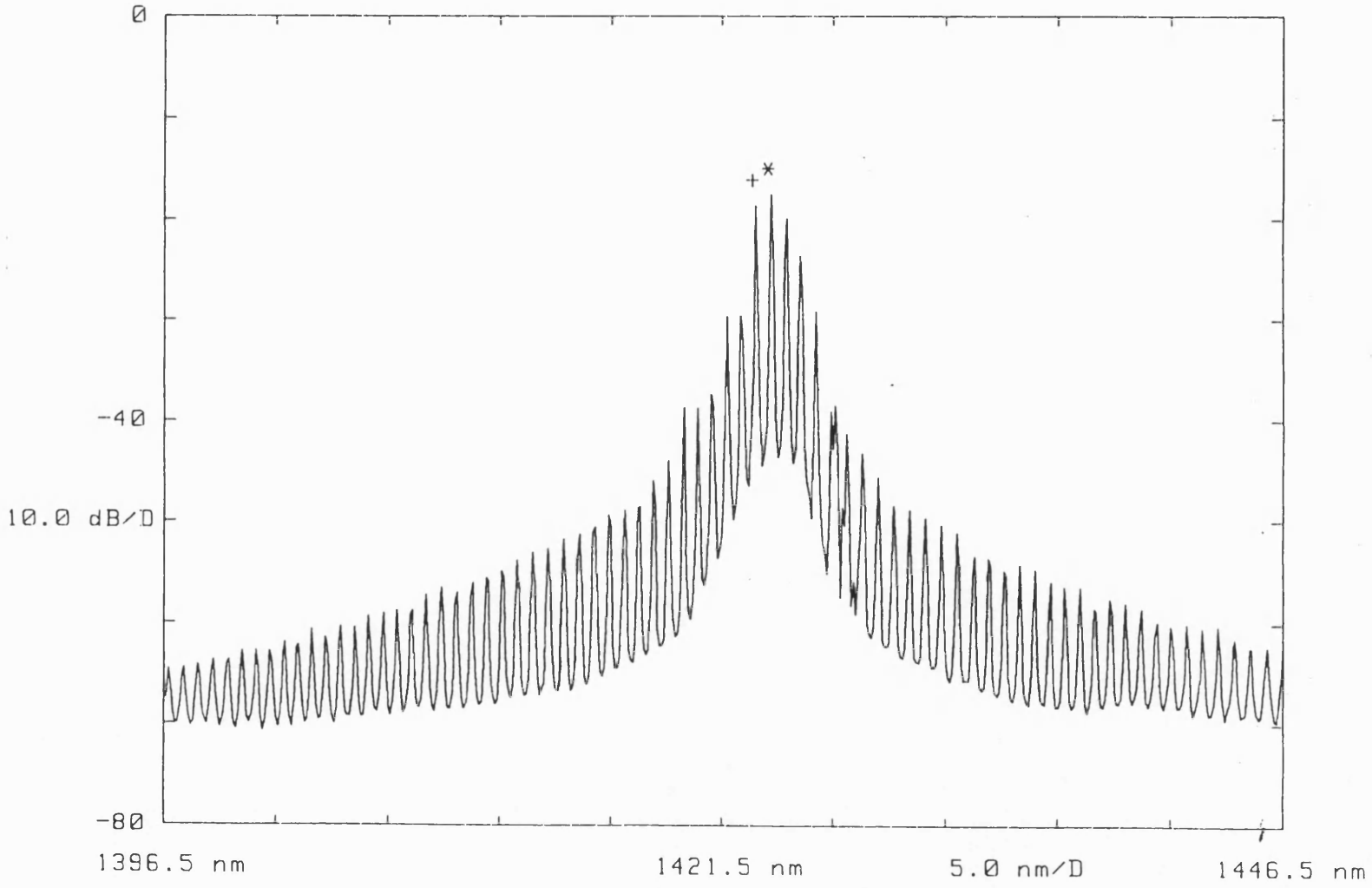

Fig 8.10 Spectrum from control device

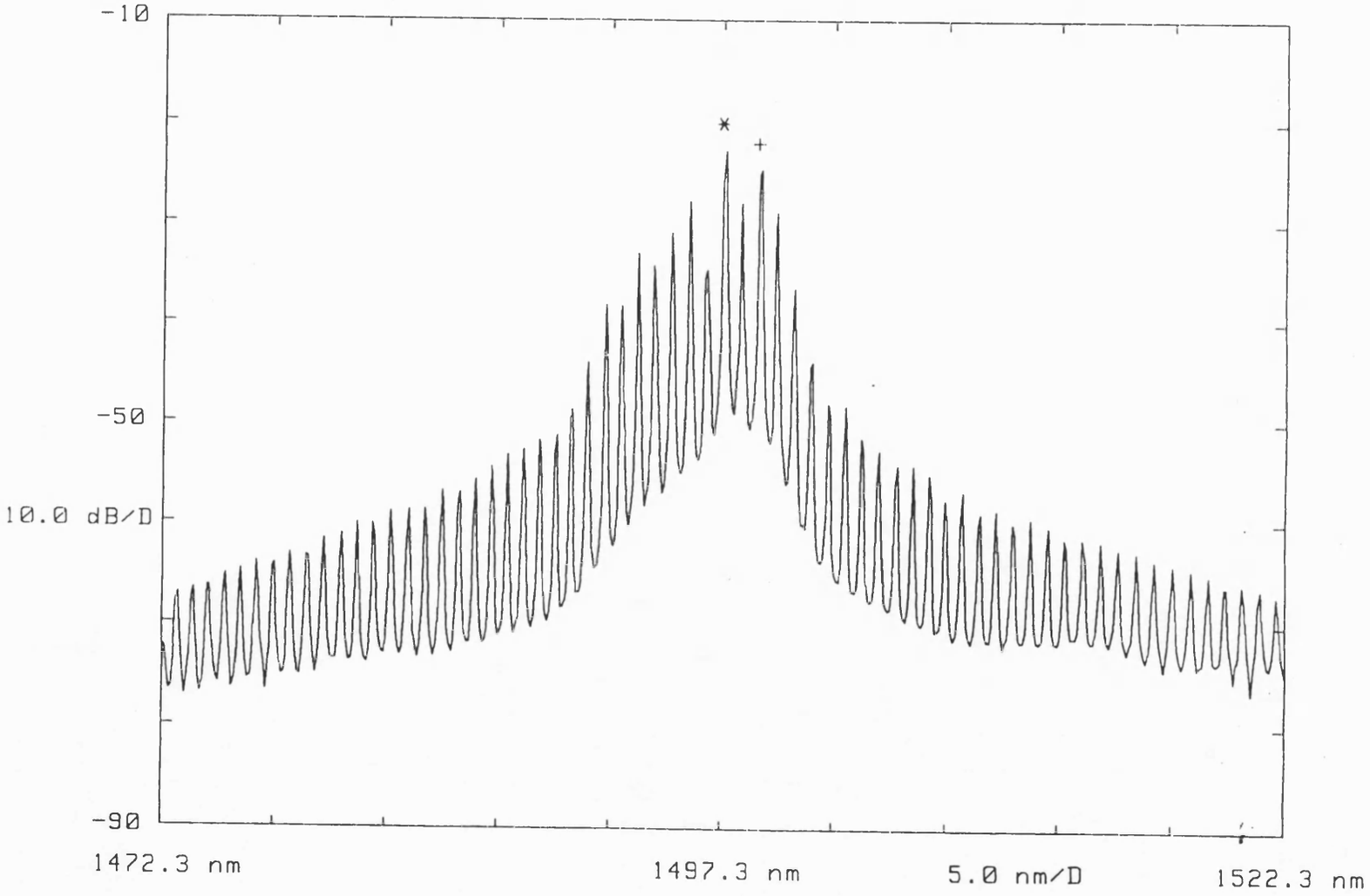

Fig 8.11 Spectrum from selectively grown device

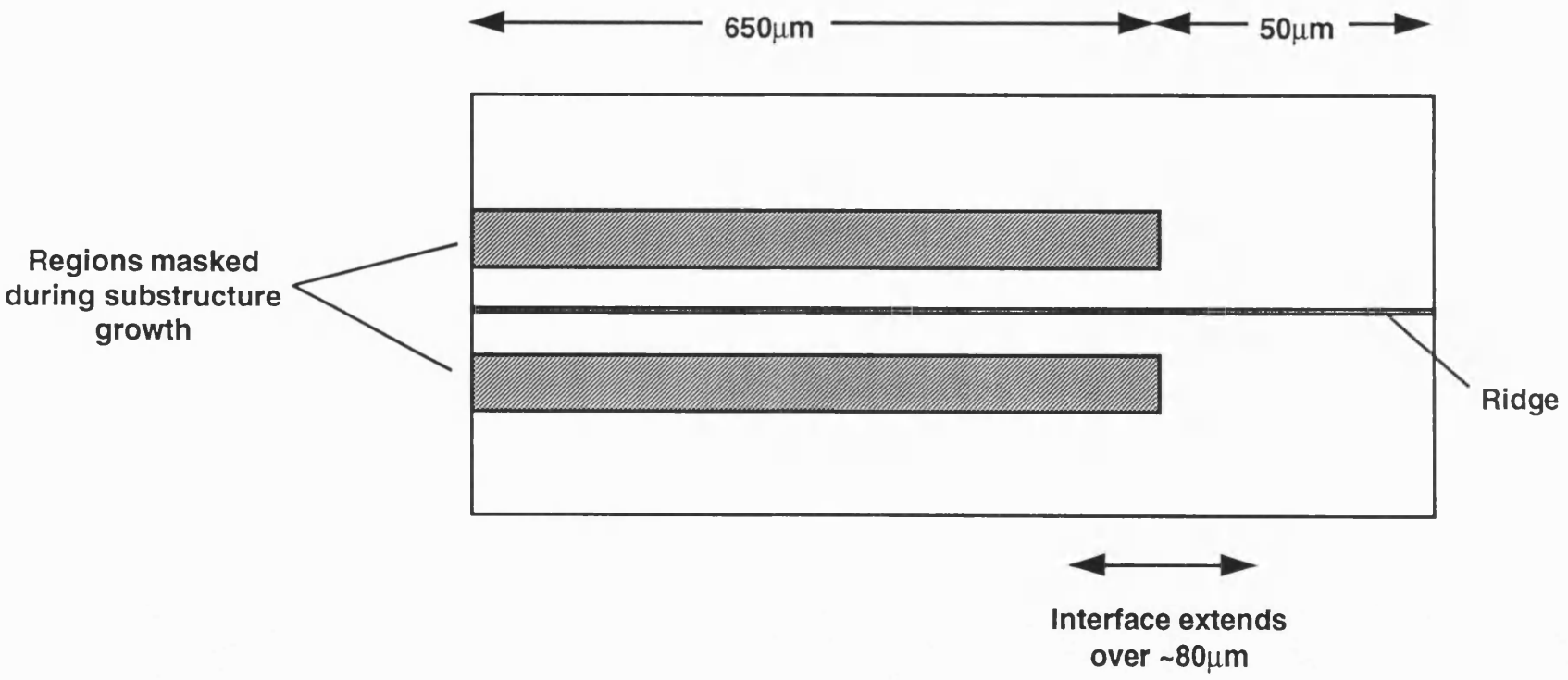

Fig 8.12 FP device for taper loss measurements

The loss of the tapered waveguides was eventually determined by comparing the above threshold currents with those from 400μm long FP lasers cleaved out of the same wafer. The latter devices did not contain any regions in which the quantum well bandgap was perturbed via selective area epitaxy. The mean threshold current of the 400μm long lasers was (32.8±0.8mA).

The devices of different length were compared by making use of the fact that the gain coefficient per well g_W in our quantum well material has been found to be related to the current density by the equation[45]

$$g_w = g_0\left(1+\ln\left(\frac{J_w}{J_0}\right)\right)$$

where J_0 is a constant related to the threshold current density of the material, J_W is the current density per well and g_0 is (6.8±0.7)cm^{-1}. If the short and long devices described above have threshold current densities of J_{W1} and J_{W2} respectively, then the difference between the gains within these devices ΔG is given by

$$\Delta G = G_1 - G_2 = ng_0 \ln\left(\frac{J_{w1}}{J_{w2}}\right)$$

where n is the number of quantum wells. The value of ΔG for the two sets of devices described above was (14.4±2)cm^{-1}.

The loss of the waveguide taper can be determined by noting that the round trip gain in both laser cavities must be unity[46], and hence, for example, in the 700μm long device.

$$10^{-\left(\frac{\Gamma}{10}\right)}.R.e^{G_2L_2} = 1$$

R is the power reflection coefficient of the laser facet and Γ is the loss of the taper in decibels. L_2 is the length of the active region in the 700μm long device. This equation can be expressed in terms of ΔG by substitution of the round trip gain condition for the shorter device. One then finds that the loss of the tapered region is given by

$$\Gamma = \frac{10}{\ln 10}\left[\ln\left(\frac{1}{R}\right)\left(\frac{L_2}{L_1}-1\right)-\Delta G L_2\right]$$

The length L_1 of the active region of the shorter device was obviously 400μm. The length L_2 of the active region of the longer device was not so obvious as it contained a transition region in which the bandgap changed. However, the threshold current of these devices was not dependent on the severity of the waveguide taper. Consequently it seemed reasonable to assume that these devices lased at wavelengths where gain was generated along the entire 700μm cavity. (If this was not true the value derived for the loss is an upper limit on

that loss.) Substituting these numbers and a facet reflectivity of 0.30 into the above equation one finds that the loss Γ is given by

$$\Gamma = (-0.4 \pm 0.6)\text{dB}$$

This means that the loss of the waveguide taper is unlikely to be greater than 0.2dB.

8.4.2. DFB Lasers

The performance of selectively grown DFB lasers was assessed by fabricating DFB devices on wafer E256. The fabrication procedure was identical to that described for the FP devices, except for the fact that gratings were written on the selectively grown material before it was overgrown. The wafer was cleaved so that the 500μm long devices included the transition region between the perturbed and unperturbed material. A schematic plan view of the chips is shown in Figure 8.13. The $2x\lambda/8$ phase shifted grating was 350μm long and was fabricated on material grown in a 30μm gap between a pair of silica masks. The widths of the masks on either side of this gap were varied from 3 to 20μm in different devices. The selective growth masks extended 50μm beyond the ends of the grating regions, thus ensuring that the grating was not fabricated on a waveguide of changing thickness and hence effective index. The grating pitches were adjusted so that each laser operated close to the gain peak (i.e. the changes in waveguide thickness and QW bandgap as a result of selective growth were taken into account). Both facets were AR coated. The grating and the planar regions were pumped through the same contact.

The devices were assessed by bonding them onto gold coated copper mounts so that their CW power output and spectral characteristics could be measured, from both the planar and the grating ends. The results are summarised in the following table.

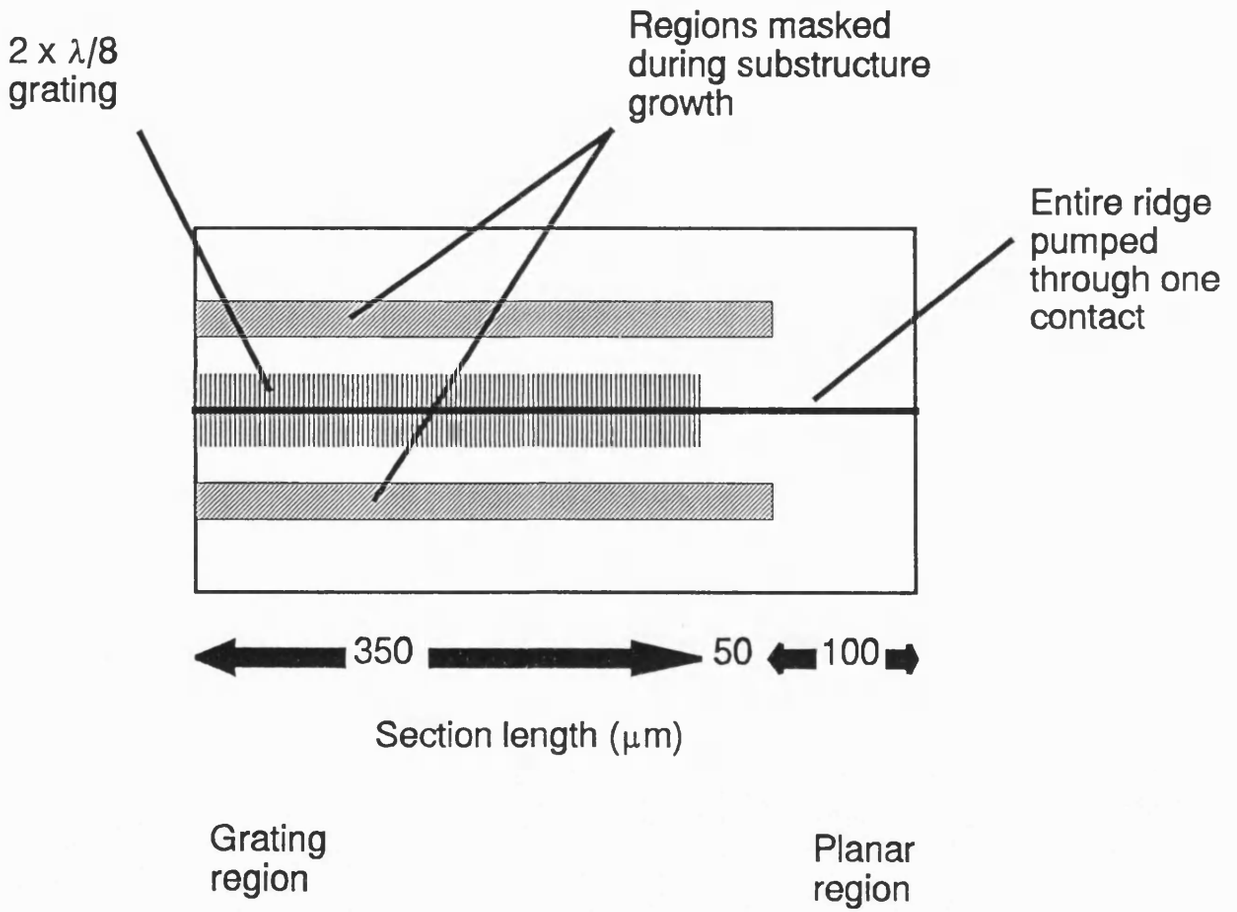

Fig 8.13 Plan view of DFB laser with selective epitaxy transition

Table 8.1 Performance of Selectively Grown DFB Lasers

Mount	Mask width (μm)	Threshold (mA)	ΔI_5* (mA)			λ (nm)		Offset from gain peak (nm). -ve if $\lambda_{lase}<\lambda_{gain}$	
			Grating end (g)	Planar end (p)	Ratio p/g	Target	Actual	Target	Actual
DF948	3	23	106	41.5	0.39	1513	1509	0	+18
DF949	7	32	89	60	0.67	1553	1550	+20	+51
DF950	11	30	87	41	0.47	1530	1528	-20	0
DF951	15	27	73	61	0.81	1565	1563	0	+18
DF952	20	30	N/A	86	N/A	1598	N/A	+20	N/A

* Current above threshold required for 5mW power output

The spectral measurements were made by coupling the outputs from the devices into a double grating monochromator. These measurements indicated that all the devices lased in a single longitudinal mode with a side mode suppression greater than 45dB at the maximum drive current of 150mA. The position of the gain peak was determined by measuring the peak in the spontaneous emission spectrum from the grating end of each device.

The optical power measurements were made into a numerical aperture of 0.5. Typical light current characteristics from devices with mask widths of 3 and 15 μm are shown in Figures 8.14 and 8.15 respectively. In all of these measurements more light was collected from the planar end than the grating end. However, the ratio of the power collected from the planar end to that from the grating end tended to decrease as the mask width increased. These observations were consistent with the fact that the planar region was acting as an amplifier. The gain of this amplifier decreased as the mask width, and hence the bandgap change across the transition, was increased. The higher power output from the planar ends of all the devices was consistent with the low transition loss calculated in section 8.4.1.2.

The above results indicated that the fabrication of DFB lasers on selectively grown material was a viable proposition. The next chapter describes how such selectively grown DFB lasers were integrated with electroabsorption modulators.

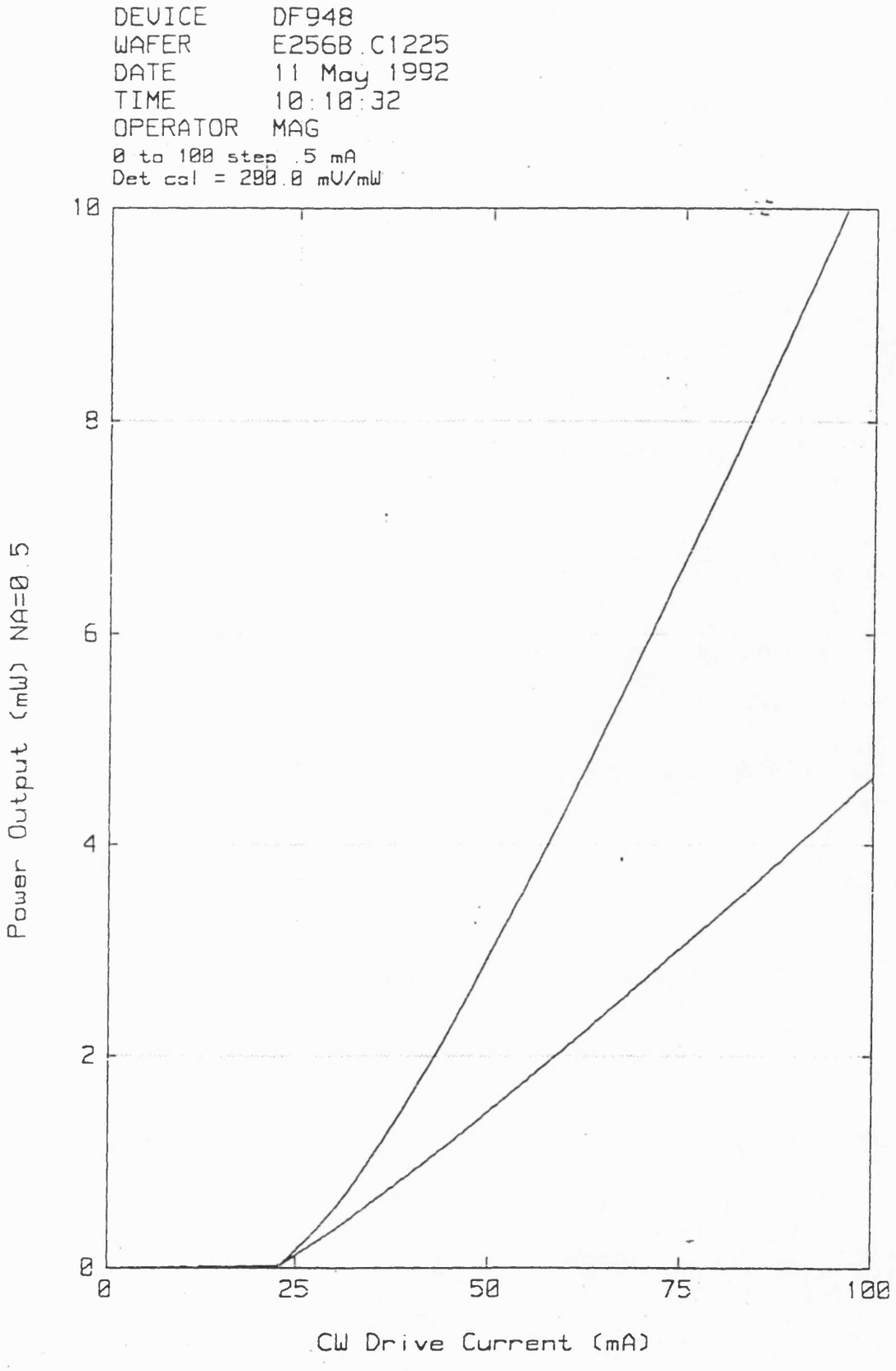

Fig 8.14 Light current characteristics from device with 3μm selective growth masks

(Higher power output is from planar end)

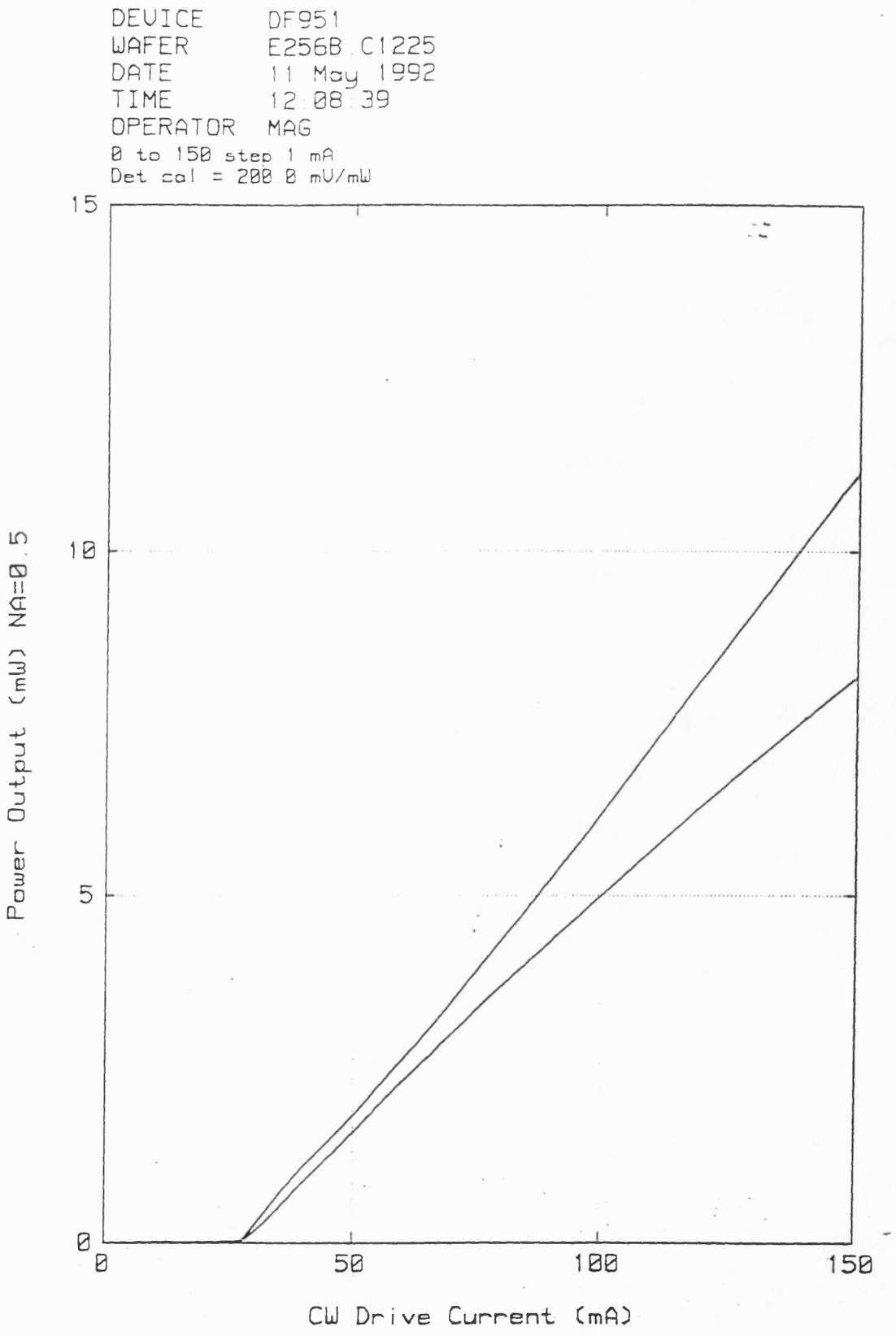

Fig 8.15 Light current characteristics from device with 15μm selective growth masks

(Higher power output is from planar end)

8.5. REFERENCES

1 G.P.Agrawal and N.K.Dutta, *"Long wavelength semiconductor lasers"*, (Van Nostrand Reinhold, New York, 1986), pp.172-219

2 C.J.Armistead, S.A.Wheeler, R.G.Plumb and R.W.Musk, *IEE Electronics Letters*, 1986, **22**, pp.1145-1147

3 C.J.Armistead, B.R.Butler, S.J.Clements, A.J.Collar, D.J.Moule and S.A.Wheeler, *IEE Electronics Letters*, 1987, **23**, pp.592-593

4 J.E.A.Whiteaway, G.H.B.Thompson, A.J.Collar and C.J.Armistead, *IEEE Journal of Quantum Electronics*, 1989, **6**, pp.1261-1279

5 M.Fukuda, *"Reliability and degradation of semiconductor lasers and LEDs"*, (Artech House, 685 Canton St., Norwood, MA02062, 1991), pp.224-244

6 G.P.Agrawal and N.K.Dutta, *"Long wavelength semiconductor lasers"*, (Van Nostrand Reinhold, New York, 1986), pp.422423

7 M.E.Jones and C.Dix, *Br. Telecom Technol. J.*, 1989, **7**, pp.25-43

8 J.E.A.Whiteaway, B.Garrett, G.H.B.Thompson, A.J.Collar, C.J.Armistead and M.J.Fice, *IEEE Journal of Quantum Electronics*, 1992, **28**, pp.1277-1293

9 J.E.A.Whiteaway, G.H.B.Thompson, C.J.Armistead, A.J.Collar, S.J.Clements and M.Gibbon, *Proceedings of 11th IEEE International Semiconductor Laser Conference*, Boston 1988, IEEE Catalog No. 88CH-2609-6, (Order from IEEE Service Centre, 445 Hoes Lane, Piscataway, NJ 08855-1331, USA), pp.104-105

10 All eptiaxial growths are performed by MOCVD. This process is described in reference 11.

11 Stringfellow G B 1989 *Organometallic Vapour Phase Epitaxy: Theory and Practice* (London: Academic Press)

12 All the silicon dioxide layers are deposited by plasma enhanced chemical vapour deposition. The deposition technique is described in reference 13. The oxide layers are removed in buffered hydroflouric acid which does not attack the semiconductor surface.

[13] P.Van Zant, *"Microchip fabrication. A practical guide to semiconductor processing"*, (McGraw-Hill, New York, 1990), pp.310-313

[14] The silicon dioxide layers described in this section are patterned by a combination of conventional photolithography and CHF_3 reactive ion etching. The photolithographic process is described in reference 15 and reactive ion etching is described in reference 16.

[15] P.Van Zant, *"Microchip fabrication. A practical guide to semiconductor processing"*, (McGraw-Hill, New York, 1990), pp.161-240

[16] B. Chapman, *"Glow Discharge Processes"* (Wiley, New York, 1980)

[17] The etchants employed to remove the p type layers are CH_3COOH:HCl:H_2O_2:H_2O followed by HCl:H_3PO_4. The former etchant is used to remove the GaInAs layer and is described in reference 18. The latter etchant removes InP but not GaInAsP. It is described in reference 19.

[18] S.Adachi, Y.Noguchi and H.Kawaguchi, *J. Electrochemical Society*, 1982, **129**, p1053

[19] K.L.Conway, A.G.Dentai and J.C.Campbell, *J. Applied Physics*, 1982, **53**, pp.1836-1838

[20] P.Van Zant, *"Microchip fabrication. A practical guide to semiconductor processing"*, (McGraw-Hill, New York, 1990), pp.342-344

[21] L. Holland, *"Vacuum deposition of thin films"*, (Chapman & Hall Ltd., London, 1963)

[22] The InP is removed by chemo-mechanical polishing in Br/CH_3OH. The details of this process are supplied by Logitech Ltd, Erskine Ferry Road, Old Kirkpatrick, Glasgow G60 5EU

[23] P.Van Zant, *"Microchip fabrication. A practical guide to semiconductor processing"*, (McGraw-Hill, New York, 1990), pp.340-342

[24] B.S.Bhumbra, D.J.Thomas and D.P.Goodchild, *To be published in the journal of Vacuum Science and Technology B*

[25] F. Stern, *Solid State Physics*, 1963, **15**, pp.299-408

[26] A. Abragam, *"Principles of Nuclear Magnetism"* (Clarendon, 1961)

[27] F.Koyama and K.Iga, *Journal of Lightwave Technology*, 1988, **6**, pp.87-93

[28] J.A.J.Fells, M.A.Gibbon, I.H.White, G.H.B.Thompson, R.V.Penty, C.J.Armistead, E.M.Kimber, D.J.Moule and E.J.Thrush, *IEE Electronics Letters*, 1994, **30**, pp.1168-1169

[29] A. Djupsjobacka, *IEEE Photonics Technology Letters*, 1992, **4**, pp.41-43

[30] K.Noguchi, O.Mitomi, K.Kawano and M.Yanagibashi, *IEEE Photonics Technology Letters*, 1993, **5**,pp.52-54

[31] S.Y.Wang and S.H.Lin, *Journal of Lightwave Technology*, 1988, **6**, pp.758-771

[32] G.Mak, C.Rolland, K.E.Fox and C.Blaauw, *IEEE Photonics Technology Letters*, 1990, **2**, pp.730-733

[33] F.Devaux, F.Forgeuille, A.Ougazzaden, F.Huet, M.Carre, A.Carenco, M.Henry, Y.Sorel, J.F.Derdiles and E.Jeanney, *IEEE Photonics Technology Letters*, 1993, **5**, pp.1288-1290

[34] T.H.Wood, *Journal of Lightwave Technology*, 1988, **6**, pp.743-757

[35] O.Mitomi, I.Kotaka, K.Wakita, S.Nojima, K.Kawano, Y.Kawamura and H.Asai, *Applied Optics*, 1992, **31**, pp.2030-2035

[36] E.Bigan, M.Allovan, M.Carre, C.Braud, A.Carenco and P.Voisin, *IEEE Journal of Quantum Electronics*, 1992, **28**,

[37] D.A.B.Miller, D.S.Chemla, T.C.Damen, A.C.Gossard, W.Wiegmann, T.H.Wood and C.A.Burrus, *Physical Review Letters*, **53**, pp.2173-2176

[38] D.A.B.Miller, D.S.Chemla, T.C.Damen, A.C.Gossard, W.Wiegmann, T.H.Wood and C.A.Burrus, *Physical Review B*, 1985, **32**, pp.1043-1060

[39] S. Gasiorowicz, *"Quantum Physics"*, (John Wiley & Sons, New York, 1974)

[40] A.J.Moseley, D.J.Robbins, A.C.Marshall, M.Q.Kearley and J.I.Davies, *IEE Electronics Letters*, pp.1301-1302

[41] E.P. O'Reilly, *Semicond. Sci. Technol.*, 1986, **1**, pp.128-132

[42] E.P. O'Reilly, *Semicond. Sci. Technol.*, 1989, **4**, pp.121-137

[43] S.C.Rashleigh, *Journal of Lightwave Technology*, 1983, **LT-1**, pp.312-331

[44] J.E.Zucker, I.Bar-Joseph, B.I.Miller, U.Koren and D.S.Chemla, *Applied Physics Letters*, 1989, **54**, pp.10-12

[45] J.E.A.Whiteaway, G.H.B.Thompson, P.D.Greene and R.W.Glew, *IEE Electronics Letters*, 1991, **27**, pp.340-342

[46] G.P.Agrawal and N.K.Dutta, *"Long wavelength semiconductor lasers"*, (Van Nostrand Reinhold, New York, 1986), pp.28-31

Chapter 9

The Application of Selective Area MOCVD to Laser Modulator Integration

9.1. INTRODUCTION

Chapters 7 and 8 described the nature of selective area MOCVD, and the component parts of an integrated laser-modulator. This chapter describes how the technologies were combined to produce an integrated device.

9.2. DESIGN PHILOSOPHY

In the first chapter I stated that photonic integration was only a practical proposition if the integrated device was relatively easy to make, so that the cost benefits in packaging were not offset by a more complicated and lower yield fabrication process. Section 6.3 discussed the application of this philosophy to the design of the laser modulator interface. However, this interface is not the only area of concern in the design of an integrated device. One also has to consider the number and optimum arrangement of photolithography and etching stages. The number of these processing steps can, to some extent, be exchanged for complexity of photolithographic masks. The reason is that one can often make more than one type of structure with a given processing procedure. I believe that additional processing steps cause fewer difficulties than multiple growths, provided that each step has a high yield. However, if possible, it seems that these additional steps should be traded for complexity in the mask layout, as masks only need to be designed once and, if a process works in one area of a wafer, then it is likely to work everywhere else.

The fabrication process for laser-modulator components can be further simplified by making the preliminary testing procedures as rapid as possible. This objective can be achieved by testing the wafer on a probe station before it is cleaved and facet coated[1]. The quality of the information obtained from such probe card testing is enhanced if a back monitor is integrated with the DFB laser. A monitor of this type is also useful in the final package, as a discrete monitor photodiode is included in the packages of most optical transmitters on the market to-day. A back monitor can be integrated with a laser-modulator

without any increase in the complexity of the fabrication process. This is achieved by incorporating QW material with the same bandgap as the laser into a device structure similar to that of the modulator.

9.3. DESIGN AND FABRICATION

A schematic of the integrated laser-modulator is shown in Figure 9.1. Cross sections through the laser and modulator regions of the device are shown in Figures 9.2 and 9.3 respectively. The device shown in these figures was fabricated in the following manner.

9.3.1. Fabrication Procedure

SiO_2 selective growth masks were deposited on an n-InP substrate by a combination of plasma enhanced chemical vapour deposition[2] and conventional photolithography[3]. The pairs of rectangular masked regions were sited on a 400μm pitch and the two masks forming each pair were separated by 38μm. The rectangular masked areas were 9, 15 and 20μm wide in different regions of the wafer. A MQW structure (see Fig 9.3a) containing 6 GaInAsP (λ_{PL}=1.58μm) quantum wells surrounded by GaInAsP (λ_{PL}=1.18μm) barriers was grown over the masked substrate by MOCVD[4]. The quantum wells were embedded in a GaInAsP (λ_{PL}=1.18μm) waveguide which was 0.46μm thick in unperturbed regions far removed from any masks. The room temperature photoluminescence emission wavelength of unperturbed regions of the QW structure was 1500nm. The emission wavelengths at the centres of the 9, 15 and 20μm mask patterns were 1539, 1558, and 1573nm respectively.

The SiO_2 regions were removed in hydrofluoric acid, and second order $2x\lambda/8$ gratings[5] were written into the top of the waveguide layer by a combination of electron beam lithography and wet etching. The grating pitches were adjusted to reflect the changes in waveguide thickness and quantum well emission wavelength that occurred as the widths of the selective epitaxy masks were varied. The wafer was overgrown with p-InP and p^+-InGaAs. The laser, modulator and monitor ridges were then defined using a combination of methane-hydrogen reactive ion etching[6,7,8,9] and selective wet etching in an $HCl:H_3PO_4$ mixture[10]. A 1μm thick layer of SiO_2 was deposited over the wafer and contact windows were opened to the separate components. The wafer was thinned to 150μm and a Ti/Pt/Au contact was deposited on the p side followed

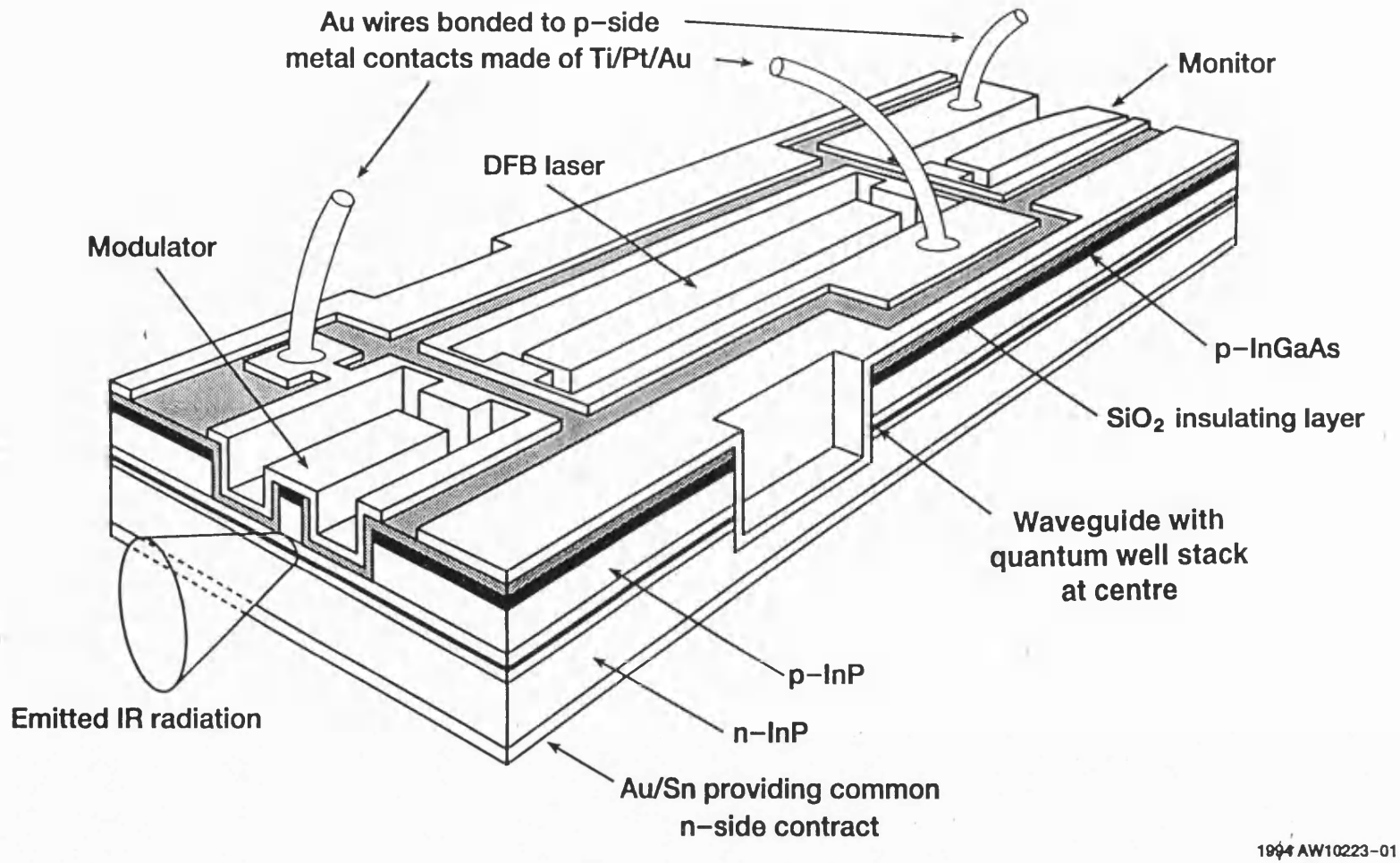

Fig 9.1 Schematic of the integrated laser modulator

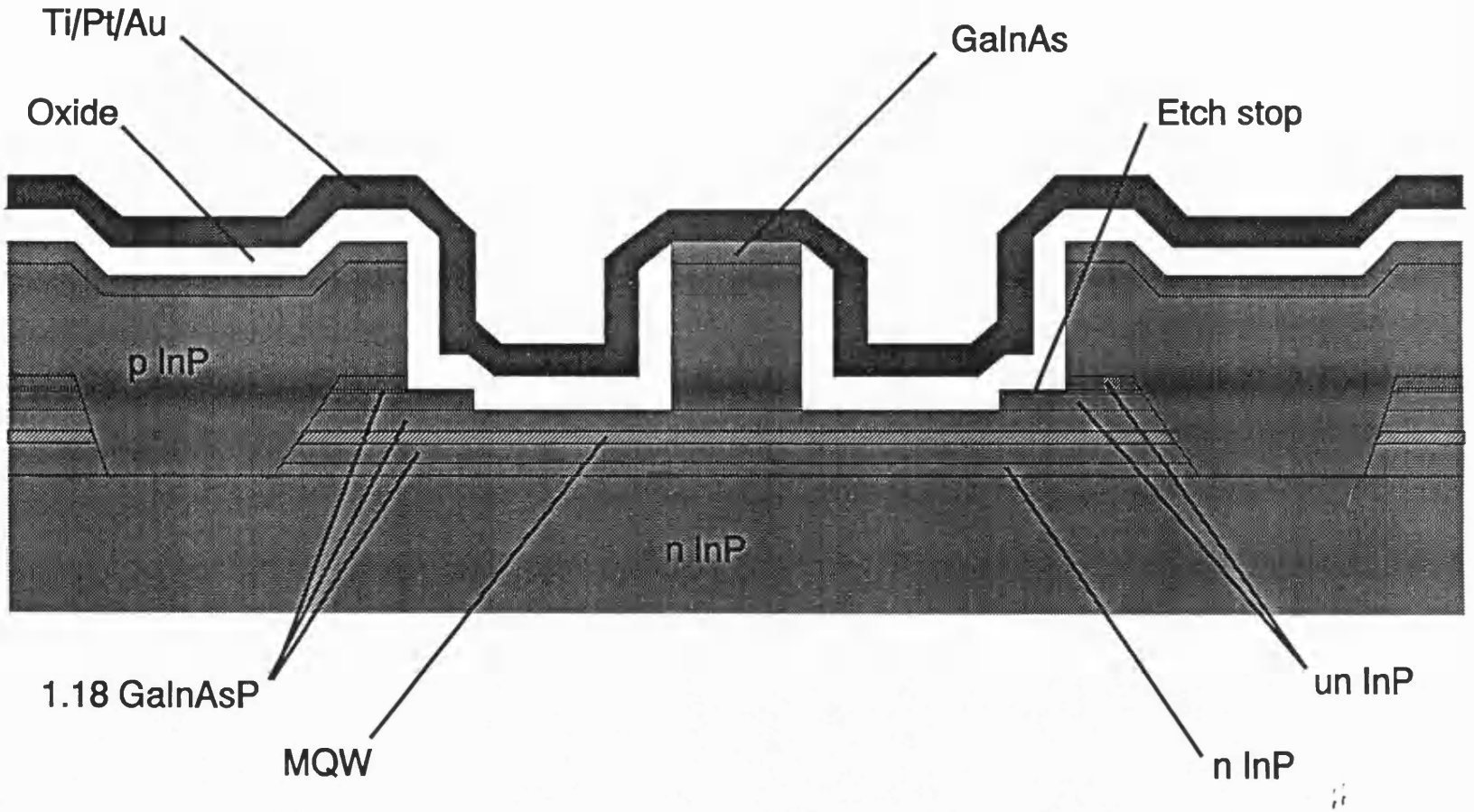

Fig 9.2 Cross section through the laser part of the integrated device

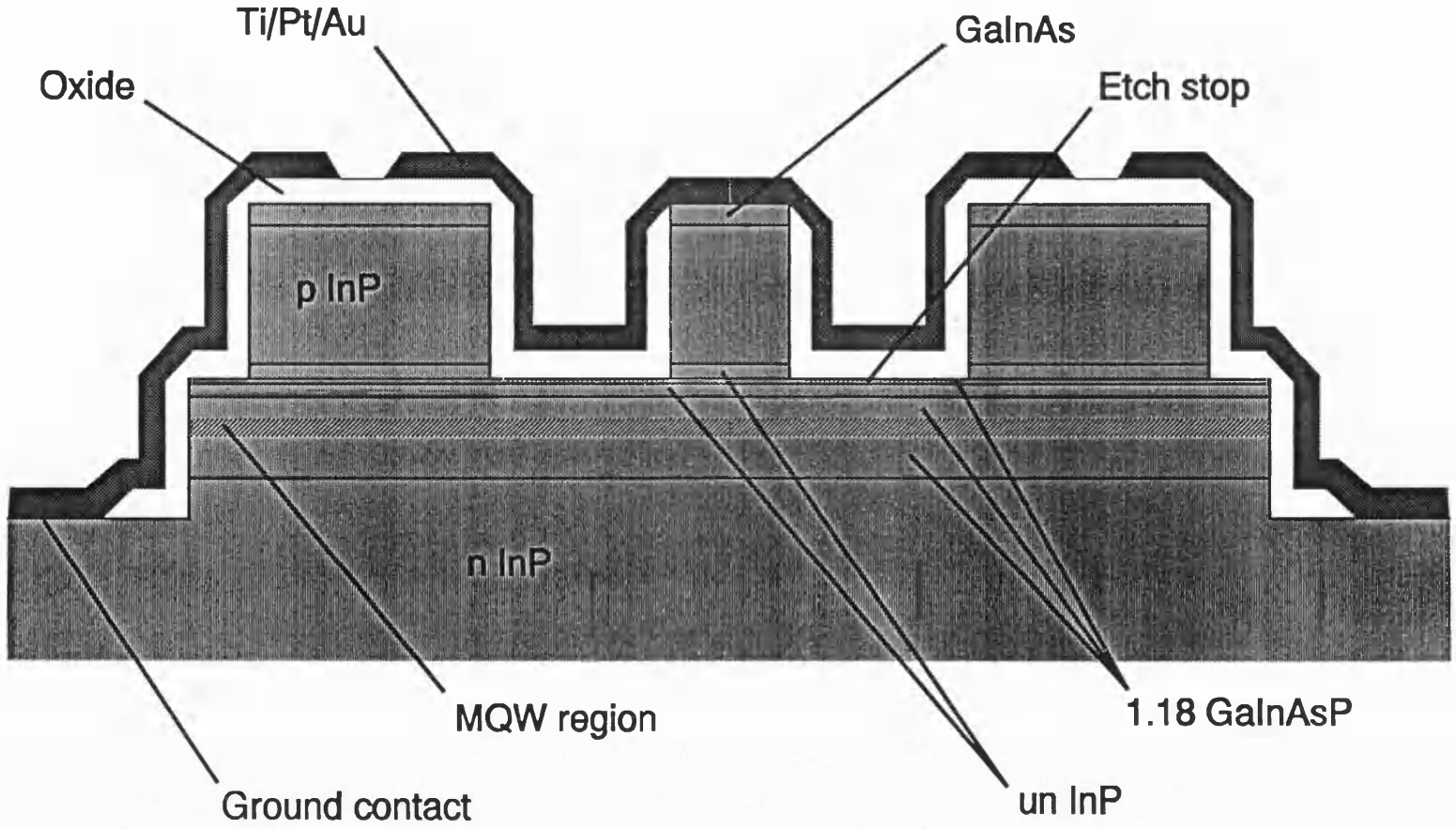

Fig 9.3 Cross section through the modulator part of the integrated device

Nominal Specification				
Layer thickness (μm)	Material		Doping	
			Type	Value (cm^{-3})
300	InP substrate		Sn	
0.2	InP buffer layer		Si	5.10^{17}
0.19	GaInAsP (λ_{PL}=1.18μm) doped lower waveguide		Si	5.10^{17}
0.043	GaInAsP (λ_{PL}=1.18μm) undoped lower waveguide		None	
0.007	GaInAsP (λ_{PL}=1.18μm) barrier	MQWs Cycle x6	None	
0.0080	GaInAsP (λ_{PL}=1.58μm) well		None	
0.14	GaInAsP (λ_{PL}=1.18μm) upper waveguide		None	
0.04*	InP spacer layer		None	
0.010*	GaInAsP (λ_{PL}=1.18μm) etch stop		None	
0.2*	InP zinc delay layer		None	
0.5	InP		Zn	5.10^{17}
1.0	InP		Zn	2.10^{18}
0.2	InGaAs contact layer		Zn	2.10^{19}

* These layers were removed from the laser region before the substructure was overgrown with p type material.

Fig 9.3a Layer structure of the integrated laser modulator

by a Au/Sn contact on the n side. Finally the p metal was patterned by chemically assisted reactive ion beam etching (CARIBE)[11].

9.3.2. Design Features of the Integrated Laser Modulator

The laser and monitor ridges were 590 and 100μm long respectively. The monitor ridge was bent with a radius of 1000μm to reduce the effects of residual reflections from the back facet. The laser grating patch was 350μm long and was terminated 70μm before the end of the areas which had been masked during the selective growth. This ensured that the grating was not fabricated on a waveguide of varying thickness and hence refractive index. The laser contact window extended down the entire length of the laser ridge, so that both the DFB region, and the taper generated by the selective growth, were pumped through one contact.

The mask for the CARIBE etching was designed so that a unique identification number was transferred into the metal layer beside each device.

A deep recess was etched through the quantum wells into the substrate in the same etching step as that for the ridge channels. The function of this recess was to provide an n side contact on the top surface of the integrated device. The n side contact was used for probe station testing. It was also electrically connected to a short length of ridge between the laser and the modulator (see Figure 9.1). The short ridge section acted as a guard terminal to prevent electrical crosstalk between the laser and the modulator.

The guard terminal was not only useful in that it reduced electrical cross talk between the integrated components. The use of this structure also simplified the fabrication process. The reason was as follows.

The CARIBE process used to separate the device contacts was only effective at removing metal from a planar surface. This meant that the laser bond pad could only be isolated from the modulator one if a bridge was left across the ridge channels as shown in Figure 9.1. If left in position, a bridge of this type would have electrically connected the ridge to the rest of the chip by conduction through the p type material that it contained. Consequently the laser and the modulator p contacts could only be isolated from the substrate by either:

a) removing the p type material from the bridge structure.

or

b) breaking the ridge at locations immediately adjacent to the bridge structure (to create the guard terminal).

The latter procedure was easy as it simply involved modifying the ridge mask so that the ridge was broken at the same time as the channels were etched. The former process would have been more complicated as it would have required an additional process step in which the p type material was removed by a combination of dry and wet etching. The depth control of such a dry etch would have been critical. This would not have been easy to achieve in such a narrow aperture.

A number of test structures were fabricated alongside the laser modulators. The presence of these test structures did not complicate any part of the fabrication process save the mask design. The advantages of using such structures are summarised below:

a) Basic materials and processing related parameters can be assessed by probe card testing as soon as processing is complete. This helps one to rapidly identify and rectify fabrication problems before they have affected a large number of wafers.
b) On wafer measurements of test structures provide a good indication of the optimum modulator length required at the cleaving stage.
c) The availability of basic materials measurements makes analysis of the laser-modulator performance easier.
d) The diversity of measurements obtained from test structures often allow one to estimate the benefits of potential design improvements.

The laser modulator mask layout included test structures to measure the absorption coefficient of the modulator, the modulator stray and junction capacitances, the sheet resistance of the p type material and the p side contact resistance.

An optical micrograph of a processed laser modulator is shown in Figure 9.4. A micrograph of a larger area of the wafer is shown in Figure 9.5.

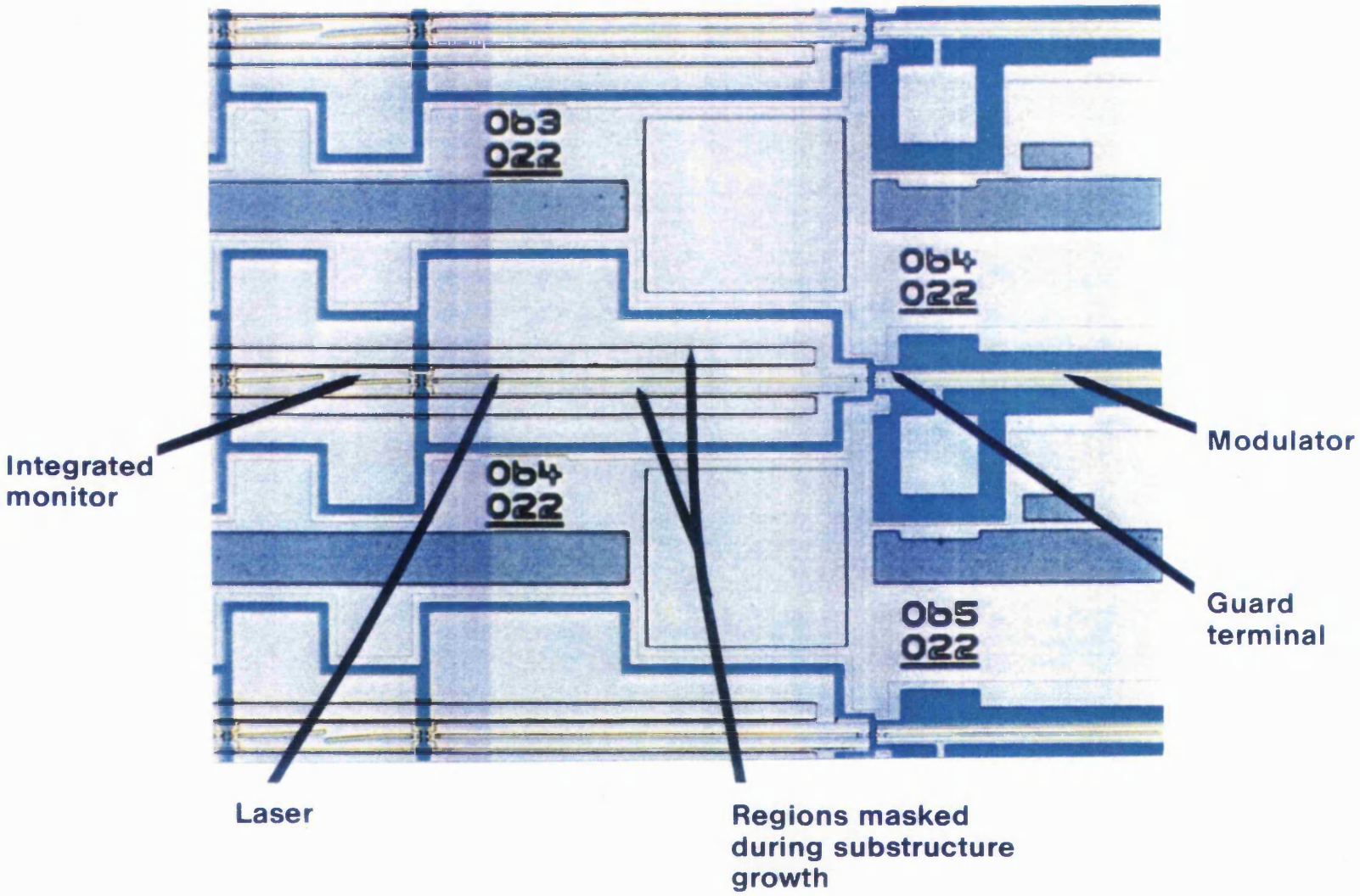

Fig 9.4 Optical micrograph of a processed integrated laser modulator

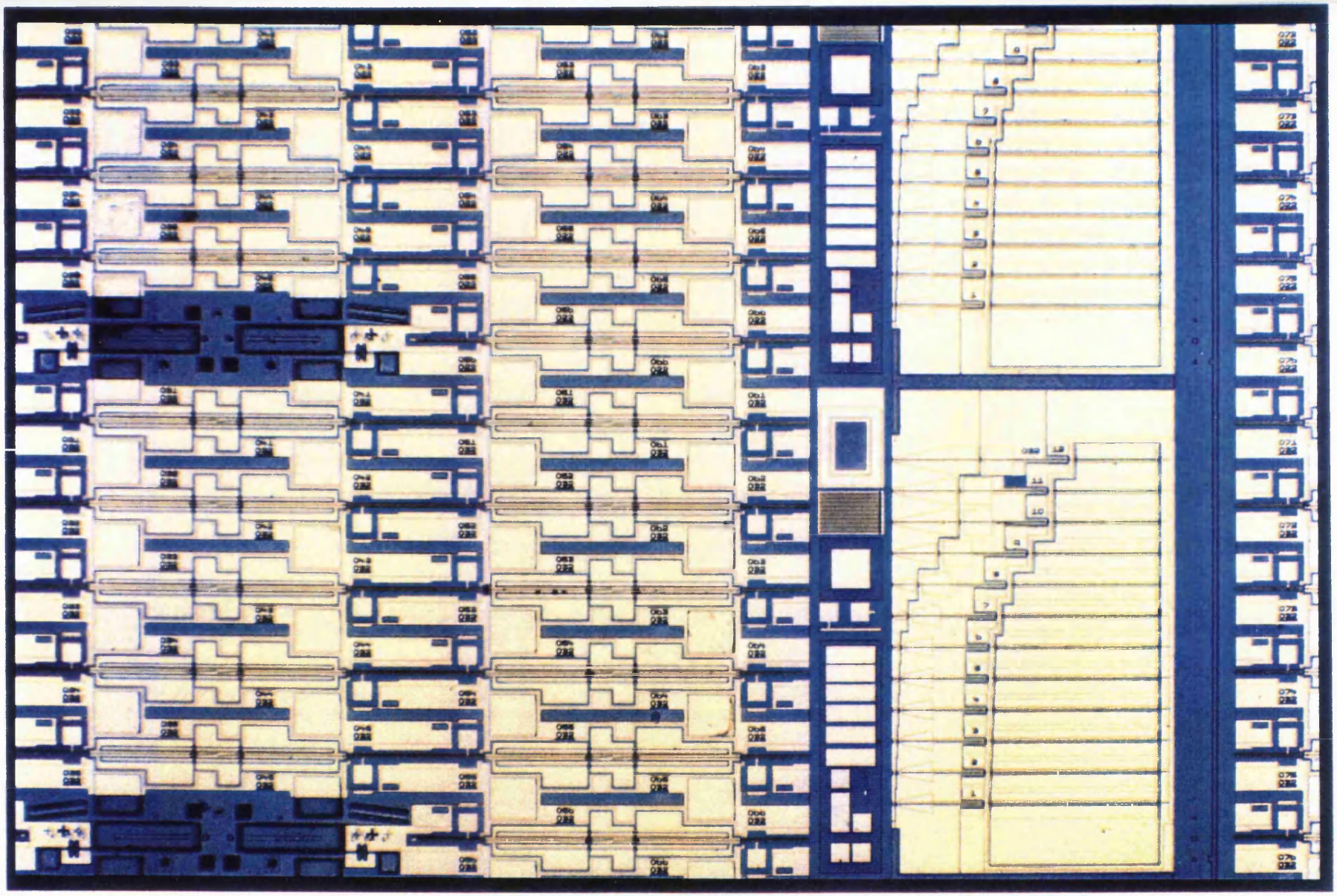

HLA 813 AW 9700 102

Fig 9.5 Optical micrograph of a processed integrated laser modulator wafer

9.4. DEVICE PERFORMANCE

The quality of the wafer was first assessed by making contact to the integrated devices via a probe station. Preliminary pulsed measurements indicated that the heating effects associated with dc measurement were small, provided that the laser current did not exceed 50mA. All subsequent measurements were dc and were made using a Hewlett Packard 4145A semiconductor parameter analyser.

Each integrated device was first tested by measuring the current voltage characteristics of the laser, monitor and modulator. The performance of the DFB laser was then tested by measuring the photocurrent generated in adjacent components as a function of laser drive current. A typical example of the photocurrent collected in a monitor as a function of the drive current in the adjacent laser is shown in Figure 9.6. From this plot one can see that the dc threshold current of the laser was 22mA. The photocurrent collected from the monitor tended to saturate with increasing laser drive current when the monitor bias voltage was low. This saturation problem was overcome by applying a reverse voltage of ~6V to increase the electric field across the monitor intrinsic region.

The performance of each modulator was investigated by making use of the fact that adjacent integrated devices on the wafer were rotated through 180°. Hence the modulator for one integrated device was continuous with that of the next and it was possible to reverse bias the neighbouring laser for use as a detector. An example of the photocurrent collected from such a detector as a function of the current supplied to the laser and the bias applied to the modulator, is shown in Figure 9.7.

27 modulators and 39 lasers and back monitors were tested in the manner described above. Only one laser and one modulator were not operational. Reverse bias breakdown voltages (10μA reverse current) for the monitors and modulators were typically in the region of 30V. The mean laser threshold current was 22mA. The standard deviation in the latter figure was only 1.5mA in spite of the fact that the DFB gratings had been written with target wavelengths spanning 60nm. The modulator insertion loss and extinction per unit applied voltage increased with decreasing laser wavelength in the manner that one would anticipate.

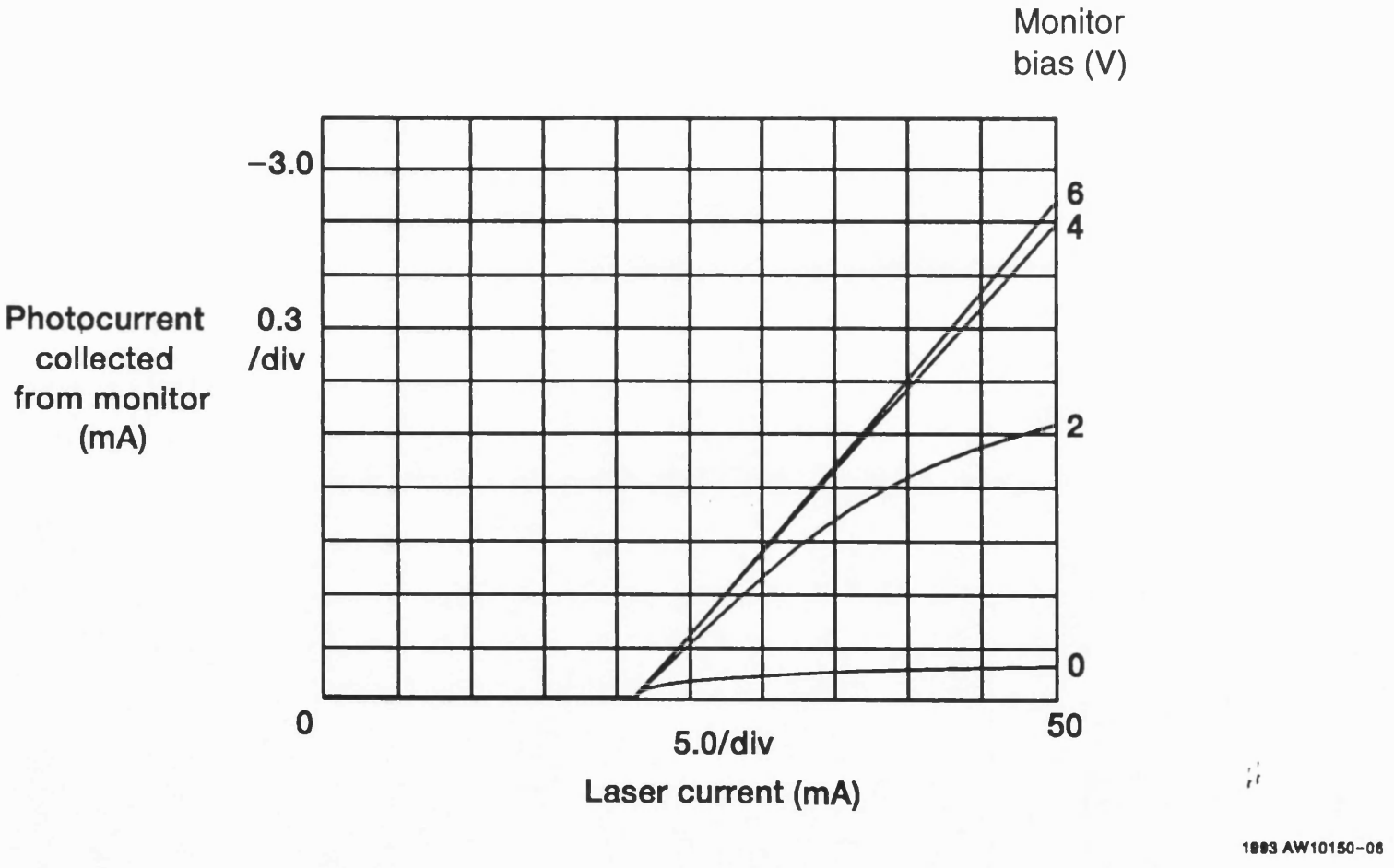

Fig 9.6 Probe station assessment of monitor

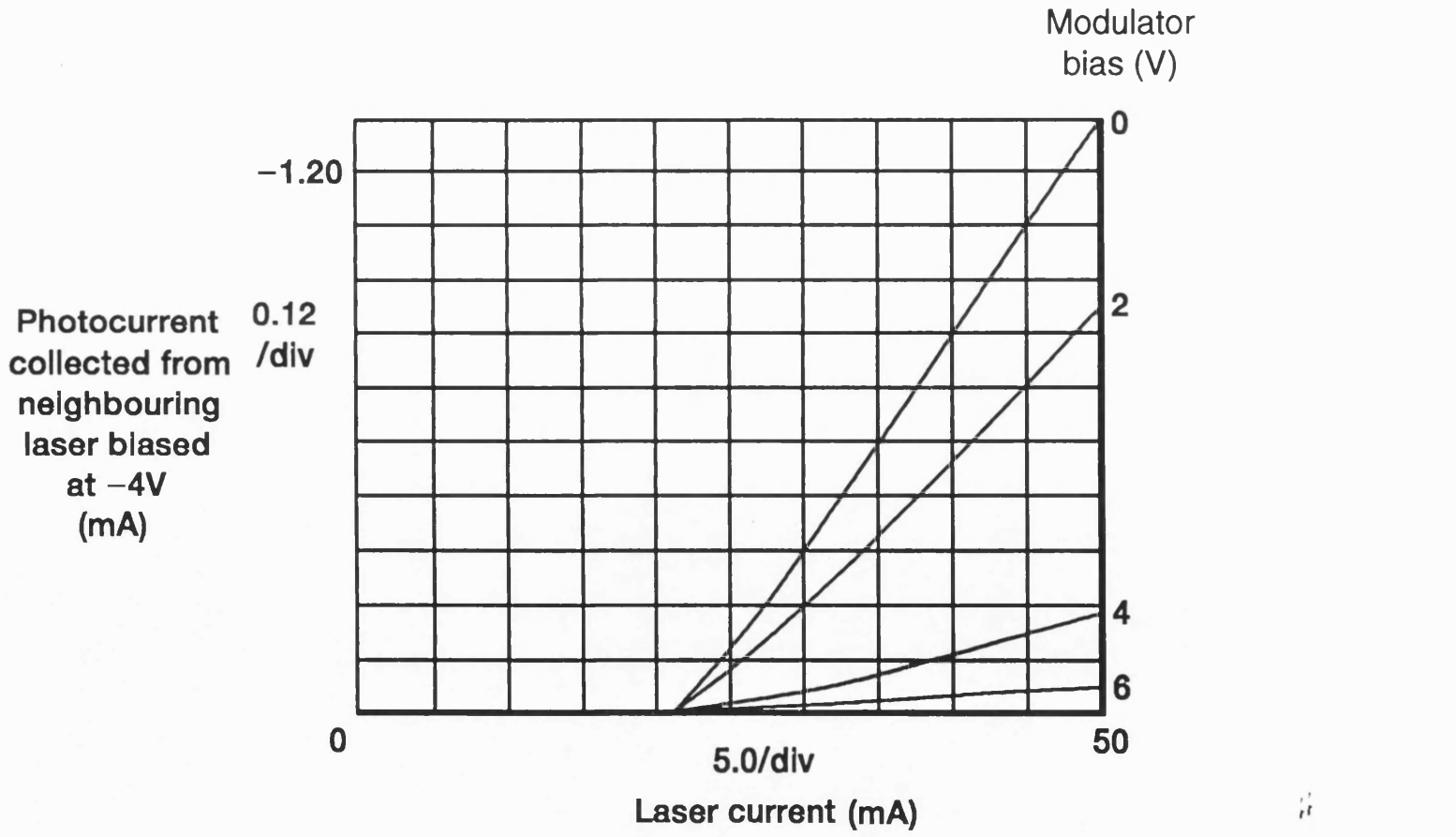

Fig 9.7 Probe station assessment of modulator

The electrical isolation between the lasers and the modulators was assessed by measuring the difference in the laser current required to obtain 20μA of photocurrent in the back monitor, with 0 and 4V applied to the modulator. The differences were too small to be measured and were less than 10μA. This result indicated that the guard terminals were effective at isolating the lasers from the modulators.

After making the above measurements the wafer was cleaved to create integrated devices with 200μm and 440μm long modulator regions. The integrated monitor was cleaved off some of the integrated devices so that light current characteristics from the laser and the modulator ends could be compared. The devices were anti-reflection coated on both ends. Six devices were bonded, p-side up, onto high speed mounts and high speed packages. Both the mounts and the packages incorporated 50Ω matching resistors. The devices which were bonded down came from regions of the wafer where the selective epitaxy mask width was either 9 or 15μm. The reason was that the modulation performance of devices between the 20μm selective growth masks was inadequate as the laser operating wavelength was too far away from the modulator bandedge. Most of the data presented in the figures below comes from two of the bonded devices, RFDF13 and ILM3. The operating wavelength of the former device was positioned closer to the modulator bandedge than that of the latter. Some parameters of interest for the two devices are listed in the following table.

Table 9.1 Characteristics of RFDF13 and ILM3

Parameter	RFDF13	ILM3
Selective growth mask width (μm)	9	9
Operating wavelength (nm)	1532	1552
Wafer exciton peak (nm)	1480	1480
Modulator length (μm)	200	440
Modulator extinction at -4V, 20°C (dB)	23.5	24
Back monitor included	No	Yes

The performance of the bonded devices was first assessed by measuring light current characteristics into a single mode lens-ended fibre. The mean threshold current was similar to that measured on the probe station at (21.5±0.5)mA. It was possible to couple optical powers in the region of 3mW into the fibre when the lasers were driven with currents of 150mA. Modulator photocurrent

measurements indicated that at least 10mW of optical power was coupled into the modulator at this laser bias current.

Light current characteristics from the laser ends of devices without back monitors were similar to those from conventional discrete $2x\lambda/8$ DFB devices. However, the light current characteristics from the modulator ends showed more curvature just above threshold than those from the laser end. An example of this behaviour can be seen in Figure 9.8 which shows light current characteristics from the modulator end of device RFDF13.

The reason for the curvature was deduced by plotting the photocurrent collected from the modulator as a function of the optical power in the output fibre. An example of such a plot is shown in Figure 9.9. The photocurrent and power levels were adjusted by ramping the bias current passed through the laser. The measurements were made at several modulator bias voltages. The photocurrents and powers were normalised to those collected at a laser bias of 150mA to enable easy comparison of the results obtained at different modulator bias levels. The plots from these measurements showed that the photocurrent tended to saturate as the laser output power was increased. The corresponding curvature in the light current characteristics indicated that the absorption coefficient decreased when such saturation occurred. Subsequent work[12] has suggested that the saturation was caused by an accumulation of holes in the quantum wells of the modulator. The space charge created by such holes reduced the electric field across the quantum well region, and hence the absorption coefficient.

The attenuation obtained on the application of a given voltage to the modulator increased as the operating wavelength of the associated laser decreased. This behaviour is consistent with measurements of typical photocurrent spectra (see Figure 8.4 for an example of spectra from similar MQW material). The device with the shortest lasing wavelength (RFDF13) exhibited 23.5dB of extinction on the application of 4V.

The amount of extinction obtained on the application of a given voltage to the modulator decreased with increasing laser current. This behaviour is consistent with the saturation measurements described above. Plots of the extinction characteristics from device RFDF13 at laser currents of 50, 100 and 150mA are shown in Figure 9.10.

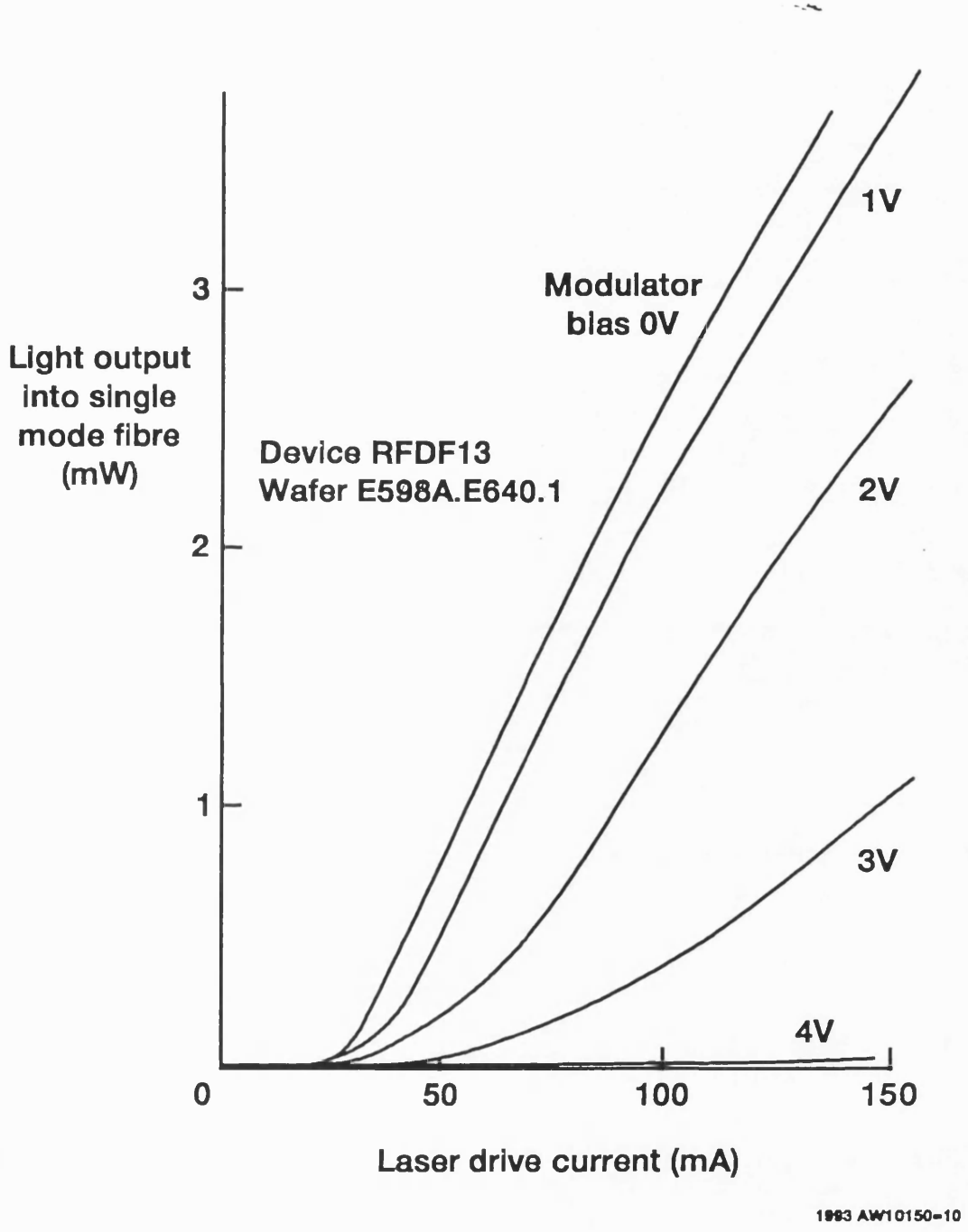

Fig 9.8 Light current characteristics from modulator end of integrated device

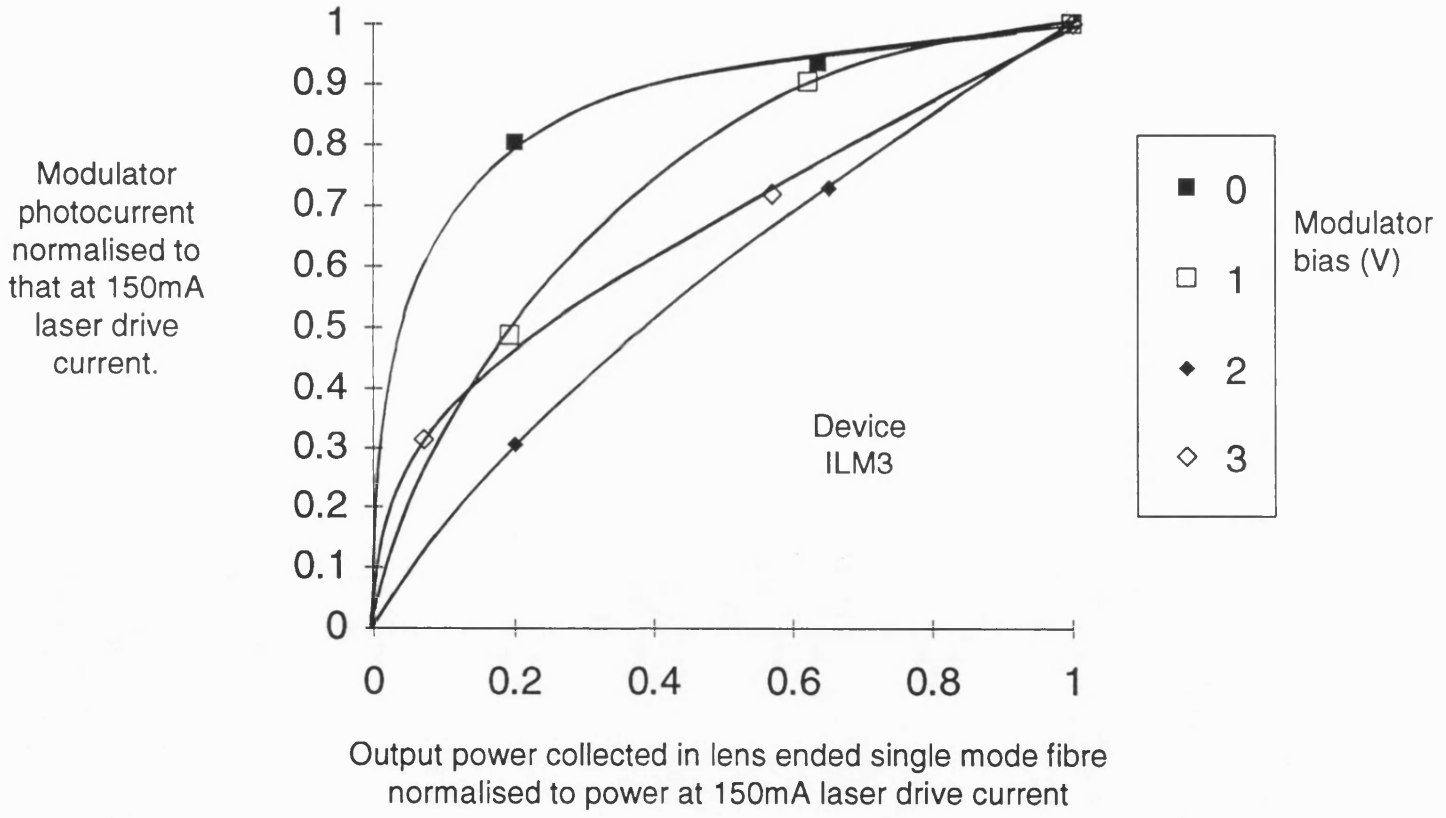

Fig 9.9 Modulator saturation characteristics

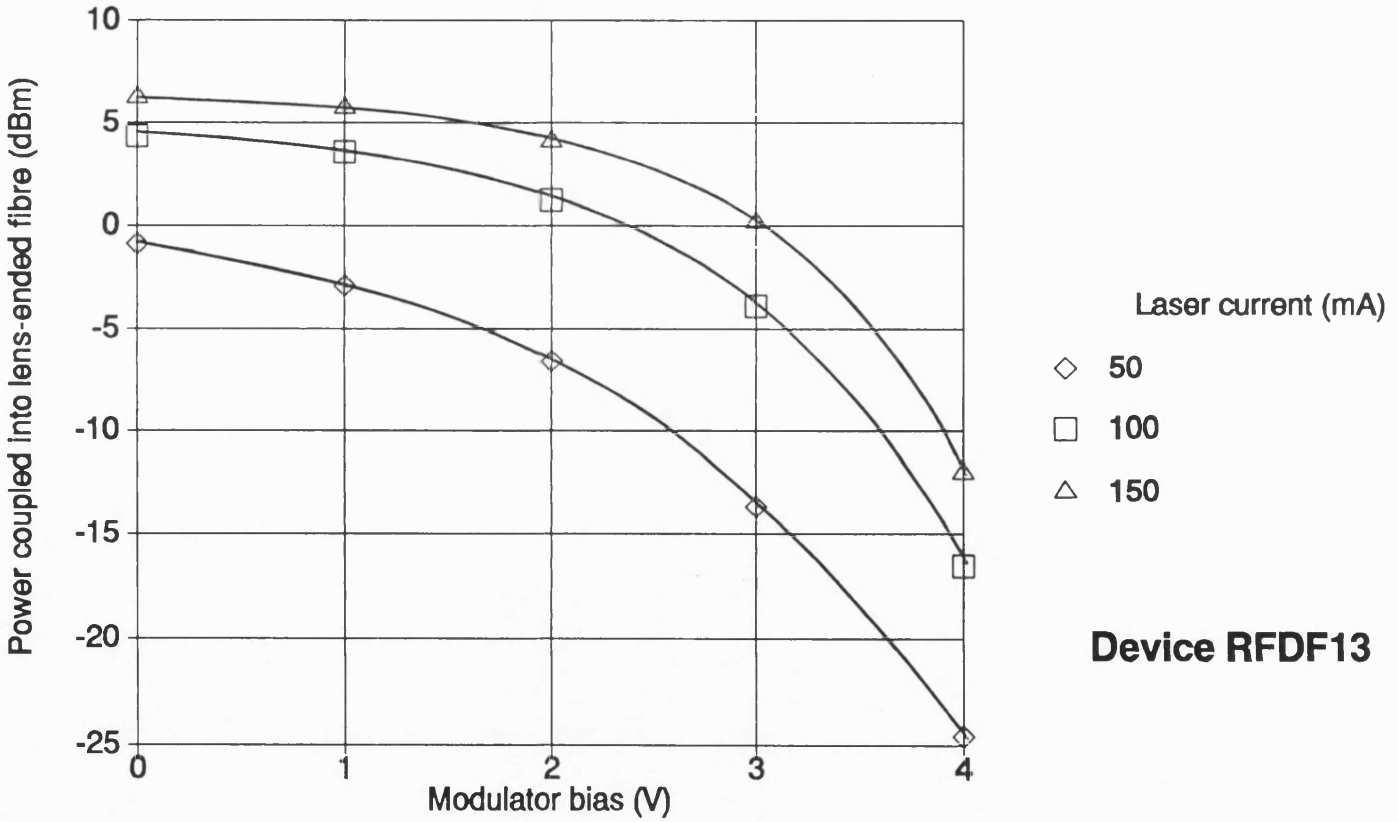

Fig 9.10 Integrated laser modulator extinction characteristics

Spectra from the integrated devices were all similar to those from conventional 2xλ/8 DFB lasers, though the absorption characteristic of the modulator was superimposed on the amplified spontaneous emission spectrum of the laser. Side mode suppression ratios were all in excess of 47dB at laser drive currents of 100mA. An example of a spectrum from an integrated device is shown in Figure 9.11.

The high speed performance of device ILM3 was assessed by driving the modulator with a 2^7-1 bit pattern at 5 Gb/s. The peak to peak voltage swing was 3V and the modulation signal was superimposed on a d.c. voltage using a bias Tee. An example of a 5 Gb/s eye[13] obtained with a 31mA laser drive current and a -2V mean modulator bias is shown in Figure 9.12. At higher laser drive currents the eye started to close as a result of the saturation problem described above.

The bit error rate[14] performance of integrated laser modulator ILM3 was further assessed by transmitting a 2^7-1 bit pattern down standard fibre at a data rate of 2.592 Gb/s. The dispersion of the fibre was approximately 17ps/nm/km. The modulator was driven with a peak to peak voltage swing of 3V and a mean bias of -2V. The laser bias current was 31mA. The data was generated by an Anritsu MP1650A pattern generator and was detected by a commercial STC receiver based on an avalanche photodiode[15]. Erbium doped fibre amplifiers[16] driven by 1480nm pump sources were used to compensate for the fibre loss. The spontaneous emission generated by these amplifiers was partially removed by a tuneable filter which was placed in front of the receiver. The system configuration employed and the results obtained are shown in Figures 9.13 and 9.14. The penalty for transmission over 380km of fibre was 3dB.

9.5. DISCUSSION

The above results indicate that the integration procedure was successful, as more than 10mW of power was coupled into the modulator and the performance of the laser and the modulator were not compromised by the integration process. The problems arose from the fact that so much power was coupled into the modulator that it was operated in a regime not previously encountered. The result was hole accumulation in the modulator quantum wells, which caused saturation effects in its dc and rf response. In an attempt to combat the saturation problem the systems measurements were made using

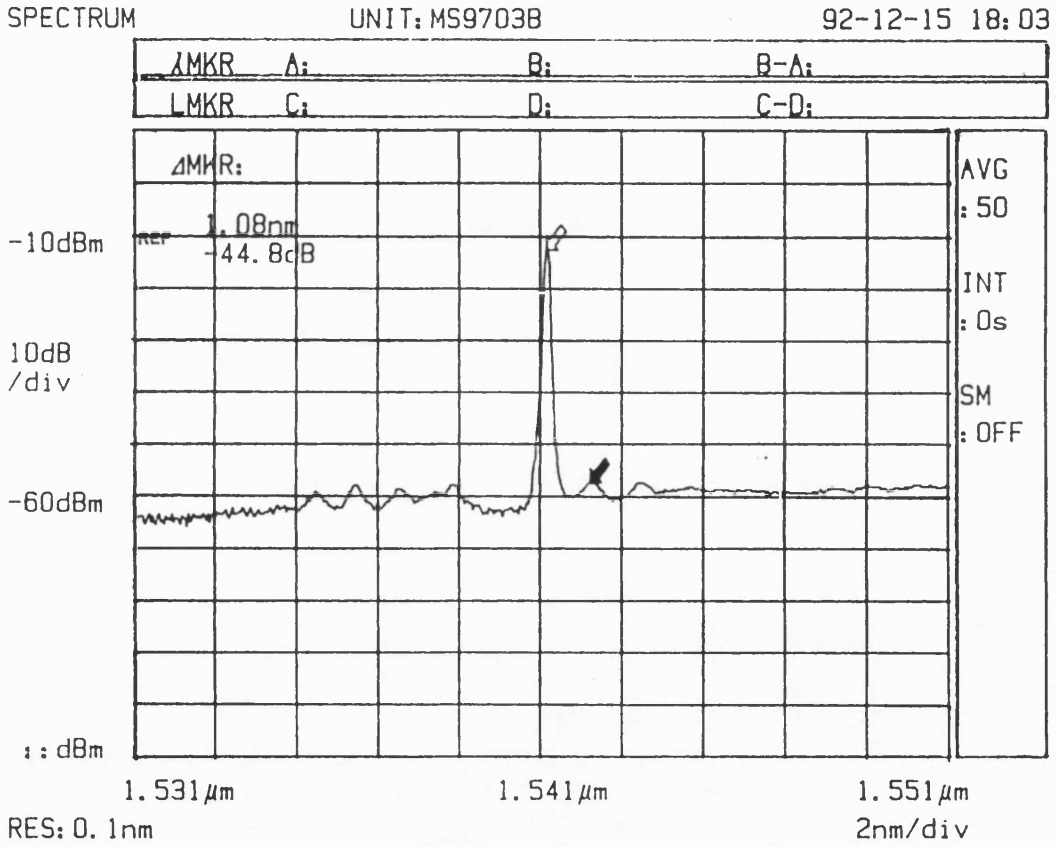

Fig 9.11 Spectrum measured at the modulator end of an integrated device

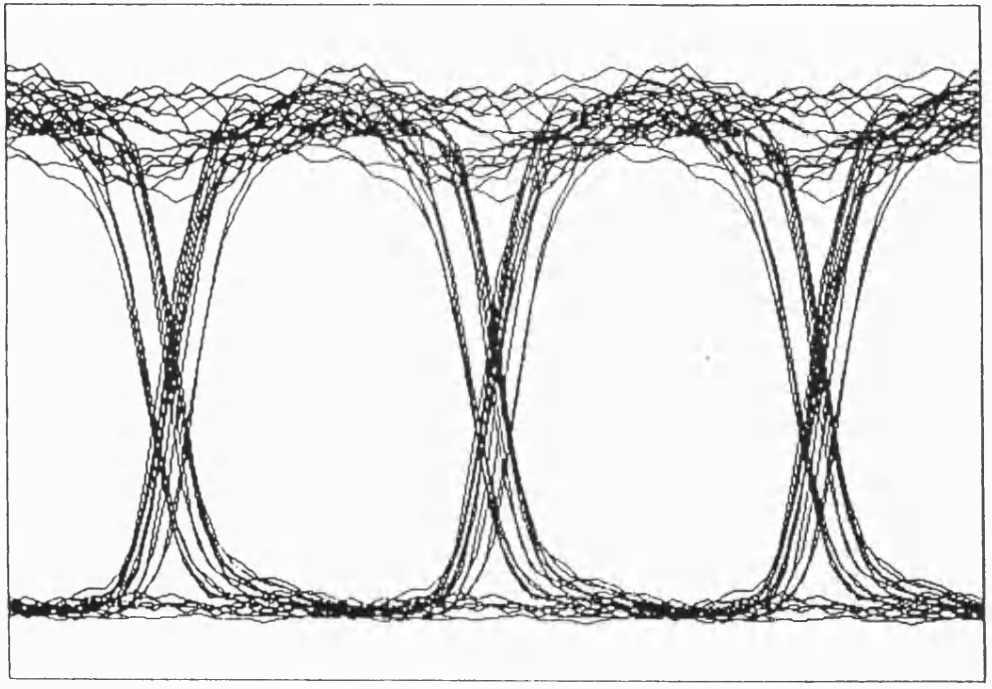

Bias voltage = 2.06V
Modulator voltage = $3V_{pp}$
Laser current = 31 mA
Temperature = 17 °C

Fig 9.12 Transmitted eye at 5Gb/s, 2^7-1 PRBS

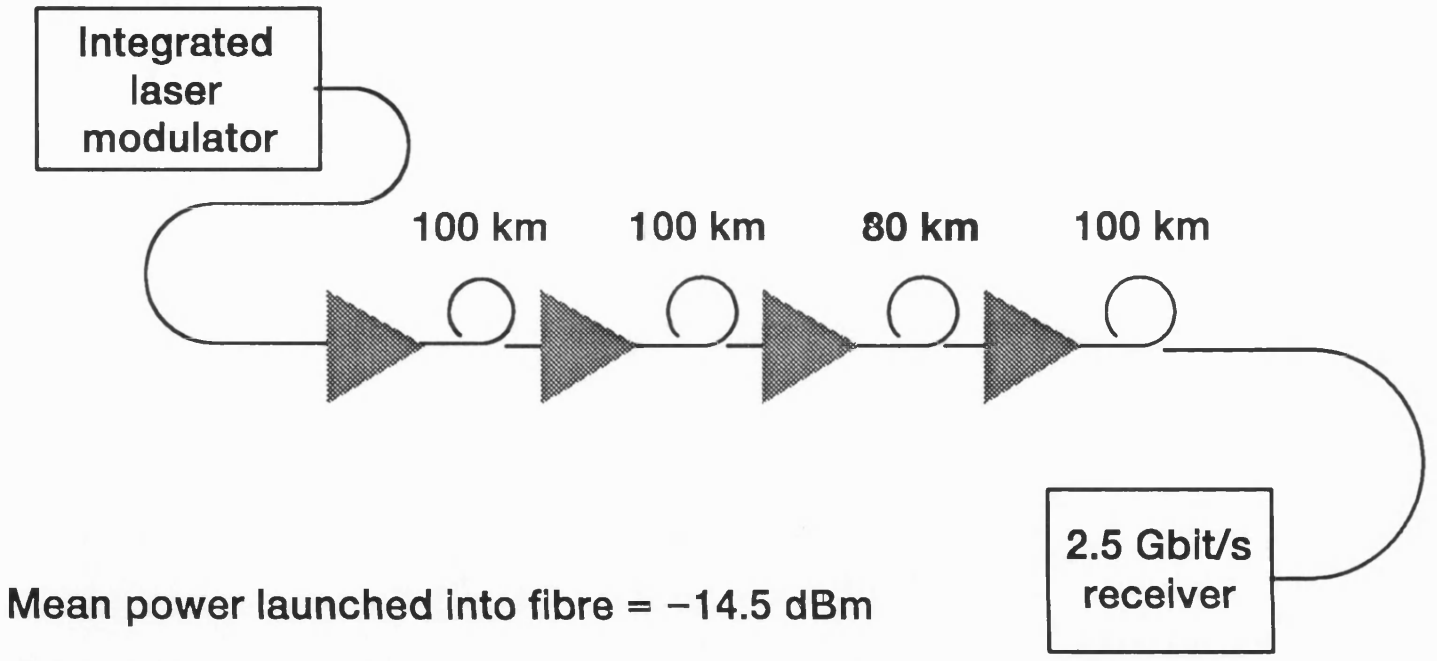

Fig 9.13 System block diagram

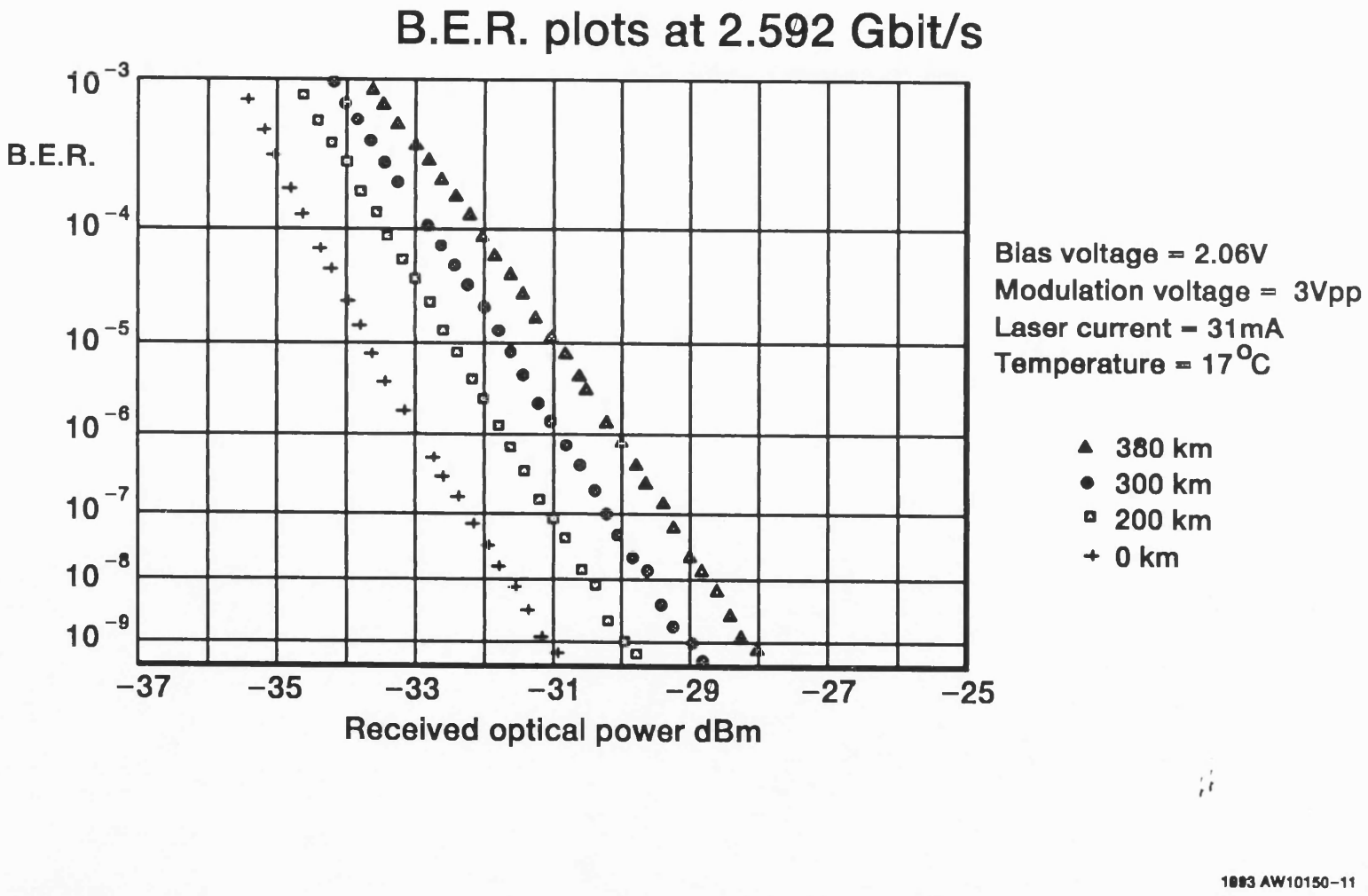

Fig 9.14 Bit error rate measurements from integrated laser modulator

a device in which the modulator absorption coefficient was lower than ideally desirable. This was achieved by choosing a integrated device with an operating wavelength which was situated a long way from the modulator band edge. One side effect of such an approach is that the modulator tends to have relatively large and positive chirp[17]. It seems likely that this is the reason why the dispersion penalty for transmission over 380km was 3dB, rather than the 0.9dB that one would anticipate for an ideal zero chirp source.

The device results indicated that the saturation problem had to be solved before the integrated laser modulator would become a practical component for use in real systems. A solution to the saturation problem was in fact discovered in a later phase of the project. An outline of this solution is given in the next chapter.

The saturation behaviour of the integrated device was the only aspect of its performance which was not satisfactory. Given that this problem was solved it is then worth reviewing the costs and benefits of the integration process.

The advantages of fabricating the laser modulator as an integrated device rather than as its discrete equivalents are as follows:

a) There is a reduction in the number of fibre or microlens alignments required in the manufacture of the transmitter.
b) There is an improvement in the coupling efficiency between the laser and the modulator, and hence an improvement in the transmitter power output.
c) The polarisation of light entering the modulator is automatically aligned to the quantum well structure.
d) On wafer probe card testing using adjacent lasers and modulators as transmitters and detectors is possible.
e) A back facet monitor can be integrated with the laser-modulator without further complication of the fabrication process.

The costs of integration are all incurred in the wafer fabrication process. They can be illustrated by listing the additional steps which laser-modulator fabrication adds to the conventional DFB process. The DFB process is described in section 8.2.1. The additional fabrication steps are listed below.

a) An oxide pattern is deposited on the substrate before substructure growth.
b) The protective InP layer deposited on the top of the substructure is only removed from selected regions of the wafer rather than its entire area.
c) The DFB gratings must be aligned to the selectively grown regions.

d) A double exposure of the ridge patterning resist is required to ensure complete development in the deep recess described in section 9.3.2.
e) A double exposure of the contact window patterning resist is required for the same reason as above.
f) The p side metal layer must be patterned.

The difficulty of each of these additional process steps can be summarised as follows.

Steps a and b involve conventional silicon dioxide deposition and patterning by photolithography. The grating alignment in step c took some time to implement, but most of the alignment is performed under computer control, and is now almost automatic. The double exposures in steps e and f involve exposing the resist through a second mask before development. The second exposure allows one to vary the dose given to different regions of the wafer and, with practice, only takes fifteen minutes.

The p side metal patterning is a greater complication as this is an entirely new process not required in the manufacture of DFB lasers. However, it is usually required for modulators, whether discrete or integrated, to help achieve the required capacitance[18]. The use of p side metal patterning also opens the opportunity for on wafer probe card testing and the use of test structures.

The overall success of the integration process can be measured by calculating the cost of a packaged integrated laser modulator, and comparing it with that of its packaged hybrid equivalent. In practice this calculation is not easy as it involves a knowledge of process costs and yields for the route which one has not taken, as well as those for the route which one has followed. The problem is complicated by the fact that it is difficult for companies to release yield and cost data for commercial reasons. However the potential cost advantage of the integrated laser modulator can be seen from the fact that the packaging of an integrated device, which only involves one optical alignment, typically costs more than the chip. In this situation it seems likely that the small cost benefits in the processing procedures for hybrid components would be greatly outweighed by the cost of the multiple alignments required in the packaging process.

9.6. REFERENCES

1 P.Vettiger, M.E.Benedict, G.L.Bona, P.Buchmann, N.Cahoon, K.Daetwyler, H.P.Dietrich, A.Moser, H.K.Seitz, O.Voegeli, D.J.Webb and P.Wolf ,*Proc 12th IEEE Internat. Semicond. Laser Conf.*,1990 , p.144

2 P.Van Zant, *"Microchip fabrication. A practical guide to semiconductor processing"*, (McGraw-Hill, New York, 1990), pp.310-313

3 P.Van Zant, *"Microchip fabrication. A practical guide to semiconductor processing"*, (McGraw-Hill, New York, 1990), pp.161-240

4 Stringfellow G B 1989 *Organometallic Vapour Phase Epitaxy: Theory and Practice* (London: Academic Press)

5 J.E.A.Whiteaway, B.Garrett, G.H.B.Thompson, A.J.Collar, C.J.Armistead and M.J.Fice, *IEEE Journal of Quantum Electronics*, 1992, **28**, pp.1277-1293

6 U. Niggebrugge, M. Klug and G. Garus, *Proc. 12th Symposium on GaAs and Related Compounds*, Karuizawa, Japan, 1985, pp.367-372

6 L. Henry, C. Vaudry and P. Granjoux, *IEE Elect. Lett.*, 1987, **23**, pp.1253-1254

7 T.R. Hayes, *Plasma Technology Seminar*, Tegal, 1989

8 T.R. Hayes, M.A. Dreisbach, P.M. Thomas, W.C. Dautremont-Smith and L.A. Heimbrook, *J. Vac. Sci. Technol. B*, 1989, **7**, pp.1130-1140

9 D.J. Thomas and S.J. Clements, *Proc. 20th European Solid State Device Research Conference ESSDERC 90*, Nottingham, 1990, pp.121-124

10 K.L.Conway, A.G.Dentai and J.C.Campbell, *J. Applied Physics*, 1982, **53**, pp.1836-1838

11 P.Van Zant, *"Microchip fabrication. A practical guide to semiconductor processing"*, (McGraw-Hill, New York, 1990), pp.231-232

12 I.K.Czajkowski, M.A.Gibbon, GH.B.Thompson, P.D.Greene, A.D.Smith and M.Silver, *IEE Electronics Letters*, 1994, **30**, pp.900-901

13 F.G.Stremler, *"Introduction to Communication Systems"*, (Addison-Wesley, New York, 1990), pp.558-559

14 H.Taub and D.L.Schilling, *"Priniciples of Communication Systems"*, (McGraw-Hill, Singapore, 1986), pp.444-446

15 S.M.Sze, *"Physics of Semiconductor Devices"*, (Wiley, New York, 1981), pp.766-783

16 C.R.Giles, *"Journal of Lightwave Technology"*, 1991, **9**, pp.147-154

17 J.E.Zucker, I.Bar-Joseph, B.I.Miller, U.Koren and D.S.Chemla, *Applied Physics Letters*, 1989, **54**, pp.10-12

18 T.H.Wood, *Journal of Lightwave Technology*, 1988, **6**, pp.743-757

Chapter 10

Recent Developments in Laser Modulator Integration

10.1. INTRODUCTION

In the period since the completion of the work described in Chapter 9 there has been a considerable amount of work on laser modulators, both at BNR Europe and at other laboratories. In this chapter I have compared the reported performances of these devices, to see they were influenced by the interface design. I have also included a brief account of the development of the laser modulator at BNR Europe, as it was in this phase of the work that the seeds sown in the design of the device blossomed and started to bear fruit.

10.2. THE LASER-MODULATOR AT BNR

The performance of the first wafer of integrated laser modulators (see chapter 9) indicated that the device was a promising candidate for use as a transmitter in 2.5 and 10Gb/s transmission systems. As a result, a larger team of people was allocated to work on the device and develop it from a technology demonstration to a practical component for production.

The first problem tackled by this team was that of power saturation in the modulator. The problem was solved by:

a) using quantum wells and barriers under compressive and tensile strains respectively[1].
b) placing the quantum well stack in the centre of the modulator intrinsic region.

The former change reduced the barrier to hole escape. The latter reduced the effect of any residual hole accumulation on the electric field in the quantum well region.

The improvement in the saturation performance meant that the device could be operated in a regime where the absorption coefficient in the modulator was higher. This allowed us to move the operating wavelength of the laser closer to the modulator bandedge, in an attempt to reduce the magnitude of the

modulator chirp[2]. As a result the penalty for transmission over 360km of standard fibre at 2.5Gb/s was reduced to ~0.4dB. A typical bit error rate plot of such performance is shown in Figure 10.1. Ironically, one side effect of the reduction in the separation between the lasing wavelength and the modulator bandedge was that selective area epitaxy was no longer necessary. The required lasing wavelength could be obtained by simply detuning the grating pitch from the gain peak. This change simplified the fabrication process and hence was adopted as the norm.

In the course of the development program the device processing was moved onto 2" wafers and the probe card testing procedures were automated. The probe card testing system can now test the 1500 or so devices on a single wafer in about 15 hours. This technique has increased the number of lasers that a small team can hope to test by at least an order of magnitude. The results of these tests can be analysed using statistical techniques to see trends that would be invisible with smaller device numbers. An example is shown in Figure 10.2, where histograms of the threshold currents of selectively grown strained MQW lasers are plotted for different mask widths. The small increase in threshold current as a result of the selective growth would be invisible if the sample size was smaller.

The fact that all the devices fabricated on a 2" wafer are tested means that one can map device parameters and correlate them with materials data, such as the photoluminescence wavelength and X-ray measurements. An example of a wafer map of threshold current is shown in Figure 10.3.

The test structures have also provided valuable information. For example, Figure 10.4 shows the extinction of a large number of 92μm long modulators as a function of the applied bias voltage. These plots show how the extinction changed as the difference between the modulator bandedge and the lasing wavelength was increased. The plots are in good qualitative agreement with photocurrent measurements. The data collected from the above test structures has also been analysed to provide information about the magnitude and uniformity of the modulator insertion loss and the modulator saturation performance.

As a result of the above improvements the integrated laser modulator is now going into production at Northern Telecom's plant in Devon. An integrated laser modulator fabricated by Fujitsu is already on the market.

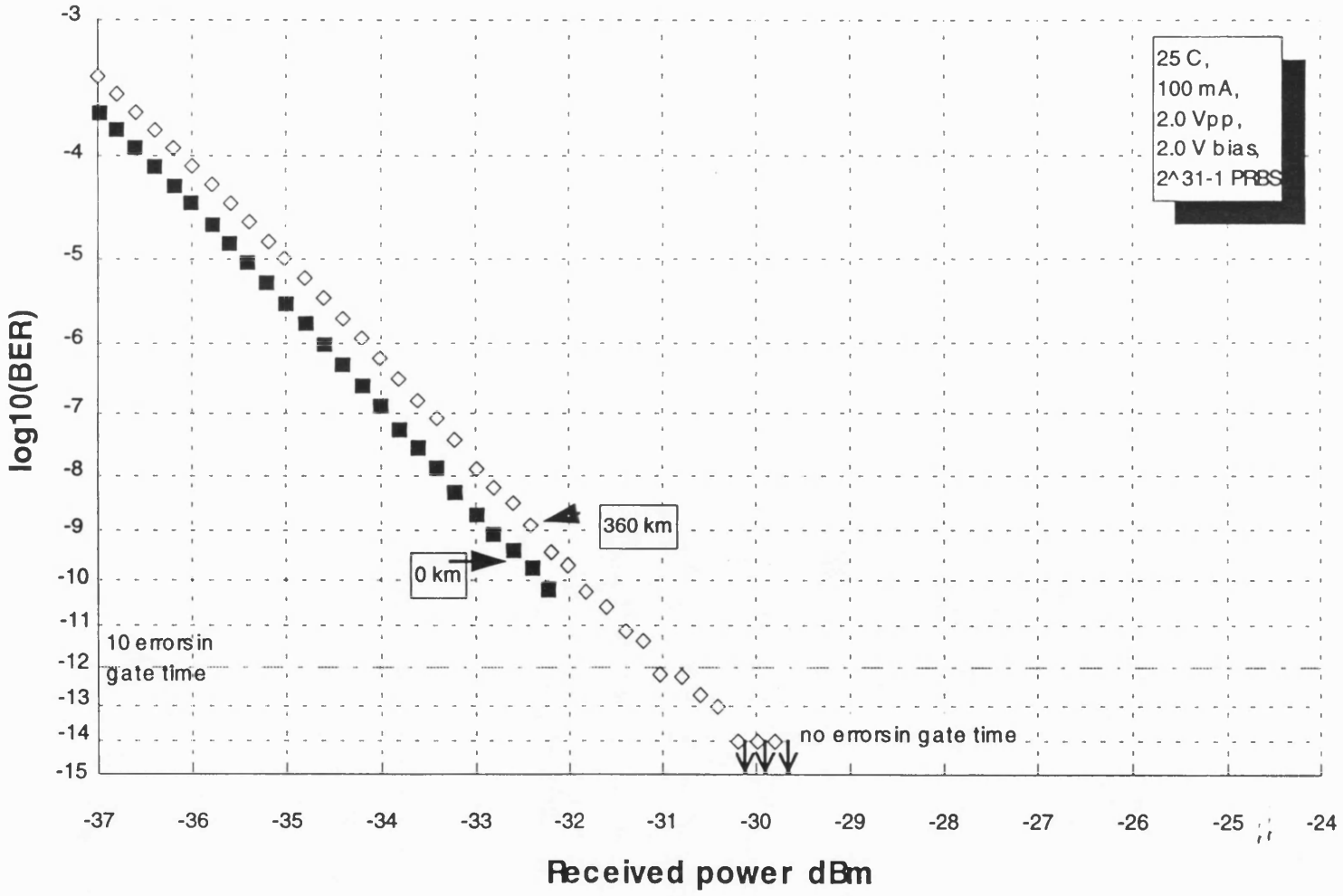

Fig 10.1 BER of strained QW integrated laser modulator at 2.592 Gb/s

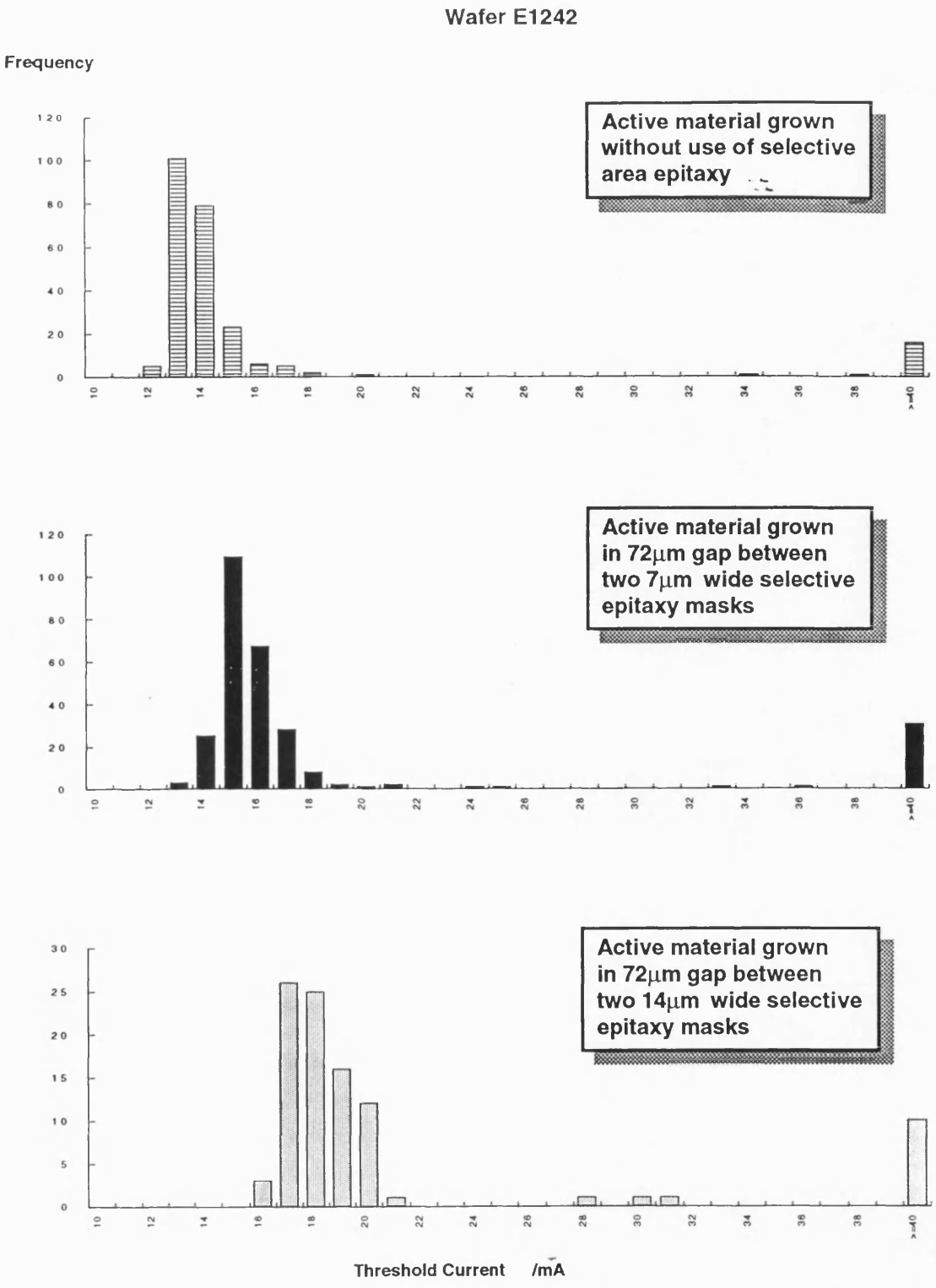

Fig 10.2 Effect of selective area epitaxy on the threshold currents of strained QW devices

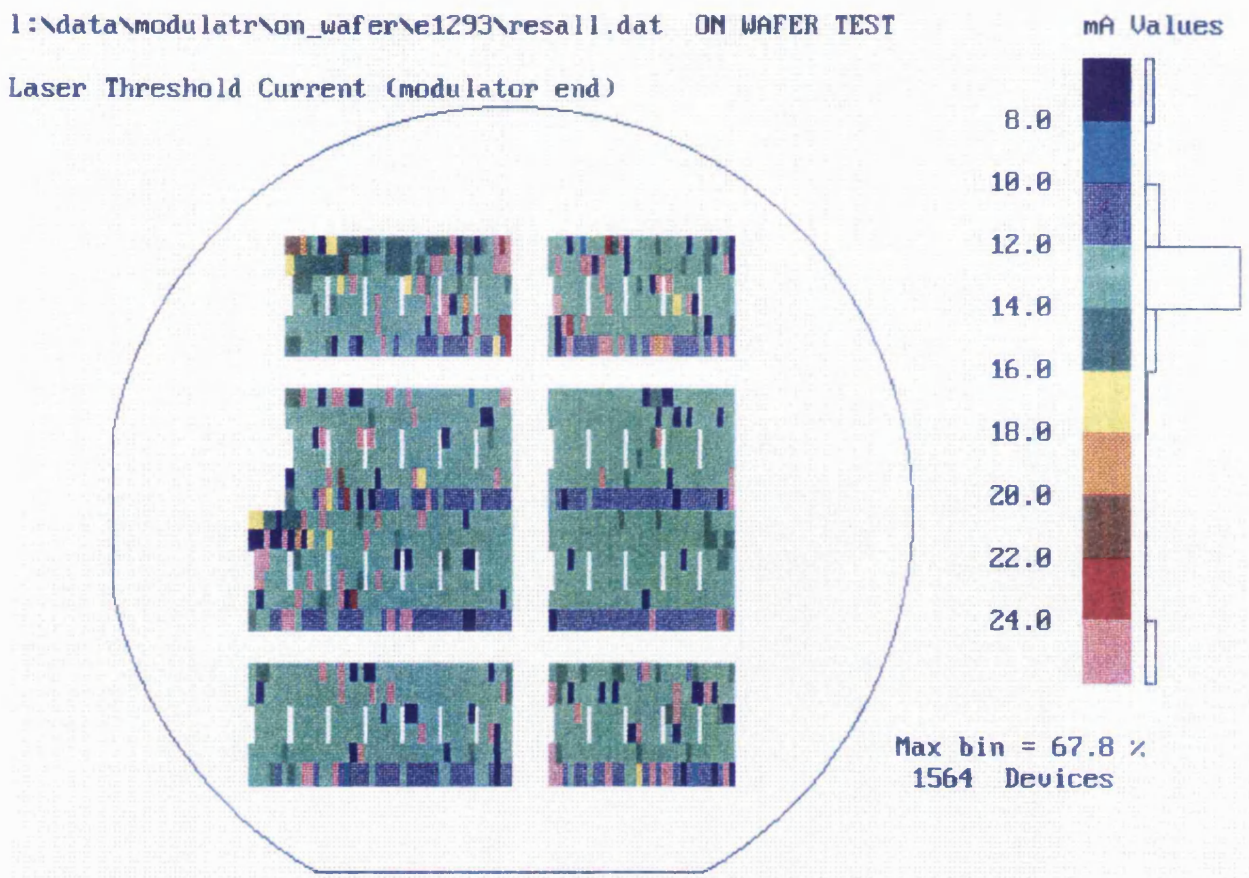

Fig 10.3 Map of laser modulator threshold current from probe card testing system

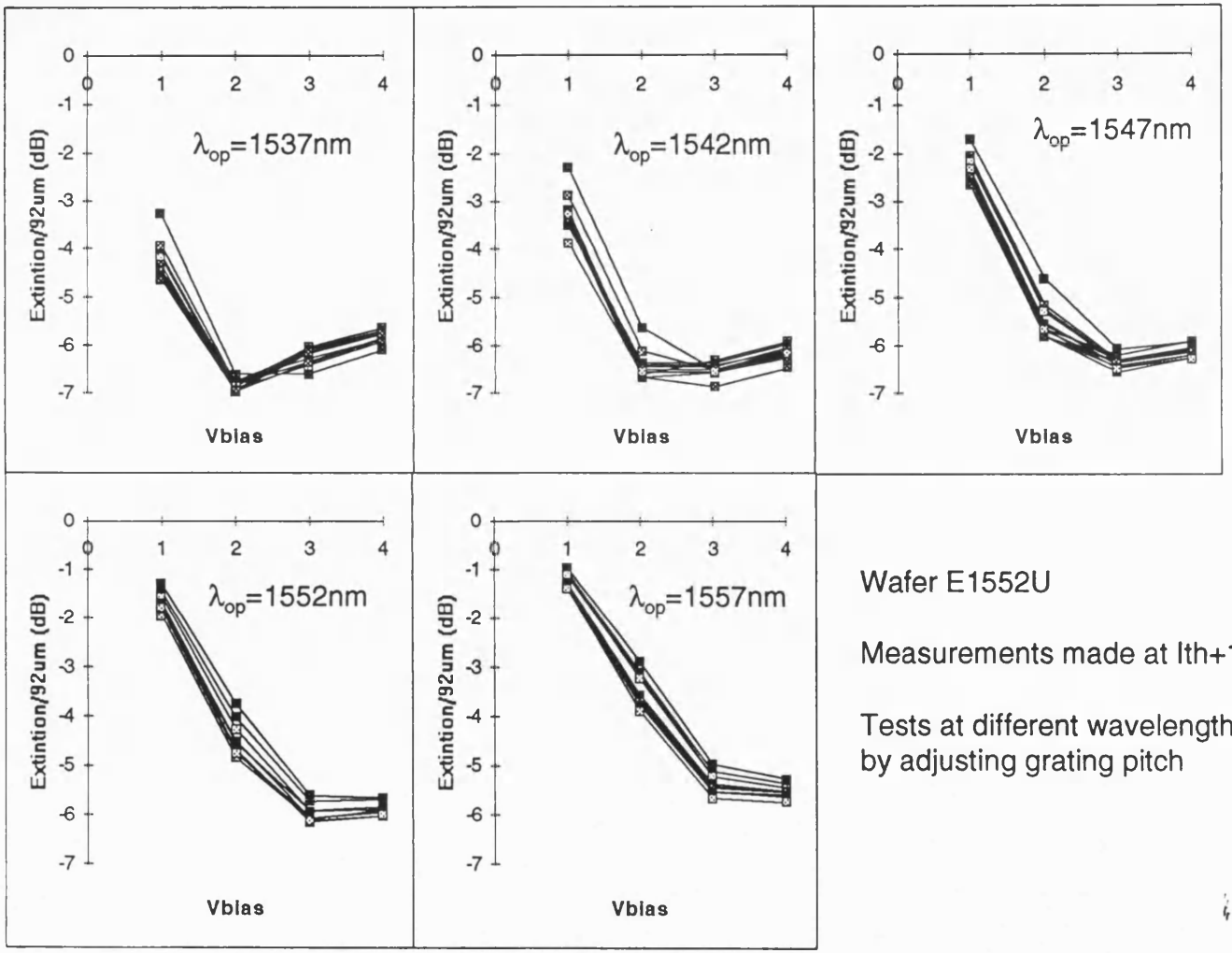

Fig 10.4 Modulator extinction as a function of bias voltage. Measurements made at a series of wavelengths and at 78 points across the wafer.

10.3. THE EFFECT OF THE LASER MODULATOR INTERFACE ON DEVICE PERFORMANCE

In the last few years there have been a number of reports on the use of integrated lasers and electroabsorption modulators for the transmission of NRZ data over digital communication links[3,4,5,6,7,8,9,10,11,12]. The behaviour of a selection of these devices is compared in Table 10.1.

The data transmission performances of the laser-modulators in the above table have been compared by calculating the product of the maximum transmission distance over standard fibre, and the square of the bit rate . This figure of merit is crudely related to the chirp performance of each device[13]. An increase in the value of the figure of merit indicates that the chirp performance of the device has become more suitable for transmission over standard fibre. In addition, the figure of merit should remain approximately constant, for a device with a given chirp characteristic, as the bit rate is varied. This means that it can be used to compare the results of transmission experiments conducted at different bit rates.

The numbers the table should be regarded with some caution as there are many adjustable parameters in the fabrication and testing of laser-modulators and, inevitably, the conditions employed tend to depend on the laboratory. This is particularly true for bit error rate measurements, where a large number of factors can have an influence on measured dispersion penalty.

If one examines Table 10.1 one can see that there is no strong correlation between the type of laser modulator interface and the device output power. However, the highest reported output power was obtained from a device with an LPE grown butt coupled interface, rather than one grown by MOCVD. This observation is consistent with the fact that LPE growth over steps appears to be less troublesome than that of MOCVD (see section 6.2.1).

There is also no obvious connection between the laser modulator interface design and its data transmission performance. This is not surprising as the transmission performance is primarily determined by the chirp behaviour of the laser-modulator. Changing the design of the interface should not affect this behaviour, though devices with different interface efficiencies may exhibit different amounts of laser chirp as a result of different levels of optical feedback from the modulator facet[14]. However such feedback is also

Table 10.1 Comparison of Laser Modulator Performance

Laboratory	Fujitsu	KDD	Philips	NTT	NEC	AT&T	Hitachi	BNR
No. of eptiaxial growths	3 LPE 1 MOCVD	≥4	≥4 MOCVD	2 MOCVD	3 MOCVD	3 MOCVD	3 MOCVD	2 MOCVD
Laser modutor interface	Butt	Butt	Butt	Evanescent	SAG	SAG	SAG	Planar
Lateral confinement	BH (Fe)	BH (Fe)	BH (Fe)	Ridge	BH	BH (Fe)	BH (Fe)	Ridge
Coating on laser facet	None	AR	?	None	None	None	HR	AR
Modulator type	FK	FK	FK	QCSE	QCSE	QCSE	QCSE	QCSE
Modulator length (μm)	200	240	250	250	200	200	200	320
Threshold current (mA)	20	?	?	15	15	12	8-15	20
Fibre coupled power (dBm)*	~8	2.8	5	3	2.5	0	6	2.7
at laser current (mA)	150	?	?	100	100	100	100	150
Extinction (dB)	13	10	7	22	13	12	22	12
for voltage swing (V)	5	1.4	2	2	3	2	2	2
3dBe bandwidth (GHz)	10.3	4.1	5	15	>4	?	8	~10
Dispersion penalty (dB)+	1.2	0	1	1	0.5	1.2	0	0.4
at bit rate B (Gb/s)	5	2.4	10	20	2.5	2.5	2.5	2.5
over standard fibre of length L (km)	55	135	37.5	100 DSF	80	517	200	360
$B^2.L$ ($km.Gb^2/s^2$)	1375	778	3750	n/a	500	3231	1250	2250
Reference	3	4	5	6,7,8	9,10	11	12	n/a

* Measurement with 0V applied to modulator

+ Penalties should be treated with caution as they are dependent on many system parameters

GLOSSARY SAG=selective area growth BH=buried heterostruture AR=anti-reflection DSF=dispersion shifted fibre
FK=Franz-Keldysh QCSE=quantum confined Stark effect HR=high reflection

influenced by the facet reflectivity, the modulator insertion loss and the modulator length. Consequently the effect of this parameter cannot easily be extracted from the table.

The only parameter in the table which shows a clear correlation with the type of interface is the number of epitaxial growths required during device fabrication. This reason is that the butt coupling technique requires one more epitaxial growth than other methods of interface construction. The additional growth required for the butt coupling scheme is often troublesome if it is performed by MOCVD, for the reasons described in section 6.2.1. Hence the fabrication schemes for butt interfaces tend to be more arduous then those for other coupling techniques.

In practice some of the performance parameters that the laser modulator interface design is likely to affect are difficult to measure. These parameters include the reliability of the device and the reproducibility of the fabrication process. Data on reliability inevitably takes some time to gather and often remains unpublished. Information on reproducibility is also rare as it can only be obtained by making a large number of measurements. Reliability and reproducibility will have a major influence on the success with which photonic integration can be applied to a particular application. However, comprehensive information on the effect of the interface design on these parameters is unlikely to be available for some time.

10.4. REFERENCES

1 I.K.Czajkowski, M.A.Gibbon, GH.B.Thompson, P.D.Greene, A.D.Smith and M.Silver, *IEE Electronics Letters*, 1994, **30**, pp.900-901

2 J.E.Zucker, I.Bar-Joseph, B.I.Miller, U.Koren and D.S.Chemla, *Applied Physics Letters*, 1989, **54**, pp.10-12

3 H.Soda, M.Furutsu, K.Sato, N.Okazaki, S.Yamazaki, H.Nishimoto and H.Ishikawa, *IEE Electronics Letters*, 1990, **26**, pp.9-10

4 H.Tanaka, M.Suzuki, H.Taga, S.Yamamoto and Y.Matsushima, *IEE Electronics Letters*, 1991, **27**, pp.390-391

[5] P.I.Kuindersma, P.P.G.Mols, G.L.A.v.d.Hofstad, G.Cuypers, M.Tomesen, T.v.Dongen and J.J.M.Binsma, *IEE Electronics Letters*, 1993, **29**, pp.1876-1878

[6] K.Sato, I.Kotaka, K.Wakita, Y.Kondo and M.Yamamoto, *IEE Electronics Letters*, 1993, **29**, pp.1087-1088

[7] K.Wakita, K.Sato, I.Kotaka, M.Yamamoto and T.Kataoka, *IEE Electronics Letters*, 1994, **30**, pp.302-303

[8] T.Kataoka, Y.Miyamoto, K.Hagimoto, K.Sato, I.Kotaka and K.Wakita, *IEE Electronics Letters*, 1994, **30**, pp.872-873

[9] T.Kato, T.Sasaki, K.Komatsu and I.Mito, *IEE Electronics Letters*, 1992, **28**, pp.153-154

[10] K.Momatsu, T.Kato, M.Yamaguchi, T.Sasaki, S.Takano, H.Shimizu, N.Watanabe and M.Kitamura, *Proceedings of the Optical Fibre Conference*, 1994, paper TuC3

[11] J.E.Johnson, T.Tanbun-Ek, Y.K.Chen, D.A.Fishman, R.A.Logan, P.A.Morton, S.N.G.Chu, A.Tate, A.M.Sergent, P.F.Sciortino, Jr., and K.W.Wecht, *Conference Digest of 14th IEEE International Semiconductor Laser Conference* 1994, (IEEE Catalog Number 94CH3379-5), pp.41-42

[12] M.Aoki, N.Kikuchi, K.Sekine, S.Sasaki, M.Suzuki, T.Taniwatari, Y.Okuno, A.Takai and T.Kawano, *IEE Electronics Letters*, 1993, **29**, pp.1983-1984

[13] F.Koyama and K.Iga, *IEEE Journal of Lightwave Technology*, **6**, 1988, pp.87-93

[14] J.A.J.Fells, M.A.Gibbon, G.H.B.Thompson, I.H.White, R.V.Penty, A.P.Wright, R.A.Saunders, C.J.Armistead and E.M.Kimber, "Improving the system performance of integrated multiquantum well laser modulators with negative chirp", *submitted to OFC'95*

Chapter 11

The Future for Photonic Integration

11.1. INTRODUCTION

The integrated laser and electroabsorption modulator is likely to be one of the first cases of photonic integration that is successful in a commercial setting. One of the reasons for this probable success is the fact that a low chirp source of this type is desirable in long haul, high bit rate transmission systems. However, the fact that the laser and the modulator have similar layer structures is also significant, as it has enabled the development of reliable devices that are manufactured using a simple and reproducible process.

There are a number of other situations, in addition to laser-modulator integration, where photonic integration could bring considerable benefits. This number is likely to increase with time, as the optical and optoelectronic parts of transmitters become more complicated, and their cost becomes more important. The challenge for these devices is to develop the device designs, and simultaneously tame the technology, until one reaches a point where such integration becomes practical. This chapter describes some of the developments that are happening now, and some that may be possible in the future.

11.2. THE DEVELOPMENT OF INTEGRATION TECHNOLOGY

The development of new integration technologies and the investigation of existing ones is likely to be a productive, though boundless, task for some time to come. Some technology developments that would be particularly useful are summarised below.

11.2.1. Control of Selective Area MOCVD

Chapter 7 showed that the behaviour of selective area MOCVD under particular growth conditions could be predicted with reasonable accuracy. However, to date, these predictions have only been verified for devices with structure in two dimensions. It would be useful to extend this analysis to three dimensions to enable accurate design of, for example, chirped gratings and

waveguide tapers. The mathematical extension of the current model to three dimensions would not be difficult. However, the way in which the solution was obtained would have to be modified if the result was to be obtained in a reasonable time interval.

The data presented in chapter 7 also showed that excess Ga diffuses further away from the silica masks than excess In during selective growth. The analysis in section 7.4.3 indicated that the different diffusion distances may be related to the fact that the methyl-gallium and methyl-indium bonds in the growth precursors have different strengths. It should be possible to deliberately engineer the strength of these bonds by developing new types of precursor, such as some of those that are currently being developed for safety and other reasons[1]. This would allow one to make the diffusion lengths of the group III species equal to one another. The advantage of this development would be the ability to obtain much greater variations in growth rate without encountering problems with lattice mismatch.

11.2.2. Butt Coupling

Butt coupling is a very attractive integration technology because of its great flexibility and high theoretical efficiency. Chapter 6 showed that low loss butt interfaces have probably been fabricated by LPE, but that there are still significant problems when this technique is combined with MOCVD. This is unfortunate as LPE has now been superseded by MOCVD in most laboratories. The reason is that the latter technique produces material with superior uniformity and sharper heterostructure interfaces.

The difficulties with MOCVD based butt coupling may well be related to the fact that the composition of GaInAsP deposited from a given source mixture depends on the crystallographic orientation of the facet on which it is deposited. A number of such crystal facets develop when conventional multilayer device structures are grown over contoured substrates[2,3,4,5]. The type and area of each facet exposed depends on, the crystallographic orientation of the step, the growth conditions, the composition of the GaInAsP layer and the time elapsed since the start of deposition[3,5]. A number of authors have made extensive qualitative studies of the way in which these crystallographic facets evolve under different conditions. However quantitative studies of the composition of such structures are rare[3]. Extensive compositional studies of this type may now be possible with the advent of techniques such as high resolution Auger analysis, and computer controlled

focused ion beam milling followed by STEM-EDX[3]. The prospect of using these techniques to develop a general model of the behaviour of MOCVD on structured substrates is daunting, as the parameter space is very large. However, high resolution analysis techniques would be an invaluable aid to the optimisation of known structures, such as butt interfaces. A study of this type would involve mapping the compositional variations across a longitudinal section through the butt interface. The composition profile obtained would then be fed into a numerical model to calculate the effect of such variations on the propagation of the optical mode through the interface. Finally the result obtained would be used to guide adjustment of growth conditions, such as the composition of the gas in the reactor, and the facets exposed at the start of deposition.

Photonic integration by butt coupling may be easier with more recently developed epitaxial deposition processes, such as CBE. Selective growth by CBE is possible[6,7,8], but relatively little is known about its behaviour. CBE growth over structured surfaces is likely to be different from that of MOCVD but, once again, data on this subject is very limited. A quantitative comparison of the integration abilities of the two technologies would be very useful.

11.2.3. Mirror Etching

Section 5.6 described how the loss on reflection from an etched mirror, such as one of those used in the two dimensional demultiplexer, has been reduced to ~1dB. The reduction in loss was obtained through the addition of carbon dioxide to the methane-hydrogen reactive ion etching mixture[9,10]. The development of the etching technology to achieve such a loss is a significant achievement. However, it is desirable to reduce the magnitude of the mirror losses to even lower levels if one wishes to fabricate complex devices. This would involve development of the existing etching technology or the use of a new completely new one.

The development of a technology to coat the walls of an etched recess with a reflective material would also be helpful. The availability of such a process would allow one to design devices in which mirror structures illuminated at normal incidence did not suffer from excessive losses. Soole of Bellcore and Cremer of Siemens have already developed metal coats for this application[11,12].

11.3. DEVICES BASED ON THE INTEGRATED LASER MODULATOR

Much of this dissertation has described the development of an integrated laser modulator for the transmission of NRZ data. However, the integrated-laser electroabsorption modulator also has a second application as a soliton[13,14] pulse generator. The pulses are generated by applying a electrical signal, which is a combination of a negative dc bias and sine wave, to the modulator. These drive conditions produce short optical pulses because the modulator spends most of the sine wave period in deep extinction. The integrated laser modulator is an attractive soliton generator because the pulse jitter of such a transmitter is simply determined by the stability of the sine wave from the electrical generator. It is also possible to integrate a second modulator onto the chip, so that data can be modulated onto the train of pulses[15].

It seems likely that the chirp requirements for transmission over long spans of standard fibre at 10Gb/s will be difficult to meet with an electroabsorption modulator. However they may be satisfied by a Mach-Zehnder device[16]. The integration of such a modulator with a laser will offer the same benefits as laser-electroabsorption modulator integration. However, the integration procedure will be more difficult for the Mach-Zehnder device as the layer structures of the laser and the modulator will inevitably be more dissimilar than those of the device discussed in this dissertation.

A device which would be easier to make, would be one in which a laser was integrated with a Mach-Zehnder structure fabricated on material suitable for absorption modulation, rather than phase modulation. This approach would allow one to use the selective epitaxy integration scheme described in chapter 9. The modulator would be in the off condition when the same bias was applied to both arms, if the one arm of the Mach-Zehnder device was half a wavelength longer than the other. Applying a bias to one of the arms would then switch the device to its transmitting state. The advantage of this device over a conventional electroabsorption modulator is that the sign of the modulator chirp is reversed. Consequently, it would be easier to operate in the negative chirp regime desirable for high bit rate transmission over standard fibre. It is difficult to obtain such chirp from conventional electroabsorption devices without incurring large insertion losses.

11.4. DEVICES INCORPORATING 2D OPTICS

In section 5.6 I stated that the 2D demultiplexer had to be integrated with photodetectors if it was to become a useful component. The integration of a demultiplexer with an array of photodiodes has, in fact, recently been demonstrated at BNR Europe. The photodiode array was integrated with the slab waveguide using a method similar to the evanescent coupling technique described in section 6.2.3. Two dimensional grating demultiplexers integrated with photodiode arrays have also been demonstrated by Soole at al[17] and Cremer at al[18].

Cremer has taken the two dimensional optics technology one stage further by using butt coupling to integrate an amplifier with a demultiplexer and photodiode combination[19]. This advance makes the losses of the mirror based components much less important. The idea of placing an amplifier before a grating is attractive because the grating automatically filters the spontaneous emission from the former component, thus improving the sensitivity of the photodiode receivers.

The 2D optics technology has applications other than the development of an integrated demultiplexer-photodiode array. One example is the integration of a laser array with a 2D grating to produce a WDM source with well controlled wavelength spacing[20]. Hybrid[21,22] and monolithically integrated[23,24] versions of such a device have already been demonstrated.

One advantage of 2D optics is that the mirrors allow one to make major changes in the angle at which an optical beam is propagating with minimal loss. Consequently the 2D technology could be used to make a compact combiner for a large number of sources on the same chip. It could also be used to perform the reverse operation. It is difficult to guide light around such large angles in purely waveguide based components, without either making the device very large, or incurring large losses.

11.5. DEVICES BASED ON SELECTIVE AREA EPITAXY

As mentioned in section 10.2, selective area epitaxy was not used in the final version of the integrated laser modulator. However it seems likely that it will find application in other areas. One example is the fabrication of waveguide tapers for mode conversion[25]. Tapers of this type could be used to expand the optical mode at the inputs and outputs of lasers[26], modulators, amplifiers and

more complex optoelectronic devices. The expansion of the optical mode in this manner increases the coupling efficiency between the device and conventional optical fibre. It also makes the coupling efficiency more tolerant of slight misalignments. Consequently mode expansion is particularly useful for low cost packaging technologies[27,28] that rely on passive rather than active alignment.

Selective area epitaxy can also be used to integrate lasers with passive waveguides. One application of the latter integration procedure is in the development of high power lasers with non-absorbing facets to prevent catastrophic optical damage[29].

Finally, if the technology was sufficiently well controlled, selective area epitaxy could be used to create a low loss lens in a slab waveguide. The refraction in such a component would arise from the changes in thickness, and hence effective index, of the slab waveguide. The fact that the waveguide would be thicker next to the dielectric masks would make the optical function of such a component similar to that of a bi-concave lens in free space optics. One application would involve inserting the selectively grown region between an optical waveguide and a mirror designed to produce a collimated beam of a given width. This approach would reduce the distance between the waveguide output and the mirror, thus allowing one to produce wide collimated beams in a device of reasonable size.

11.6. REFERENCES

1 G.B.Stringfellow and J.J.Coleman, *"Metalorganic vapour phase eptiaxy 1992"*, (North-Holland, The Netherlands, 1992), pp.64-158

2 H.Sugiura, A.Rudra, J.F.Carlin, H.J.Buhlmann, D.Araujo and M.Ilegems, *Semiconductor Science and Technology*, 1993, **8**, pp.1063-1068

3 E.J.Thrush, J.P.Stagg, M.A.Gibbon, R.E.Mallard, B.Hamilton, J.M.Jowett and E.M.Allen, *Materials Science and Engineering* , 1993, **B21**, pp.130-146

4 E.J.Thrush, M.A.Gibbon, J.P.Stagg, C.G.Cureton, C.J.Jones, R.E.Mallard, A.G.Norman and G.R.Booker, *Journal of Crystal Growth*, 1992, **124**, pp.249-254

5 B.Garrett and E.J.Thrush, *J.Crystal Growth*, 1989, **97**, pp.273-284

6 Tsang W T, Yang L, Wu M C and Chan Y K 1991 *Electron. Lett* **27** 3

7 Wang Y L, Feygenson A, Hamm R A, Ritter D, Weiner J S, Temkin H and Panish M B 1991 *Appl. Phys. Lett.* **59** 443

8 Andrews D A, Rejman-Greene M A Z, Wakefield B and Davies G J 1988 *Appl. Phys. Lett.* **53** 97

9 S.M.Ojha, G.H.B.Thompson, C.G.Cureton, C.B.Roders, S.J.Clements, M.Asghari and I.H.White, *IEE Electronics Letters*, 1993, **29**, pp.805-807

10 G.H.B.Thompson, S.M.Ojha, S.Clements, I.H.White and M.Asghari, *Proceedings of the European Conference on Integrated Optics*, (Switzerland, 1993)

11 J.B.Soole, A.Scherer, Y.Silberberg, H.P.LeBlanc, N.C.Andreadakis, C.Caneau and K.R.Poguntke, *Electronics Letters*, 1993, **29**, pp.558-560

12 C.Cremer, N.Emeis, M.Schier, G.Heise and G.Ebbinghaus, *IEE Proc. J*, 1993, **140**, pp.71-74

13 L.F.Mollenauer and R.H.Stolen, *Fibreoptic Technology*, April 1992, pp.193-198

14 M.Suzuki, H.Taga, N.Edagawa, H.Tanaka, S.Yamamoto and S.Akiba, *IEE Electronics Letters*, 1993, **29**, pp.1643-1644

15 K.Sato, K.Wakita, I.Kotaka, Y.Kondo and M.Yamamoto, *Proceedings of 19th European Conference on Optical Communication (ECOC93)*, (Druckerei Richterswil, Switzerland, 1993), pp.313-316

16 C.Rolland, R.S.Moore, F.Shepherd and G.Hillier, *IEE Electronics Letters*, 1993, **29**, pp.471-472

17 J.B.Soole, A.Scherer, Y.Silberberg, H.P.LeBlanç, N.C.Andreadakis, C.Caneau and K.R.Poguntke, Electronics Letters, 1993, **29**, pp.558-560

18 C.Cremer, G.Ebbinghaus, G.Heise, R.Muller-Nawrath, M.Schienie and L.Stoll, Applied Physics Letters, 1991, **59**, pp.627-629

[19] C.Cremer, M.Schier, G.Baumeister, G.Ebbinghaus, H.Huber, W.Kunkel, J.G.Bauer, G.Kristen, J.Rieger, R.Schimpe and R.Strzoda, *IEE Electronics Letters*, 1994, **30**, pp.1625-1626

[20] P.A.Kirkby, *Journal of Lightwave Technology*, 1990, **8**, pp.202-211

[21] K.O.Nyairo, I.H.White, P.A.Kirkby and C.J.Armistead, *IEE Proc. J*, 1991, **138**, pp.337-342

[22] K.O.Nyairo, I.H.White, C.J.Armistead and P.A.Kirkby, *IEE Electronics Letters*, 1992, **28**, pp.261-263

[23] J.B.D.Soole, K.Poguntke, A.Scherer, H.P.LeBlanc, C.Chang-Hasnain, J.R.Hayes, C.Caneau, R.Bhat and M.A.Koza, *IEE Electronics Letters*, 1992, **28**, pp.1805-1807

[24] K.R.Poguntke, J.B.D.Soole, A.Scherer, H.P.LeBlanc, C.Caneau, R.Bhat and M.A.Koza, *Applied Physics Letters*, 1993, **62**, pp.2024-2026

[25] E.Colas, A.Shahar,T.B.Soole,W.J.Tomlinson,J.R.Hayes, C.Caneau and R.Bhat, *J. Crystal Growth*, 1991, **107**, p.226

[26] H.Kobayashi, H.Soda, M.Ekawa, N.Okazaki, S.Ogita and S.Yamazaki, *Conference Digest of 14th IEEE International Semiconductor Laser Conference* 1994, (IEEE Catalog Number 94CH3379-5), pp.191-192

[27] J.W.Parker, P.M.Harrison, P.J.Ayliffe, T.V.Clapp, M.C.Geear and R.G.Peall, *Microelectronic Engineering*, 1992, **19**, pp.215-218

[28] J.W.Parker, P.J.Ayliffe, T.V.Clapp, M.C.Geear, P.M.Harrison and R.G.Peall, *IEE Electronics Letters*, 1992, **28**, pp.801-803

[29] G.P.Agrawal and N.K.Dutta, *"Long wavelength semiconductor lasers"*, (Van Nostrand Reinhold, New York, 1986), pp.420-430

Appendix A

Grating Performance

Consider the situation shown below

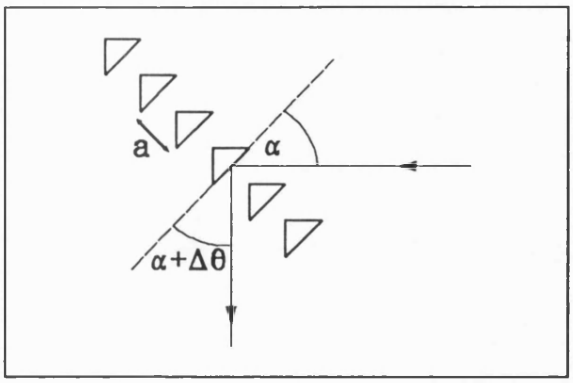

For diffraction into the N^{th} order

$$a[\sin\alpha+\sin(\alpha+\Delta\theta)]=\frac{N\lambda}{n} \tag{A.1}$$

where λ is the free space wavelength, n is the effective index and a is the grating period. Differentiating with respect to λ one finds that the dispersion along the output facet is then given by

$$l\frac{d\Delta\theta}{d\lambda}\approx\frac{2l}{\lambda}.\left(1-\frac{\lambda}{n}\frac{dn}{d\lambda}\right).\tan\alpha \tag{A.2}$$

where l is the focal length of the focusing mirrors.

Similarly for diffraction into the $(N+1)^{th}$ order

$$a[\sin\alpha+\sin(\alpha+\Delta\alpha+\Delta\theta)]=\frac{(N+1)\lambda}{n} \tag{A.3}$$

where Δα is the angle between the N^{th} and $(N+1)^{th}$ orders. Subtracting (A.1)

from (A.3) one finds that the separation between diffraction orders at the output facet is given by

$$l\Delta\alpha \approx \frac{l\lambda}{an.\cos\alpha} \qquad \text{(A.4)}$$

If the grating is illuminated with light of two wavelengths then two sets of diffraction orders are generated. The wavelength separation $\Delta\lambda$ required to make the diffraction orders of one wavelength superimpose with the adjacent orders of the other, is given by dividing the order separation (A.4) by the dispersion (A.2).

$$\Delta\lambda = \frac{\lambda^2}{2an.\left(1-\frac{\lambda}{n}\frac{dn}{d\lambda}\right).\sin\alpha} \qquad \text{(A.5)}$$

This formula is only valid for large N.

The extent of the diffraction pattern is determined by the effective width of each grating element. The series of grating elements can be regarded as a comb function convoluted with an element aperture. The diffracted beam is the Fourier transform of this arrangement. This is another comb function (representing the series of diffracted orders) multiplied by an envelope function which is the Fourier transform of the element aperture. The width of the element aperture presented to the incoming beam is a.cos α. Consequently the electric field envelope function E is given by

$$E = A\ sinc\left(\frac{\pi n}{\lambda}.\ a.\cos\alpha.\ \sin(\Delta\theta)\right) \qquad \text{(A.6)}$$

where A is a constant.

The resolution of the grating is determined by its total width and the profile of the incident illumination. This can be expressed in terms of Fourier diffraction theory by stating that the Fourier transform of the illumination profile, truncated by the grating width, is convoluted with the comb function of output orders described above. An approximate analysis of the effect of the grating width on the wavelength resolution of the device, can be made by assuming that the grating is illuminated with a Gaussian beam. The electric field envelope

function F to be convoluted with each diffraction order is then given by

$$F = B.\int_{-\frac{w_g}{2}}^{\frac{w_g}{2}} e^{-\frac{4y^2}{w_0^2}}.\, e^{i\frac{2\pi n.\sin(\Delta\theta)}{\lambda}.y}\, dy \qquad \text{(A.7)}$$

w_0 is the width of the Gaussian beam measured to the $-1/e^2$ intensity points, w_g is the width of the grating projected onto the incident wavefront and B is a constant. An approximate solution to the above equation can be found by turning the integration into a sum. This sum can either be regarded as a numerical solution to the above integral, or as the addition of the amplitude and phase components from each grating element. In practice the effective width of each grating element is $\sim w_0/10$ and hence this is an appropriate unit of division for the approximation of the integral. If one uses this approach then the electric field envelope function is given by

$$F = \frac{Bw_0}{10}\sum_{r=-b}^{b} e^{-\frac{r^2}{25}}\, e^{i\frac{2\pi.n.w_0}{10\lambda}.r.\sin(\Delta\theta)} \qquad \text{(A.8)}$$

where b is the nearest integer to $\frac{5w_g}{w_0}$

Appendix B

Device Specifications

Layer Structure	
Substrate	InP (Fe doped)
Buffer layer	
Material	InP (undoped)
Thickness	1 μm
Guide layer	
Material	GaInAsP (undoped)
λ_{PL}	(1.31±0.01)μm
Thickness	(0.6±0.1)μm

Derived Parameters

Effective relative permittivity (λ=1.51μm)

TE mode	10.87±0.18
TM mode	10.71±0.20

Lateral Guiding

Ridge waveguide

Rib depth	37 nm

Layout

Number of grating elements	16
Grating spacing	14.087 or 14.248 μm
Angle of grating illumination	45°
Parabolic mirror focal length	620 μm
Mirror Width	175 μm

Appendix C

Effect of Non-Uniform Effective Index on Position of Device Output

As discussed in section 4.2 a gradient in the effective index will cause the collimated beam to deviate from its intended path. If such deviations occur before the final mirror, this mirror will be illuminated at an incorrect angle of incidence and the output will be displaced from the intended position as shown below.

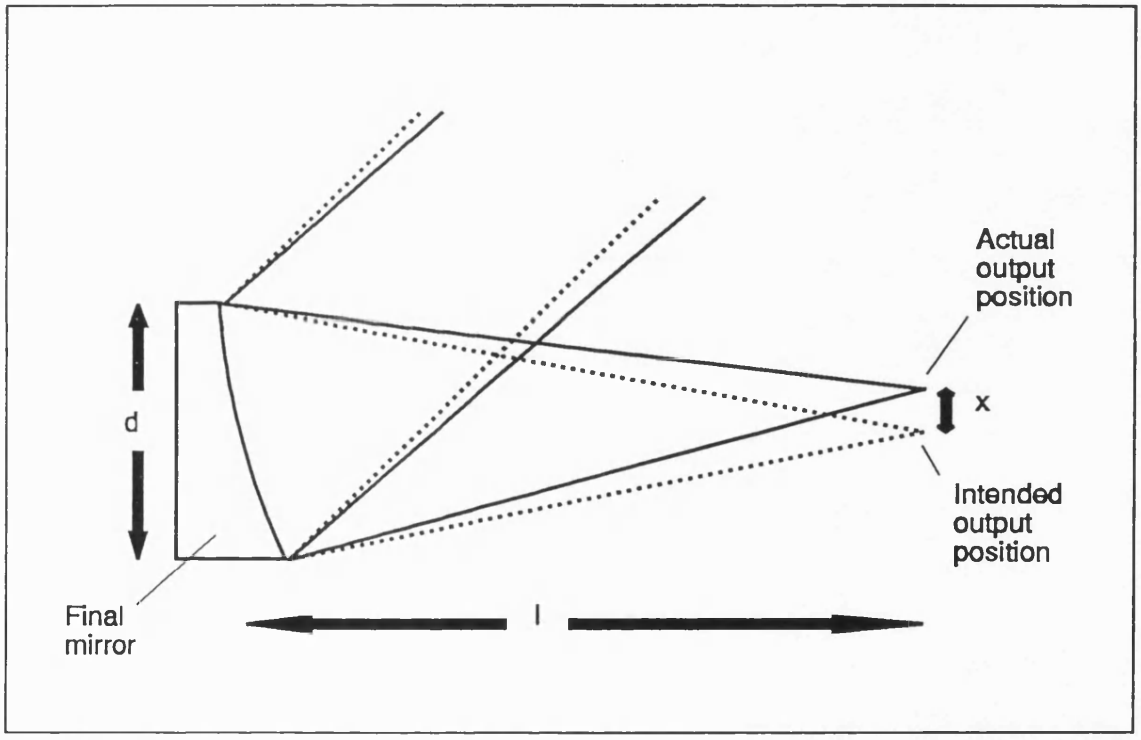

Effective index gradients after the final mirror will have less effect as their "optical leverage" is reduced.

The incorrect angle of incidence at the final mirror can be represented by an

additional path difference between the light incident at the top and the bottom of this mirror. If we assume that all of the path difference is introduced before the final mirror (the worst case), and that its value is the $\lambda/5$ benchmark quoted in chapter 4, then the deviation of the output can be established from the diagram below.

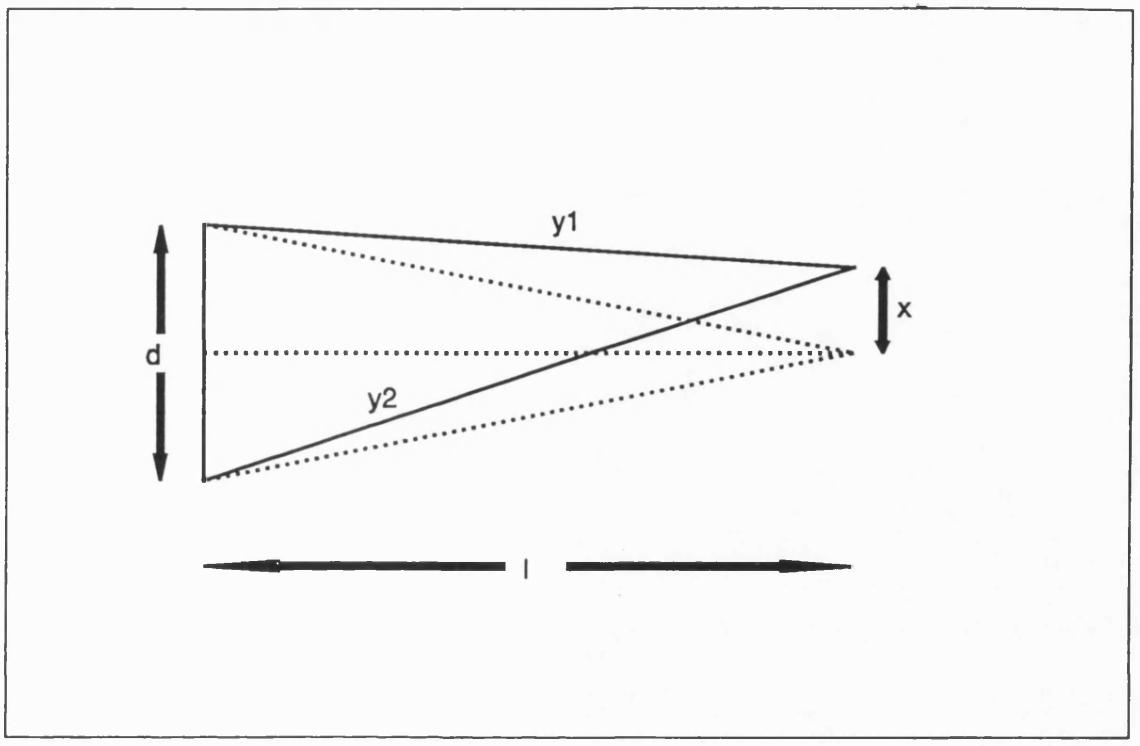

$$y_2 - y_1 = \frac{\lambda}{5} = \left[l^2 + \left(\frac{d}{2} + x\right)^2\right]^{\frac{1}{2}} - \left[l^2 + \left(\frac{d}{2} - x\right)^2\right]^{\frac{1}{2}} \qquad \text{(C.1)}$$

$$\therefore x \propto \frac{\lambda l}{5d} \qquad \text{(C.2)}$$

so if λ=0.46μm, l=620μm and d=175μm then x≈0.3μm

Appendix D

Effect of Strain on Bandgap of InP and GaInAsP

(Data from references 12 and 13 of Chapter 4, and from private communication with Dr Eoin O'Reilly of the University of Surrey)

Consider a thin layer of GaInAsP grown on top of an thick InP substrate. If the lattice constant of the epitaxial layer differs from that of the substrate then it will be left under biaxial tension or compression. In this situation the components e of the strain tensor are given by

$$e_{xx}=e_{yy}=-\gamma \tag{D.1}$$

and

$$e_{zz}=\frac{-2\sigma}{1-\sigma}e_{xx} \tag{D.2}$$

where γ is the lattice mismatch, z is the growth direction and σ is Poisson's ratio. The deformation can be represented as the sum of a hydrostatic volume change

$$\frac{\Delta V}{V}=e_{xx}+e_{yy}+e_{zz}=-2\frac{1-2\sigma}{1-\sigma}\gamma \tag{D.3}$$

and an axial strain (in which there is no volume change).

$$e_{ax}=e_{zz}-\frac{1}{2}(e_{xx}+e_{yy})=\frac{1+\sigma}{1-\sigma}\gamma \tag{D.4}$$

The former distortion increases the energy of the conduction band by ~100 meV /% strain. The latter deformation does not affect the position of the conduction band minimum but splits the light and heavy hole valence band maxima equally about their original locations with the magnitude of the separation being ~60 meV /% strain. The combined effect of the two distortions on the Γ point band structure is as shown below.

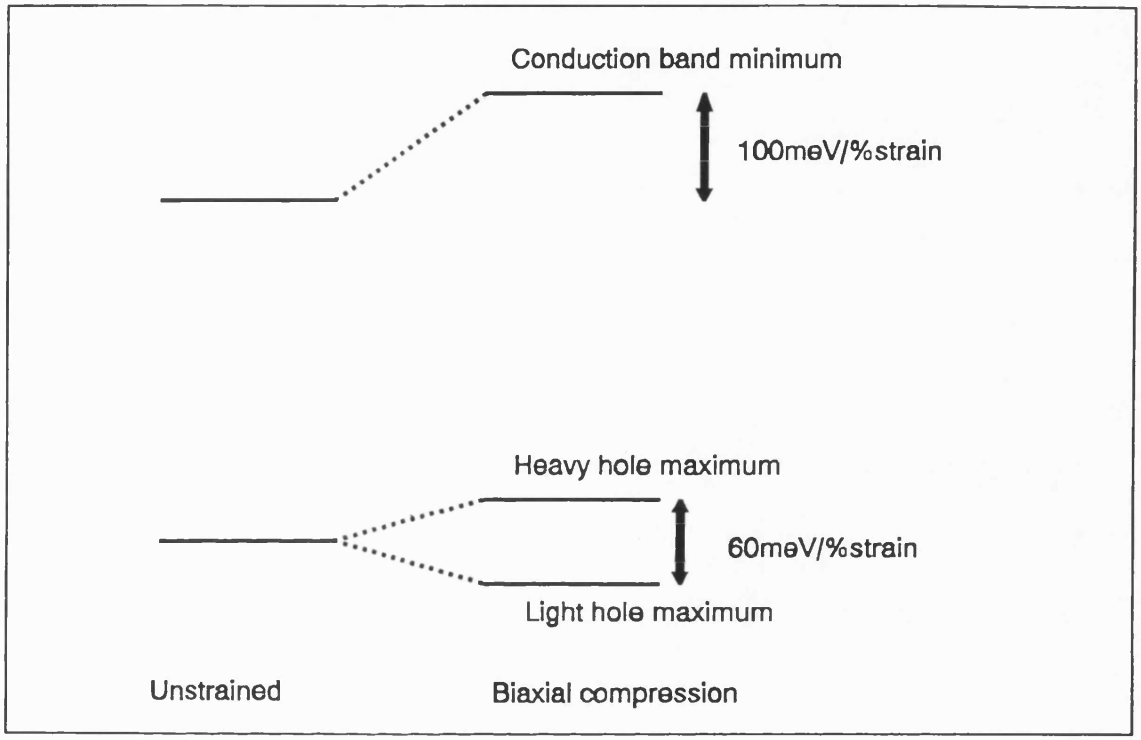

Appendix E

Effect of Compositional Variations on Butt Joint Coupling Efficiency

Section 6.2.1 describes how the composition of a GaInAsP alloy deposited from a given MOCVD source mixture depends on the crystallographic orientation of the facet on which it is deposited. This phenomenon is likely to have an impact on the coupling efficiency of a butt joint. The reason is that alloys with different compositions will, in general, have different refractive indices. Unfortunately, the problem is complicated, as the type and area of each facet exposed depends on the nature of substrate, the growth conditions, the nominal composition of the GaInAsP alloy and the time elapsed since the start of growth. Consequently a full analysis would entail mapping the compositional variations across the interface region. As far as I am aware, nobody has reported such a comprehensive survey. However, Thrush et al have measured the composition of a GaInAsP alloy deposited on two different crystal planes[1]. I have used this data to assess whether the compositional variations seen in such epitaxial growth are sufficient to cause significant losses in butt coupled interfaces. It should be emphasised that the calculation is very approximate, and that accurate analysis would require a great deal of further study.

Thrush et al observed that $Ga_{0.15}In_{0.85}As_{0.3}P_{0.7}$ and $Ga_{0.1}In_{0.9}As_{0.5}P_{0.5}$ were deposited on different crystallographic planes from the same source mixture[1]. I have used the above compositions to calculate that the bandgaps of the materials were 1144 and 920meV respectively[2]. These bandgaps were then converted into refractive indices for light of 1.55μm in wavelength. This was achieved by assuming that the refractive indices were the same as those of lattice matched GaInAsP alloys with identical bandgaps. The justification for this assumption was that the Kramers-Kronig relationships[3,4] indicated that changes in the energy levels of bands far away from the bandgap would have little effect on the refractive index. The index calculation[5] was performed using the Afromowitz modified single oscillator model[6,7,8]. The refractive indices for the two compositions were 3.27 and 3.41 respectively.

The effect of these variations in refractive index on the propagation of light through a butt interface was estimated as follows. It was assumed that the two regions of different refractive index grew next to the butt interface in the

manner illustrated in Figure E.1. The angle of deflection for a ray propagating through the interface was then determined from Snell's law[9]. The power transmission coefficient for the ray was also determined using the Fresnel coefficients[10]. The indices used in these computations were the effective indices of 0.4μm thick waveguides clad with InP, and containing material of the refractive indices calculated above. The reason for the use of the effective indices was that the compositional variations were only found in the waveguide layer, and not in the cladding around it.

The loss caused by the deflection of the waveguide mode was then approximately calculated by assuming that the optical mode had a Gaussian profile with a radius, w, which gave it the same optical width as the true waveguide mode. The loss Γ when one such Gaussian mode was coupled into another at an angle of θ radians was given by

$$\Gamma(\mathrm{dB}) = \left(\frac{\pi\theta w}{\lambda}\right)^2 \log_{10} e \qquad \text{(E.1)}$$

where λ was the wavelength of light in the waveguide[11].

The combined interface transmission loss as a result of the reflection and deflection of the Gaussian mode was plotted as a function of the interface angle α. This plot is shown in Figure E.2.

The results shown in Figure E.2 indicated that the loss caused by the change in index was small, when α was small. However, it rose rapidly as α became large because the deflection of light passing through the interface, and the power reflection from it, both increased. In addition, when the material of higher refractive index was placed next to the butt joint, the condition for total internal reflection was achieved when α was greater than 76.9°.

The above calculations indicated that butt coupled interfaces may suffer from severe losses if the epitaxial material next to the butt joint is of unusual composition, and is deposited on planes slightly inclined to (100). The deposition of epitaxial material on planes slightly inclined to (100) is common in such regions[12]. However, I am not aware of any information on the composition of such material. It seems that this is an area worthy of further study.

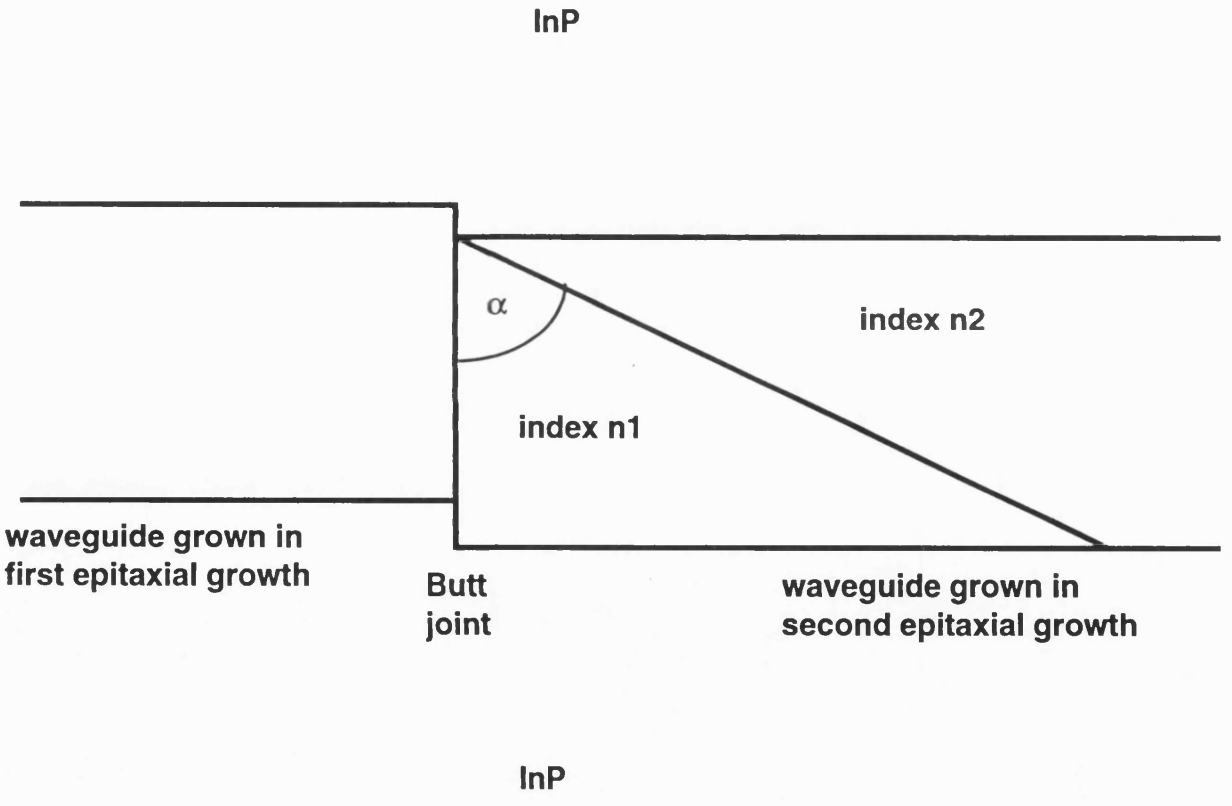

Fig E.1 Model of butt interface for loss calculations

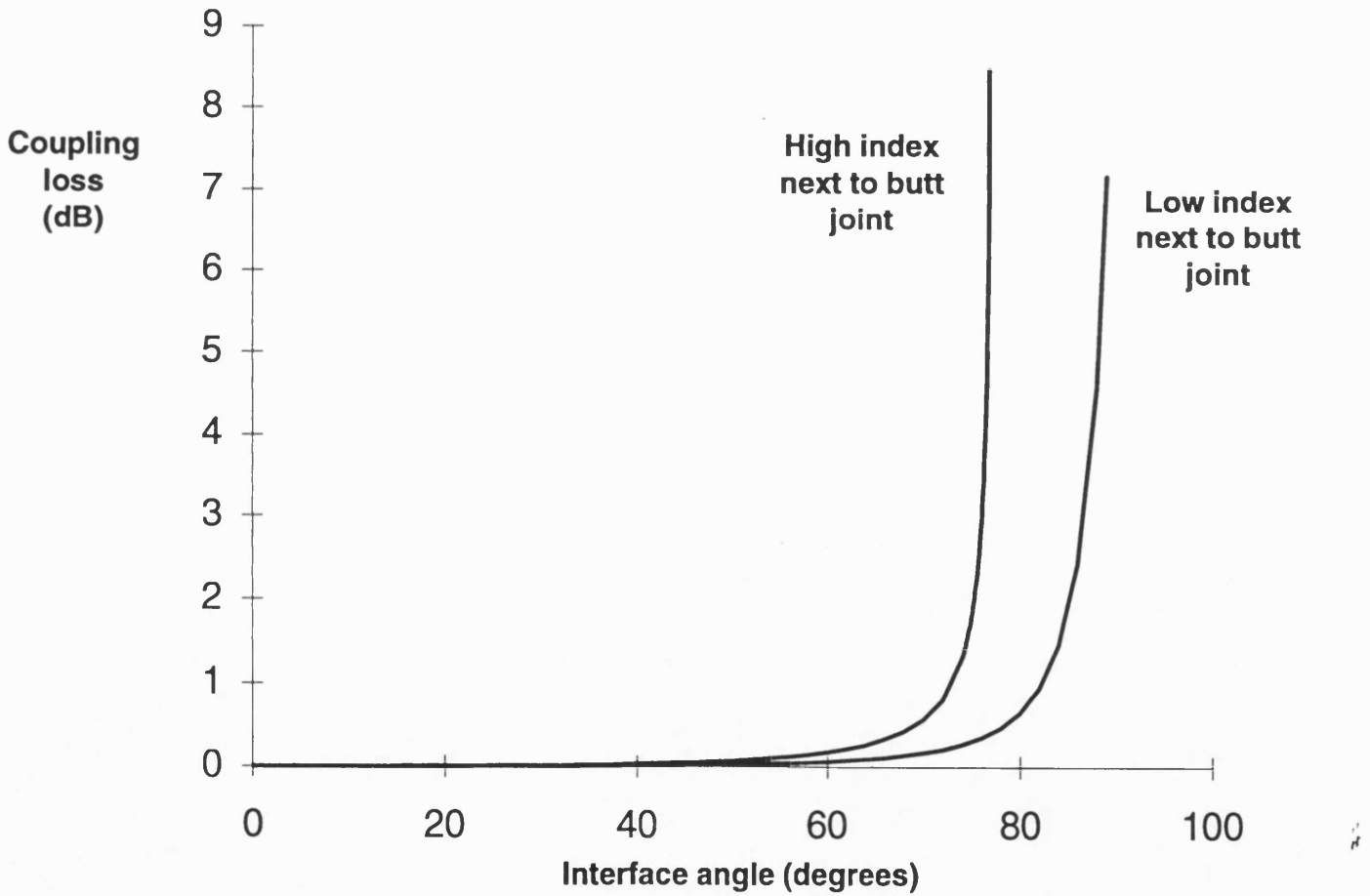

Fig E.2 Effect of compositional variations on butt joint coupling efficiency

REFERENCES

1 E.J.Thrush, J.P.Stagg, M.A.Gibbon, R.E.Mallard, B.Hamilton, J.M.Jowett and E.M.Allen, *Materials Science and Engineering* , 1993, **B21**, pp.130-146

2 Computer program to make this calculation supplied by Mark Silver, Department of Physics, Surrey University.

3 F. Stern, *Solid State Physics*, 1963, **15**, pp.299-408

4 A. Abragam, *"Principles of Nuclear Magnetism"* (Clarendon, 1961)

5 Computer program to make this calculation supplied by James Whiteaway, BNR Europe, London Rd, Harlow, Essex CM17 9NA

6 M.A.Afromowitz, *Solid State Commun.*, 1974, **15**, pp.59

7 K. Utaka, Y.Suematsu, K.Kobayashi and H.Kawanishi, *Jpn. J. Appl. Phys.*, 1980, **19**, pp.L137-L140

8 B.Broberg et al, *J.Appl.Phys.*, 1984, **55**, pp.3376

9 E.Hecht and A.Zajac, *"Optics"*, (Addison-Wesley, Reading, Massachusetts, 1974) p.63

10 E.Hecht and A.Zajac, *"Optics"*, (Addison-Wesley, Reading, Massachusetts, 1974) p.71-80

11 M.Saruwatari and K.Nawata, *Appl. Optics*, 1987, **18**, pp.1847-1856

12 B.Garrett and E.J.Thrush, *J.Crystal Growth*, 1989, **97**, pp.273-284

Appendix F

Iterative Fourier Method for Selective Growth Model

The physical model used for selective growth is described in section 7.4.1 and is shown in Figure 7.16. I am not aware of an analytic solution to this problem. Indeed the boundary conditions are fundamentally incompatible with any form of analytic Sturm-Liouville analysis[1]. However, when faced with the need to use a numerical method it seemed worthwhile to use a technique whereby the iterative matching could be reduced to a line, rather than having to take place over the whole area covered by the problem. The reduction of the problem was achieved by separation of the variables as shown below.

If one looks at the problem in Fig 7.16 one can choose a solution of the form

$$n = n_0 - X(x)Z(z) \tag{F.1}$$

but

$$\nabla^2 n = 0 \tag{F.2}$$

therefore

$$\nabla^2 X(x)Z(z) = 0 \tag{F.3}$$

and the new boundary conditions are as shown in Fig F.1.

Now if we choose X(x) to be

$$X(x) = \sum_{\alpha=0}^{\alpha=\infty} A_\alpha \cos\left(\frac{\pi\alpha x}{w}\right) \tag{F.4}$$

then we have allowed X(x) to be any function that satisfies the lateral boundary conditions. The solution for Z(z) is now uniquely defined for each value of α so that

$$n = n_0 - A_0(d-z) - \sum_{\alpha=1}^{\alpha=\infty} A_\alpha \cos\left(\frac{\pi\alpha x}{w}\right)\sinh\left(\frac{\pi\alpha}{w}(d-z)\right) \tag{F.5}$$

and by differentiating we find that

$$\left[\frac{\partial n}{\partial z}\right]_{z=0} = A_0 + \sum_{\alpha=1}^{\alpha=\infty} A_\alpha \cdot \frac{\pi\alpha}{w}\cos\left(\frac{\pi\alpha x}{w}\right)\cosh\left(\frac{\pi\alpha d}{w}\right) \tag{F.6}$$

We can set A_0 to one without loss of generality as it simply changes the unperturbed growth rate, and we are looking for changes in the normalised growth rate. This decision defines the concentration n_0 at the top of the window to be

$$n_0 = \left(\frac{D}{k} + d\right) \tag{F.7}$$

The model can be started by assuming that

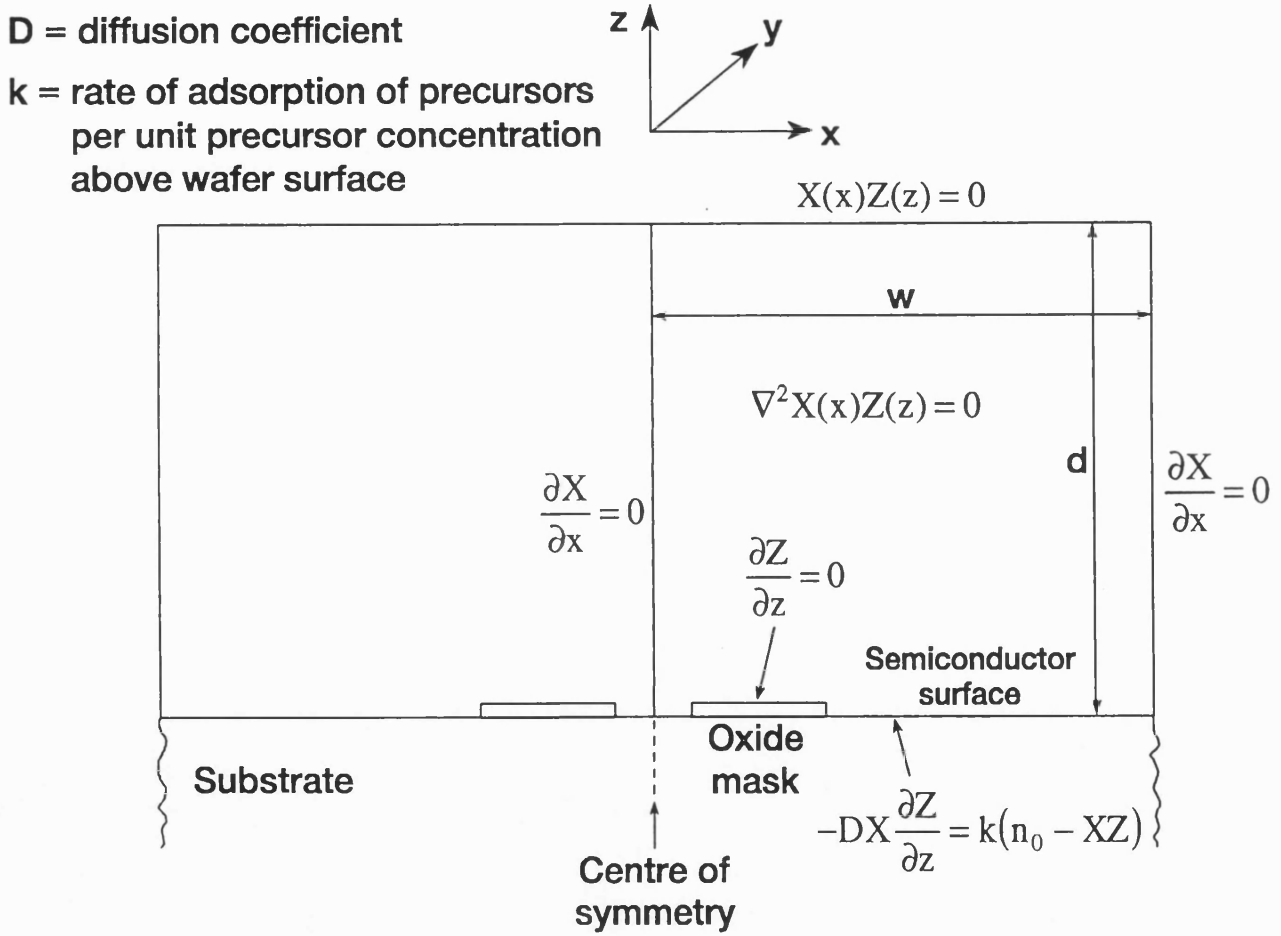

Fig F.1 Geometry and boundary conditions used in MOCVD growth model

$$\left[\frac{\partial n}{\partial z}\right]_{z=0} = 0 \quad \text{over the mask and 1 everywhere else} \qquad \text{(F.8)}$$

The Fourier components A_α can be calculated from this function and equation F.6, by numerical integration. The calculated components can then be used to calculate the functional form of the concentration of the reactive species n, using equation F.5. This allows us to calculate the error E.

$$E = \left[\frac{k}{D}.n\right]_{z=0} - \left[\frac{\partial n}{\partial z}\right]_{z=0} \qquad \text{(F.9)}$$

The boundary conditions in Figure F.1 indicate that if we have the correct solution then E will be zero. However we started by assuming that there was no excess deposition next the mask (i.e. A_0=1) and hence the concentration of reactive species n, in the gas next to the mask will be too large. Consequently E will be greater than zero and will decay slowly as we move away from the masks. We can start to rectify this situation by making

$$\left(\left[\frac{\partial n}{\partial z}\right]_{z=0}\right)_{second\_iteration} = \varepsilon E + \left(\left[\frac{\partial n}{\partial z}\right]_{z=0}\right)_{first\_iteration} \qquad \text{(F.10)}$$

where ε is a number between 0 and 1 chosen to make the method converge as fast as possible, without creating instabilities. The above process is repeated for a large number of iterations until E becomes smaller than a set value.

REFERENCES

1 K.F.Riley, *"Mathematical Methods for the Physical Sciences"*, (Cambridge University Press, Cambridge, 1974), p.176